Non-Intrusive Measurement Techniques for Flow Characterization of Hypersonic Wind Tunnels

P. M. Danehy, J. Weisberger,

NASA Langley Research Center, Hampton Virginia, 23681, USA

C. Johansen,

University of Calgary, Calgary, AB, T2N 1N4, CANADA

D. Reese, T. Fahringer,

National Institute of Aerospace, Hampton Virginia, 23681 USA

N. J. Parziale,

Stevens Institute of Technology, Hoboken, New Jersey, 07030, USA

C. Dedic,

University of Virginia, Charlottesville, Virginia 22911, USA

J. Estevadeordal

North Dakota State University, Fargo, North Dakota, 58108, USA

and **B. A. Cruden,**

AMA Inc at NASA Ames Research Center, Moffett Field California, 94035, USA

ABSTRACT

This manuscript describes the wide variety of optical measurement techniques for characterizing the flow in hypersonic wind tunnels. The introduction briefly describes different types of hypersonic wind tunnels, why they are used, and typical freestream conditions including fluctuating quantities. Description of these conditions defines the challenge for measurement techniques which have varying degrees of accuracy and precision, and work only in certain temperature, density and/or speed regimes. The rest of the manuscript is broken up into sections, by measurement technique. Each technique is described and then several examples are provided. The concluding chapter compares and contrasts different aspects of the measurement techniques including accuracy, precision, spatial resolution and temporal resolution.

1. Introduction: The need for characterization of hypersonic wind tunnels

1.1. Challenges in computing the physics & chemistry of hypersonic flight

Hypersonic vehicles fly at thousands of meters per second. At such high speeds, these vehicles impart energy to and heat the surrounding air. The air, in turn, heats the vehicle. The faster the vehicle, the hotter the air and the more difficult to keep the vehicle from degrading thermally and structurally. These high temperatures result in numerous fluid mechanical phenomena that are insignificant in subsonic through supersonic flight. In addition to laminar-to-turbulent transition, turbulence, compressibility, flow separation, and combustion, which are typical fluid mechanical "physics" challenges with subsonic through supersonic flight, hypersonic flight has the additional complications of so called "real gas effects" including dissociation, ionization, vibrational and electronic excitation, non-equilibrium chemistry, and vibrational non-equilibrium. Furthermore, the vehicle's response to the high temperature environment results in degradation to the materials through processes including oxidation, nitridation, and spallation. Effects such as catalycity and radiative heat transfer are also important as they affect heat transfer to the vehicle surface.

To successfully design hypersonic vehicles these phenomena all need to be understood to a sufficient level of detail to allow quantitative prediction of aerodynamic, aerothermodynamic, thermo-structural, and flow-control behaviors. However, the physics and chemistry of these phenomena and the interactions between these phenomena is complex and difficult to compute exactly. Typically, the physics and chemistry are modelled, sometimes simplistically. Examples of models include turbulence models and reduced chemistry models which simplify hydrocarbon chemistry into a limited number of solvable equations. Models for various aspects of non-equilibrium are also used. These models are embedded in the codes used to design hypersonic vehicles, but many of these models are oversimplified and/or untested at the conditions where they are being use, especially in the field of hypersonics. While sophisticated flow physics and chemistry models are sometimes available, they are often overlooked (especially by industrial applications) because of high computational costs. Either way, whether low- or high-fidelity models are being used to compute hypersonic flow, detailed experimental data is required to validate these codes and gain confidence in their use for predicting flight.

When computational methods are used to compute high-speed flows and disagreement is found between the experiments and the computations, two possibilities exist: either the computational method is wrong or the method could be correct but didn't simulate the same experiment. That is, the initial and boundary conditions may have been incorrectly specified or implemented. To eliminate the second option, accurate and precise flowfield data is critically needed especially in the freestreams of hypersonic facilities. Measuring facility freestream flow is the main focus of this manuscript. In addition to the

mean quantities, both the fluctuations in these mean quantities and run-to-run repeatability are of great importance. As stated in the *CFD Vision 2030* report: "*Variability and uncertainty of inputs (boundary and initial conditions, parameters, etc.) to fluid dynamic problems are largely unquantified.*"[1] Non-intrusive optical measurement technologies have the potential to enrich and complement conventional measurement techniques used to characterize facility freestreams. (*N.B.*: Conventional, typically probe- or surface-based instrumentation are outside the scope of this manuscript.)

1.2. The need for different types of hypersonic facilities

Unfortunately, it is not possible to reproduce all of the various important effects of hypersonic flight (e.g. flight velocity, thermodynamic conditions, real gas effects, etc.) in a single ground test facility. Instead, different types of facilities have been developed to simulate different aspects of hypersonic flight on the ground. Many wind tunnels run up against some physical limit, such as the condensation of the freestream gas at low temperatures or material limits in high temperature tunnels. For example, expanding room temperature air to ~Mach 4 drops the static temperature low enough to cause condensation of the air, so to achieve hypersonic flow (defined here as Mach > 5, though other aspects such as real gas effects are also important aspects of hypersonic flight) the air must be heated in some way. Different facilities, designed to test different aspects of hypersonic flight, use different methods of heating the gas depending on factors such as cost, run-duration needed, physical scale required, cleanliness of the flow, turn-around-time between runs, etc. Methods of heating the gas include electrical heating, combustion, electric-arc, and shock-wave heating. An important distinction in this discussion is the difference between the aerodynamic Mach number and the enthalpy associated with an actual vehicle flying at a certain Mach number. In flight these states are equivalent but in wind tunnel tests they can be unequal. For example, a specification of Mach 6 might indicate either the aerodynamic Mach number being 6 or the enthalpy associated with flight at that Mach number at a particular altitude. If Mach number of a facility's operating condition is specified, it should be clarified whether this refers to the aerodynamic Mach number or the enthalpy. Aerodynamics and aeroheating facilities often just simulate the aerodynamic Mach number (usually defined by the area ratio of the facility nozzle), while combustion facilities and materials testing facilities usually need to simulate the correct enthalpy associated with flight at a certain Mach number but may not require a specific aerodynamic Mach number. This flow enthalpy is determined by the flowrate and the amount of heat addition. For example, a Mach 7 enthalpy flow can pass through a Mach 2 nozzle to simulate some part of a hypersonic vehicle such as the combustion chamber.

Below, several types of hypersonic facilities are briefly described along with at least one example cited and a brief description of the primary types of data that are obtained from these facilities. The list is

incomplete but it does help to show the range of types of facilities and challenges associated with optical instrumentation. As will be shown from reviewing several types of facilities and by viewing the typical operating conditions of a few different facilities, there is an enormous range of possible freestream conditions that these hypersonic facilities can produce. Knowledge of the basic operating principles and conditions produced by these facilities is thusly important for designing measurement systems; a wide range of different instrumentation is required to accommodate the broad operational envelopes encountered in these facilities.

1.3. Brief description of several different types of hypersonic facilities

In 2002, Lu and Marren surveyed and provide detailed descriptions of many different types of hypersonic wind tunnels and their features and operating conditions.[2] More recently, Chazot and Panerai reviewed high-enthalpy facilities and plasma wind tunnels.[3] These reference provide much more detailed information about hypersonic flow facilities. Still a quick review is provided herein. Few references are given in this section. Most of the tunnels described below can be found in Refs. 2 and 3:

- Blowdown air tunnels, such as the NASA Langley 20" Mach 6 and 31" Mach 10 tunnels are used primarily for aeroheating and aerodynamic studies. These tunnels typically have a high pressure reservoir upstream and a vacuum sphere downstream of the nozzle and test section. They have run durations of about a minute, limited typically by the size of the vacuum sphere the flow is filling. The air is electrically heated to temperatures just high enough to avoid condensation in the freestream.
- Blowdown nitrogen tunnels, such as AEDC Tunnel 9 can heat the gas to higher temperature than air blowdown tunnels and thus can achieve higher Mach numbers before the onset of condensation. Such tunnels are typically electrically heated and have run durations on the order of 10's of seconds. AEDC Tunnel 9 has nozzles with Mach numbers between 7 and 14.
- Ludwieg tubes are a class of tunnels where a supersonic nozzle is mounted on the end of a long tube. The nozzle and tube are separated by a diaphragm and high pressure gas is put in the tube while the nozzle and an attached vacuum chamber are evacuated. When the diaphragm is ruptured flow begins through the nozzle and test section into the vacuum chamber. Flow continues at a steady rate until the expansion wave propagates to the end of the tube and returns. Such tubes can be made to have "quiet flow" with minimal turbulence. The Boeing/AFOSR Mach-6 Quiet Tunnel at Purdue University is such a quiet hypersonic tunnel. This tunnel was primarily built to study the effects of laminar-to-turbulent transition. Run durations are typically ~10 sec. Again, heating the tunnel gas allows higher Mach number operation. Ludwieg tubes are relatively less expensive to operate than other types of tunnels and are used widely at universities.
- Shock tubes have a diaphragm separating two sections of tube, the higher pressure side called the driver gas and the lower pressure side called the driven gas. When the diaphragm is ruptured a shock wave passes into the driven gas, elevating the temperature, density and velocity of the gas to carefully controlled values which can then be used to study various phenomena such as chemical kinetics[4] or particle drag.[5] The shock wave can also be allowed to reflect off the end

wall of the tunnel and pass back through the gas, further elevating the temperature and density and bringing the gas nearly to rest. This process allows further phenomena to be studied. Various methods are used to increase the temperature of the driver gas which increases the shock wave speed and produced higher temperatures and velocities. Examples are electrical heating, electric arc heating,[6] and heating the gas through isentropic compression by using a free piston.[7]

- Shock tunnels literally extend shock tubes by placing a nozzle at the end of the terminal end of the flow path. The gas at this location, which has been heated and pressurized by the reflected shock, provides a short duration, relatively steady, high temperature, high density reservoir to flow through the nozzle. Typically the throat of the nozzle is smaller than the shock tube diameter so the conditions upstream of the nozzle stay relatively constant for a few tens or hundreds of milliseconds resulting in steady, high-enthalpy flow through the nozzle. By varying the strength of the shock, different flow enthalpies can be obtained. Varying the area ratio of the nozzle produces different aerodynamic Mach numbers. Shock tunnels, including free-piston shock tunnels, can produce high-enthalpy flow suitable for studying real-gas effects. By changing the gas (for example running with air or nitrogen or argon or mixtures thereof) different physics can be isolated and studied. Several high-enthalpy free piston shock tunnels exist and are in use around the world, including T4 (Australia), T5 (USA), HEG (Germany), and HIEST (Japan). In shock tunnels, as the enthalpy is increased the stagnated gas becomes progressively more dissociated, and unfortunately this gas does not recombine in the nozzle. The resulting freestream gas contains undesirable atomic and molecular contaminants (such as NO) as well as metallic species from the facility.

- Expansion tubes and tunnels were developed to explore even higher enthalpy flows than shock tubes and shock tunnels. An expansion tube is a variation of a shock tube using an extra diaphragm that creates an unsteady expansion to produce a relatively short flow duration that has high enthalpy but relatively less dissociation since the gas was never stagnated like in a shock tube or tunnel. This expanded gas can be studied or it can be further expanded by a nozzle to increase the Mach number. Examples of large expansion tubes and tunnels are the X3 tunnel in Australia and the Lens XX tunnel in the USA.

- Combustion heated tunnels are a class of tunnels which use hydrogen or a hydrocarbon fuel to heat the test fluid. Typically oxygen is consumed and water (and sometimes CO_2) is produced by these facilities. In combustion applications the oxygen must be replenished and mixed with the test fluid to enable testing of high enthalpy combustion components such as fuel injectors or engines. The presence of water or carbon dioxide in the incoming flow must be understood and taken into account in analyzing test results. Examples of large combustion heated tunnels in the USA are APTU and the NASA Langley 8-Foot High Temperature Tunnel. These facilities are generally larger and more expensive to build, maintain and operate than many of the other facilities described above.

- Arc-Jet facilities, or closely related plasmatrons, are a class of facilities where an electric arc is used to heat a continually flowing the test gas. When running in air, the arc generates nitric oxide which stays mostly in a chemically frozen state through the nozzle and, again, must be taken into account when performing arc jet experiments. The high-enthalpy air can either flow directly over a test article or can pass through a converging diverging nozzle and pass supersonically or hypersonically over a test sample. Arc jets are used to study supersonic combustion, for example

at NASA Langley's AHSTF in the USA and also for materials testing, for example at NASA Ames' IHF arc jet, also in the USA. The 1200 kW Induction Plasmatron at VKI in Belgium uses an inductively coupled plasma technology to reduce gas contamination from electrodes. Again, these facilities are relatively more expensive to build, maintain and operate than many of the facilities described above.

Facility	Type	Mach Number	Enthalpy (MJ/kg)	Velocity (m/s)	P_{static} (kPa)	T_{static} (K)	Density (kg/m3)
VKI Mach 6 H3	Blowdown Air	6	--	939	1.28	61.0	0.073
AEDC Tunnel 9	Blowdown N2	13.2	1.9	1920	0.5	51	0.003
Purdue Boeing Mach 6 Quiet Tunnel	Ludwig Tube	5.93	--	872.7	0.37	53.9	0.024
EAST	Shock Tube	4	94	9400	30	10000	0.005
T5	Free Piston Shock Tunnel	5.1	11.9	4320	34	1800	0.062
Lens XX	Expansion Tunnel	7.3	20.7	6086	3.68	1881	0.0068
NASA Ames IHF	Arc Jet	4	20	4000	3	1500	0.004

Table 1.1. Freestream conditions from selected facilities. While most of these facilities operate over a range of conditions, typically varying Renolds and Mach numbers and/or enthalpies, only a single "typical" operating condition is shown here for each facility.

1.4. Freestream conditions produced by hypersonic facilities

Table 1.1 shows typical operating conditions from several different types of facilities. To limit the quantity of data in the table, just a few example facility types are shown and a single "typical" condition is shown for each type of facility. Most of these facilities can operate over a wide range of pressures to simulate different Reynolds numbers and some can operate over a wide range of enthalpies. The point of this table is to show the wide range of conditions produced to study different aspects of hypersonic flow.

As shown in the table, the operating conditions can vary wildly depending on the type of facility. Freestream temperatures vary from roughly 50 K to over 2000 K (ranging by a factor of 40). Freestream pressures vary from 0.37 to 50 kPa (ranging by a factor of 135). Velocities vary from less than 1000 m/s to 7000 m/s (factor of 7). The densities are all well below atmospheric conditions (1.17 kg/m^3), and vary by a factor of about 500. These numbers are critically important for choosing which measurement techniques to use. Some techniques only work well in certain ranges of conditions. For example, Rayleigh scattering works best at high densities. Other techniques may only work in a certain temperature range. Table 1 will help establish connections between the performance of certain

measurement capabilities and the actual conditions where they will be used. An advantage of having data like that shown in Table 1.1 is that instrument developers may use this data to try to simulate similar conditions in the laboratory to optimize a technique before bringing it to the facility.

Facility	Type	U'/U	T'/T	m'/m (rho'/rho)	P'/P
VKI Mach 6 H3	Blowdown Air	0.6%	0.8%	5.2%	1.0%
Purdue Boeing Mach 6 Quiet Tunnel	Ludwig Tube	--	--	0.2%	0.01%
T5	Free Piston Shock Tunnel	--	--	<1% @ high frequency	--

Table 1.2. Freestream fluctuation measured or computed in selected facilities.

Another consideration for measurement technique development for freestream quantification is the fluctuations in the freestream. If it is desired to measure the freestream fluctuations it is important to have a rough idea of the expected magnitude of these fluctuations, so that the precision of potential measurement techniques can be assessed for their potential to resolve the facility freestream fluctuations. Ideally an instrument's measurement precision should be better (smaller) than the fluctuations being measured. Table 2 shows the measured, predicted, or inferred freestream fluctuations found in some of the tunnels shown in Table 1. The freestream fluctuations in the freestream of conventional (non-quiet) tunnels is on the order of 1%. To resolve these fluctuations instrumentation should have measurement precision better than 1%. Quiet tunnels have even lower fluctuations that are fractions of a percent. As we shall see, few optical measurement techniques have demonstrated the ability to measure such small freestream fluctuations. Still, if the fluctuating quantities cannot be measured non-intrusive techniques can still provide valuable mean flow data. For example, mean flow data can be useful in establishing run-to-run repeatability or for validating computations of the facility and nozzle flow. Finally, they can provide valuable boundary conditions for subsequent computations.

1.5. Hypersonic nozzle flow and freestream

The flow of gas through hypersonic nozzles is described in detail elsewhere.[8,9] A brief qualitative introduction is given here. Figure 1.1a shows a low-enthalpy hypersonic nozzle flow that can be assumed to be in thermodynamic equilibrium. These conditions would be representative of facilities that have reservoir temperatures well below 1000 K, which is roughly where N_2 and O_2 begin to have significant populations in their excited vibrational states and coincidentally is roughly where O_2 begins to dissociate and produce both O-atoms and nitric oxide (NO). As the gas expands through the nozzle, the temperature, pressure, and density all decrease smoothly until the test section is reached where, ideally, steady flow freestream conditions occur. Low-temperature reservoirs lead to low temperature freestream

flows: commonly on the order of 50 K (limited by the condensation of the components of air). Such flows can be computed successfully assuming laminar flow,[10] though laminar computations ignore the turbulent boundary layers building on the nozzle walls as well as laminar-to-turbulent transition that occurs somewhere along the nozzle walls. Corrections based on conventional probe or rake measurements are used to estimate wall boundary layer thicknesses and improve estimates of the freestream flow.
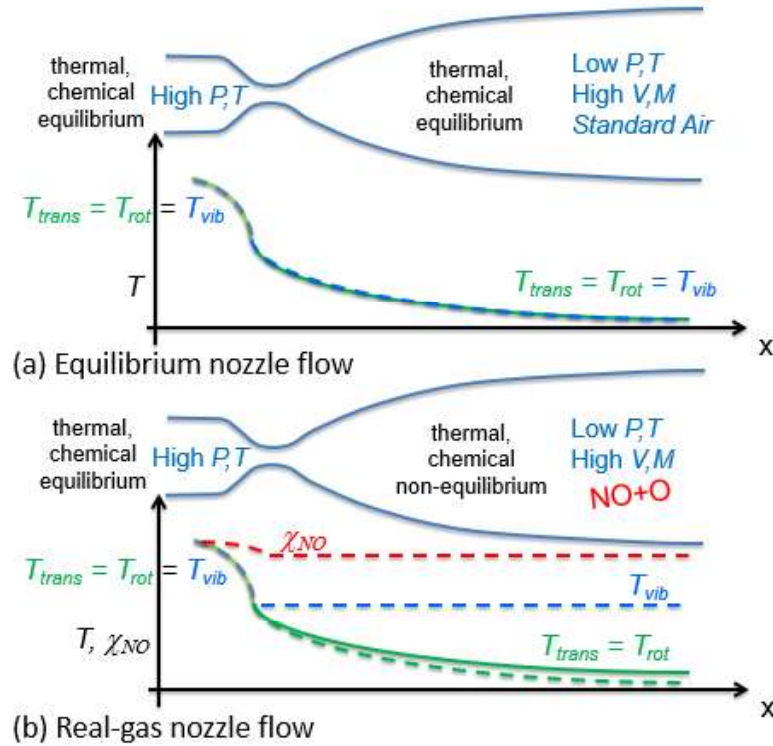
Figure 1.1. Schematics of low-enthalpy equilibrium and high-enthalpy, real-gas nozzle flows.

In a hypersonic flow with real-gas effects, the temperature of the high pressure gas in the reservoir is typically well above 1000 K so the gas is dissociated, producing O and N atoms as well as NO in the case of air. Electronic excitation can occur and some of the species can become ionized, producing O^+, N^+, and NO^+, as well as free electrons. Excited vibrational modes of O_2 and N_2 are populated in high-enthalpy air flows. As the gas expands through the nozzle the gas cools, and collisions keep the flow in equilibrium at first. As the temperature decreases, the excited and dissociated species begin to recombine as the chemical and thermal energy is transferred to kinetic energy of the flow. However, somewhere in the expansion the rate of collisions is not sufficient to keep the flow in equilibrium and the flow enters a non-equilibrium state. For example, the NO does not convert back to N_2 and O_2 even though the temperature may drop below room temperature. Also, the vibrational energy stays frozen in the excited

vibrational states of the different diatomic molecules. Typically the translational and rotational temperatures remain in equilibrium with each other while being significantly different than the vibrational temperature. These processes are depicted in Fig. 1.1b. The dashed red curve shows the trend in the NO mole fraction, the dashed blue curve shows the vibrational temperature, and the dashed green curve shows the translational and rotational temperatures. The solid green curve shows the temperature that would have occurred had equilibrium been maintained. Since energy is conserved, the energy stored in vibrational causes lower (dashed) rotational and translational temperatures than equilibrium. The optical measurement techniques described in subsequent sections endeavor to quantify these many equilibrium and non-equilibrium phenomena.

1.6. Layout of this manuscript

This manuscript is meant to complement two previous von Karman Institute Lecture manuscripts[11,12] and an AIAA Book chapter.[13] The past manuscripts were more pedagogical, including derivations of the theoretical equations of each measurement technique. They were more broadly focused on measurement techniques for aerospace, hypersonic, and non-equilibrium flowfields. The current manuscript focuses specifically on hypersonic freestream measurements with an emphasis on molecular, laser-based, quantitative flowfield measurement techniques (though some non-laser based and non-molecular techniques are also described). There is little or no derivation of the theory behind the techniques described herein. At most, one equation is provided per section, in an effort to make the material approachable for the non-expert, and also to not repeat content from previous manuscripts. The eight sections below each describe a measurement technique or a class of measurement techniques. Each provides an introduction and a brief overview of the theory in layman's terms, including numerous references where the reader can go for further details. Several examples are then cited for each technique. The method of selection of examples differs for each technique's section, where examples are cited for different variations of the technique (as in the section on Laser Scattering Techniques) or as a function of another parameter (as in the section on Particle Image Velocimetry (PIV) where Mach number was used to sort the examples). Laser-based methods are described first, roughly in the order of complexity. Among the laser based methods, PIV is shown last since it requires particles to be seeded into the flow. The last "technique" section describes emission spectroscopy which is not a laser-based technique but which nonetheless can provide quantitative measurements in hypersonic facilities. Finally, the conclusion shows comparisons from the different measurement techniques and provides some example performance specifications for the methods.

2. Absorption Spectroscopy

2.1. Introduction to Absorption Spectroscopy

Laser absorption spectroscopy (LAS) measures the light absorbed through a gas sample of interest. When light of a specific wavelength interacts with atoms or molecules in a gas flow, the light will be absorbed at specific wavelengths. By shining a light source through a gas and measuring the incident intensity on a detector on the other side, various properties of that gas can be discerned. Absorption measurements generally operate as a pitch-catch system, where the pitch side contains the light source and any reference cells needed, and the catch side detects and records the transmitted light signal. The strength, shape, and integrated absorbance of the characteristic spectral features are used to determine the numerous gas properties.

LAS has the ability to measure temperature, T, (translational, rotational, vibrational), pressure (P), species concentrations (number density or mole fraction, X), density (ρ), and velocity (V) of gases of interest. Using these measurements, mass flux can also be determined. Theoretically, all the gas properties can be measured simultaneously with a single well-selected laser, and many studies do include multiple measurements using a single laser. Light from multiple lasers can also be combined together (multiplexed) in a single sensor to measure multiple species and properties. LAS is commonly a path-averaged measurement (that is, integrated along a line of sight). However, the technique can also be used to tomographically reconstruct all the aforementioned properties with an appropriate experimental setup, providing spatial resolution. Laser selection guidelines help assist the researcher when choosing a spectral region to interrogate.[14,15]

Species including CO_2, CO, H_2O, NO, O_2, O, K, Ar, OH, and Rb are all potentially present in the freestream (depending on the facility in question), and can be probed by this technique. Measurements of the freestream have been conducted at the VKI Longshot free-piston facility (T, P, X, and V using CO_2 and CO),[16,17,18] CUBRC LENS expansion and shock tunnels (X and V using NO and H_2O),[19-21] ONERA F4 arc-driven tunnel (T, V, ρ, X using NO and CO_2),[16,22,23] DLR HEG shock tube and ONERA S4MA low enthalpy facility (T, V, and X using NO and H_2O),[23,24] Calspan 96-inch shock tunnel (T, X, and V using H_2O and K),[25,26] NASA Langley Direct Connect Supersonic Combustion Test Facility (DCSCTF) (T, V, and mass flux using H_2O, including tomography),[27,28] and the UVA Direct Connect Scramjet Combustor (UVaSCF) (T, V, and column density using H_2O, including tomography).[29,30] Measurements in shock tubes or expansion tubes have also had a strong foundational impact on the technique.[31-38] Identification of test gas arrival, test gas contact surface arrival, and driver gas arrival is also possible with LAS.[39]

Spectroscopy measurements can be traced back to the 1600s, with the separation of sunlight into its spectrum through a prism. By the early 1800s, the absorption of radiation from the sun was researched by

Fraunhofer, and are known now as the Fraunhofer lines. Broad-spectrum light sources other than the sun were also used, including deuterium, hydrogen, halogen, and tungsten lamps to name just a few. Much knowledge of the structure of atoms and molecules was determined using spectroscopic techniques. When lasers became available in the 1960s, they enabled spectroscopists to make high-resolution measurements of single absorption transitions, which were able to fill in gaps of information in previously recorded spectra that could not be resolved before with the broader light sources (see Ref. 40). In 1977, measurements were made in a shock tube to measure high-temperature, shock-heated CO.[31] Harmonic detection at higher modulation frequencies had been explored at the same time, and in 1978, first and second harmonic detection was used to increase the sensitivity over direct absorption measurements.[41] In the early 1990s, Philippe and Hanson demonstrated both an air mass flux sensor[32] and a sensor for T, P, and V[33] for shock tube flows using wavelength modulation spectroscopy. The wavelength modulation was 10 MHz, while the scan rate was 10 kHz in order to capture high-speed transients in the flows. The study incorporating wavelength modulation to obtain high accuracy for velocity, along with the single sensor design for density measurements (this was used in the low speed tunnel at Stanford). After the initial success of the LAS technique, applications of LAS to hypervelocity flows[19,21,22,26,42] and scramjet combustors[43,44] continued in the 1990s and 2000s. Work in characterizing hypersonic facilities using laser absorption spectroscopy has been an ongoing endeavor from the late 1970s until present day.

Absorption measurements are only as accurate as the spectral data supplied to the models.[45,46] Regions in the near-to-mid IR have been extensively studied by researchers in many fields (medical, atmospheric sciences, combustion, and hypersonics), and much of the spectral data is well established. As new spectral regions are explored due to their accessibility with new lasers, accurate spectral information is needed for the absorption transitions. The subject of many papers is to more accurately define the spectral parameters (such as line strengths, collisional broadening and shift parameters, etc.) of less-investigated portions of the spectrum for molecules that would be of use in future measurements. For example, spectroscopic parameters were investigated for CO_2 near 2.0 μm[47] and for H_2O near 2.5 μm.[48]

2.2. Basic theory of Absorption Spectroscopy

From quantum mechanics, absorption from gas molecules is predicted at discrete wavelengths matching atomic or molecular resonances. However, absorption lines are in fact spectrally broadened to become finite-width absorption features. Consider shining a monochromatic light source through a gas. The incident intensity is measured before passing through the gas, and the transmitted intensity is measured after passing through the gas. The ratio of the transmitted-to-incident intensity is a measure of the transmission through the gas, and from this value, properties of the gas can be extracted. The Beer-Lambert law is the fundamental relation for absorption spectroscopy, shown in Eq. 2.1 below. This

expression governs the transmission of monochromatic light through a homogeneously absorbing medium. The fractional transmission is related to the absorbing path length (L) and to a term called the spectral absorption coefficient (k_v), which depends on the absorbing gas properties such as temperature, pressure, and concentration through the lineshape broadening mechanisms (natural, Doppler, collisional). For details of these mechanisms and how they are computed see Danehy *et al.*[13]

$$\frac{I}{I_0} = exp(k_v L) \tag{2.1}$$

The Doppler-broadened lineshape arises from the Maxwellian spread of velocities of the absorbing atoms or molecules relative to the observer (detector). The width of a Doppler-broadened absorption feature is used to determine the translational temperature of the gas. The rotational/vibrational temperatures are found by taking the ratio of integrated absorbances of two features that have a sufficiently different lower-state energy. Collisional broadening arises due to the collision of molecules, where it is assumed that collisions are binary (only two bodies per collision) and the transition time is fast compared to the collision duration. The pressure of the absorbing species can be determined from the width of a collisional-broadened feature. The concentration of the gas (mole fraction, number density, etc.) can be determined using the integrated absorbance of the feature when temperature and pressure are known. When the laser beam is angled with respect to the flow direction (i.e. not perpendicular to the flow axis), the absorption features are shifted to either lower/higher wavelengths depending on whether the beam is pointing downstream/upstream relative to the flow. The shift of the peaks in wavelength (termed the Doppler shift) is used to determine the flow velocity. By using a double-pass system, where one beam-pass is pointed upstream and the other downstream, the sensitivity of the velocity measurement can be increased since twice the Doppler shift is observed (assuming that the shift is large enough to result in two discrete peaks). Mass flow rate can be computed by taking the product of the previously calculated number density and velocity.

Another method that is widely used is to simulate the absorption spectrum as a function of the gas properties. Quantities of the unknown properties are then iterated and the resulting simulations compared to the measured data. The simulation parameters that yield the best fit between the simulation and measured data is then assumed to represent the gas conditions.

A basic laser absorption spectroscopy setup can be seen in Fig. 2.1a. The system operates as a pitch-catch setup, where the laser (L) is pitched from one side through the gas of interest, and caught on the other side by an appropriate detector (D). The laser wavelength is very finely controlled using a laser diode driver and temperature controller (LDD-TEC). A wavelength reference (WR) is used to accurately define the wavelength tuning of the laser so the measured data can be compared to spectral simulations. The data acquisition system (DAQ) collects the raw data from the wavelength reference and the detector.
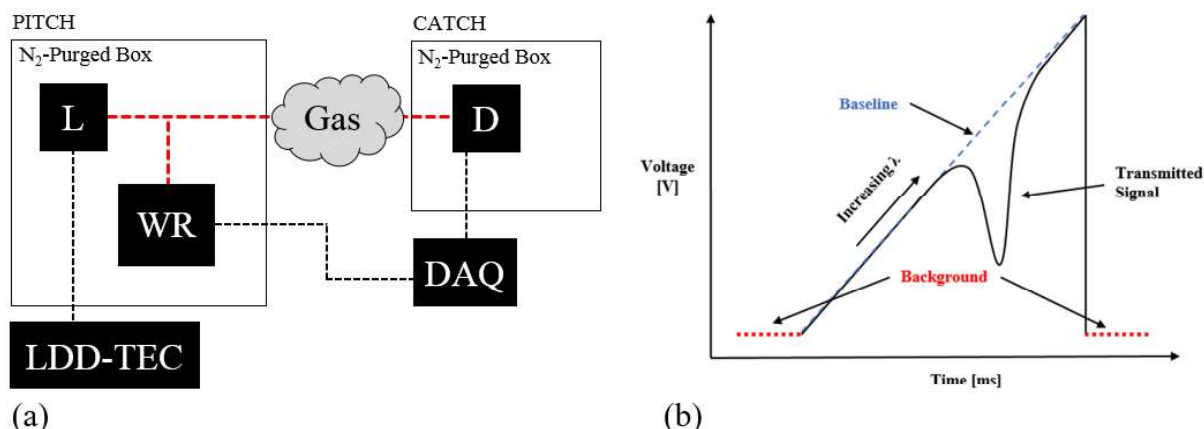
Figure 2.1. (a) Basic laser absorption spectroscopy setup, showing the laser (L), wavelength reference (WR), laser diode driver and temperature controller (LDD-TEC), detector (D), and data acquisition system (DAQ), and (b) a typical ramp used to injection-current tune the wavelength of the laser across absorption features.

The wavelength is typically scanned across the absorption feature of interest using a ramp such as that shown in Fig. 2.1b. The laser is tuned (changed in wavelength) by rapidly varying the injection current through the use of a function generator. At low currents, the laser is below threshold and does not emit light, which provides a background signal (dotted red). As the current increases, the laser emits at increasing intensities, corresponding to an increase in wavelength. The transmitted signal (solid black) and the non-absorbing baseline signal (dashed blue) are used to determine the fractional transmission. The baseline signal can be obtained in many ways, for example by evacuating the flow path and acquiring a scan prior to measurement.

Many fundamental (ground to first excited level) transitions for molecular absorption fall in the infrared (IR) range, so near- to mid-IR laser sources are required (although atomic transitions do occur near the visible spectrum for oxygen at around 770 nm, for example). Many types of lasers are ideally suited for absorption measurements.[49,50] Lead-salt lasers were used in early methods because they were the most commonly available, but operated with cryogenic cooling and had low power output.[31,41] Advances in semiconductor lasers has allowed extensive research in absorption spectroscopy, due to the widespread availability of less-expensive laser diodes, and customer-specific wavelength selections. Distributed feedback (DFB) lasers have output powers of approximately 10-50 mW, with a wavenumber tuning interval of about 1-3 cm^{-1} at rates up to the MHz range, with emission linewidths narrower than 10 MHz. In most applications, temperature of the diode is used to coarsely tune the laser to a wavelength, and injection current is used as a high-speed wavelength tuning. However, rapid temperature tuning for DFB lasers has also been investigated.[51] External Cavity Diode Lasers (ECDL) have very narrow

emission linewidths (smaller than 1 MHz) with a wide tuning range, but require precise alignment and calibration of the mechanical components of the external cavity. Quantum cascade lasers (QCL) are designed for the mid-IR spectral range between 3-20 μm. Slow temperature tuning ranges can be as large as 20 cm^{-1}, while faster injection current tuning ranges fall between 2-4 cm^{-1}. External cavity QCLs (EC-QCL) can have even larger tuning ranges (100 cm^{-1}) while maintaining the narrow laser linewidths (30 MHz) needed for accurate lineshape determination. Vertical cavity surface emitting lasers (VCSEL) have lower powers than DFB lasers (0.5-5 mW), but have a broader tuning range on the order of 30 cm^{-1} (total spectral range from approximately 750 nm - 2.4 μm). Fourier domain mode locked lasers (FDML) have a broadband spectral range (100 nm in the near-IR) with high repetition rates (10 kHz − 1 MHz), and relatively narrow laser linewidths.

To keep costs low, a factor used in absorption transition and laser selection is to use lasers developed for the telecommunication industry's wavelength range (typically in the near-IR). In this range, fiber optics are also readily available and inexpensive. Using optical fibers makes multi-beam systems easier to set up than free-space systems. When concentrations are low, stronger absorption transitions further into the mid-IR range may need to be used. Care must be taken to ensure the optics used are transparent to these wavelengths. For windows, less expensive BK-7 which is transparent in the near-IR can no longer be used; instead, CaF_2, sapphire, or germanium are used, but are also significantly more expensive.

Absorption spectroscopy relies on the precise control of emitted wavelength with time. While the current and temperature of the laser sets the emission wavelength, it does not determine nor measure the absolute wavelength itself. A wavelength reference is needed, such as a wavemeter, a solid etalon, an air-spaced etalon, or a reference gas cell at known conditions.

Detector selection is another important step in the system design. The wavelength range of the detector must match that of the emitted radiation from the laser while also providing adequate sensitivity and bandwidth. InGaAs sensors are sensitive from 800 nm to 2600 nm, with bandwidths ranging from low MHz range up to over 1 GHz. InSb detectors are sensitive in the range between 3 μm and 5 μm, and are generally liquid nitrogen cooled to reduce noise. InAsSb detectors cover an approximate range from 1 μm to 5.8 μm, and can be operated with a thermoelectric cooler to reduce noise, while exhibiting MHz range bandwidths. Ge detectors operate in generally the same range as InGaAs detectors, but have higher levels of thermally induced noise and bandwidths in the hundreds of kHz. Another option in the 1 μm to 4.8 μm range are the less expensive PbS and PbSe detectors, but these have lower bandwidths, which can be suitable for slower direct absorption spectroscopy (DAS) measurements. To reach the lower wavelength regions necessary for O_2 measurements, inexpensive (a couple hundred dollars) Si photodetectors are used, and have a sensitive range between 200 nm to 1100 nm with hundreds of MHz

bandwidth. To extend the cutoff wavelength into the far-IR, HgCdTe detectors are used with thermoelectric coolers, and cover the range from 2.5 μm to above 10 μm, with bandwidths in the potentially hundreds of MHz. Note that the responsivity of the detectors over the wavelengths mentioned in this section are not constant. That is, there is generally a peak responsivity at a certain wavelength, and a drop-off at other wavelengths.

Direct absorption spectroscopy is the simplest and most intuitive version of LAS. The laser wavelength is scanned across the absorption features, and the absorbance can be directly determined by dividing the absorbing signal by the non-absorbing baseline signal as in Fig. 2.1b, and using the Beer-Lambert law. This technique is useful when simple interpretation of the data is needed, for smaller data sets, and allows the use of less expensive detectors and data acquisition systems (lower bandwidth). Problems arise in DAS when beam steering, window fouling, and beam path etaloning (wavelength-dependent constructive/destructive interference between parallel-faced optics) cause interference and non-absorption intensity attenuation of the signal. Flow luminosity of high-temperature flows can be problematic for wide spectral-range measurements, but generally does not affect narrow spectral measurements like those used to scan a single absorption transition. This is because the luminosity is spectrally much wider than the transition itself, and the signal will look like it is riding on a constant intensity background, which can be subtracted before processing the data. For low density hypersonic facilities, beam steering is less of an issue. Window fouling can be prevented by purging the surfaces with non-absorbing nitrogen. Etaloning can be mitigated by using wedged optics wherever possible along the beam path. Log-ratio detection of DAS can be used, and has been demonstrated to be an effective way of correcting for stray light falling on detectors.[52]

Wavelength or frequency modulation spectroscopy (WMS/FMS) takes the simple DAS wavelength tuning ramp and adds an extra, high-frequency sinusoidal modulation on top.[53-55] This shifts the absorption information to harmonics of the modulation frequency which can be isolated using a lock-in amplifier, reducing the interference from low-frequency noise that can dominate in DAS measurements. By normalizing the 2f (lineshape-sensitive) signal by the 1f (laser intensity-sensitive) signal, noise from non-absorption losses is suppressed. For extremely high frequency measurements (MHz range), fixed-wavelength WMS (FW-WMS) can be used. The downsides of FW-WMS is that the precise modulation-centered wavelength must be known. To alleviate this need, scanned-wavelength WMS (SW-WMS) allows for a reference cell (as in DAS) to be used to characterize the wavelength scanning in time, but also decreases the measurement bandwidth. The analysis of the raw data from WMS/FMS methods is more intensive than that of DAS measurements.

Cavity ringdown spectroscopy (CRDS) inserts the probe beam into a reflective cavity, and measures the time it takes for the photons to attenuate, which can then be related to the absorption, length of the cavity, and the reflectivity of the mirrors.[56] Cavity enhanced absorption spectroscopy (CEAS) increases the effective optical path length through the gas sample, and the measured absorbance can be related to the single-pass absorbance using a cavity absorption gain factor. Using CEAS, uncertainties of post-shock temperatures of ±1% and of excited-state populations of ±10% for atomic oxygen have been reported at scanning rates of 50 kHz.[57]

Time-division multiplexing is used in many studies to probe multiple species/features in different spectral locations using more than one laser, but propagating along a single beam and detected on a single detector.[58]

The glaring limitation inherent in absorption spectroscopy is that the measured signals are path-integrated. Line-of-sight discretized absorption feature simulations have been performed to couple CFD simulations to absorption spectra,[27,59,60] and also to take advantage of the path-integrated nature of the measurement. Tomographic LAS systems have been used to provide temporally and spatially resolved measurements of gas properties at high tuning rates (~50 kHz).[61]

Noise is inherent in every measurement system from the light source, detectors, and acquisition systems. The real absorption signal must stand out from the noise. The lower limit of detection is different for the different methods. DAS needs higher SNR, while WMS is order of magnitude more sensitive than DAS.

Early DAS measurements reported low ppb detection limits.[41] Sub-ms temporal resolution, along with experimental uncertainties of 75 m/s, 0.07 atm, and 75 K for velocity, pressure, and temperature, respectively, were reported in the early 1990s.[32,33] For early WMS measurements, sensitivities of 10^{-4}-10^{-5} fractional absorption were achieved with modulation in the kHz range. Recent studies report accuracies of <0.5% for velocity, <1% for relative wavenumber linecenter determination, <4% for temperature, <2% for mass flux, and <1% for integrated absorbance. The spatial resolution along the beam path is limited by the beam diameter, usually on the order of a millimeter, but spatial resolution using tomography is increased by using more lines-of-sight in the reconstruction of the flow field.

Commonly detected species in hypersonic flows are CO_2,[16-18,42,62-68] CO,[31,37,42,65-67,69] NO,[20-23,70,71] O_2,[32,33,60,72,73] and H_2O.[19,23,25,27-30,34,36,38,72,74,75] Less common species that have also been used as markers in hypersonic flows are K,[26] Ar,[76] OH,[77] O,[78] and Rb.[79]

2.3. Examples of Absorption Spectroscopy

2.3.1. P, T, and V using CO_2 Measurements at VKI Longshot

A scanned-wavelength direct absorption spectroscopy system was used to probe the CO_2 transition at 1.6 μm to measure freestream pressure, temperature, and velocity.[17,18,64] Longshot is a short duration free-piston facility with test times on the order of 20-40 ms, and freestream temperature and pressure of approximately 100 K and 500 Pa, respectively. Due to the high plenum temperatures and pressures just before the expansion nozzle, real gas effects need to be considered. During the expansion through the nozzle, the large pressure drop results in vibrational freezing of the test gas and potential condensation. The transducer-based approach for determining freestream conditions at the Longshot facility uses reservoir/plenum pressure, and total pressure and wall temperature (which is used to compute the stagnation heat flux in the freestream) on a hemisphere probe in the freestream of the test section. A model based on an expanding flow and Fay-Riddell heat transfer correlation is used.[80] The model assumes an initial guess for the reservoir temperature, and is iterated until the reservoir temperature converges to its actual measured value. Uncertainties of the model's freestream values for temperature, pressure, and velocity have been reported as 10.1%, 7.2%, and 3.2%, respectively (for N_2, since no uncertainties have been computed for CO_2).

The external cavity diode laser (ECDL) used had a narrow scanning range of about 1.5 cm^{-1} to 2 cm^{-1}, which probes a single rovibrational transition of CO_2. The Doppler wavelength shift in the Longshot facility is limited in one respect by the available beam propagation angles across the tunnel (10º-20º). A double-angle beam propagation setup was used (one pointing downstream, one pointing upstream), where the angle from the perpendicular was ±19.3º. A raw data absorbance trace for test 1622 can be seen in Fig. 2.2, where the measured raw data are shown with black circles and the double Voigt peak fitting is shown in red. Two peaks are seen due to the Doppler shift; one peak is shifted lower in relative wavenumber and the other shifted higher in relative wavenumber due to the downstream/upstream propagation angles.
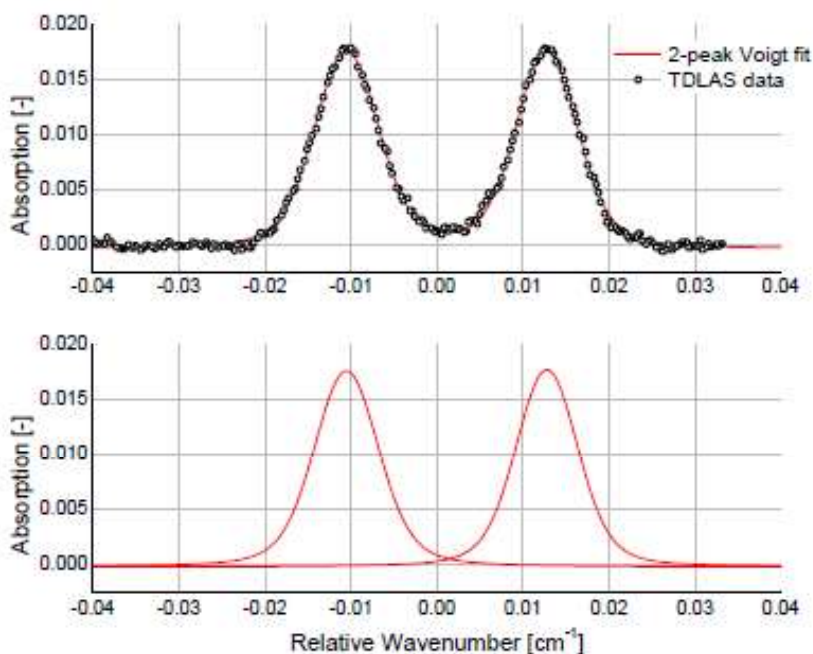
Figure 2.2. Fit to absorption data utilizing a 2-peak Voigt model. Top plot shows raw tunable diode laser absorption spectroscopy (TDLAS) data superimposed onto the total fit function. The bottom plot shows the separate contributions to the total fit. Reprinted with permission of the authors.

Temperature, pressure, velocity, and enthalpy results can be seen in Fig. 2.3. The most up-to-date data reduction and interpretation can be found in Meyers *et al.*[18] The measurements are separated by (and averaged over) approximately 1.6 ms due to the 600 Hz scanning rate, resulting in about 15 data sets per run. The higher discrepancies between TDLAS and model-computed values for temperature is because of difficult baseline fitting of the raw data due to vibrations. This error can be seen to carry into the pressure results as well. Freestream velocity results are less sensitive to the baseline fitting errors because they use the separation of peaks of the Doppler-shifted features. The velocity agrees well with Longshot facility values. The uncertainty of the velocity measurements was reported as approximately ±100 m/s out of a flow velocity of about 1500 m/s. The enthalpy was computed using the temperature and velocity, and shows good agreement with the facility model values (±10% uncertainty). This is because the major contribution to enthalpy in hypervelocity flows is from the velocity, and not the less well-defined temperature. These results demonstrate that although temperature and pressure can be hard to fit accurately when harsh conditions exist, the velocity and thus enthalpy of the facility can still be accurately determined.
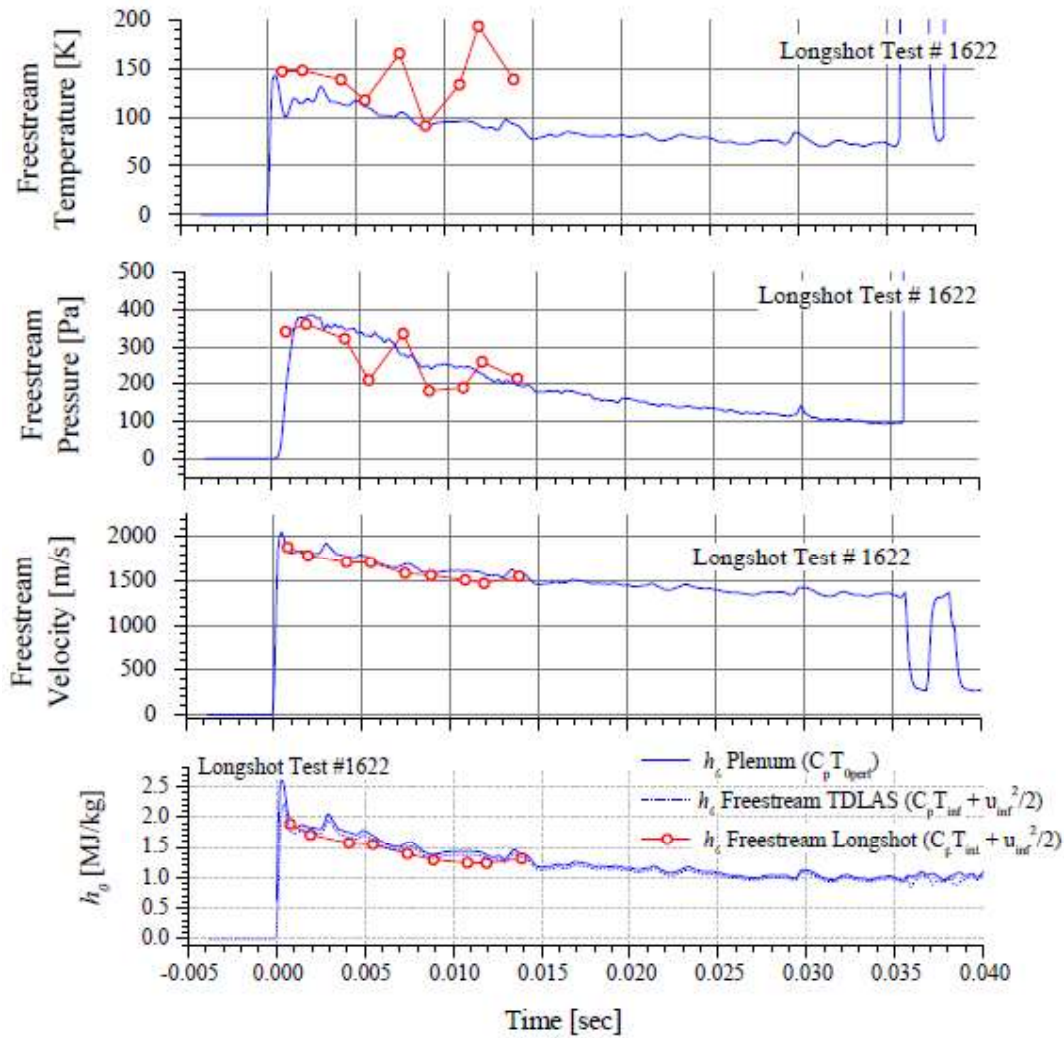
Figure 2.3. Freestream (a) temperature, (b) pressure, (c) velocity, and (d) computed enthalpy for test 1622, with comparison to Longshot facility model values. Adapted with permission of the author.

2.3.2. *T using electronically excited O in NASA Ames IHF*

Measurements at the NASA Ames high power (60 MW) interaction heating facility (IHF) were performed by Nations *et al.* to monitor the gas temperature in the plenum before the expanding nozzle to help characterize the test environment.[78] Accurate knowledge of flow enthalpy is vital for determining test conditions in the facility. To tailor the flow enthalpy, additional air (add-air) is injected and mixed with arc-heated gases just upstream of the expansion nozzle. The add-air mixing plenum was initially 3.7 cm long, but since the turbulent mixing process is not well understood, the mixing may be incomplete and temperature gradients at the nozzle inlet manifest as non-uniformities in the test section.

Computational fluid dynamics (CFD) models are used to determine the state of the gas in the test section, but due to the complexity of the arc-heating, they typically only model from the inlet of the nozzle to the testing chamber. The accuracy of these models then relies on the knowledge of the nozzle inlet boundary conditions, which for this facility uses multiple discrete radial rings, each assuming fully mixed, local thermodynamic equilibrium flow. The purpose of the laser sensor was to determine whether the add-air was sufficiently mixed with the arc-heated gases before entering the nozzle.

A fiber optic system split an external cavity diode laser into four separate beams, which were then pitched across the plenum chamber and detected on the other side. The electronically excited atomic oxygen (O*) transition located at 777.2 nm was probed at a scanning rate of 100 Hz. A moving average of 100 scans was used, resulting in an effective measurement rate of 1 Hz. The laser tuning range was approximately 2 cm^{-1}, which was just wide enough to scan through a single transition. The absorption of a single scan of one of the four laser beams can be seen in Fig. 2.4. The baseline signal in Fig. 3.4a shows what the intensity would be if no O* were absorbed along the path length. The absorbance was calculated using the Beer-Lambert law, and fit with a Voigt profile in Fig. 3.4b, along with the residual of the fit below it.
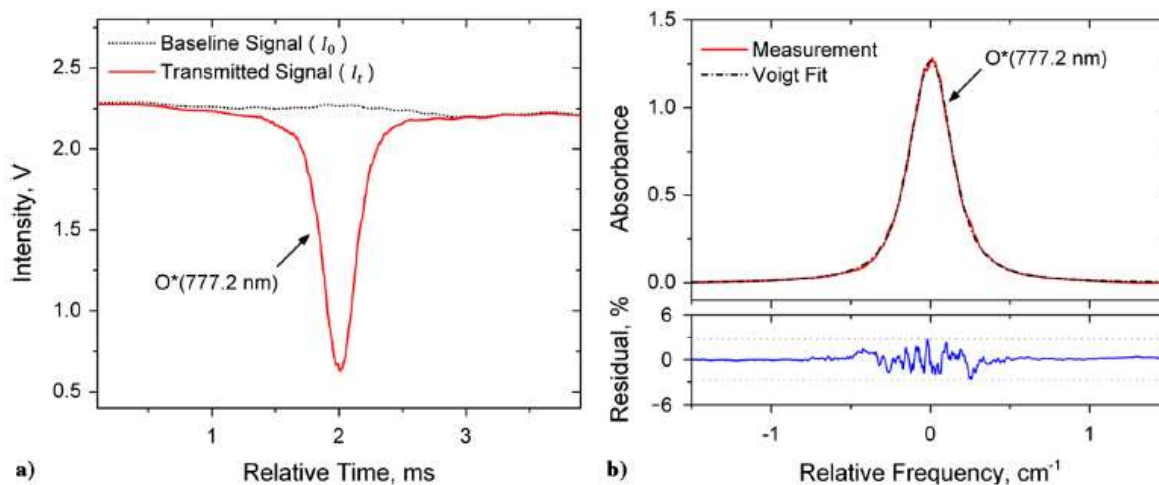

Figure 2.4. Measured O* absorption from a single laser scan a) raw transmitted intensity b) absorbance versus wave number.[78] Reprinted with permission of the authors.

Due to the unavailability of high-temperature spectroscopic parameters (collisional broadening coefficients and potential Zeeman broadening), the Doppler widths, and thus temperatures, were not extracted from the fit Voigt lineshape. Instead, the Voigt profile was used to compute an integrated absorbance (3% overall uncertainty) to determine the temperature (4% overall uncertainty at 7260 K). When the signal-to-noise ratio decreased below a threshold of unity, the detection limit of the system was reached, which occurred at about 4500 K for this absorption transition and setup. Two add-air conditions

were tested: the first (condition I) was for a ratio of add-air to main air of 0.27, and the second (condition II) was for a ratio of add-air to main air of 0.93. Significant differences of temperature in the four laser measurement paths indicated that mixing was incomplete for both add-air conditions.

To increase mixing, the length of the plenum chamber before the nozzle inlet was extended such that the new length was approximately 38 cm. Optical measurements could also then be made in 10 cm axial increments along this new plenum. Axial measurements of the path-averaged temperatures along the plenum indicated a reduction in temperature signifying an increase in mixing, but also showed that the modified plenum length was still not long enough to ensure complete mixing.

To compare the original and modified plenum designs, CFD simulations of the nozzle inlet were compared to laser measurements at the plenum exit (3.7 cm and 38 cm downstream of the add-air inlet for the original and modified plenums, respectively). Results for add-air condition I and II are shown in Fig. 3.5a and b, respectively.
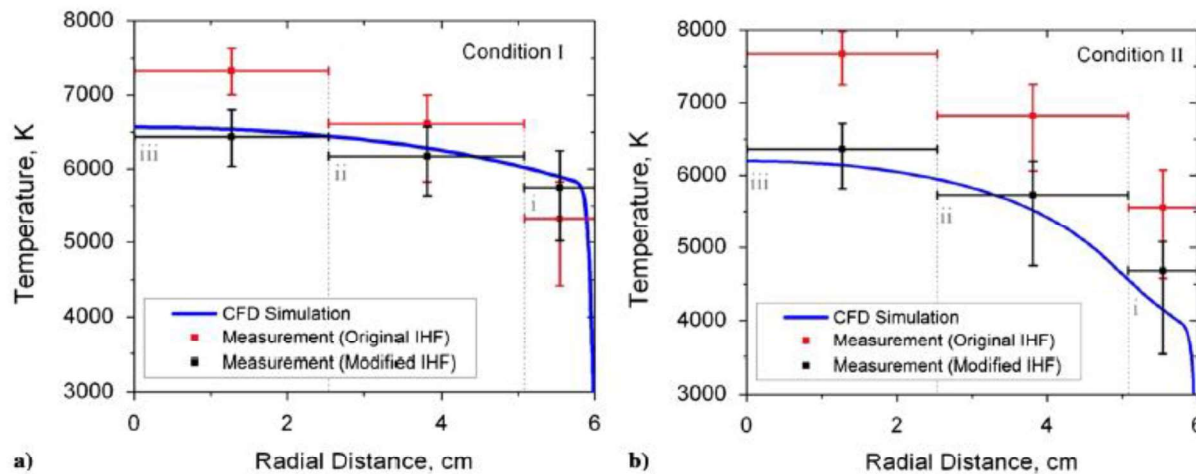
Figure 2.5. Simulated (blue line) and measured temperature distributions a) condition I and b) condition II with upper (red) points in original and lower (black) points in modified IHF.[78] Reprinted with permission of the authors.

For both add-air conditions, the modified plenum design resulted in increased agreement between the laser measurements and the computational results for the radially stratified temperature. The radial temperature gradient was also captured for both conditions using the modified plenum, suggesting a well-mixed combination of add-air and arc-heated flow. The authors suggest further improvements by increasing the number of lines-of-sight for higher fidelity comparisons with CFD. In this facility, the absorption spectroscopy measurements aided a redesign of the facility to improve the uniformity of flow entering the nozzle, which can then provide a more accurate state of the flow in the testing chamber.

2.3.3. V, T, and Mass Flux using H₂O in NASA Langley DCSCTF

Chang *et al.* performed measurements of mass flux in the vitiated flow of the NASA Langley Direct-Connect Supersonic Combustion Test Facility (DCSCTF).[27] The WMS method was used to measure the temperature and velocity of H_2O transitions at 1349 nm and 1341.5 nm. One of the lasers pointed upstream at 45° while the other pointed downstream at 45°, for a total crossing angle of 90°. At the selected wavelengths, optical fibers could be used to simplify the setup, and relatively inexpensive BK-7 glass was also used. The scanning rate was 50 Hz, which was sufficient due to the longer run times of the DCSCTF (~50 s). The mass flux was then determined from measured temperature and velocity, in addition to facility pressure measurements.

To obtain spatial profiles across the channel in the vertical and horizontal directions, the system was mechanically translated along either axis, and one second of data was taken at each of the 10 discrete locations until the system had scanned from one wall to the other. The total time for the acquisition along one axis was 13 seconds, which included time for acquisition and movement.

CFD simulations of the flow in the duct were used to compute path-integrated lineshapes for both the upstream and downstream laser beams. Results of the velocity from the Doppler shift for various duct boundary layer thicknesses showed a linear reduction of the velocity with increased boundary layer thickness. The decrease in measured velocity was due to the path-integration through the slower boundary layer flow in addition to the freestream core flow. The CFD predicted that 10% of the path length was in the boundary layer flow in the facility, resulting in a decrease of the measured velocity relative to the core velocity of just 2%. From these CFD results, a velocity correction could be used for actual facility measurements.

Results for the transient mass flux from the velocity and temperature measurements of the LAS measurements are shown in Fig. 2.6, for both the (a) uncorrected and (b) corrected velocities. Both the upstream and downstream facing beam traces are shown and are in good agreement. The predicted value from the facility model is shown with a blue line, and agrees well with the LAS computed mass flux. The slow decrease of mass flux with time is due to a decrease in the O_2 mass flowrate supplied to the facility.
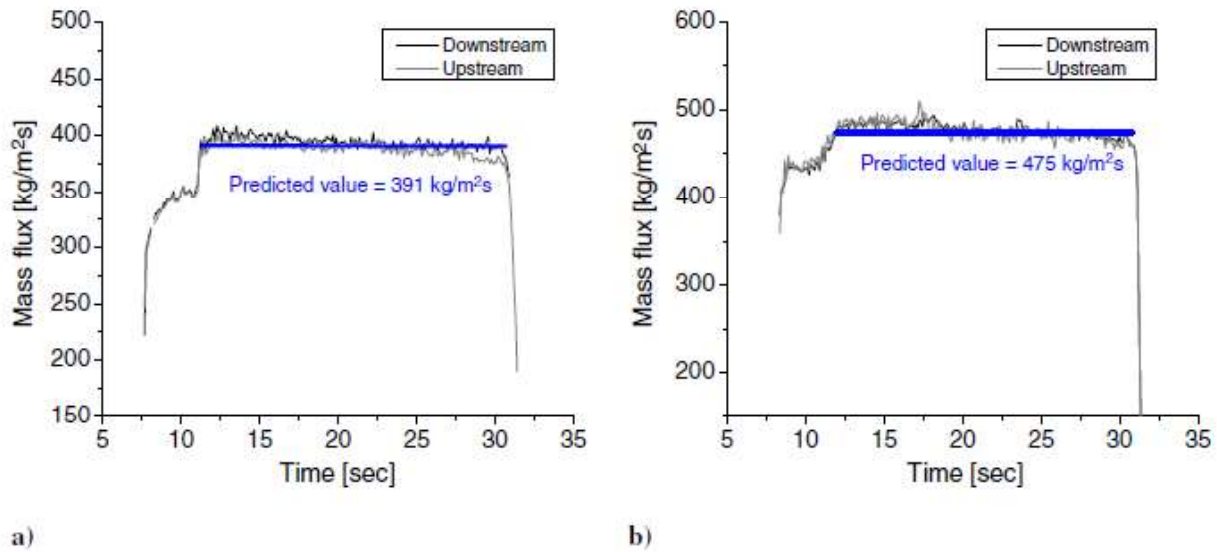
Figure 2.6. Mass flux using temperatures taken with downstream- and upstream-pointing beams: a) in the center horizontal plane for the Mach 7 flight condition and b) in the center vertical plane for the Mach 6 flight condition. Facility model value is also shown in blue. Reproduced with permission from the authors.

By scanning the measurement system in both the vertical and horizontal center-planes at discrete points, the measured values were determined at transverse points across the duct, providing a spatial measurement of the flow properties. The mass flux along the vertical and horizontal center-planes is shown in Fig. 2.7a and (b), along with the corresponding CFD solution across the duct.
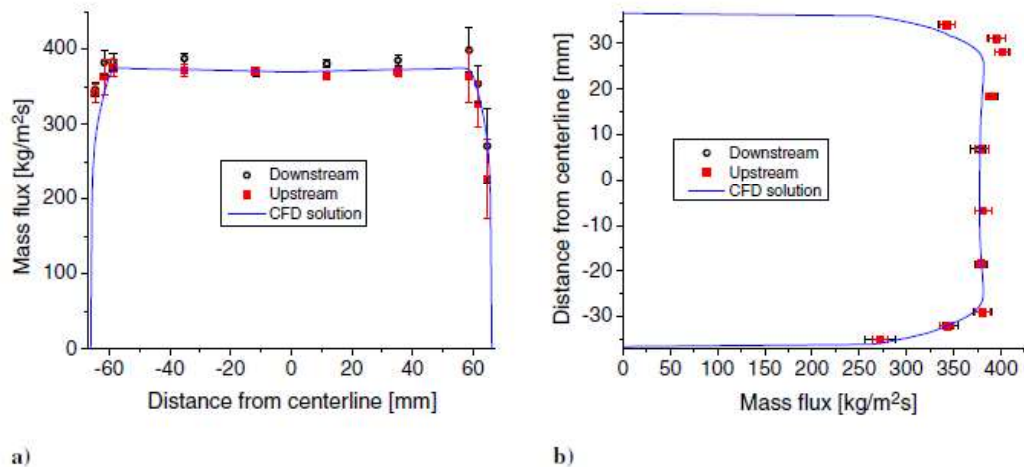
Figure 2.7. Spatially resolved mass flux at Mach 7 condition plotted from a) left to right of channel (facing downstream) in vertical planes and b) top to bottom of channel in horizontal planes. Reproduced with permission from the authors.

The measurements and CFD agree well, which is expected due to the excellent agreement of the velocity and temperature measurements. The uncorrected velocity is about 1.7% lower than the facility-predicted value, and after correction is within 0.25% of a 1630 m/s flow. The standard deviation of the average temperature is approximately 10 K. The error bars on the measured data are from the standard deviation over the one second of data acquisition time at that measurement location. When measuring through mostly freestream core flow, the measurements and CFD agree very well with small errors. When measuring through mostly boundary layer flow, the measurements and CFD differ more and have higher errors. The good agreement between mass flux measurements and facility models over the entire tunnel cross section indicates the usefulness of this technique for future mass flux measurements, given that velocity and temperature can be accurately measured.

2.3.4. *Tomographic H_2O Concentration at NASA Langley DCSCTF and UVaSCF*

The path-integrated nature of normal absorption measurements is a limitation when trying to analyze cross sections of flow in hypersonic test facilities. By using many lines-of-sight simultaneously, a tomographic reconstruction of the flow field can be obtained. Measurements of H_2O number density were performed by Busa *et al.* at both the University of Virginia Supersonic Combustion Facility (UVaSCF) and at DCSCTF. The initial demonstration is given in Busa *et al.,*[28] and the updated results from the tomographic-reconstruction are given in Busa *et al.*[30] The purpose of these measurements was to assess the flow at the exit of a scramjet engine to quantify its combustion efficiency. The H_2O results, along with a known injected hydrogen flowrate to the engine, could then be used as an assessment of combustion efficiency, much like CO_2 and H_2O are used as combustion efficiency indicators in the burning of hydrocarbons.

The initial system at DCSCTF used five individual laser pitch/catch boxes (called Tomographic Emitter-Detector, or TED, boxes) mounted equidistant radially on a rotational ring around the exit plane of the facility. Each TED box can rotate about its own axis in steps of 1.3º to scan a total range of 26º, creating a fan. The entire five-TED box setup only needs to rotate 72º to capture all possible angles and lines-of-sight. In order to probe multiple transitions at the same time (low and high lower-state energy transitions), three lasers were multiplexed into a single fiber. The first two lasers probed "cold" transitions, while the third laser probed "hot" transitions. Using fibers over free-space optics is critical for tomography because the setup would be both expensive and cumbersome otherwise. Run times to obtain a complete reconstruction required about seven minutes.

The same tomographic technique was used at the UVaSCF, and the tomographically reconstructed H_2O number density was obtained. A stereoscopic PIV (SPIV) setup was used to measure three-component velocities at the same plane as the absorption measurements. The density of H_2 at the

measurement plane was calculated using the H_2O number density using the assumption that all the H_2 molecules exist either as H_2O or as the unburned H_2 fuel. The mass flow rate of H_2 could then be calculated using the H_2 density, velocity, and the area of the spatial pixel (2 mm x 2 mm) in the measurement plane. Combustion efficiency was finally computed by comparing the total mass flow rate of H_2 at the exit to the known injected H_2 fuel.
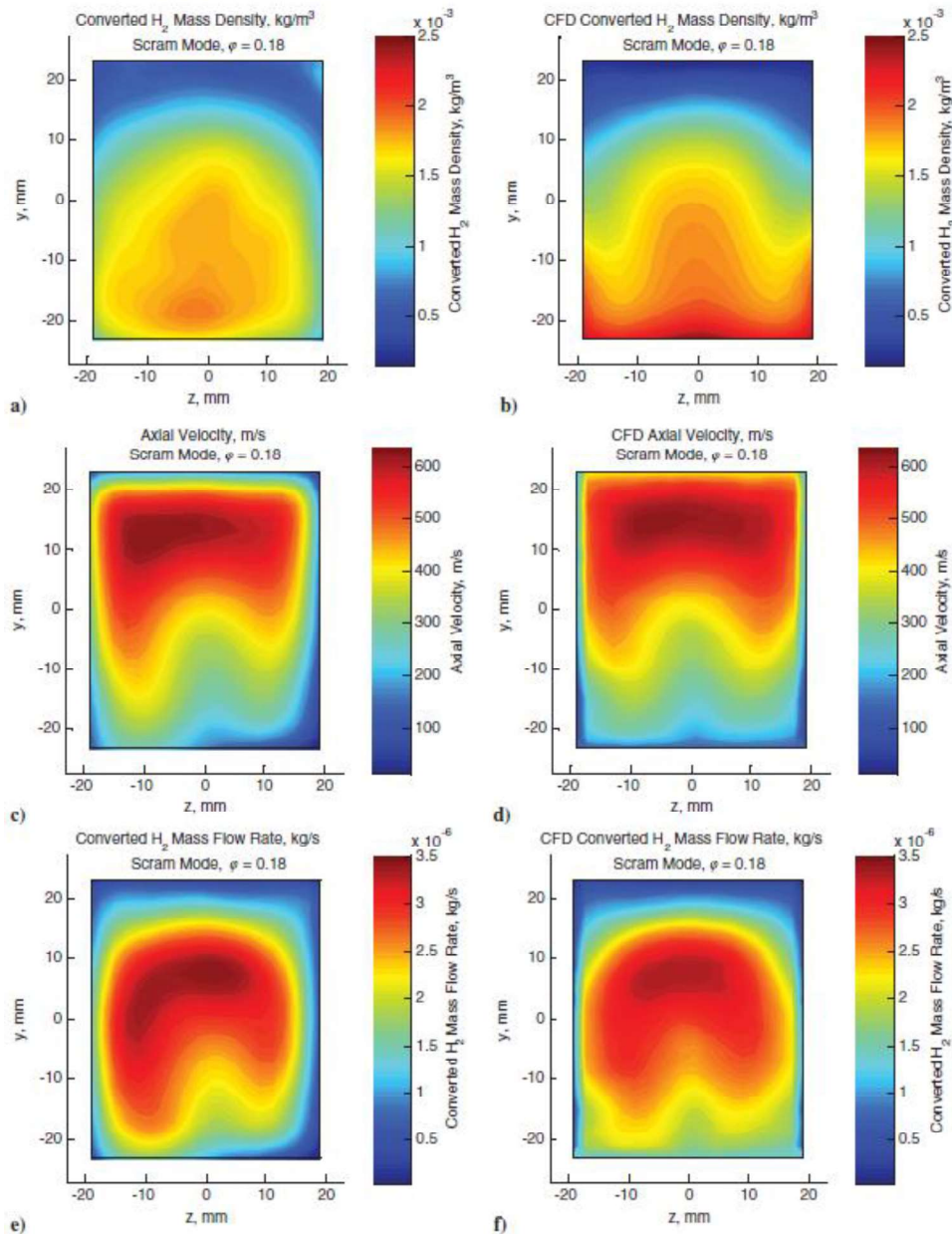
Figure 2.8. Measurement plane H2 density, axial velocity, and H2 mass flow rate (2 mm x 2 mm pixel area) via absorption/SPIV (a,c,e) and CFD (b,d,f).[30] Reprinted with permission of the authors.

Measurements using the tomographic setup (now with just a single TED box) were conducted at the UVaSCF, and the tomographically reconstructed H_2 density, axial velocity, and H_2 mass flow rate were compared to CFD simulations of the same quantities, shown in Fig. 2.8. Measurements were performed at a plane 5 mm downstream of the exit of an H_2-fueled dual-mode scramjet engine. The comparison between experimental and numerical solutions shows good agreement, although the asymmetry is higher in the experimental data. The mass flow rate of the H_2 at the measurement plane has an uncertainty of ± 8.5%. The combustion efficiency calculated from the experimental measurements and those obtained from CFD simulations are very close (98.4% ± 8.5% from experimental vs. 99.5% from CFD).

When running tests at the UVaSCF, only a single TED box was used because flow duration was long. When moving the system to a facility with shorter run times such as the DCSCTF, five TED boxes were used instead to decrease the measurement time by a factor of five. Testing was still segmented because a full reconstruction using the five boxes took seven minutes, requiring eight runs for a complete database (maximum run time of approximately 50 seconds). Tomographic measurements like those demonstrated here can provide real spatial resolution of hypersonic facility freestream flows, whereas single line-of-sight measurements are always path-integrated.

2.4. Conclusions for Absorption Spectroscopy

Absorption spectroscopy has many benefits as an optical diagnostic in hypersonic flows. The measurements are non-intrusive, *in situ*, and easy to analyze (especially with DAS). Measurement rates can be very fast if the facility requires it (expansion tunnels). If the wavelength selection allows it, fibers can be used to facilitate the simple pitching and catching of light, which can be especially useful for multiple laser/line-of-sight measurements (such as tomography). Selection of isolated transitions makes the results species-specific and unambiguous. Lasers currently used for absorption spectroscopy are typically low power, small, lightweight, robust, and relatively inexpensive. The entire systems can be somewhat easily transitioned over to a flight-test instrument, which is also made easier because the systems are robust. If multiple lasers are used to probe multiple lines or species, multiplexing can be used to avoid purchasing more optics and detectors. Their biggest benefits are the ability to provide quantitative, multi-property, time-resolved, multi-species measurements with a single instrument.

Although there are many benefits to LAS methods, every optical technique has its limitations. The biggest limitation for simple measurements is their path-integrated nature. If large gradients in flow properties are present along the beam axis, it can be hard to de-convolve the actual properties of the gas at the location of interest. Since absorption is path-averaged, the tunnel boundary layers will be included in the measurement if the laser passes through them. This can be somewhat mitigated by looking at the Doppler shift to see which lines are in the faster core flow versus the slower boundary layer flow. Using

CFD models to simulate the laser absorption along the line-of-sight and compare to measured data has also proven useful. Tomographic reconstruction can compute a 2D spatial reconstruction of the flow volume at fast tuning rates, but the setups are more complex, expensive, and take longer to obtain the reconstructed results. Depending on wavelength choice, which is limited by species transition strengths, optical materials may be more expensive, and fiber systems may not be available or are prohibitively expensive. When lower limits of detection are needed, high-frequency modulation techniques can be used, but they also require faster, more expensive detectors and data acquisition systems. Systems can range from low-cost and simple, to high-cost and complicated. The path to take is clearly governed by many factors, and is ultimately up to the engineer.

3. Planar Laser-Induced Fluorescence (PLIF)

3.1. Introduction to PLIF

Planar laser-induced fluorescence is a well-established non-intrusive laser diagnostic used to study a wide range of fluid mechanic problems, including hypersonic flow.[13] Typically, a laser beam is expanded using sheet forming optics and directed into a region of interest in the test section of a hypersonic flow facility. Optical access into the test section allows for a detector, normally a digital camera (CCD or CMOS) with an intensifier, to image the fluorescence emitted from a tracer species that interacts with the laser sheet in the flow. PLIF is most commonly used as a qualitative visualization technique to observe various fluid mechanic and combustion features in high-speed flows. While PLIF can be used for molecular tagging velocimetry (MTV) that is described in Section 4. Figure 3.1 shows a high-level schematic of an example PLIF visualization experiment to observe the separated near wake behind a hypersonic re-entry vehicle model. In this scenario, a PLIF tracer species is injected into the wake via the sting.
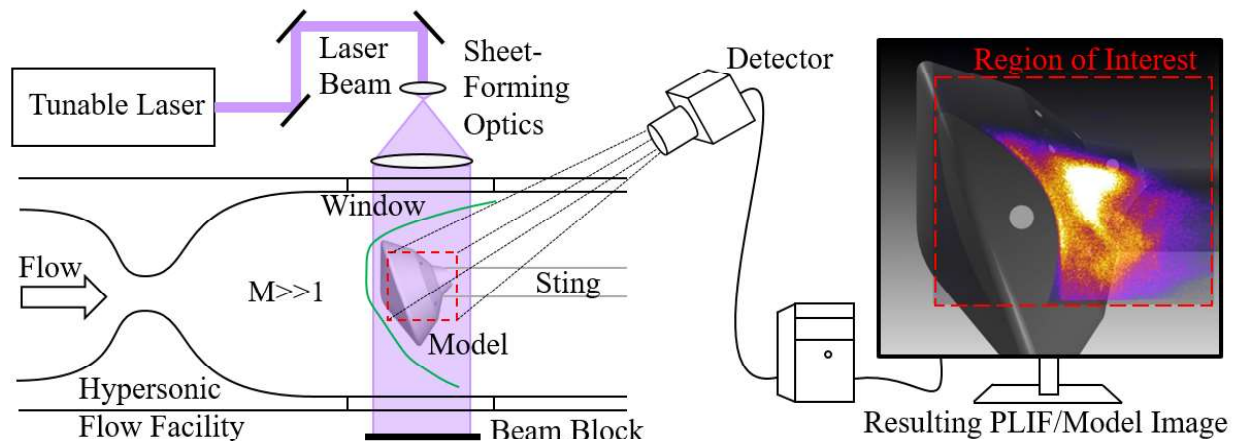

Figure 3.1 PLIF flow visualization setup; image (right) reproduced from Ref. 81, with permission from the authors.

3.2. Basic Theory of PLIF

Common tracer species used in PLIF visualization experiments of hypersonic flows include iodine (I_2), krypton (Kr), nitric oxide (NO), hydroxyl radical (OH), and toluene (CH_3).[82-87] NO and OH can occur naturally in certain flowfields. The absorption of photons from the laser excites a portion of the tracer species population to a higher energy state, setting the fluorescence process in motion. As indicated in the left schematic of Fig. 3.2, after absorption the excited species quickly return to a lower energy state, resulting in the emission of photons (i.e. fluorescence). Typically, the detector collects light at wavelengths longer than that of the laser, while spectral filters are used to block the laser's wavelength

(reducing scattered light interference). Since the fluorescence emits isotropically, only a small fraction of the emitted light is captured by the lens and directed to the camera. The camera can be operated with an image intensifier whose role is to gate the signal, amplify the signal, and in some cases convert the signal from the UV to the visible region where cameras are more sensitive. The right drawing of Fig. 3.2 shows the spectral profiles of a broad-band and narrow-band laser along with a sketch of a typical absorption profile. Since tunable lasers can adjust the wavelength of the laser, flow visualization experiments normally have the centers of the absorption and laser profiles to be coincident, whether a broad-band or narrow-band laser is used. If the laser is spectrally scanned during a wind-tunnel run, the convolution of these profiles (i.e. overlap integral) results in a spectrum, which can be directly compared with simulated excitation spectra from software (e.g., LIFBASE).
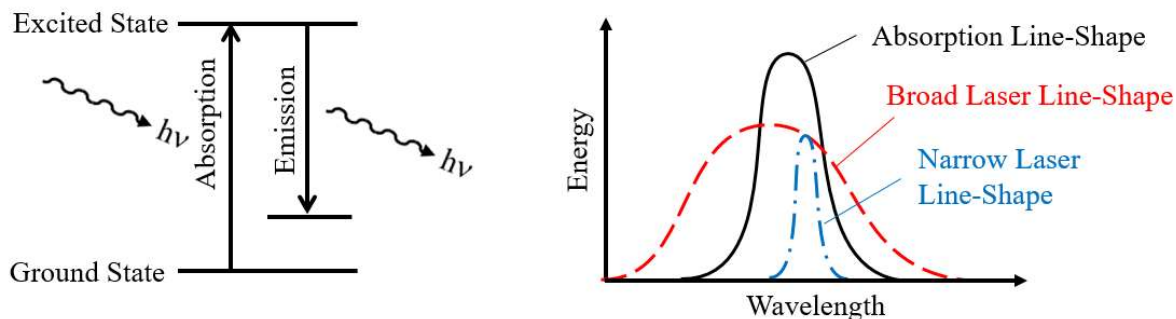
Figure 3.2 Fluorescence energy diagram (left); spectral overlap of laser and absorption (right).

Quantitative thermodynamic (pressure, temperature, density, mole fraction) and flow (velocity) measurements can be extracted through the analysis of the spectral position, shape and/or magnitude of one or more PLIF transitions obtained in an experiment. Thermodynamic, flow, and spectroscopic transition dependencies are shown below in the low-excitation, two-level, LIF signal (S_f) equation:[13,88,89]

$$S_f = \chi_s N_T(P,T) B_{12}(J'',v'') F_B(T,J'',v'') IG(\chi_s,P,T,U)\Phi(\chi_s,\chi_i,P,T) t_{\det} V \frac{\Omega}{4\pi}\eta \qquad (3.1)$$

where $\chi_s, \chi_i, N_T, B_{12}, F_B, I, G, \Phi, t_{\det}, V, \Omega, \eta, P, T, U, J''$, and v'' are the fluorescence species mole fraction, collisional species mole fraction, total population of molecules per unit volume, Einstein B absorption coefficient, Boltzmann fraction, laser irradiance, spectral overlap integral, fluorescence yield, detection time of the detector/camera, volume probed by the laser, detection, solid angle, the detector efficiency of the camera being used, pressure, temperature, velocity, rotational quantum number, and vibrational quantum number, respectively. If PLIF measurements can be obtained with a fixed optical system at steady flow conditions, then many of the terms in Eq. 3.1 can be cancelled if a ratio of S_f is considered.

The left-most drawing in Fig. 3.3 shows the effect of translational temperature on the spectral width of a single transition while the right drawing shows the effect of rotational temperature on the relative amplitudes of two transitions in the same vibrational band. Note that the overbar indicates normalized

values. Vibrational temperature affects the relative amplitudes of transitions in a similar way to rotational temperature, if the transitions being compared have different vibrational quantum numbers. If the width or relative amplitudes of transitions can accurately be extracted from experiments, and other dependencies in Eq. 3.1 can be controlled, then the corresponding translational, rotational, and/or vibrational temperatures can be measured. Similarly, Fig. 3.4 shows how the spectral width and position of the transitions are affected by pressure and the gas velocity component coincident with the laser's direction. Tracer species traveling towards the laser source experience a blue-shift in their absorption line-shape, which results in a red-shift of their transition profile. Conversely, tracer species traveling away from the laser source experience a red-shift in their absorption lineshape, resulting in a blue-shift of their transition profile. The Doppler shift of the transition, (Δ_{DS}) is related to the ratio of the gas velocity component in the laser direction to the speed of light.
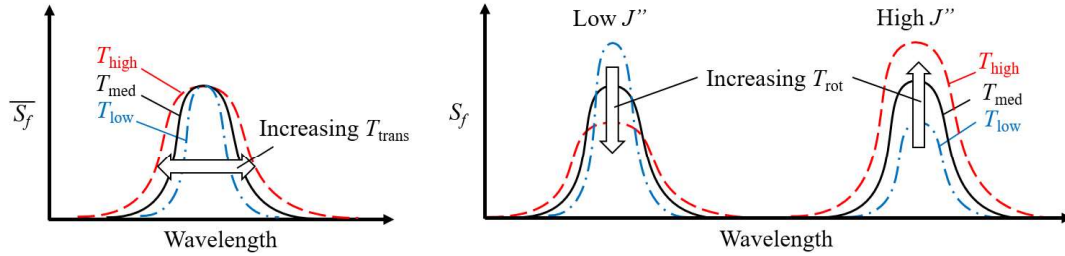
Figure 3.3 Transition dependence on translational (left) and rotational (right) temperatures.
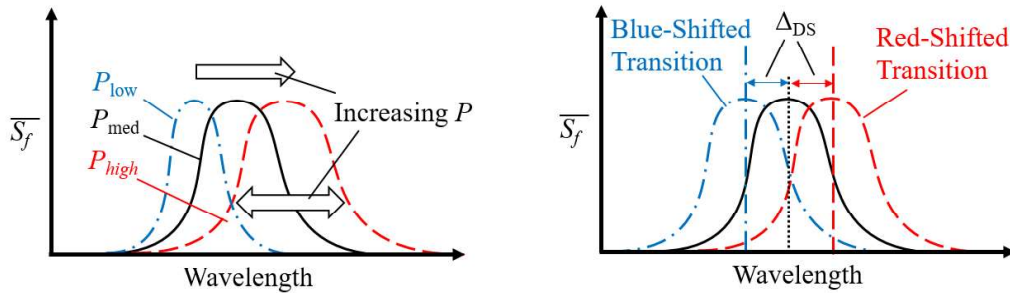
Figure 3.4 Transition dependence on translational pressure (left) and gas velocity (right).

Accurate measurements of the spectral shifts from PLIF data can be used for pressure measurements and/or Doppler-shift velocimetry. Finally, since the LIF signal is proportional to the tracer species concentration, it is possible to obtain density or relative mole fraction measurements by analyzing the magnitude of the fluorescence signal. Often, these techniques rely on the comparison to LIF obtained from a reference gas cell at known concentrations of the tracer species. The transient decay in the LIF signal is related to the rate of collisional quenching, which is included in the fluorescence yield term (Φ) in Eq. 3.1. Therefore, if the decay rate of a LIF signal can be obtained from a photodiode (PD) or photomultiplier tube (PMT), then a correction for a concentration measurement is possible. If the

sensitivity of the LIF signal to temperature and concentration can be minimized or taken into account (using equation of state), then pressure can be extracted.

Note that PLIF can be used for molecular tagging velocimetry (MTV), but such applications will be treated in Section 5.

3.3. Examples of PLIF

3.3.1. Flow Uniformity and Visualization

PLIF has often been used to assess flow uniformity. For example, O'Byrne *et al.* performed NO PLIF measurements to investigate the flow uniformity (see Fig. 3.5) downstream of a Mach 7.9 nozzle in the T2 free-piston shock tunnel facility at the Australian National University.[92] A Lambda Physik excimer laser was used to pump a ScanMate2 dye laser and frequency doubled to produce 226 nm of light for the measurement. PLIF measurements were used to identify the entrainment of cold boundary layer gas as one the causes for the non-uniformity. Lam *et al.* performed Kr PLIF measurements in a Mach-6 Ludwieg tube hypersonic wind tunnel.[90] They were able to show good agreement for shock shape between PLIF, schlieren, and CFD. Jiang *et al.* performed 10 kHz NO PLIF in the Calspan University at Buffalo Research Center's (CUBRC) 48-in Mach 9 hypervelocity shock tunnel using a custom pulse burst laser.[91] Flow visualization of a jet in cross-flow was performed with the technique.
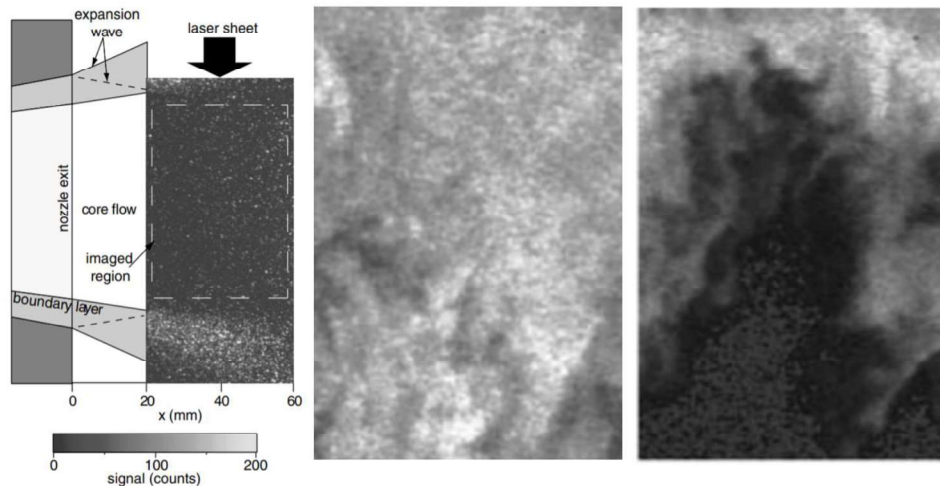
Figure 3.5 Flow uniformity (middle, right) from NO PLIF in a shock tunnel (left); adapted from Ref. 92, with permission from the authors.

Although flow visualization is normally used for qualitative comparisons, quantitative information can be extracted through image analysis. For example, McRae *et al.* performed proper orthogonal decomposition and autocorrelations of PLIF data from a supersonic combustion experiment at the University of Virginia Supersonic Combustion Facility (UVaSCF).[93] The analysis helped show how fuel

equivalence ratio can effect length scales associated with combustion. Inman *et al.* performed statistical analysis of NO PLIF data obtained in a Mach 5 arc-jet flow in NASA Langley's Hypersonic Materials Environmental Test System (HyMETS).[94] Observed fluctuations in NO PLIF signal at different tunnel enthalpy conditions were used to characterize the HyMETS facility. Simultaneous NO and O-atom LIF freestream measurements were also performed in the HyMETS facility at various tunnel enthalpy conditions.[83]

### 3.3.2. Rotational and Vibrational Thermometry

Analysis of the PLIF spectra from multiple transitions has been used to extract rotational and vibrational temperatures. Beck *et al.* performed rotational LIF thermometry measurements in the freestream and across a bow shock of a model in the High Enthalpy Shock Tunnel Göttingen (HEG).[95] McDougall *et al.* performed rotational thermometry from NO PLIF data obtained in a Mach 8.2 hypersonic boundary layer.[104] A wedge model with an NO seeding slot was placed in the 31-in Mach 10 wind tunnel at NASA Langley. Figure 3750.6 shows experimental and fitted spectra along with the processed temperature profile (x = 85 mm downstream of leading edge). The error was estimated to be less than 3% near the edge of the boundary layer with an uncertainty of 4%. Several fitting methods and saturation models were assessed in this work. Sanchez-Gonzalez *et al.* demonstrated an uncertainty of 6% to 7% for rotational NO LIF thermometry in a Mach 4.6 flow in a repetitively pulsed facility at Texas A&M University.[96] Shot-to-shot power fluctuations of the probe lasers were determined to be the main contributor of uncertainty. Good agreement between LIF thermometry and CFD predictions for a wake flow in the same facility was demonstrated in the work. Cecil and McDaniel performed rotational thermometry using iodine PLIF over a flat plate positioned in a rarefied Mach 12 flow.[97] A very low temperature (T = 11.5 K) was measured in the flow, but neither the error nor uncertainty were reported.
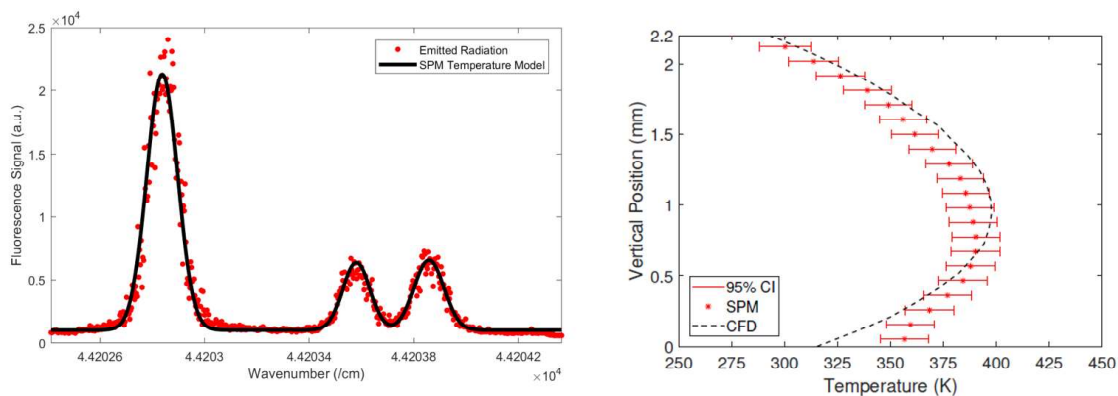
Figure 3.6 Rotational temperature (right) extracted from NO PLIF spectra (left) in a Mach 8.2 boundary layer in a blowdown tunnel; adapted from Ref. 98, with permission from the authors.

Palma *et al.* performed both rotational and vibrational temperature measurements in a Mach 7 nozzle flow of the T2 shock tunnel.[99] Simultaneous measurements allows for the investigation of thermal non-equilibrium, which is a major challenge in hypersonic flow modeling.[100] It was determined that fluctuations in the distribution of energy amongst the cavity modes of the laser contributed the most to uncertainty (25%) in a single image. The strategic choice of the transitions, which ensured a wide separation in rotational quantum numbers, reduced the uncertainty associated with the subsequent temperature measurement (4%). Adverse effects of saturation on the temperature were minimized by intentionally saturating transitions in weak braches to the same level ($I/I_{sat} \sim 2\%$).
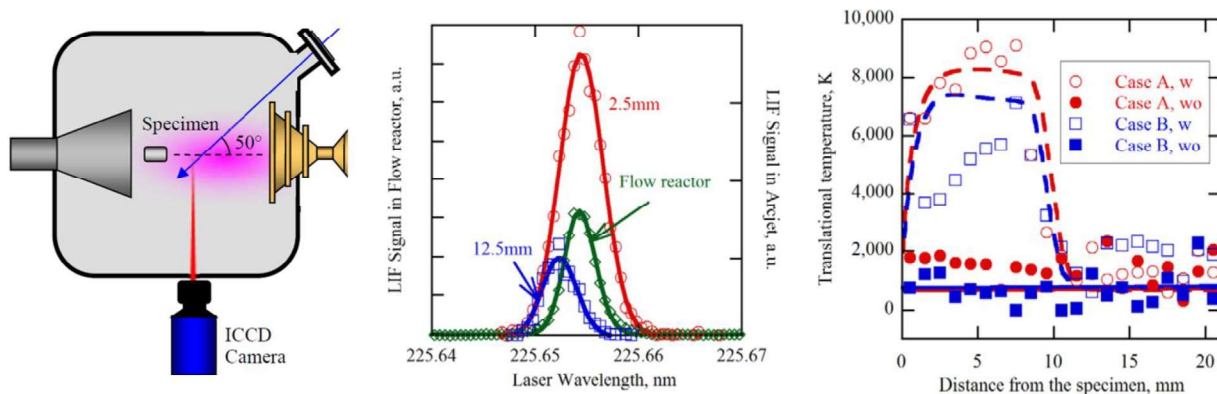
Figure 3.7 Translational temperature (right) extracted from O-atom LIF spectra (middle) for an arcjet (left); adapted from Ref. 101, with permission from the authors.

3.3.3. Translational Thermometry

Takayanagi *et al.* performed translational temperature measurements in the freestream and post-shock region ahead of a sample in the 750kW arc heated wind tunnel at the JAXA Chofu Space Center.[101] As shown in Fig. 3.7, a laser scan was used to extract the spectral width of a transition of atomic oxygen. An Nd:YAG (Spectra-Physics Quanta-Ray) laser was used to pump a ScanMate2E dye laser (Lambda Physik) and then frequency doubled in a BBO-crystal to produce 225.65 nm light needed for the two-photon transition of atomic oxygen. Although neither uncertainty nor accuracy were reported in the work, the scatter in Fig. 3.7 (right) is approximately ±1000 K, which is 100% and 11% of the freestream and stagnation temperatures, respectively.

3.3.4. Mole Fraction

Rossmann *et al.* performed mixture (mole) fraction measurements of a mixing layer (Mach 5.1 and 0.3 streams) in a high-stagnation enthalpy shock-tunnel-fed mixing facility.[102] Nitric oxide was generated naturally in the high-temperature stagnation air produced in the facility. The left drawing in Fig. 3.8 shows the tunnel configuration that produced the mixing layer. A relatively temperature-insensitive

transition ($J'' = 18$) of NO was chosen such that the uncertainty in the mixture fraction did not exceed 10% over the expected temperature range. Other errors due to laser attenuation (<2%), local shock waves (<4%), and random shot noise (<7%) were also discussed. The resulting mixture fraction plot is shown in Fig. 3.8 (right), with select line plots.
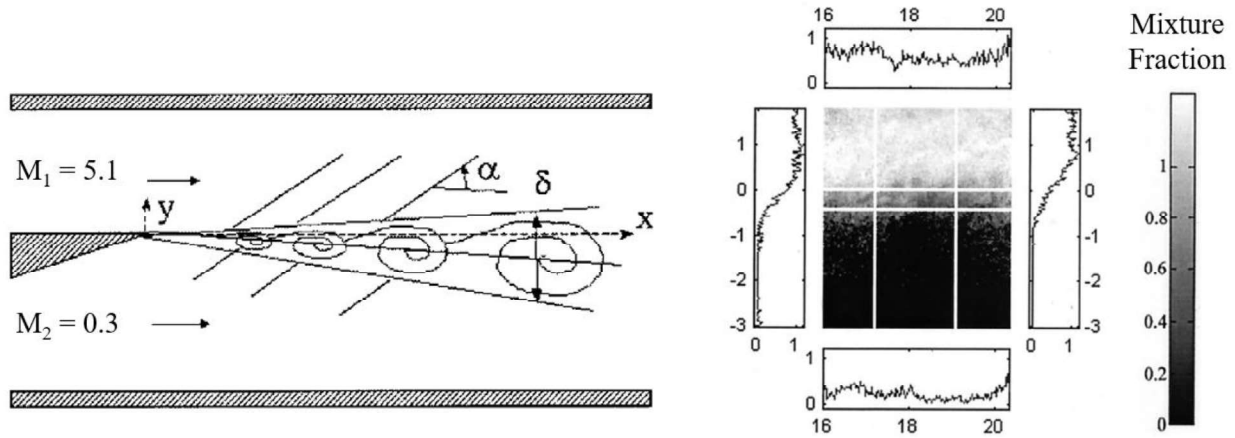
Figure 3.8 Mixture fraction (right) extracted from NO PLIF in a Mach 5.1 mixing layer (left). Adapted from Ref. 102, with permission from the authors.

Gamba *et al.* performed tracer number density measurements in a Mach 2.3 flow using toluene PLIF. Using temperature data measured using ratio thermometry, relative mole fraction measurements were extracted.[103] McDougall *et al.* extracted off-body mole fraction in a Mach 8.2 boundary layer in the 31-in Mach 10 facility.[104] An NO mass flow controller was used using combination with the PLIF data to perform the measurement. The measurement uncertainty varied throughout the boundary layer, but was maximum near the wall ($\sim 25\%$).

3.3.5. Density

Balla and Everhart used iodine PLIF to measure air density in the near wake of a multipurpose crew vehicle model in NASA Langley's 31-in Mach 10 facility.[105] A calibration cell of known density was used for the measurement. The uncertainty of the wake density measurement was reported to be 7% ($\sim 1\%$ of freestream density). Fletcher and McDaniel used iodine LIF to measure density, velocity, and temperature in a Mach 2 flow with a transverse jet.[106] The uncertainty for the density measurements was not reported. Narayanaswamy *et al.* obtained density measurements in a Mach 4.5 underexpanded jet using krypton PLIF.[107] An assumption of constant self-quenching cross-section and isentropic flow was used to compute the density and temperature fields. Measurements of density showed good agreement (< 7%) with predictions from CFD.

3.3.6. Pressure

The majority of supersonic pressure measurements reported in the literature are below Mach 5. Lachney and Clemens extracted the pressure field in the near wake of a thick plate in a Mach 3 flow (see Fig. 3.9) using NO PLIF.[108]
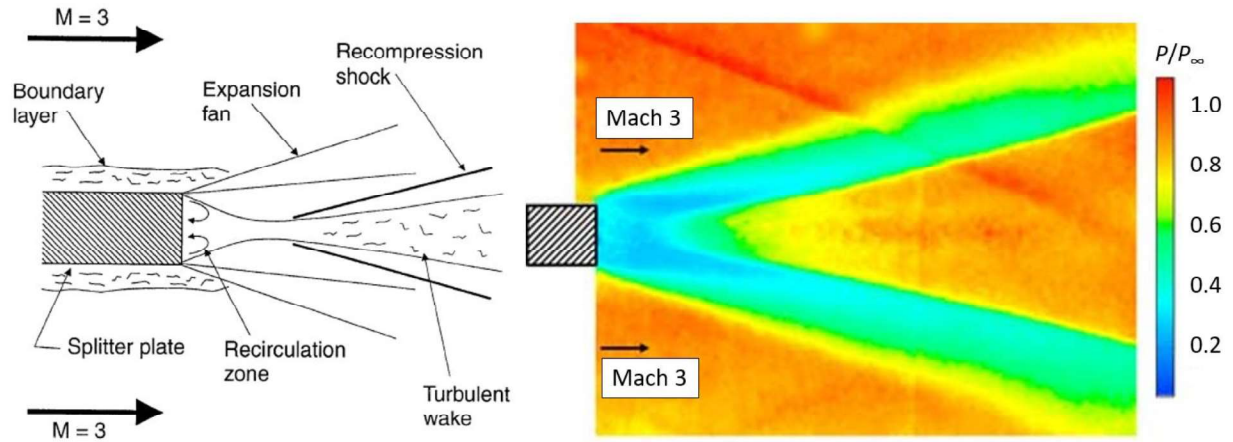
Figure 3.9 PLIF pressure measurement in a Mach 3 wake. Adapted from Ref. 108, with permission from the authors.

The pressure dependence of the LIF signal through N_T was exploited in the low-quenching limit (Q<<A). In this case, the LIF signal becomes linearly proportional to pressure and has a non-linear dependence on temperature, which was also measured using ratio thermometry. The relationship between the pressure and temperature uncertainties was discussed in detail. The error of the PLIF pressure measurements was reported to vary between 10% and 30% based on comparisons to side-wall pressure transducers.

Lemoine and Leporcq used iodine LIF to measure pressure in supersonic underexpanded jet.[109] Transition and conditions were chosen to minimize temperature effects on the measurement. The accuracy of the method, determined using a static vessel, was 5%. Hiller and Hanson performed similar, but planar (2D), pressure measurements using iodine PLIF in a Mach 1.5 underexpanded jet.[110] The uncertainty was reported to be 8%.

3.3.7. Doppler-shift Velocimetry

Inman *et al.* performed NO Doppler-shift velocimetry in a Mach 5 flow in NASA Langley's HyMETS arc-jet facility.[94] Figure 3.4. 10 shows the resolved spectra at quiescent flow conditions compared to red- and blue-shifted transitions. Radial velocity was extracted from the Doppler shift and combined with molecular tagging velocimetry (MTV) results for the axial velocity component to produce the middle image in Fig. 3.10. Uncertainty in the radial velocity varied from ±26 m/s (5%) to ±62 m/s (~13%). The

main contributor to the uncertainty was noise in the spectra, which is related to laser power fluctuations. Asymmetric error bars associated with the uncertainty are shown on the right image of Fig. 3.10. These radial velocity measurements were combined with flow tagging velocimetry in the same experiment to produce flow vectors shown in the middle panel of Fig. 3.10.
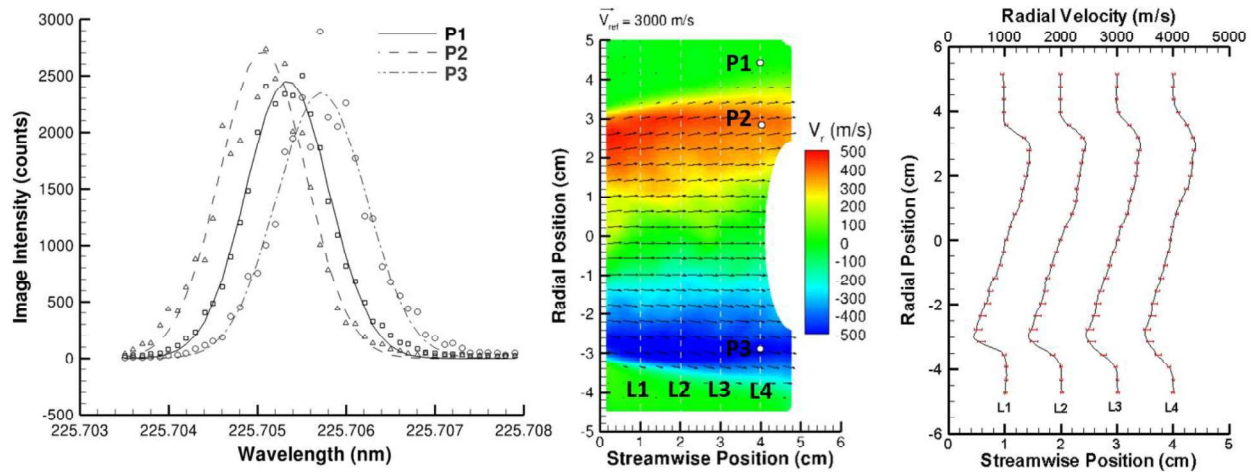
Figure 3.10 Doppler-shift velocimetry (middle, right) extracted from NO PLIF spectra (left) in a Mach 4 arcjet; Adapted from Ref. 94, with permission from the authors

Danehy *et al.* performed NO PLIF Doppler-shift velocimetry of a hypersonic, separated flow over a cone with a Mach 7 freestream.[111] The PLIF spectra were acquired in the T2 free-piston shock tunnel on a shot-by-shot basis. Uncertainties in the freestream were estimated to be ±50 m/s (~10% of maximum radial velocity). Hruschka *et al.* performed two-component Doppler-shift PLIF velocimetry in the T-ADFA free-piston shock tunnel (Mach 10).[112] Uncertainty of the radial freestream velocity was reported as ±50 m/s (~2% of axial freestream velocity or 10% of maximum radial velocity in wake). Takayanagi *et al.* performed Doppler-shift velocimetry using O-atom LIF in JAXA's 750 kW arc-jet.[101] The flow velocity difference between the freestream and shock layer ahead of the sample was determined to be 3,600 ±400 m/s (~11%). Suess *et al.* used two-photon LIF to obtain Doppler-shift velocimetry, translational temperature, and mass fraction in the NASA Johnson Space Center's arc-jet facility.[113] The LIF measurements were combined to produce total enthalpy measurements. Although the uncertainty in the velocity measurements were not reported, scatter in the results were approximately ±500 m/s (~10%). Finally, McDaniel *et al.* performed iodine PLIF Doppler-shift velocimetry in a Mach 5 underexpanded jet.[114] Good agreement between the experiment and CFD predictions were reported with a measurement uncertainty of 2%.

3.4. Conclusions for PLIF

Laser-induced fluorescence has been used as for non-intrusive measurement of various quantities (thermodynamic and flow) in hypersonic flows. Since modern quantitative PLIF techniques typically rely on image analysis, flow visualization data can also be acquired in the process. Advances in digital camera and intensifier technology result in PLIF data with fine spatial resolution (<0.1 mm), short gate times (~ 100 ns), and high signal-to-noise ratio (SNR). The ability to block laser scatter with a spectral filter, but passing fluorescence, which occurs at longer wavelengths, also improves signal quality near surfaces. While some single- or two-laser PLIF techniques can provide a measurement on a single-shot basis (typically 10 Hz), many require a spectral scan over an absorption profile that can take much longer (>60 s). As a result, these longer-duration PLIF techniques can only provide a mean measurement in a continuous flow facility operating at steady conditions, or a mean measurement based on an accumulation of runs in an impulse facility. The recent development of pulse-burst lasers for PLIF have allowed for multiple measurements to be obtained in a single run of an impulse facility (e.g., shock tunnel). While seeding of tracer species is sometimes required, many hypersonic flow facilities naturally produce the required tracer species at the high stagnation temperatures.

The major drawbacks of PLIF compared to absorption spectroscopy, which is a closely-related technique, are cost, complexity, and safety. Lasers used for PLIF are typically higher power, larger, and more expensive compared to systems used for absorption spectroscopy. Many of the PLIF tracer species are toxic and require laser light in the ultraviolet (UV) spectrum. The production of UV light from a PLIF laser typically requires multiple sub-systems (e.g., pump laser, dye laser, frequency mixing unit), each producing light at different wavelengths. As a result, multiple laser safety goggles, in combination with a carefully-planned safety procedure, are required when tuning the laser. On the other hand, PLIF laser systems are simpler than, and produce beams of lower energy than alternative techniques like CARS.

4. Molecular Tagging Velocimetry (MTV)

4.1. Introduction to MTV

Molecular tagging velocimetry (MTV) encompasses a broad class of non-intrusive optical techniques that allow for velocity measurements through the utilization of molecular flow tracers. In this method, one or more lasers are used to excite (or "tag") molecules in the flow, causing luminescence at a point or along a line. The tagged region of fluid is then imaged at two or more time delays, and the ratio of the calculated Lagrangian displacement to the time between images yields an estimate of the flow velocity. Depending on the particular MTV method used, molecular tagging can measure three-component velocity and acceleration, as well as scalars such as concentration, pressure, and temperature.

Having been successfully implemented to provide velocity measurements in flow regimes ranging from subsonic to hypersonic, the applicability of MTV is exceedingly wide-ranging while the limitations of molecular tagging depend on the specific technique being utilized. Provided the presence of an appropriate tracer molecule, velocity can be determined as long as the luminescence from excited molecules is sufficiently high to be detected and tracked. Consequently, MTV allows not only for unseeded measurements where the tracer molecule is naturally present in the testing environment (e.g. N_2 in air/nitrogen flows or NO in high enthalpy flows), but also measurements in any flow where atomic or molecular tracers may be produced or introduced. Theory of the MTV technique has been developed and discussed in Refs. 13, 115, and 116. A number of review articles have also been written summarizing the technique.[117-120]

4.2. Basic Theory of MTV

One of the many advantages of MTV is the simple setup needed to implement the technique. For some methods, one laser, a single camera, and a flow containing tracer molecules are the only requirements for performing velocimetry. A typical MTV experimental setup is shown in Fig. 4.1, where a laser beam enters the field of view of the camera and tags a region of fluid. A reference image is captured at the time of the tagging, and after a small time (Δt) the tagged molecules have advected downstream with the flow and a second image is obtained showing the signal displaced by Δx. An estimate for the velocity can then be obtained by $V = \Delta x / \Delta t$. This one-component measurement is often used to provide single-shot velocity profiles; however, MTV can be extended to afford two-component measurements by tagging a grid pattern or point, rather than a line. Three-component velocity measurements have also been made by providing two (preferably orthogonal) views of the tagged region.[121]
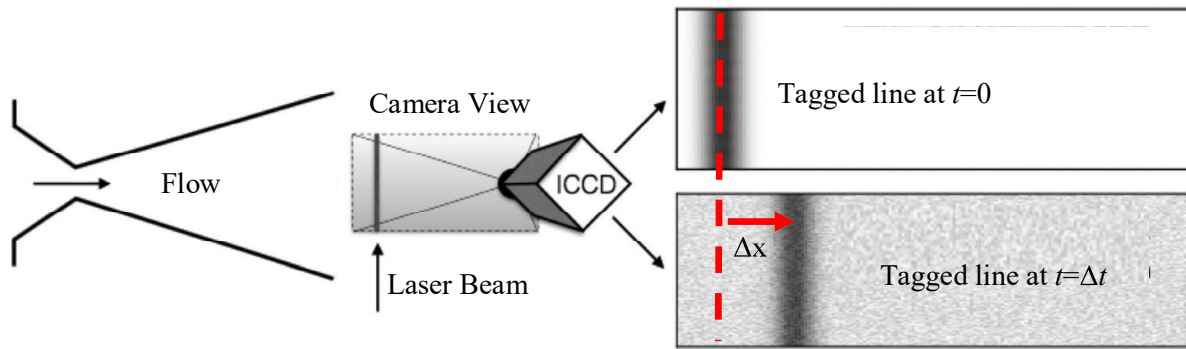
Figure 4.1. Simplified typical MTV experimental setup. Adapted from Ref. 122. Also shown are two images illustrating a tagged-flow image at t=0 and a displaced tagged-flow image at t=Δt. Modified and reprinted with permission of the authors.

Traditionally, researchers captured time-delayed images on a single-frame detector, and results were compared against an initial reference image. In early MTV experiments, the reference image was captured once at the start of the experiment and was assumed to remain stationary for all subsequent time-delayed images. This introduced errors attributable to shot-to-shot displacements in the position of the initial tagged region caused by effects such as beam steering or movement of optics due to facility vibrations. To help mitigate these effects, later experiments included a second single-frame detector (with a field-of-view matched to the first) so that a reference signal could be captured for each time-delayed image.[123] However, this method introduced issues of its own associated with camera alignment and field-matching to sub-pixel accuracy. With the advent of the interline-transfer CCD camera, the unfounded assumption of a stationary initial reference could be avoided by offering the same capability as the two-detector method, but without the need for tedious alignment of multiple detectors or the associated errors. With more recent advancements in detector technology, researchers are now able to capture high resolution digital images at ultra-high speeds (hundreds of kHz). This allows for an initial reference image to be captured, followed by multiple time-delayed images, providing not only more precise velocity estimates, but also acceleration and signal lifetime measurements.
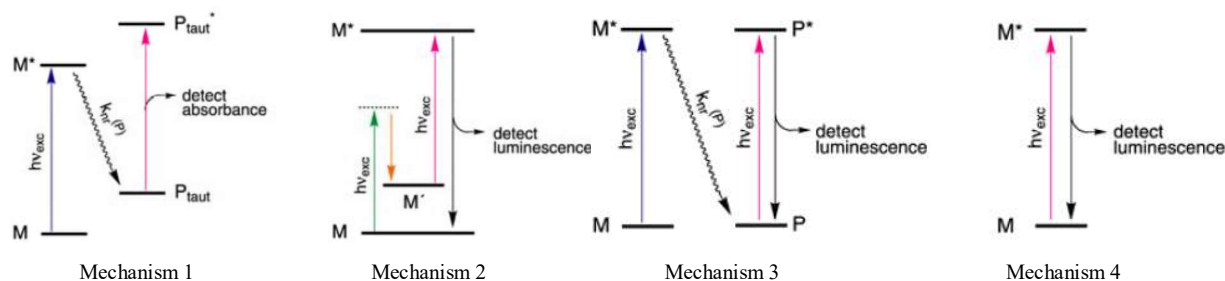
Figure 4.2. The different mechanisms of MTV. Adapted from Ref. 115. M and M* designate a molecule in its ground and electronic excited state, respectively, and P indicated the formation of a new molecule. Solid arrows describe radiative transitions and wavy arrows indicate nonradiative transitions. The excitation lines are color coded to emphasize the number of different frequencies typically needed for each experiment. Processes denoted by black arrows occur spontaneously and don't require a laser. The different diagrams summarize the photochemistry and photophysics that give rise to the various MTV techniques. Modified and reprinted with permission of the authors.

Though the concept of tagging molecules and tracking the marked region over time to determine flow velocity is common for all MTV methods, the details of the tagging mechanism is dependent on the particular technique considered and the flow parameter(s) being measured. There are four basic mechanisms (as defined in Ref. 115) comprising molecular tagging techniques: absorbance, vibrational excited-state fluorescence, photoproduct fluorescence, and direct luminescence. A schematic illustrating these different mechanisms is given in Fig. 4.2. In the first of these mechanisms, absorbance, a laser is used to electronically excite a molecule which then nonradiatively transitions to another molecule. Since the product molecules are more strongly absorbing than the original ground-state molecules, the tagged region of fluid appears darker when illuminated by a secondary (either a white-light or laser) source.[124-128] Littleton et al. used this technique to make freestream velocity measurements with 1% error in a Mach 6.7 flow.[129] This mechanism is used in laser-induced photochemical anemometry[130] (LIPA), and unlike the other three methods (which utilize luminescence to tag the flow), this is the only MTV technique that relies on measuring absorbance.

The second mechanism, vibrational excited-state fluorescence, is used in the Raman excitation and laser-induced electronic fluorescence (RELIEF) technique. Originally reported by Miles et al., RELIEF is a multi-laser method that tags the flow by vibrationally exciting molecular oxygen via Raman pumping.[131-135] This technique is valuable in that the molecular tracer (oxygen) is naturally present in most hypersonic facilities; however, its reliance on three frequencies to tag the fluid makes it challenging to implement. Additionally, this method is limited to temperatures below 750 K since oxygen molecules are vibrationally excited above this temperature, making tagged molecules nearly indistinguishable from the untagged fluid.[136] The RELIEF method has shown potential precision of approximately 1 m/s for single shot images, and sub-m/s for time-averaged images.[137]

In photoproduct fluorescence, the third MTV mechanism, a laser is used to photo-dissociate a non-tracer molecular species to form a tracer product species that may then be probed with a second laser. There are many techniques that utilize this mechanism for molecular tagging, and each is named depending on the tracer used to tag the flow. In hydroxyl tagging velocimetry[138-143] (HTV), photo-dissociation of H_2O molecule is used to generate the OH radical. The ozone tagging velocimetry[140,144,145] (OTV) method uses ozone (O_3) created from oxygen (O_2) as the tracer. Photosynthesis of metastable krypton atoms is used in krypton tagging velocimetry[162-165] (KTV). Nitric oxide laser-induced fluorescence[146-148] (NO-LIF) utilizes NO photo-dissociated from N_2O,[149] NO_2,[146] or N_2/O_2. Air photolysis and recombination tracking (APART) is another velocimetry technique that utilizes N_2 and O_2 to make unseeded measurements in air.[150,151] While nitric oxide is naturally present in shock tunnels and arc-heated facilities, it is not present in most types of facilities and is corrosive and toxic if seeded in the flow. These methods generally have precisions of 0.1-1%, and measurements rates of 10 Hz; however, slightly less precise measurements (~2%) have been made at 500 kHz.[152]

The fourth and final mechanism, direct luminescence, uses a single laser to produce a long-lived luminescent excited state. Some examples of this technique include acetone tagging velocimetry,[153,154] iodine tagging velocimetry,[155] and phosphorescence of biacetyl molecules.[156] Another promising class of methods involves using a laser to dissociate molecular nitrogen into atomic nitrogen, thereby tagging the flow through tracking of the photons emitted during recombination. Since molecular nitrogen is present in most hypersonic facilities, this MTV class allows for unseeded measurements of velocity. If a femtosecond laser is used to dissociate the N_2, this is known as femtosecond laser electronic excitation tagging[157] (FLEET). It should be noted that FLEET thermally perturbs the flow and the laser can potentially damage models, windows, and facilities. Quadrupling the laser frequency allows for a resonant version of the tagging mechanism, providing a less thermally-perturbative method known as selective two-photon absorptive resonant FLEET (STARFLEET).[158] A picosecond laser can also be used to dissociate the N_2 molecule in a high rep-rate technique known as picosecond laser electronic excitation tagging (PLEET).[159] While PLEET allows for seedless velocimetry at 100 kHz, these methods typically provide measurement rates of 1 kHz and have demonstrated precisions near 1% (with some methods allowing for precisions below 0.5%).[169]

4.3. Examples of MTV Measurements

Many of the aforementioned MTV techniques have been applied in the hypersonic regime to yield velocity results. One such technique is Krypton Tagging Velocimetry (KTV), where krypton can be seeded locally or globally into the flow and used as a tracer by either: a) photosynthesizing metastable Kr atoms, or b) locally ionizing the Kr to trace movement. The use of a metastable noble gas as a tagging

velocimetry tracer was first suggested by Mills et al.[160] and Balla and Everheart.[161] KTV has been demonstrated as a two-laser/one-camera technique using photosynthesized metastable Kr as tracer,[162] and more recently as a one-laser/one-camera technique with ionized Kr as the tracer.[163] To date, KTV has been shown to work with 1% Kr global seeding for high-speed N_2 flows and 5% Kr global seeding in high-speed air flows. Applications include: 1) small, underexpanded air or N_2 hypersonic jets;[162,163] 2) mean and fluctuating turbulent boundary-layer profiles in a Mach 2.7 N_2 flow;[164] and 3) twenty simultaneous profiles of streamwise velocity and velocity fluctuations in a 20x20 mm area in a N_2, Mach 2.8 shock-wave/turbulent boundary-layer interaction.[165] Krypton is used as a tracer species for diagnostics because it is nominally thermochemically inactive at atmospheric or typical high-speed wind-tunnel flow conditions. As such, it is safe/simple to implement in the lab and does not distort the mean flow of interest when introduced in dilute concentrations. That is, there is the potential for implementation in flows where the thermochemical state of the gas is difficult to prescribe or predict (e.g., a combustion environment[166,167] or when introduced in the high-temperature/pressure reservoir of a high-speed wind tunnel).

Recently, krypton tagging velocimetry (KTV) was employed in the Arnold Engineering Development Complex (AEDC) Hypervelocity Wind Tunnel Number 9 (T9) to return freestream velocity profiles at four tunnel conditions. These experiments were performed with the two-laser/one-camera approach. To make nonintrusive KTV measurements, Mustafa et al.[163] used 532 nm output from an Nd:YAG laser to pump a dye laser; the dye laser then output a 644.1 nm beam which was frequency-tripled to produce a 214.7 nm tagging (or "write") laser beam. This write beam tagged krypton which was seeded globally throughout the base flow. The "read" laser system consisted of an Nd:YAG laser which pumped a dye laser at 532 nm to produce a 769.5 nm beam. The read laser beam was then passed through sheet-forming optics to create a "read sheet" that re-excited the metastable tagged Kr tracer atoms. Images of the "write" and "read" lines were captured on a Princeton Instruments PIMAX-4 camera at 10 Hz. Typical images are shown for the Mach 10 case in Fig. 4.3a, and for the Mach 14 case in Fig. 4.3d. Velocity is extracted for every row of each dataset using a Gaussian peak finding algorithm to find the line centers of the reference "write" and shifted "read" signal. A sample velocity profile is shown in Fig. 4.3b for the Mach 10 flow, and in Fig. 4.3e for the Mach 14 case. KTV velocity measurements are also shown in time compared against the T9 conventional method in Fig 4.3c and 4.3f for the Mach 10 and Mach 14 conditions, respectively. Standard deviation of the freestream velocity profiles fell within a range of 0.2-1.25% and showed agreement with T9 calculations to approximately 2%.[168]

Krypton gas-bottle cost is a potential issue for implementation of KTV efforts. Estimates indicate that the seeding cost per run of 1% Kr mole fraction ranges from ≈10 USD (e.g., Ludwieg tubes, shock

tunnels, and moderate reservoir pressure blow-down facilities) to ≈100 USD in large-scale, high-reservoir-pressure, long-duration (10 second) blow-down hypersonic tunnels (e.g., Tunnel 9 at AEDC White Oak).[162] The cost of using globally seeded KTV in a large-scale, continuous, high-speed wind tunnel would be higher still; however, cost concerns could be alleviated by utilizing local seeding.
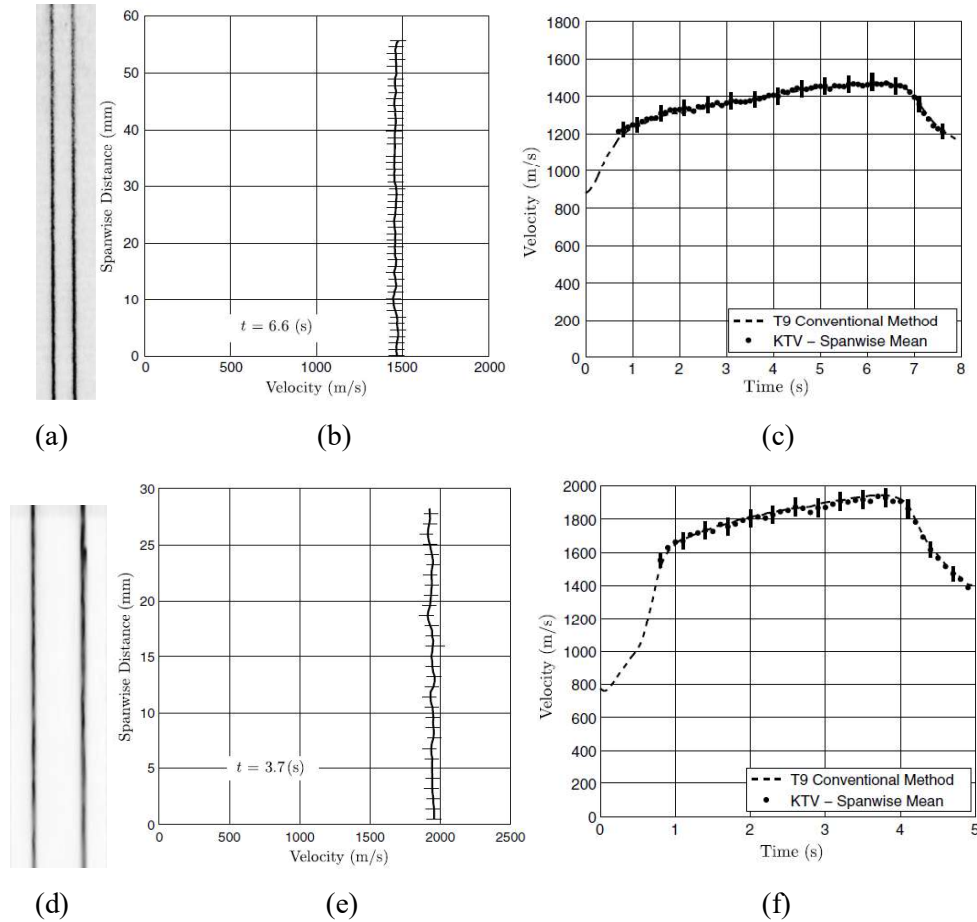

Figure 4.3. KTV results from AEDC Tunnel 9. Write and read lines for (a) Mach 10 and (d) Mach 14. Freestream velocity profile for (b) Mach 10 and (e) Mach 14. Freestream velocity as measured by KTV and the T9 conventional method for (c) Mach 10 and (f) Mach 14. From Ref. 168, reprinted with permission of the authors.
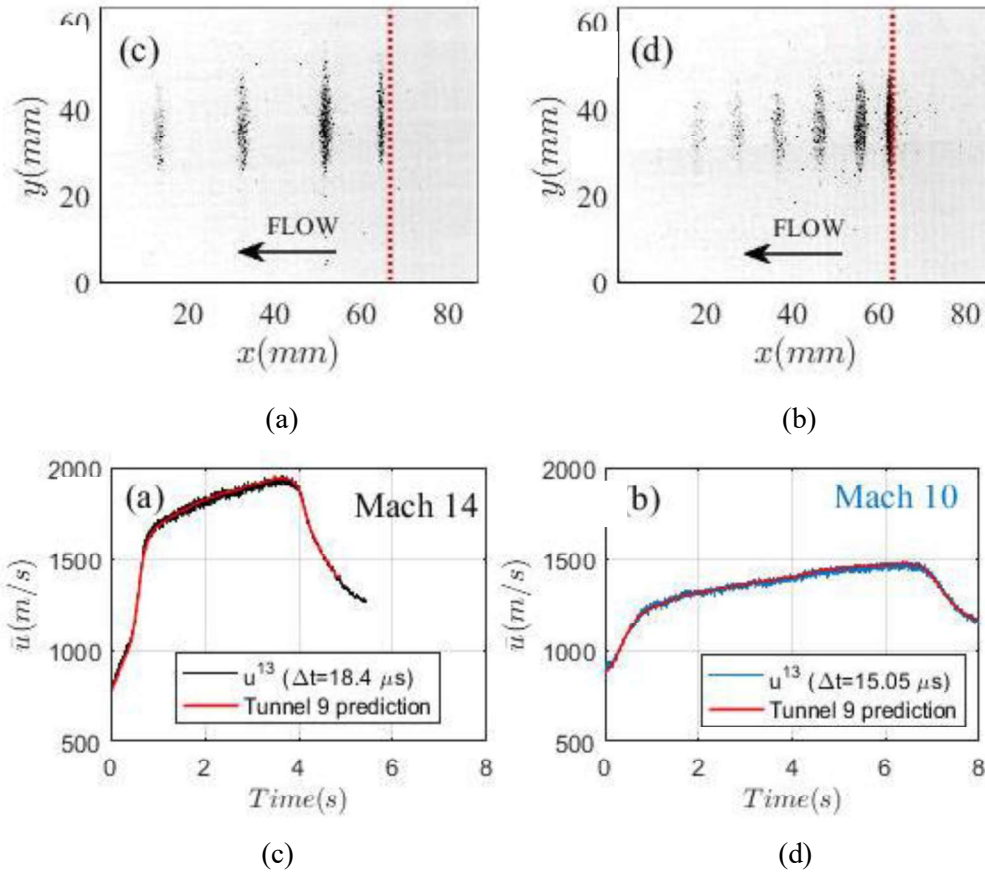
Figure 4.4. Single-shot FLEET images taken in Mach 14 and Mach 10 freestream flow; dotted line marks the position of the laser beam. Time dependency of FLEET instantaneous mean velocity and Tunnel 9 velocity prediction for Mach 14 and Mach 10 freestream flow. From Ref. 169, reprinted with permission of the authors.

Another MTV method proven at hypersonic speeds in AEDC's T9 is the FLEET technique. Like KTV, FLEET was utilized to obtain time-resolved freestream velocity measurements at Mach 10 and Mach 14; however, unlike KTV, FLEET allowed for unseeded measurements in both air and nitrogen at 1 kHz. This was achieved by using a single 800 nm Ti:Sapphire laser to excite and dissociate naturally-occurring nitrogen molecules. Images of the luminescence resulting from recombination of the nitrogen atoms were captured using a gated image intensifier with a high-speed CMOS camera, which allowed for capture of a reference FLEET line and multiple delayed lines. Example single-shot FLEET images are shown at several delays in Fig. 4.4a and 4.4b for the Mach 14 and Mach 10 flows, respectively. Displacement between FLEET lines was used to give an estimate of the flow velocity, and velocity measurements are shown versus the T9 predicted value as a function of time in Fig. 4.4c for Mach 14, and Fig. 4.4d for Mach 10. FLEET velocity results showed "remarkable consistency" with the T9 prediction, and measurement precision below 0.5% was attained.[169]
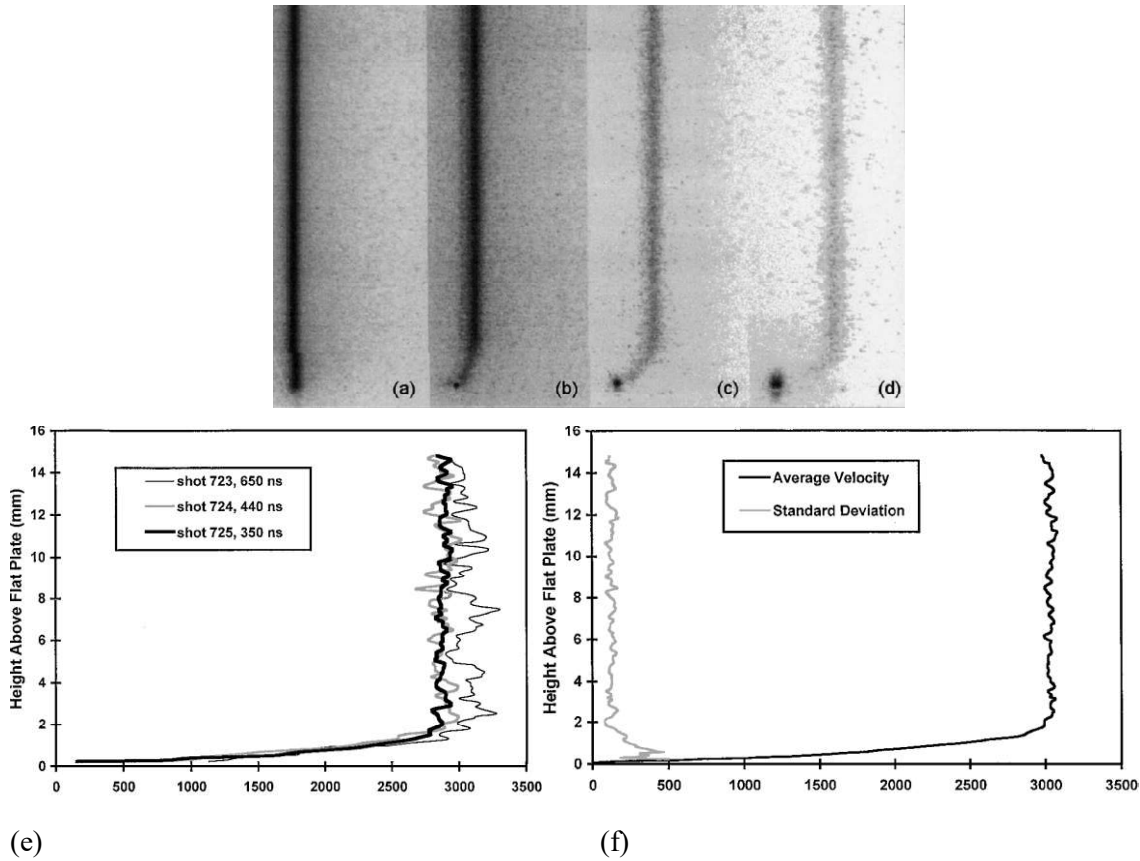
Figure 4.5. NO LIF results. Raw images at taken at time delays of (a) 0 ns, (b) 250 ns, (c) 500 ns and (d) 750 ns. (e) Three typical single-shot velocity measurements. (f) Average and standard deviation of velocity profiles. From Ref. 170, reprinted with permission of the authors.

Nitric oxide laser induced fluorescence (NO-LIF) employed at the Australian National University (ANU) T2 free-piston shock tunnel is a third example of MTV applied to hypersonic freestream flows. In this study, output of an excimer-pumped dye laser is frequency-doubled to create a 225 nm laser beam. This beam was used to tag NO seeded into the test section prior to each shock tunnel run to obtain a reference (zero-velocity) image for the subsequent run. The test section was then evacuated, and the same laser was used to tag NO during the shock tunnel operation. Images were obtained using an intensified CCD camera at several time delays, and example images are shown in Fig. 4.5a-d. As with the previous examples discussed in this section, these tagged lines are used to extract a velocity profile. Three typical single-shot velocity measurements are given in Fig. 4.5e, while an average and standard deviation of velocity profiles are shown in Fig. 4.5f. Single-shot velocity measurement uncertainty in the freestream was found to be 3.5%, based on 90% confidence.[170]
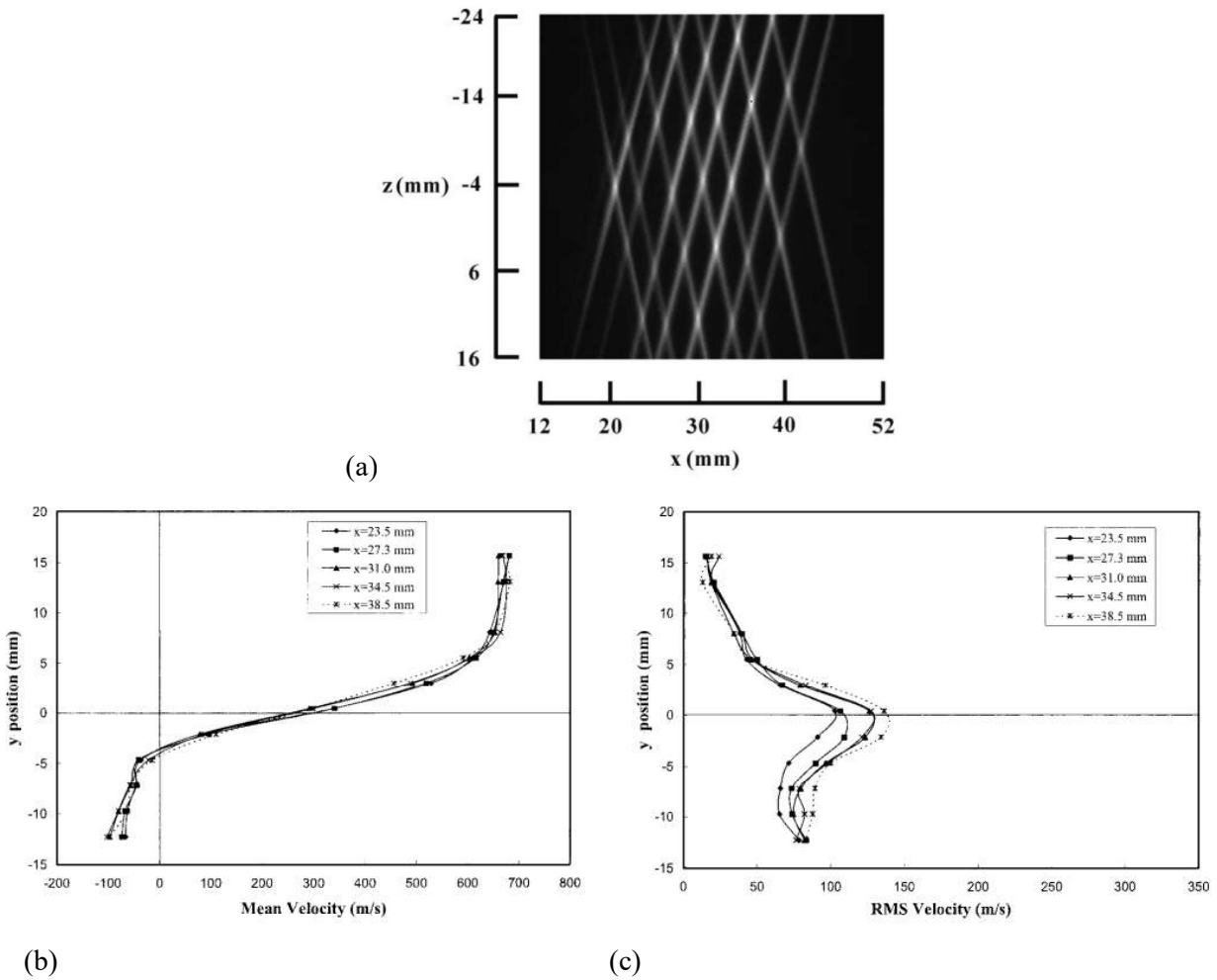
Figure 4.6. (a) Averaged HTV reference grid. (b) Mean velocity profiles at various streamwise locations. (c) RMS velocity profiles at various streamwise locations. From Ref. 171, reprinted with permission of the authors.

Though not yet applied in a hypersonic flow, hydroxyl tagging velocimetry (HTV) has been proven by Pitz et al. to make measurements of supersonic flow over a cavity which contains some freestream flow outside of the cavity.[171][171] In this study, conducted at the supersonic flow facility in Research Cell 19 at the Air Force Research Laboratory, in Dayton, OH, an ArF excimer laser beam (193 nm) was formed into a 7-by-7 grid to dissociate H_2O and tag the product OH tracer molecules. This grid of tagged molecules was then tracked using planar laser-induced fluorescence from an Nd:YAG pumped dye laser with a frequency-doubler (282 nm). Fluorescence of the grid was captured using a PIMAX intensified CCD camera, which used 2-by-2 binning to improve signal strength. An average HTV reference image is shown in Fig. 4.6a. The crossing point on this grid were tracked in post-processing which allowed for extraction of approximately 50 velocity vectors of the Mach 2, two-dimensional flow. Mean velocity profiles at various streamwise locations are shown in Fig. 4.6b, while RMS velocity profiles are shown in

Fig. 4.6c. Error of about 1% was achieved in this study.[171] HTV can potentially be very useful in combustion-heated hypersonic flow facilities which contain ample water vapor in the freestream.

4.4. Conclusion for MTV

Molecular tagging velocimetry is a diverse class of measurement techniques that is applicable throughout a wide-range of supersonic and hypersonic flow conditions. For MTV to work, a native, seeded (locally or globally), or synthesized tracer gas must be present. Additionally, the presence of this tracer must be imaged over at least two time delays. The promise of MTV methods is that they provide non-intrusive, off-surface measurements that have augmented researchers' ability to characterize hypersonic wind tunnels in new and underexplored regimes. These tools have been put into practice in facilities ranging from small-scale, supersonic wind tunnels to large-scale, hypersonic test wind tunnels. These new measurements are possible because of recent advancements in laser and detector technology. MTV has not only seen rapid improvements in the quality and breadth of data obtained, but also benefited from enhanced ease-of-application of its methods. Researchers are working avidly to apply MTV in new flow regimes/facilities, as well as working with industry to develop new laser/camera technology to further improve MTV capability.

5. Focused Laser Differential Interferometry (FLDI)

5.1. Introduction to FLDI

FLDI enables measurement of short-wavelength, high-frequency density disturbances in a gas that are not currently possible with conventional instrumentation such as pressure transducers or hot wires. An example experimental setup, methodology of data extraction, and example results are presented. This method generally has accuracy of 5%, precision of 5%, and uncertainty of 5%. Measurement can be made at >50 MHz, with spatial resolutions of 350 μm and 20 mm in the flow streamwise and spanwise directions, respectively.

5.2. Basic Theory of FLDI

To measure the freestream tunnel noise and acoustic instability on a slender body in a large-scale high-enthalpy, hypersonic ground-test facility (such as the T5 reflected-shock tunnel at Caltech), six requirements of the diagnostic are clear:

1) High sensitivity to an unstable quantity in the boundary layer (in this case, density fluctuations),

2) High temporal resolution of the measurement technique (> 10 MHz),

3) High spatial resolution to resolve the small wavelength of the disturbance (< 1 mm),

4) Insensitivity to mechanical vibration,

5) The capability to have a small focal volume in the freestream or near the surface of the cone, and

6) A straightforward and repeatable means of extracting quantitative data from the technique.

The FLDI method meets these requirements. Two essential aspects for instability measurement with the FLDI method are identified as the ability to make localized measurements and record long, high-resolution data records. The ability to make localized measurements of fluctuation is necessary because the turbulent shear-layers from the facility nozzle can dominate a line-of-sight integrating optical measurement technique. The ability to probe only a small volume near the center of the test section significantly raises the achievable SNR relative to a line-of-sight integrating scheme. Smeets made measurements of localized turbulent fluctuations in a turbulent, free-jet experiment utilizing a system similar to the one presented in the next section.[172,173,174] Advances in technology have been crucial to the success of the measurement relative to the time Smeets was executing his free-jet experiments in the 1970's at the French-German Research Institute of Saint-Louis. Low cost, high vertical-resolution digitizers that are able to operate at high sampling rate for long duration are now available. This allows researchers to perform exceedingly detailed measurements at sufficient speed for instability work. Additionally, high-speed, low-cost, low-noise amplifiers are also now available. High-quality amplifiers

allow researchers to be prudent in how they set up the data acquisition, specifically, how the signal is terminated and digitized so that ambient electrical noise (RF) maybe reduced to acceptable levels.

The example experimental layout discussed here is nominally the same as in Smeets, but the dimensions, kinematics, and plane of laser beam separation are specifically designed for the purposes of high-enthalpy, hypersonic instability measurement. An annotated schematic of the experimental setup used for the examples in this section is presented as Fig. 5.1. The laser used is a Spectra-Physics Excelsior diode pumped solid state continuous-wave laser (532 nm wavelength, 200 mW power). The high-quality beam (TEM00) does not require additional beam conditioning for use in an interferometer. Following the optical path in Fig. 5.1, starting from the laser (L), the beam is turned by a periscope arrangement for precise directional control. The beam is expanded by a lens, C_1 (10 mm focal length), and linearly polarized by P_1 at 45° to the plane of separation of the first Wollaston prism, W_1. The normal to the plane of separation of W_1 is chosen to be orthogonal to the freestream flow or streamlines in the boundary layer of the five-degree, half-angle cone. The prism splits the light by a narrow angle (2 arc minutes) into orthogonally polarized beams. The separation of the beams in the streamwise direction is fixed at 175 μm by a lens, C_2 (300 mm focal length), while the diameter of the beams is reduced to small values in the center of the test section. This arrangement creates two beams with orthogonal polarization that are slightly displaced in the streamwise direction and traverse much of the same optical path, except near the focus. The orthogonally polarized beams do not share the same optical path within ±10 mm of the focal point (along the beam direction, centered at A in Fig. 5.1). In this region the beams are calculated to be less than 100 μm in diameter, and traverse separate but very closely spaced volumes. It is primarily within this small focal region that the diagnostic is sensitive to changes in optical path length (OPL). The spatial resolution of the technique (350 μm) is set by doubling the beam spacing to satisfy the Nyquist sampling theorem. FLDI is a finite differencing technique and fluctuations with a length scale below this spatial resolution may be ambiguously registered at the photodetector. Beyond the beam focus, the optical paths are again nearly common and an additional lens, C_2 (300 mm focal length), re-focuses the beams. The second Wollaston prism, W_2, and polarizer, P_2, recombine and then mix the orthogonally polarized beams, such that the interference will be registered as irradiance fluctuations by the photodetector, a high speed (14 ns Rise Time) silicon photodiode.
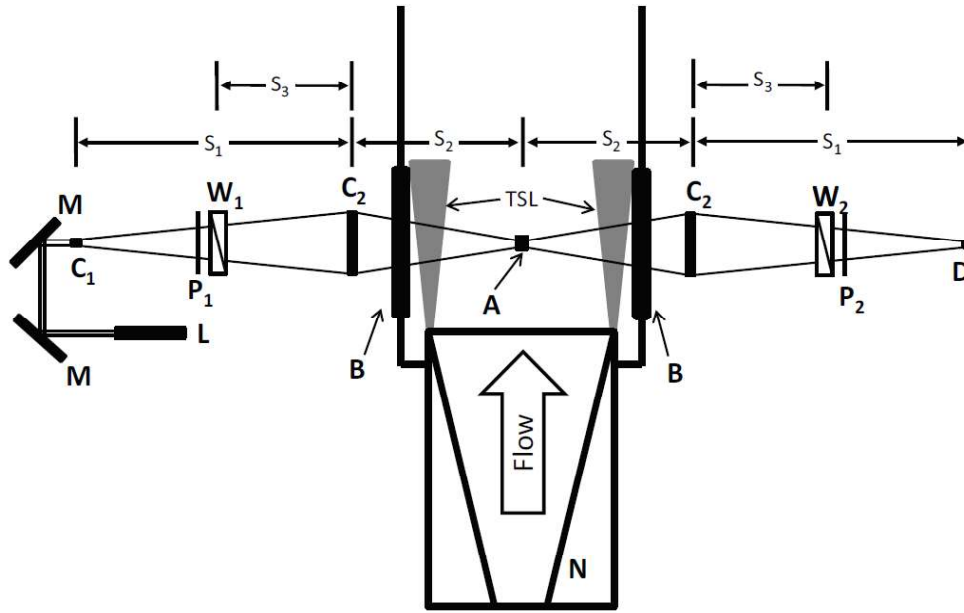
Figure 5.1. Annotated schematic of the FLDI. TSL, turbulent shear layer; L, Laser; M, mirror; C_1, 10 mm focal length lens; C_2, 300 mm focal length lens; P, polarizer; W, Wollaston prism; B, BK7 window; A, probe volume; D, photodetector; N, nozzle, $s_1 = 718$ mm, $s_2 = 515$ mm, $s_3 = 300$ mm. Reprinted with permission of the author.[175]

The FLDI technique detects differences in phase primarily due to the density differences at the two focal regions, which are separated in the streamwise direction, making the interferometer sensitive to spatial density differences in the streamwise direction. A relation between the fluctuations in density and output voltage from the photodetector is needed for post-processing. A simple approach to finding this relation is found by considering the region within ±10 mm of the focal point, along the beam direction (where the optical paths are not common), to be a two-beam differential interferometer. The result is

$$\frac{\Delta\rho}{\rho_L} = \frac{\lambda_0}{2\pi K L \rho_L} \sin^{-1}\left(\frac{V}{V_0} - 1\right) \tag{5.1}$$

where $\Delta\rho/\rho_L$ is the change in density normalized by the local mean density, λ_0 is the laser wavelength, K is the Gladstone-Dale constant for the gas being probed, L is the assumed integration length of the interferometer, and V/V_0 is the instantaneous photodetector voltage normalized by the photodetector voltage when the instrument is set to the midpoint of an interference fringe.

5.3. Examples of FLDI Measurements

5.3.1. *Freestream Noise Measurement in the T5 Reflected-Shock Tunnel[176]*

FLDI has been used to quantify the freestream density perturbations in the T5 reflected-shock tunnel. The investigation of reflected-shock tunnel disturbances is motivated by the study[175,177] of high-enthalpy, hypersonic boundary-layer instability and transition. Results are reported here for high-enthalpy,

hypersonic air flows at reservoir enthalpies between 5 and 18 MJ/kg at Mach 5.5 (Fig. 5.2 – Top Right). Spectrograms show that the freestream disturbance level is constant throughout the test time (Fig. 5.2 – Bottom Right). Power spectral density estimates of each of the experiments are found to collapse upon each other when the streamwise disturbance convection velocity is used to eliminate the time scale (Fig. 5.2 – Left). Furthermore, the disturbance level depends strongly on wavelength. If the disturbance wavelength range of interest is between 700 μm and 10 mm, the tunnel noise is measured to be less than 0.5 % with the FLDI.
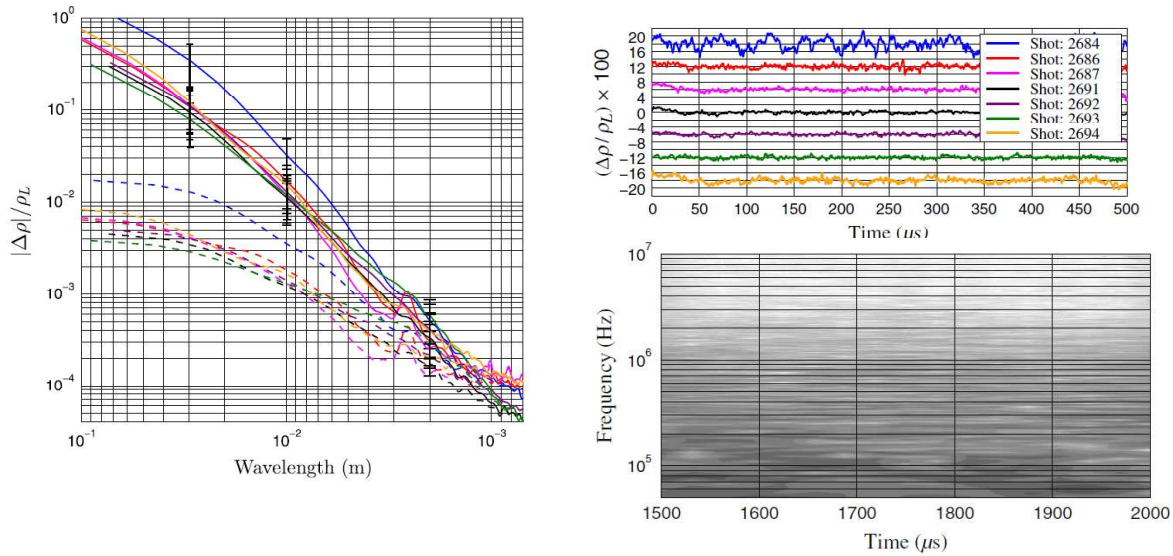

Figure 5.2. *Left*: Wavelength spectrum of tunnel noise time traces. There are two sets of wavelength spectrum plots of the same data. The lower amplitude data has not been corrected for the sensitivity of the FLDI technique to wavelength (dashed lines). The higher amplitude data has been corrected for the sensitivity of the FLDI technique to wavelength (solid lines). *Top Right:* Filtered time traces of $\Delta\rho/\rho_L$ (filter cutoffs: 5 kHz-20 MHz). Each trace is offset 6 % along the ordinate and is 500 us of the steady test time. Note that shot 2684 has a notably larger amplitude than the other shots due to an experimental blunder. *Bottom Right:* Spectrogram (contours of power spectral density plotted in time–frequency space) of shot 2693; this illustrates how the spectral content of the fluctuations in the free-stream evolve throughout the test time. Reprinted with permission of the author.[175]

5.3.2. *High-Enthalpy, Hypersonic Boundary-Layer Instability Measurement[178,179]*

High-frequency density fluctuations (up to 3 MHz) that precede laminar to turbulent boundary layer transition have been detected using FLDI in a high-enthalpy, hypersonic flow. Experiments were carried out in the T5 reflected-shock tunnel to generate flows in air, nitrogen, and carbon dioxide with speeds between 3.5 and 5 km/s (Mach numbers between 4 and 6) over a 5 degree half-angle cone at zero angle-of-attack. Simultaneous measurements are made at two locations approximately midway along a generator of the 1-m-long cone. With increasing Reynolds number (unit values were between 2

and 5 x 10^6 1/m), density fluctuations are observed to grow in amplitude and transition from a single narrow band of frequencies consistent with the Mack or second mode of boundary-layer instability to bursts of large-amplitude and spectrally broad disturbances that appear to be precursors of turbulent spots (Fig. 5.3). Disturbances that are sufficiently small in initial amplitude have a wavepacket-like signature and are observed to grow in amplitude between the upstream and downstream measurement locations (Fig. 5.4). A cross-correlation analysis indicates propagation of wavepackets at speeds close to the edge velocity. The scaling of the observed frequency with the inverse of boundary-layer thickness and directly with the flow velocity are consistent with the characteristics of Mack's second mode, as well as results of previous researchers on hypersonic boundary layers.
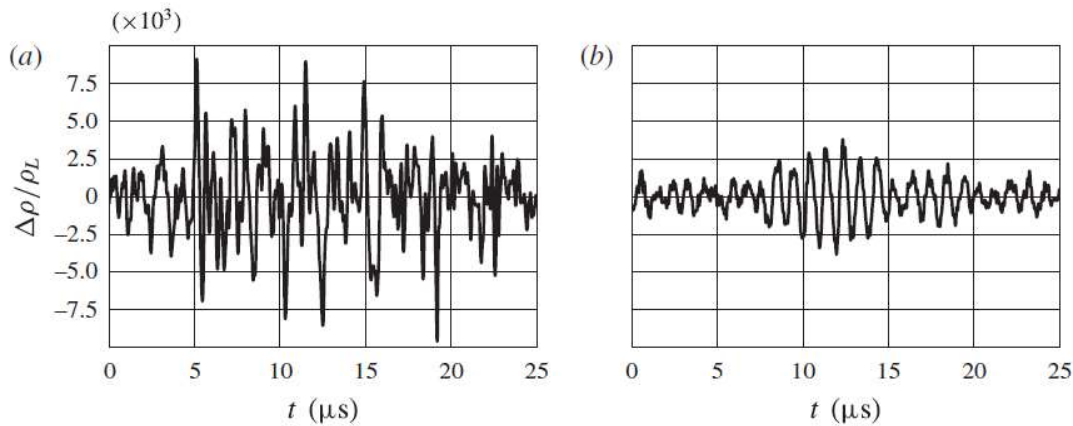
Figure 5.3. Examples of the two principal signatures observed in FLDI signals: (a) broadband, large-amplitude signal characteristic of locally turbulent flow; (b) narrow-band, small amplitude signal, characteristic of a wavepacket in laminar flow. These examples are for an air boundary layer (shot 2743) with reservoir enthalpy h_R=9:1 MJ/kg. Reprinted with permission of the author.[175]
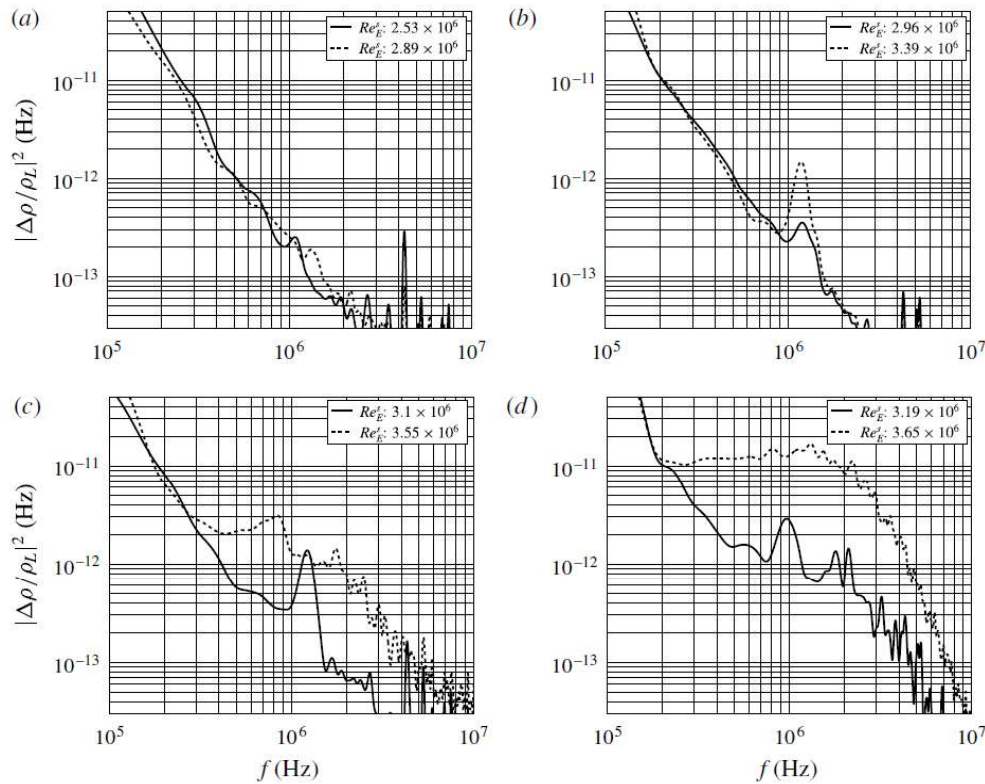
Figure 5.4. Power spectral density estimates of $\Delta\rho/\rho_L$ for the high-enthalpy air shot series. The solid line marks the upstream detector, the dashed line marks the downstream detector. Going from a-d is a ramp in Reynolds number. (a) shot 2788: $Re = 4.03\text{x}10^6$ 1/m, nominally quiescent flow, (b) shot 2789: $Re = 4.73\text{x}10^6$ 1/m, 1.5 MHz disturbances growing in amplitude between upstream and downstream detectors, (c) shot 2790: $Re = 4.94\text{x}10^6$ 1/m, beginning of transition to turbulence, (d) shot 2787: $Re = 5.08\text{x}10^6$ 1/m turbulent flow. Reprinted with permission of the author.[175]

5.3.3. *Comparison of Pitot-Pressure Spectra and FLDI Spectra in the NASA Langley 20-Inch Mach 6 Tunnel[180]*

Work by Chou et al.[180] compared FLDI freestream measurements recorded over a range of tunnel conditions and to spectra recorded by Pitot-probes. The spectra shown in Fig. 5.5 (left) are of relative density fluctuations in the 20-Inch Mach 6 freestream for a sweep of unit Reynolds numbers tested and two flow-off conditions. The absolute sensitivity of this instrument to density fluctuations has not yet been determined so these spectra are in arbitrary units. The solid black curve in Fig, 5.5 (left) shows the FLDI measurements with no flow at ambient conditions. The very-narrow spikes in the 20-kHz to 1-MHz region are from unidentified electronic noise. The dashed black curve in Fig. 5.5 (left) shows the FLDI measurements with no flow while the tunnel is at vacuum. This curve shows that the instrument is sensitive to the fluctuations caused by slow leaks in the test box and thus may not show a true noise floor

for the FLDI. The main feature of the flow-on data in Fig. 5.5 (left) is the broadband nature of the freestream density fluctuations from 1-30 kHz. The solid and dashed green curves illustrate the repeatability of the combined instrument for two runs at the highest Reynolds number. This repeatability was consistent for the other Reynolds numbers as well.

A comparison of the power spectra of measured Pitot-probe pressure fluctuations to the power spectra of measured density fluctuations is given in Fig. 5.5 (right). Note that the quantities measured by the Kulite and PCB pressure transducers and the FLDI instrument are different: the probes measure fluctuations in pitot pressure while the FLDI measures fluctuations in density. It is uncertain that flush mounted pressure transducers in a Pitot probe configuration produce a faithful representation of the noise level in a supersonic or hypersonic freestream.[176] This is a major motivator for the use of non-intrusive optical diagnostics such as FLDI to assess the freestream fluctuation levels. The interaction of freestream fluctuations with the bow-shock wave that forms in front of the Pitot-probe may thwart the goal of resolving a wide range of disturbance length scales. This interaction is known to be a function of the obliqueness and the strength of the shock wave. The complexity of the subsonic flow field behind the bow-shock wave may further obscure the fidelity of freestream disturbance measurement, especially in the frequency domain. In Fig. 5.5 (right), the power spectra of the Kulite and PCB measurements are truncated to the quoted bandwidths of each sensor. At the lowest Reynolds number, the slope and roll-off of the FLDI and Kulite spectra agree well for the bandwidth of 1 kHz to 20 kHz. The power spectra of the PCB probe data in Fig. 5.5 (right) appears to deviate from the FLDI measurement for the Reynolds number shown here. A major difference is that the FLDI is less sensitive to the electronic noise. Further work is required to calibrate the FLDI response and assess the differences in the spectra.
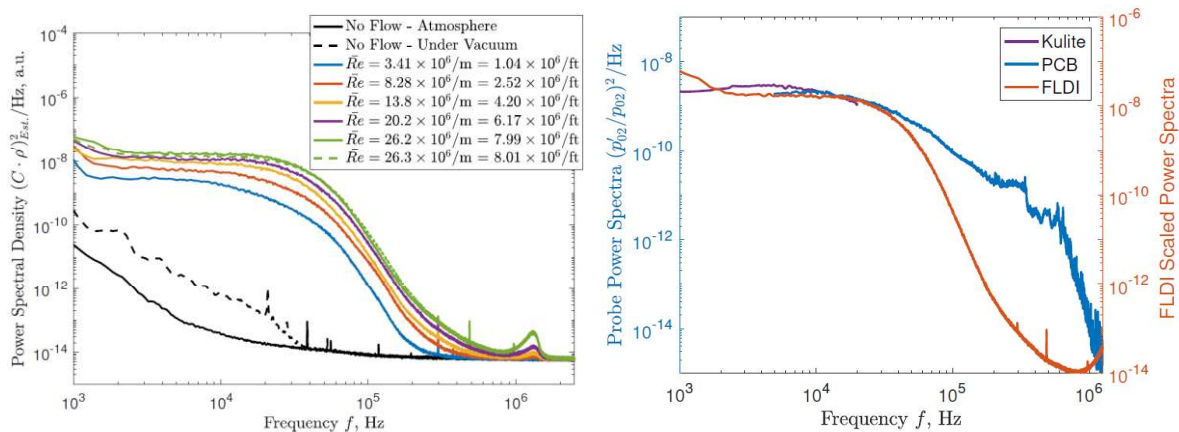
Figure 5.5. *Left:* Power spectral density of measurements made with the FLDI for various Reynolds numbers. *Right:* Qualitative comparison of FLDI spectra and pressure spectra at $Re = 7.99 \times 10^6$ 1/ft = 26.3×10^6 1/m. Reprinted with permission of the author.[180]

5.4. Conclusions for FLDI

Focused laser differential interferometry has been used to measure high-frequency density fluctuations in high-enthalpy, hypersonic flow regimes where other measurement technologies cannot be used. This section highlighted FLDI implementation in the Caltech T5 Reflected-Shock Tunnel where the freestream and boundary-layer instability fluctuations were measured. Additionally, a comparison of Pitot-pressure spectra and FLDI spectra in the NASA Langley 20-inch Mach 6 tunnel was presented.

One issue with FLDI is that there is some line-of-sight integration with the signal that adds to uncertainty of the spectra reported here. That is, the FLDI technique is sensitive at the focus ±15 mm (in this implementation; ultimately it will depend on the optical design), but also to a lesser extent past this 15 mm. To resolve this issue, researchers[181-183] have been working to derive transfer function formulas that may be applied to account for this. To apply these transfer functions to the data, it must be transformed into wavenumber space which requires knowledge of the local convective velocity. Researchers are also working on a modification to the FLDI setup where two FLDI's or dual-FLDI (or D-FLDI) is implemented with a streamwise displacement on the order on 1 mm. This setup enables convective velocity measurement. Jewell et al.[184] first demonstrated disturbance speed measurements using cross-correlated D-FLDI in a shock tube, as well as a reflected-shock tunnel boundary layer as part of the broader high-enthalpy slender cone campaign.

Hedlund et al.[185] used LDI to characterization of Mach 4.5 flow over a flat-plate model with a 30 deg compression ramp was performed with low-enthalpy (T_0=300 K) and high-enthalpy (T_0 = 800–1250 K) flow conditions for a wide range of unit Reynolds numbers. Harris et al.[186] used LDI as an approach to characterizing freestream disturbance levels. Sayler et al.[187] used feedback stabilized LDI for supersonic blunt body receptivity experiments. Ceruzzi and Cadou[188] used FLDI and LDI to investigate fluctuating density gradients in a simple turbulent air jet in preparation for making fluctuation measurements in larger-scale wind tunnels. This recent bout of activity is indicative of the promise of the FLDI technique in high-speed and reacting flow.

6. Laser Scattering Techniques

6.1. Introduction to laser scattering techniques

The interactions of light and the molecules or particulates within a gaseous medium can provide a great deal of insight into the flow properties of the gas. Typical interactions, and measurements thereof, include absorption, fluorescence, and light scattering. This section focuses on the measurement of light scattering from molecules and particles, with processes broken down into three categories: Mie, Rayleigh, and Raman scattering. Mie scattering occurs when light scatters from particles whose diameter is on the order of the wavelength of incident light or larger. Scattering from molecules or particles whose diameter is much smaller than the wavelength of light is broken down into two categories: spontaneous Rayleigh scattering if the scattering is elastic, and spontaneous Raman if the scattering is inelastic. The difference between elastic and inelastic scattering is shown in Fig. 6.1. As shown in the energy level diagram, scattering occurs when a photon ($h\nu$) excites a molecule from its ground state (1) to a 'virtual' state (2). If the molecule relaxes back to the ground state, emitting a photon in the process, the scattering is considered elastic since there is no net energy transfer between the photon and the molecule. Mie and Rayleigh are both elastic scattering processes. If, instead, the molecule relaxes to a different state (either rotational or vibrational as in Raman scattering), thereby transferring a quanta of energy between the photon and the molecule, the scattering is considered inelastic. Relaxation to a higher-lying state than the initial is termed Stokes Raman scattering, while relaxation to a lower-lying state is termed anti-Stokes Raman scattering. Physically, Stokes Raman occurs when the molecule absorbs a quanta of energy from the incoming light and anti-Stokes Raman occurs when the molecule imparts a quanta of energy to the scattered photon. Such spontaneous scattering is in all directions although the intensity of the scattering in different directions varies with angle.
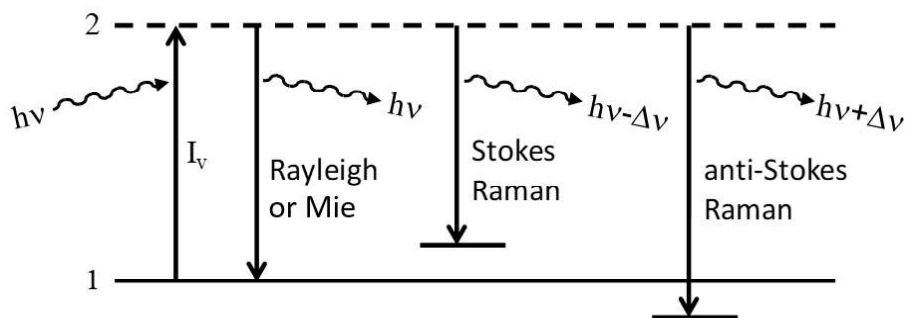
Figure 6.1. Energy level diagram showing elastic and inelastic scattering methods.

Typical laser-based techniques which directly measure the light scattering for fluid measurements include: Doppler global velocimetry (DGV) which uses Mie scattering, filtered Rayleigh scattering

(FRS), interferometric Rayleigh scattering (IRS), and spontaneous Raman spectroscopy (SRS). A typical experiment using these techniques would utilize a narrow-linewidth laser, tuned to a specific wavelength, shaped into a thin beam, or sheet, in the area of interest and a CCD/CMOS camera for imaging the scattering. Simple measurements of the gas density using Rayleigh scattering are possible using the aforementioned setup; however other quantities such as velocity, translational temperature, and pressure require the use of light frequency discriminators, such as Fabry-Perot interferometers and atomic-vapor cells, to measure the spectrum of the Mie/Rayleigh scattered light. To measure the rotational/vibrational temperature or concentration of a species the Raman spectrum needs to be analyzed which requires the scattered light to be dispersed, typically via a grating. An additional concern is the signal, or lack thereof, especially for Rayleigh and Raman measurements. For Mie scattering, the amount of scattered light is proportional to the diameter of the particle squared. Therefore if one needs more signal, a larger particle could be used; however, larger particles make for worse tracers, especially at hypersonic speeds. (See Section 8 of this manuscript for further discussion of particle lag issues.) Rayleigh scattering generally produces orders of magnitude less signal than Mie scattering since the particles are smaller, and therefore requires a higher gas density and laser energy to achieve detectable signal levels. Raman produces even less signal, typically by three orders of magnitude. Because of the lack of relative signal, an image intensifier or other camera gain mechanism may be necessary to perform Rayleigh and Mie scattering experiments for lower density environments typical of supersonic and hypersonic flows.

6.2. Basic Theory of Laser Rayleigh Scattering Techniques

6.2.1. Doppler global velocimetry

DGV, also known as planar Doppler velocimetry (PDV), determines the fluid velocity by measuring the frequency shift of light scattering from particles immersed in the fluid, known as the Doppler shift.[189] This shift, $\Delta \nu$, is directly proportional to the velocity of the particle as given by:

$$\Delta \nu = \frac{(\hat{o} - \hat{\imath}) \cdot \vec{V}}{\lambda} \tag{7.1}$$

where $\hat{o}$ is unit vector in the direction of the observer, $\hat{\imath}$ is the unit vector in the direction of laser propagation, $\vec{V}$ is the velocity of the particle, and λ is the wavelength of the incident laser. It is important to note that the velocity vector measured by a single DGV observer is in the $(\hat{o} - \hat{\imath})$ direction, as shown in Fig. 6.2 (*left*). Basically, the measured component is in the direction that bisects the incident and detected light. In addition, if the full 3-component velocity field is desired, three separate DGV observations are required, and, in practice, a fourth observer is sometimes added for robustness.[190]

The measurement of the Doppler shifted frequency is typically accomplished by measuring the absorption of the scatted light imaged through an atomic or molecular vapor filter. The most common

molecular vapor filter is Iodine due to its numerous absorption features in the frequency range of frequency-doubled Nd:YAG lasers (532 nm) and argon ion lasers (for example at 514.5 nm), and its features having steep cut-off frequencies.[191] Other species such as Mercury and Cesium are generally used for 254 nm and 850 nm, respectively. To measure the Doppler shift using a molecular filter, the laser frequency is tuned such that the laser frequency plus the nominal Doppler shift induced by the mean particle velocity is located at the mid-point along the side of an absorption feature, as shown in Fig. 6.2 (*right*). If a particle moves faster than the mean, thereby creating a larger Doppler shift, the Iodine will absorb more of the light, and create a darker image. If the particle is moving slower, the image will appear brighter.
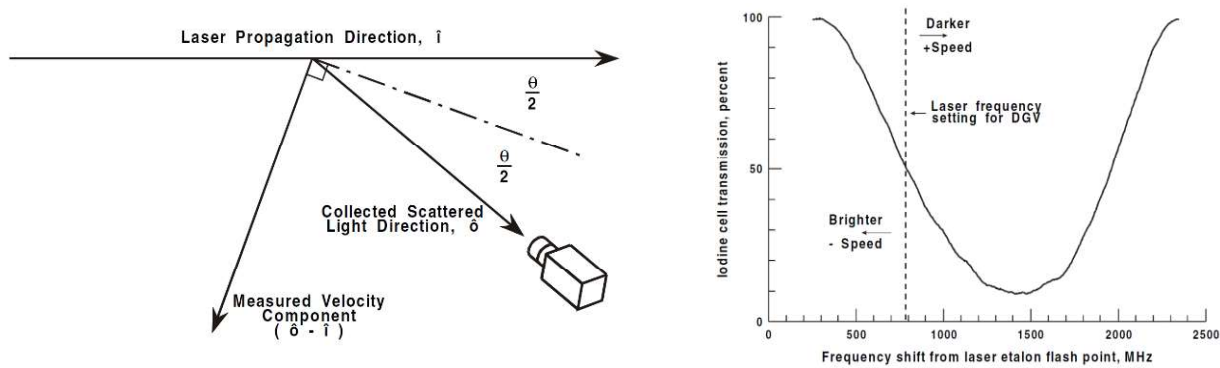
Figure 6.2. (*left*) shows the geometry of the measured component of velocity and (*right*) shows the working principle of DGV. From Meyers et al.[192] Reproduced with permission by the authors.
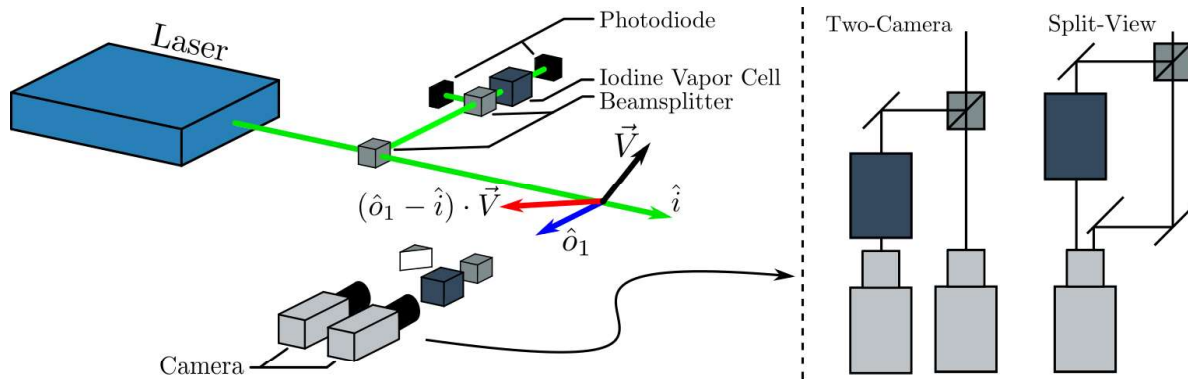
Figure 6.3. Example 1-view DGV experimental setup.

A typical experimental configuration is shown in Fig. 6.3. A narrow-linewidth, tunable laser passes through sheet-forming optics into the region of interest. Imaging the scattered light are two cameras, one that directly views the scattered light, known as the reference camera, and one that views the scattered light through an Iodine vapor cell, known as the signal camera. The reference image is necessary to

account for inconstancies in the laser sheet and other optical aberrations in the beam path as well as variations in seed density. The ratio of these two images yields the absorption, and therefore the Doppler-shifted frequency. In order to determine the velocity, the frequency of the incident laser must also be determined such that the difference can be calculated. Typically this is performed using the same signal/reference system as described before, termed the laser frequency monitor (LFM), but instead of measuring the scattered light from particles, a small portion of the incident laser is picked off before the sheet-forming optics and measured. This method only yields the frequency relative to an absorption feature, therefore it is necessary to determine a-priori which Iodine feature is adjacent to the laser. An alternative to using an LFM to determine the frequency output of the laser is to use it as a feedback mechanism to lock-in the laser frequency, which is possible for some lasers. Variations of DGV, which use an interferometer (I-DGV), are able to eliminate the need to tune the laser to specific absorption lines,[193] as well as eliminate the use of the atomic vapor cells entirely.[194] These I-DGV techniques are capable of measuring the Doppler shift more accurately than the standard system, but at the expense of optical complexity and temporal resolution.

The laser used to perform DGV measurements needs to have a narrow linewidth to increase the sensitivity and dynamic range of the measurement. As such, typical DGV experiments use continuous wave lasers as injection-seeded pulsed Nd:YAG lasers tend to have much higher line-widths (120 MHz) compared to an argon-ion laser (10 MHz). In addition, it has been found that these pulsed lasers have frequency variations from pulse-to-pulse (of about 80 MHz) as well as spatially across the beam profile due to variations in the flatness of the rods.[192] A pulse-burst laser can give the narrow line-width necessary while having pulsed operation, in addition to allowing for MHz rate measurements.[195]

One of the drawbacks of using the side of the absorption feature to measure the Doppler shift, is that the dynamic range of the measurement is limited to the size of the feature. Typically these features are around 500 MHz in spectral bandwidth corresponding to roughly 350 m/s, depending on the properties of the atomic vapor cell and the observation angle. Measurements outside this frequency range would create ambiguity as a single absorption level would correspond to multiple Doppler shifts. Cross-correlation DGV (CC-DGV[196]) extends the dynamic range by scanning over multiple absorption features, then computes the cross-correlation of the measured absorption and the absorption from the LFM. The peak of the cross-correlation is the time-averaged Doppler shift over the scan duration. Cadel and Lowe[196] report measurements with a mean velocity of 600 m/s with measurement uncertainties ranging from 0.5-17 m/s. The authors note that the technique itself has an effectively infinite dynamic range theoretically, but they are limited to 3000 m/s by domain of their frequency scan. Due to this increased dynamic range, this

variation shows promise for high-speed (supersonic and hypersonic) flows; however, it is only capable of measuring the mean velocity.

One of the most common sources of error in a DGV experiment is the registration between the reference and signal images for each observation. It is imperative that these images are aligned to sub-pixel accuracy as even a 0.1 pixel misalignment can lead to a ± 5 m/s error.[197] Additionally, the beam-splitters used to create the reference/signal paths have 3-5%[192,198] variation in the split ratio which can lead to a ± 7 m/s velocity error in fixed wavelength schemes.

The standard two-cameras-per-view creates an expensive diagnostic since one needs 6-8 cameras to perform the planar measurement. Some cost effective variations of the two-camera setup include splitting the views onto a single camera (shown in Fig. 6.3), as well as using fiber bundles, where each fiber bundle images a different observation angle and all the bundles are imaged onto a single camera. The downside of both these options is that they decrease the spatial resolution of the measurement, and in the case of the fiber bundles, they decrease the amount of light captured. Variations of the technique seek to overcome these limitations. Two-frequency DGV ($2v$-DGV[198]) minimizes the number of cameras needed for each observation from two to one without the need for a split-view configuration, eliminating registration issues between the signal and reference views; however since the two laser pulses are imaged sequentially this technique is a time-averaged measurement where the data is effectively averaged over the time between the signal and reference measurements. Frequency modulated DGV (FM-DGV[199]) removes the need for a reference image entirely, by computing the Doppler shift in the frequency domain after modulating the incident laser frequency. By removing the need for a reference image, the uncertainty of the measurement is reduced by an order of magnitude in principle. Fischer et al[199] reports minimum standard deviations of 0.02 and 0.04 m/s, with a dynamic range of ± 350 MHz or ± 240 m/s. As with the previous technique, extra temporal information is required such that FM-DGV is a time-averaged measurement. An alternate version of this concept, using four discrete frequencies is the so-called frequency-shift-key DGV (FSK-DGV).[200] Since this technique requires four images to reconstruct a velocity field, the temporal resolution is determined by both the rate at which the different frequencies can be generated as well as the frame rate of the cameras.

The major benefits of DGV as a measurement technique are its high signal intensity, leading to low uncertainty (typical 2-3 m/s[201,202] and optimally ± 0.5 m/s[192,203]), and its ability to use small particles, when compared to PIV. Since the particles do not need to be individually resolved, they can be smaller or the field of view can be larger if sufficient laser energy is available. Both of these situations are beneficial to hypersonic free-stream measurements since smaller tracers follow the flow more accurately and larger fields-of-view allow for a more complete measurement of the freestream.

6.2.2. Filtered Rayleigh scattering (FRS)

FRS is conceptually very similar to DGV, using the same equipment, but different seeding; molecules naturally present in the flow are probed. By using molecular scattering the technique does not require seeding, which can be a huge benefit in facilities where adding particles is problematic. Particles are difficult to uniformly seed in some flows while in others, particles are not allowed because of contamination concerns. In addition, Rayleigh spectra can be used to measure velocity, pressure, temperature, and density simultaneously whereas DGV and PIV typically only measure velocity. The velocity measurement is based on the Doppler shift as described earlier; whereas pressure and temperature are measured based on the line-shape of the Rayleigh spectra while the gas density is measured from the overall Rayleigh signal intensity.

In order to measure Rayleigh spectra, the laser frequency is typically scanned, and the resulting Rayleigh scattering is measured through an atomic/molecular vapor cell. The measured signal is therefore a convolution between the Rayleigh line-shape and the absorption properties of the vapor cell. Since the absorption properties of the cell can be measured or modeled, the signal can be deconvolved to recover the Rayleigh lineshape. It is noted that while the velocity could be theoretically recovered without scanning, via the same process as DGV, the sensitivity would be lower due to the broadness of the Rayleigh spectra with respect to the molecular absorption features.

A very brief explanation of Rayleigh scattering theory is presented herein. For a more complete explanation the reader is referred to Miles et al.[191] In reference to Fig. 6.4 (*left*), which shows the complete light scattering from a diatomic molecule, the Rayleigh spectrum lies closest to the incident laser light central to the bands of rotational Raman. This lone spectral feature is caused by the random translational motion of the molecules, whereas the bands on either side represent rotational modes, and the Stokes/anti-Stokes bands represent vibrational modes. There are two regimes for translational motion. At low pressure or high temperature, the motion is thermally dominated leading to a thermally-broadened Gaussian spectral profile. On the other hand, if the motion is collision-dominated at the hydrodynamic limit, the line-shape shows prominent acoustic sidebands, whose shape is a Lorentzian profile, located at frequencies corresponding the speed of sound in the medium. If the experiment is conducted between these two regimes (as is commonly the case), the profile has both thermal and acoustic features. If the molecule is anisotropic, a portion of the rotational Raman scattering (rotational Q-branch) is added to the Rayleigh signal. The combination of these features results in the Cabannes profile as shown in Fig. 6.4 (*left*).
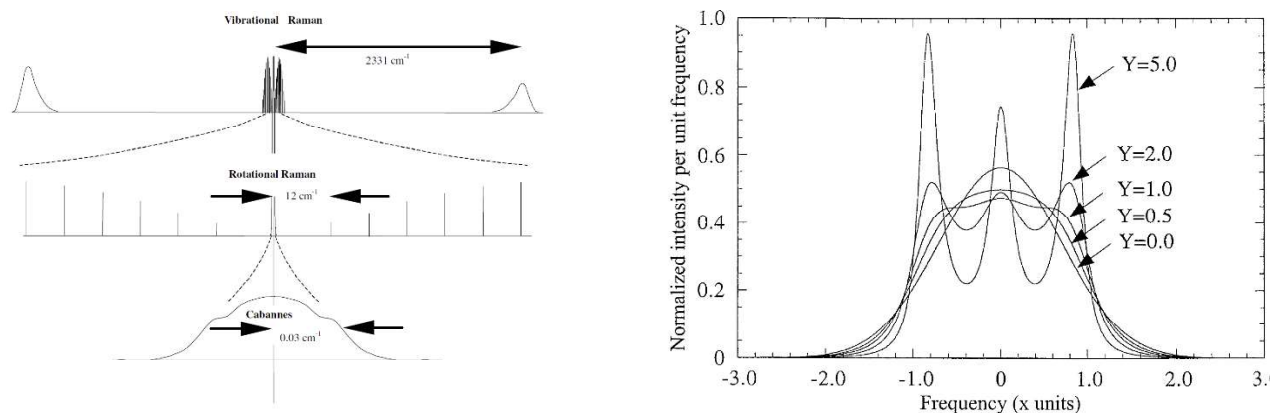
Figure 6.4. (*left*) shows the scattering components of a diatomic molecular gas (e.g. N) from laser illumination, at increasing resolutions, focusing on the elastic Rayleigh scattering and (*right*) shows the Rayleigh-Brillouin profiles for various y-parameters. From Miles et al.[191] and reprinted with permission of the authors.

The combination of the thermal and acoustic processes results in a complex line-shape known as the Rayleigh-Brillouin line-shape shown in Fig. 6.4 (*right*). This line-shape is the combination of the Cabannes line-shape generated via Rayleigh scattering and the acoustic sidebands generated from 'Brillouin-Mandel'shtam scattering'. The prominence of the acoustic or thermal modes is based on the temperature and pressure. Models of this line-shape, most notably the S6 model developed by Tenti et al[204], define a non-dimensional quantity as the ratio between the scattering wavelength to the mean free path, known as the y-parameter. This parameter is a function of temperature, pressure, laser wavelength, and observation angle, and the effect of changing the y-parameter is shown in Fig. 6.4 (*right*). It is shown that a y-parameter of 0 represents a thermally dominated gas while large values represent a collision-dominated gas with combinations of the two in between. For FRS, the measured Rayleigh-Brillouin lineshape is recovered, and can therefore be fit to the data of the Tenti S6 model to obtain the temperature and pressure, while the overall spectral shift (Doppler shift) can yield the velocity. Reported uncertainty for FRS measurements, made in a Mach 2 jet, are ± 2 m/s (2-3%), ± 38 Torr (4-5%), and ± 3.2 K (2%) for velocity, pressure, and temperature respectively.[205]

6.2.3. *Interferometric Rayleigh scattering (IRS)*

IRS is a technique which spectrally analyzes Rayleigh scattering by isolating specific frequencies using a Fabry-Perot interferometer[206] (etalon), which is made up of two partially-transmitting planar mirrors, as shown in Fig. 6.5 (*left*). This set of mirrors acts as a multiple beam interference device which generates an Airy pattern. The image generated by the IRS technique is the convolution of this Airy pattern, generated by the etalon, and the spectra of the scattered light, as shown in Fig. 6.5 (*right*). If the scattered light is spectrally narrow (i.e. a single-mode laser) the image appears as thin concentric rings,

called fringes, whose spacing is determined by the free spectral range of the etalon. If the scattered light is spectrally broadened (as the Rayleigh scattering is) the fringes broaden accordingly, and provide a means to measure temperature. The velocity can be determined by the spatial shifting of the rings via the Doppler shift, and the density can be measured by the amplitude of the signal. The IRS technique can also be designed to measure multiple components of velocity on a single detector as demonstrated by Bivolaru et al.[207] where they were able to encode two orthogonal components of velocity onto a single detector by placing a mirror on the opposite side of the probed region, along the optical access, to reflect the scattered light along the same optical path through the interferometer.
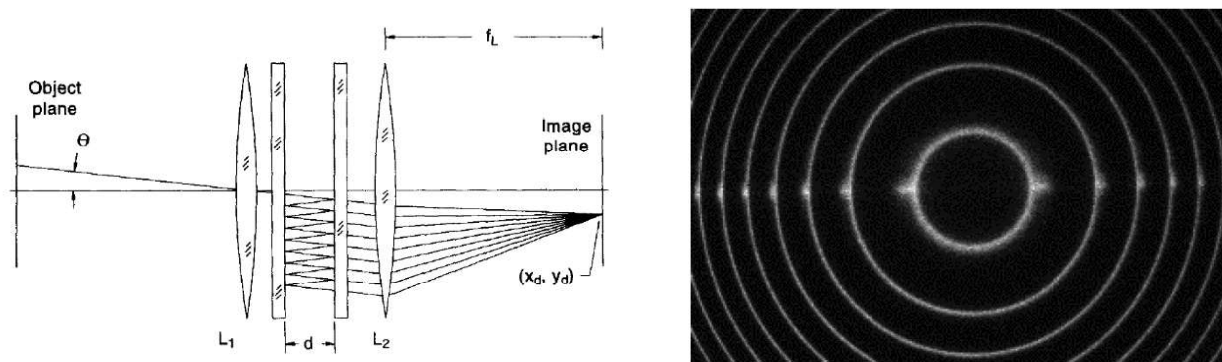
Figure 6.5. Fabry-Perot Interferometer (*left*) and IRS image of a supersonic jet (*right*). From Seasholtz et al[206] and reprinted with permission of the author.

The major tradeoff between filtered and interferometric Rayleigh scattering measurements is that FRS provides a 2D time-averaged measurement while IRS provides a 0D (pointwise) instantaneous measurement at one or a few points in a flow. Therefore the user must decide if spatial or temporal resolution is more important when choosing between these approaches.

6.2.4. *Spontaneous Raman scattering (SRS)*

SRS measures the Raman spectrum, which is sensitive to individual rotational and vibrational transitions. This spectra is created from the scattering from molecules occupying different energy states. Stokes Raman, where a quanta of energy is absorbed by the molecule, can occur for a molecule starting in any state, while anti-Stokes Raman is only available for molecules in excited states (above the ground state). When compared to Rayleigh scattering, the signal intensity of Raman scattering is lower (typically three orders of magnitude). Rayleigh scatter is caused by an incoming photon perturbing the electron cloud. The perturbation is unstable and the energy is scattered at the same wavelength (neglecting Doppler shifts). Raman involves nearly the same process except that the molecule (very occasionally, with low probability) undergoes a change in rotational or vibrational state during the scattering process with the balance of energy imparted to the scattered photon. This is why Raman is much weaker than

Rayleigh. For gases in thermal equilibrium, the Stokes spectra is stronger than the anti-Stokes, since more molecules occupy the ground state. From the population distribution of the energy states, it is possible to measure rotational and vibrational temperature, from its fundamental definition, as well as species concentration.

Experimentally, SRS is typically performed using pulsed Nd:YAG lasers equipped with pulse-stretching optics to have as much energy as possible while not causing laser induced breakdown. These lasers are typically focused to a point in the flow which is then imaged through a spectrometer onto a linear array or a camera, such that the spectra can be resolved. One common issue with SRS measurements is the intensity of the Rayleigh spectra overwhelming the Raman spectra. To overcome this issue, notch filters, tunable filters, etc. are used to remove the Rayleigh spectra.

Figure 6.6 shows an example Raman spectrum obtained from a high-pressure CH_4 flame.[208] This spectra shows many different spectral features which are directly related to the rotational and vibrational temperatures as well as the different concentrations of the products in the flame. Models of such spectra exists allowing for data fitting analysis where the temperatures and concentrations can be determined directly from measured spectra. Rotational temperature can be determined by analyzing the rotational bands of the Raman spectrum as the strength, position, and shape of the lines/envelope vary with rotational temperature. Vibrational temperature can be calculated based on the relative heights of the vibrational Raman bands. The Stokes and anti-Stokes N_2 band is commonly used since it is a common constituent in supersonic, hypersonic, and combusting flows, a well understood molecule, and is spectrally isolated from other common bands. Another method of measuring the vibrational temperature is to spectrally fit the vibrational bands of a molecule as shown below.
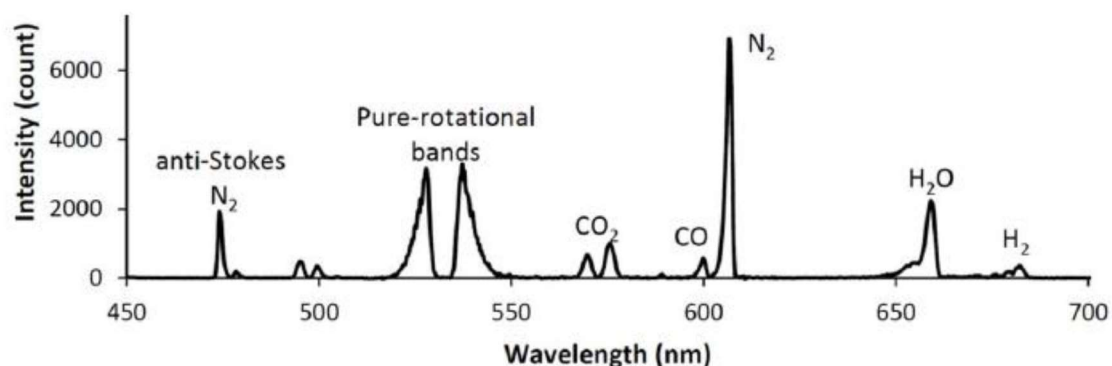

Figure 6.6. Five-hundred-pulse-average Raman spectrum in a high-pressure CH_4 air flame. The excitation laser wavelength was 532 nm. A 532 nm filter blocks Mie, Rayleigh and spurious laser scattering as well as some of the low-rotational-quantum-number rotational Raman lines. A subframe burst gating (SBG) technique was also used to subtract background emission from this spectrum. (From Kojima and Fischer[208]) Reprinted with permission of the authors.

6.3. Example of Laser Scattering Experiments

DGV, FRS, IRS, and SRS are measurement techniques capable of measuring velocity, temperature, pressure, and species concentration in hypersonic flow fields. Some of these techniques have yet to be applied directly in hypersonic facilities, but no physical phenomena limits their capability. In fact, the use of small particles, or no particles for Rayleigh/Raman, is a boon for hypersonic test conditions as large tracers are restricted in their ability to follow the flow, especially through shocks and other large velocity gradients as described in the PIV section of this manuscript. An issue that might preclude the use of Rayleigh/Raman in a particular facility is that the signal is a direct function of density, and hypersonic facilities typically operate at low densities. This can be overcome with increases to laser power, camera sensitivity, or observation time, but low signal is a drawback nonetheless. Examples are provided to illustrate the capability of the techniques.

Thurow et al.[195] used a pulse-burst laser to perform time-resolved (250 kHz) DGV measurements of a rectangular Mach 2.0 jet. The system was capable of producing 28 images/burst at 250 kHz with 9 mJ/pulse of energy. Measurements were conducted approximately 6-12 jet heights downstream of the nozzle exit, and one velocity component was measured. Figure 6.7 (*top*) shows the velocity obtained with full field of view, and Fig. 6.7 (*bottom*) shows a zoomed-in time-sequence of the area indicated via the white rectangle. These images show the technique's ability to temporally resolve small flow features contained in the jet's mixing layer.
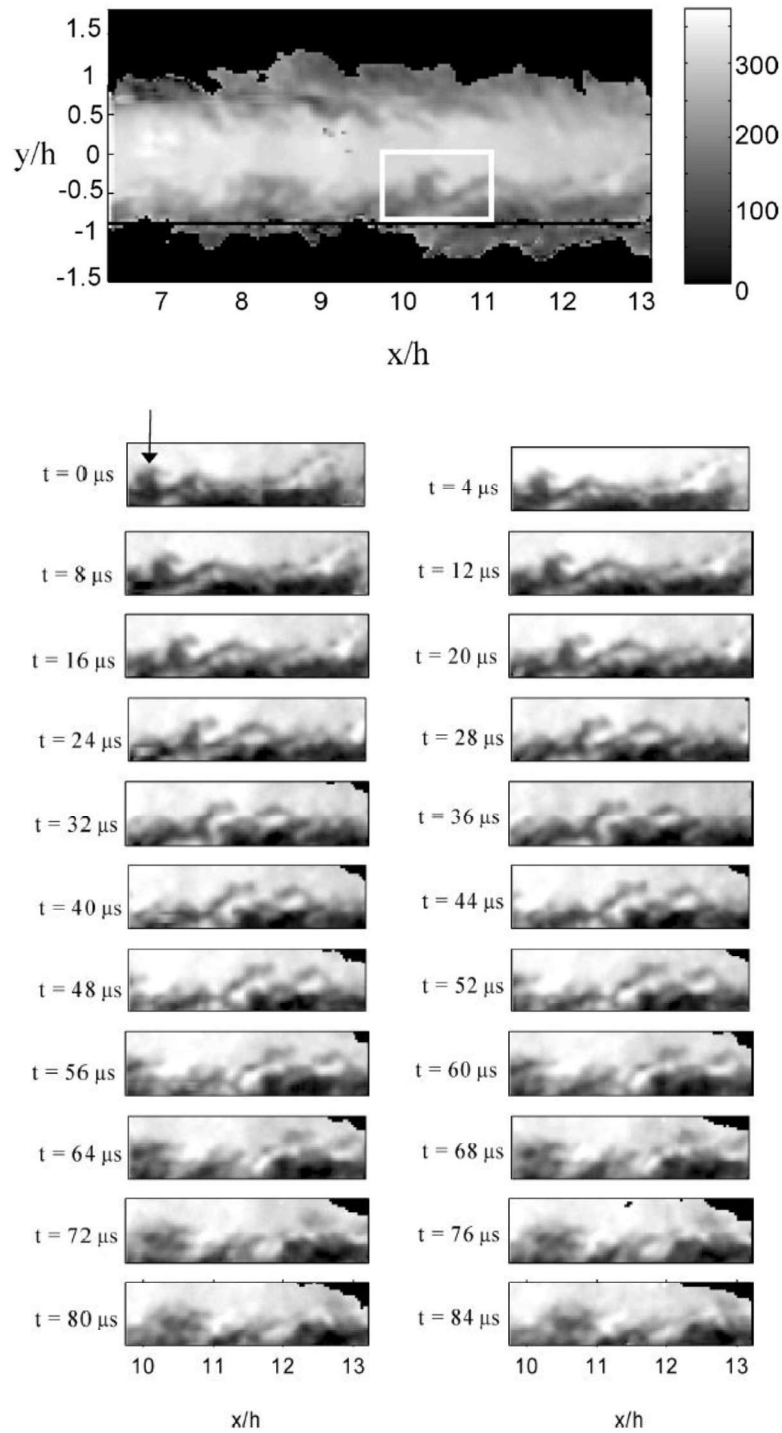
Figure 6.7. Velocity obtained using pulse-burst DGV: (*top*) shows full field of view with rectangle marking large-scale structure within mixing layer and (*bottom*) shows sequence of 22 velocity images of the highlighted structure. Data was acquired at 250 kHz. (From Thurow et al.[195]). Reprinted with permission of the authors.

An example of FRS is shown in Fig. 6.8 for a Mach 2 free jet flow.[205] Contour maps of temperature (*left*), pressure (*center*), and velocity (*right*) are provided. These measurements were compared to RELIEF data which provided uncertainty estimates of $\pm$2-3% for velocity, $\pm$2% for temperature, $\pm$4-5% for pressure for these time-averaged measurements.
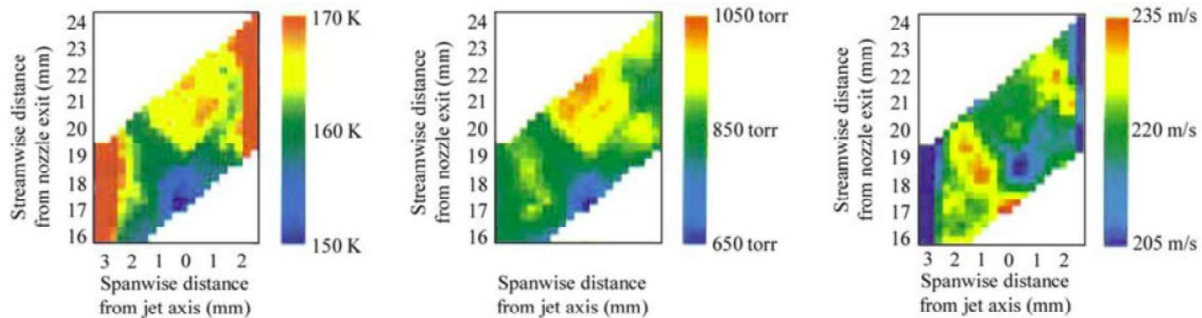
Figure 6.8. Temperature (left), pressure (center) and velocity (right) measured in a Mach 2 supersonic jet flow using Rayleigh scattering observed through a gas vapor cell using a frequency-scanned, injection-seeded Nd:YAG laser. (From Forkey et al[205]). Reprinted with permission of the authors.

An example of SRS being applied to a hypersonic flow is given by Sharma et al.[209] where they measured the rotational and vibrational temperature of N_2 to study the evolution of the vibrational relaxation. To induce vibrational-rotational non-equilibrium, a two-dimensional converging-diverging nozzle was inserted into the Electric Arc Shock Tube (EAST) facility at NASA Ames Research Center. The addition of this nozzle caused a reflected shock generating a reservoir of high-pressure, high-temperature N_2 gas. The result of the gas undergoing rapid expansion through the nozzle is vibrational-rotational non-equilibrium. Figure 6.9 (*left*) shows an example of the Raman spectrum fit for rotational and vibrational temperature and Fig. 6.9 (*right*) shows the normalized temperature profile taken along the centerline of the nozzle.
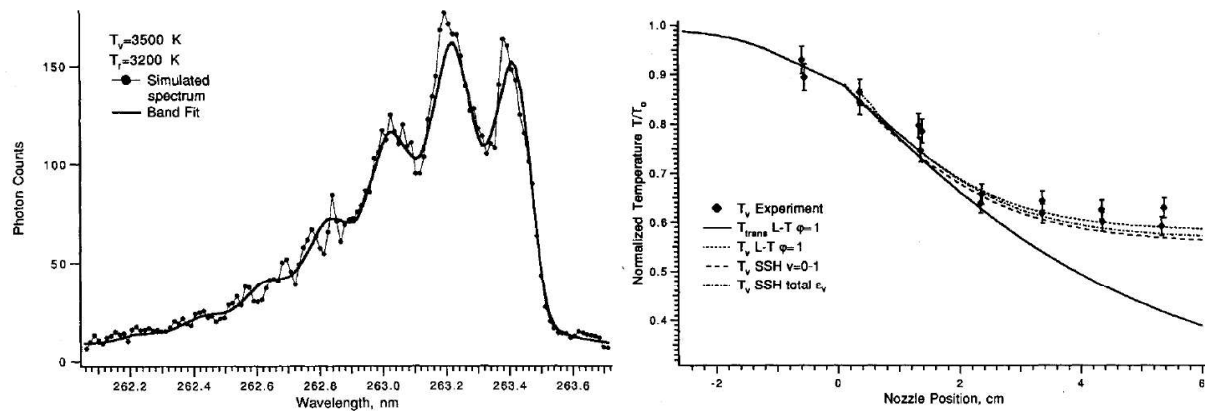
Figure 6.9. Example Raman spectrum of N_2, acquired in a Electric Arc Shock Tube, fitted for rotational and vibrational temperature (*left*) and Normalized temperature profile taken along centerline of nozzle. From Sharma et al.[209] Reprinted with permission of the authors.

6.4. Conclusions for Laser Scattering Techniques

Laser Scattering techniques, including methods based off Mie, Rayleigh and Raman scattering, offer a variety of different measurement capabilities. All use a single incident laser beam, typically at 532 nm. The methods differ in the way the laser light is focused into the flow and the way that the signal is collected and analyzed. Mie scattering based techniques such as DGV generally have much larger signal intensities than Rayleigh and Raman and thus can be done using lower energy density lasers and/or over a larger field of view in a flowfield. However, DGV is limited to measuring only velocity while Rayleigh scattering can measure density, temperature, and pressure as well as velocity. The signal from Raman spectroscopy is much weaker than Rayleigh scattering but the method is used nonetheless because it can detect multiple species simultaneously with the same measurement system. Raman can also probe rotational and vibrational temperatures while Rayleigh only measures the translational temperature. Thus, these three measurement technologies, though having common physical origins, provide complementary types of data.

# 7. Coherent anti-Stokes Raman scattering

7.1. Introduction to CARS

Coherent anti-Stokes Raman Scattering (CARS) is a nonlinear spectroscopic technique that targets Raman-active molecular transitions between vibrational or rotational energy states using the frequency difference between two laser pulses, establishing a "coherence" of molecules prepared by the laser into certain states. A third laser pulse is used to probe the Raman coherence, and the result is a laser-like signal that contains information about the thermodynamic state of the sample, as well as molecular species concentration information. This technique is orientated similar to a "pitch and catch" laser measurement. Here, three laser beams are sent into a sample or flowfield and focused to a point, as shown in Fig. 7.1 from the right. The generated coherent signal exits on

Figure 7.1. Simplified CARS experimental setup shown implemented in a tunnel.

the other side of the flowfield as a fourth laser beam, and is then directed into a paired spectrometer and camera for data acquisition. Signal is generated just at the point where all beams overlap and focus, providing a spatially-resolved measurement, an advantage in environments that exhibit spatial nonuniformities.

CARS is applicable to a wide variety of supersonic, hypersonic, and combustion flows, and is not limited to a range of flow velocities. The main constraint is requiring a Raman-active molecule to sample. However, a wide variety of molecules are Raman active, including N_2, O_2, H_2, CH_4, C_2H_4, CO, and CO_2, and at least one of these molecules is generally present in hypersonic applications (e.g. air, combustion products).[210,211,212] For most applications, CARS can be employed for the measurement of temperature, and, in some cases pressure and species concentration, using a single laser pulse to make an instantaneous (≤ 10 ns) measurement. This capability allows for accurate measurements in a temporally varying environment. Additionally, because CARS is a nonlinear technique—generated using more than a single electric field or laser pulse—and uses a coherently driven transition, it can typically be implemented at lower number densities (lower static pressure) and better temporal resolution when compared with gas-phase linear spectroscopy techniques like spontaneous Raman scattering. However, CARS is typically implemented for single-point measurements, as shown in Fig. 7.1.

7.2. Basic theory of CARS

Originally observed in the condensed phase,[213,214] CARS was applied to gas-phase measurements initially for combustion studies.[215,216] Early CARS technique development and theory were reviewed and
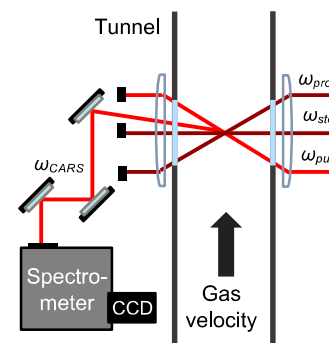
summarized by Eckbreth.[217,210] More recent development and implementation was reviewed by Roy with a focus on reacting flows.[211]

Early implementations of CARS used pulsed nanosecond (ns) laser sources to excite vibrational and rotational Raman transitions to meet the requirement of high electric field strength for gas-phase measurements,[210] and CARS measurements employing ns lasers—referred to here as ns CARS—remains a useful and accurate tool for reacting and high-speed flows. When targeting multiple Raman transitions, both temperature and species concentration can be determined by comparing to spectral simulations,[218] eliminating the need for time-intensive calibration or quantification of absolute irradiance. Although this technique relies on the precise overlap of multiple laser beams in space and time, ns CARS has been used for measurements in a number of realistic combustors and other harsh measurement conditions.[212,219-226]

Despite its many successes, ns CARS measurements are complicated by nonresonant background signal[227] and collisional broadening at high pressures,[228] both of which require detailed knowledge of total number density and all species present in the targeted environment. With the advent and commercialization of regenerative pulse amplification, picosecond (ps)[229-232] and femtosecond (fs)[233-235] laser sources were employed for CARS measurements, offering higher acquisition rates (1-10 kHz instead of 10-30 Hz), more reliability, and lower shot-to-shot variation. A particular advantage of ps CARS that has applications to wind tunnel measurements is the convenient ability to deliver the three laser pulses to the sample (or tunnel) through fibers.[236] Hybrid femtosecond/picosecond (fs/ps) CARS is an approach that combines the broadband excitation of a femtosecond laser with narrowband picosecond detection,[237,238] and will be discussed in detail. Similar to ns CARS, fs/ps CARS has been employed for flame thermometry,[239-246] species identification,[247,248] and concentration measurements.[246,249,243,250] The ps probe can be delayed in time to measure the decay rate of individual rotational transitions,[251-253] and this feature coupled with the near-instantaneous fs excitation enables "collision-free" thermometry[254] or can be employed to measure gas pressure.[255] Although it presents additional experimental complexities, fs/ps CARS has recently been applied to challenging measurement environments including propellant flames,[256] detonations,[257] high-pressure combustion,[258] nonequilibrium plasmas,[259] and plasma assisted combustion.[250,260]

Although in essence all variations of CARS rely on the same theory, some fundamental differences do exist, such as between ns and fs/ps CARS. These differences can be understood through the frequency and timing schematics shown in Fig. 7.2. In either case, the frequency difference between two laser pulses, denoted ω_{pump} and ω_{Stokes}, is tuned to match the Raman transition of interest. The selected transition can correspond to either a change in vibrational states (*v*), as shown, or a change in rotational states (*J*), which in many cases requires only a small difference in frequency between the two pulses. For

example, the fundamental vibrational transition of N_2 is at 2330 cm^{-1}, while its pure-rotational transitions lie in the range of 5-300 cm^{-1}. Because the energy of the transition is matched by the frequency *difference* of two laser pulses, visible laser wavelengths can be chosen for ω_{pump} and ω_{Stokes}, while maintaining the benefit of coherently driving the molecular transition. For instance, 532 nm and 608 nm can be used to excite the vibrational transition of N_2.
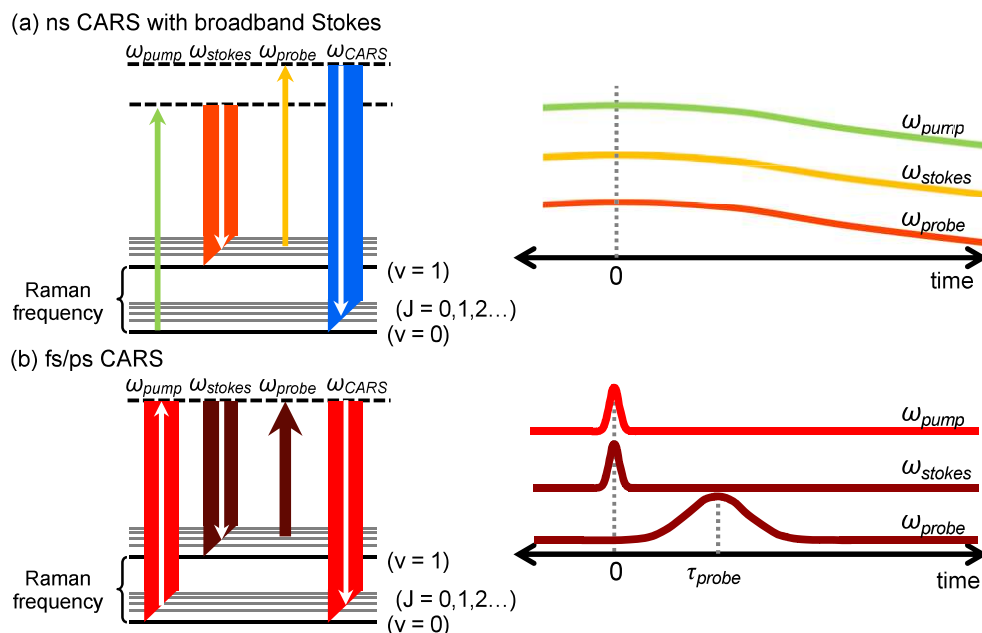
Figure 7.2. Frequency (left) and timing (right) diagrams shown for (a) ns CARS and (b) fs/ps CARS.

For the case of ns CARS, shown in Fig. 7.2a, both ω_{pump} and ω_{Stokes} have a pulse width on the order of 10 ns. The typical linewidth for an unseeded, 10 ns pulse at 532 nm is <1 cm^{-1}, represented by a thin arrow for the relatively narrowband pulse ω_{pump}. On the other hand, ω_{Stokes} is generated using a broadband dye laser, and is depicted by a wide arrow. This allows for the excitation of multiple vibrational transitions originating from different rotational levels, as shown in Fig. 7.2a. Although this figure only shows the excitation of vibrational transitions from $v = 1$ to $v = 0$, the broadband ω_{Stokes} pulse also enables the excitation of higher energy vibrational transitions (i.e. $v = 2$ to $v = 1$, etc.), and, if sufficient bandwidth exists, transitions from multiple species (i.e. N_2 and CO). Next, a second narrowband pulse, ω_{probe}, is used to probe the excited Raman coherence. If this pulse is frequency shifted to another color using a narrowband dye laser, as shown in Fig. 7.2a, ω_{pump} and ω_{probe} can effectively swap places to access even more species (i.e. O_2 and CO_2) without any change in alignment. This is referred to as dual-pump CARS.[261,262] Example dual-pump CARS spectra are shown later in Fig. 7.3a and b.

Figure 7.2b shows the frequency diagram for fs/ps CARS, and at first glance it looks very similar to its ns CARS counterpart. For fs/ps CARS, however, both ω_{pump} and ω_{Stokes} have a pulse width ≤ 100 fs. In addition to the ability to probe molecules on a shorter time scale, these pulses are capable of simultaneously exciting many molecular transitions due to their inherent broadband nature (150 cm^{-1}), as dictated by the Heisenberg uncertainty principle. To maintain sufficient spectral resolution for traditional frequency-domain detection, a longer (and spectrally narrower) picosecond pulse is used for ω_{probe}. Typical pulse widths of ω_{probe} range from 1-100 ps with bandwidths <10 cm^{-1}. One variation, dual-pump fs/ps CARS, uses a fourth laser pulse to allow for the excitation of vibrational and rotational transitions,[249] and sample spectra using this variation are shown later in Fig. 7.3c and d.

One of the fundamental benefits of employing fs/ps CARS can be observed by considering the CARS process in the time domain as shown on the right hand side of Fib. 7.2b. The two fs pulses, ω_{pump} and ω_{Stokes}, are timed together to excite the Raman coherence "instantaneously". The picosecond probe pulse is then typically delayed relative to the initial excitation (τ_{probe}) to avoid temporal overlap with the first two pulses. Such an arrangement avoids the collection of nonresonant background,[230,229,263] a four wave mixing signal generated from the laser interacting with all species present in the sample, not just the species resonant with $\omega_{pump}-\omega_{Stokes}$. Additionally, if a relatively short (i.e. <10 ps) pulse is used as ω_{probe} and the probe delay is minimized, the entire CARS measurement is completed before a significant number of molecular collisions have occurred. This increases the accuracy of the CARS measurement when the exact collisional environment is not precisely known. If the probe pulse is delayed further relative to the initial excitation, the resulting CARS signal can be used to determine pressure if temperature and species have already been determined. Varying this probe delay from early to late has been used to measure temperature and pressure using CARS.[264,255] In comparison, all three pulses for ns CARS occur simultaneously as shown on the right hand side of Fig. 7.2a.

The schematics shown in Fig. 7.2b do not encompass all variations of ns and fs/ps CARS but do provide an accurate introduction into CARS theory. A third implementation of CARS that is not discussed in detail here uses only a ps laser, and is referred to as ps CARS. It generally looks similar to ns CARS in that it requires the use of a broadband OPO or dye laser to generate a single or multiple broadband pulses, but the Raman excitation is within a time domain that still offers some of the benefits of delaying the ps probe. An advantage of ps CARS is that the laser beams are lower powered than ns CARS and thus can be delivered through optical fibers to the measurement location.[236]

The interaction of the three laser pulses shown in Fig. 7.2 with the resonant molecules of the sample induces a third-order polarization field, resulting in the CARS signal that can be collected and analyzed.

This coherent, laser-like signal is dependent upon the temperature and pressure of the sample. The CARS signal intensity, I_{CARS}, can be represented in the frequency-domain by

$$I_{CARS}(\omega_4) \propto \left| P_{res}^{(3)}(\omega_4) \right|^2 \propto \left| \chi_{CARS}^{(3)} E_1(\omega_{pump}) E_2(\omega_{Stokes}) E_3(\omega_{probe}) \right|^2 \qquad (7.1)$$

where E_1, E_2, E_3 represent the electric fields of the pump, Stokes, and probe laser pulses, respectively. The CARS portion of the third-order nonlinear susceptibility, $\chi_{CARS}^{(3)}$, is a function of the thermodynamic information about the sample being probed, including temperature, species concentration, and number density or pressure. Thus, the intensity and relative shape of the spectra obtained experimentally can be compared to theoretically calculated spectra to determine this thermodynamic information.[218,265] Regarding the temperature measurement, CARS can directly probe Boltzmann rotational and vibrational distributions. In cases of nonequilibrium, the Boltzmann distribution expands to include multiple temperatures describing different energy modes (i.e. T_{vib}, T_{rot}, etc.) which CARS can measure directly[266,259] Additionally, if the nonequilibrium is severe enough to preclude the use of Boltzmann statistics, CARS can be used to quantify energy level populations instead of temperatures.[267-269,259] This is an important distinction—the CARS process is a function of the populations of different energy levels, not just the translational temperature of the gas.

Although three laser pulses are required for CARS signal generation, they usually originate from a single laser which simplifies timing. For ns CARS, the second harmonic of a pulsed Nd:YAG laser at 532 nm is employed. This output is typically split into three separate beams. One beam is unaltered and used as ω_{pump}. The second beam is used to pump a broadband dye laser to generate the broad ω_{Stokes}. The third beam can be used directly as ω_{probe} or is used to pump a narrowband dye laser to access more species, as shown in Fig. 7.2a. Alternatively, the third harmonic of the Nd:YAG can also be used to pump each dye laser, depending on the molecules being sampled. The three beams are focused and crossed, generating the laser-like CARS signal beam as shown in Fig. 7.1. A spectrometer and CCD camera are used to spectrally disperse and record the CARS signal. In most cases where the expected number density is low, an electron-multiplied CCD (EMCCD) is recommended to achieve single-laser-shot results. The high-energy requirement of this technique typically limits it to the use of a 10-30 Hz flashlamp pumped Nd:YAG laser. By substituting the dye laser(s) with solid-state optical parametric oscillators (OPO), higher measurement rates can be achieved for short bursts of time through the use of a burst-mode laser, as was done using a ps burst mode laser operating at 100 kHz.[270]

The equipment and experimental setup required for hybrid fs/ps CARS differs from that used for ns CARS. A regeneratively-amplified Ti:sapphire laser is typically used as the fs laser source. Its output is split to form ω_{pump} and ω_{Stokes}, and the pump pulse can be frequency converted to the desired wavelength

to access vibrational transitions using the frequency-doubled output of an optical parametric amplifier (OPA). An OPA is unnecessary if rotational transitions are studied instead (commonly called "pure rotational CARS"), simplifying the experimental setup. The ps pulse used as ω_{probe} can either be generated through pulse-shaping techniques from the fs laser[263,242] or, when higher probe energy is desired, from a separate ps laser synchronized to the fs system.[245] This can be accomplished using a regeneratively-amplified ps laser, limiting the repetition rate of the measurement to ~10 Hz, or using a flashlamp or diode-pumped burst-mode laser, where the measurement rate for a single burst is limited by the fs laser (1-5 kHz). Compared to ns CARS, the setup and alignment of fs/ps CARS is more complex, owing to the challenge of overlapping three pulses with 100 fs precision (matching beam paths within 30 μm) instead of merely 10 ns precision (matching beam paths within 3 m). Because of this, motorized translation stages are often employed for the precise and repeatable alignment of different beam paths.

The spatial resolution of CARS is dictated by the spatial extent over which the three laser beams are overlapped, phase matching is satisfied, and the electric field strength is sufficient. Although not discussed in detail here, phase matching meets the conservation of momentum requirement, and can be accomplished through a variety of beam crossing configurations.[271] Essentially, the three beams need to cross in space and be focused to a small enough cross section to generate a large electric field. As the beams focus and cross, they form an ellipsoidal probe volume. As long as the beams all cross at their smallest cross section, the minor diameter of the ellipsoid will be on the order of 25-75 μm as predicted by Rayleigh focusing. Additionally, if a shorter focal length combining lens is chosen or if the beam crossing angle is increased, the length of the probe volume will decrease. Typically, the length of the CARS probe volume is estimated to be 1-2 mm, although shorter probe volumes have been reported (650 μm).[259] Although traditionally limited to single-point measurements, fs/ps CARS arrangements have been used to measure one- and two- dimensional fields. Their spatial resolutions will be discussed later.

The accuracy and precision of ns and fs/ps CARS is dictated by the measurement environment (i.e. temperature, number density) as well as the CARS system employed (i.e. probe energy, size of probe volume, etc.). The measurement error and precision reported for ns CARS thermometry range from 2-5% and 3-5% respectively.[272] The error reported for fs/ps CARS thermometry is moderately lower, 1-5%, with a notable improvement in precision of 1-3%.[243,239,241]

One implementation of ns CARS is dual-pump CARS employing different wavelengths for ω_{pump} and ω_{probe}. Because these two pulses are overlapped in time, they can switch roles: accessing molecules with transition frequencies equal to $\omega_{pump}-\omega_{Stokes}$ and $\omega_{probe}-\omega_{Stokes}$. This configuration was initially applied to excite vibrational transitions of N_2 and O_2 or N_2 and propane,[261] and was expanded to include a greater number combustion relevant species by employing dye mixtures that resulted in a larger bandwidth

coverage by ω_{Stokes}.[226,273,274] Sample spectra obtained using dual-pump ns CARS by Cutler et al.[275] is shown in Fig. 7.3a and b. The bandwidth of ω_{Stokes} was 600 cm^{-1}, enabling the excitation of N_2, O_2, H_2, CO, CO_2, and C_2H_4—all of the major species of ethylene-air combustion besides water. The species concentration for each of these molecules can be obtained by comparing to a spectral model, allowing for the concentration of water vapor to be inferred from the nonresonant signal. The single-laser-shot spectrum shown in Fig. 7.3a was measured within the cavity of a scramjet combustor facility located at the University of Virginia. For this work, the electrically heated air was discharged through a Mach 2 nozzle, and fuel was injected at a global equivalence ratio of 0.40. The temperature was determined by comparing the measured spectrum with calculated spectra at various temperatures. The best fit theoretical spectrum corresponded to a temperature of 1453 K, and is shown on the plot as a red curve. A shot-averaged spectrum is shown in Fig. 7.3b, and the spectral features of various molecules are labeled on the plot. Although the Raman frequencies for O_2 and N_2 are separated by almost 800 cm^{-1}, the CARS signal generated from each of these species appear within 150 cm^{-1} of each other. This is due to the use of two different "pump" pulses (swapping ω_{pump} and ω_{probe}), conveniently enabling collection of signals from both species using a single spectrometer and camera with sufficient spectral resolution. Additionally, using a higher resolution spectrograph also allows for the partial resolution of vibrational transitions originating from different rotational levels (i.e. transition from ($v=1$, $J=10$) to ($v=0$, $J=10$); ($v=1$, $J=11$) to ($v=0$, $J=11$); etc.), as shown in other publications using the same dual-pump ns CARS instrument.[262,266] This enables observation of the population distribution among rotational and vibrational energy levels, allowing for the measurement of non-equilibrium temperatures.

Sample fs/ps CARS spectra are shown in Fig. 7.3c and d for rotational and vibrational transitions, respectively.[276] These spectra were generated using dual-pump vibrational/rotational fs/ps CARS, a technique developed by Dedic et al. to excite both rotational and vibrational transitions of N_2 simultaneously, and was first used to measure temperatures ranging from ambient conditions to flame conditions and measure O_2, N_2, CH_4, and H_2 simultaneously.[249] This measurement uses two fs pump pulses at different wavelengths and shares a single ω_{Stokes} and ω_{probe}, and the signal generated at different wavelength ranges can be collected using a single spectrometer and two cameras.[259] The vibrational spectra shown in Fig. 7.3d demonstrate the lower spectral resolution of fs/ps CARS due to the use of a ps probe pulse instead of a narrowband ns pulse. In this case, the resolution is no longer limited by the resolving power of the spectrometer, but instead by the ps probe pulse. Because of this, the fine structure from spectral lines originating from different rotational states are difficult to use to measure rotational temperature independent from vibrational temperature with reasonable accuracy. Instead, dual-pump vibrational/rotational CARS can be employed to measure the rotational energy distribution separately to

characterize nonequilibrium enviornments.[259] The spectra shown in Fig. 7.3c and d were measured within an unsteady atmospheric pressure dielectric barrier discharge in a He-N_2 environment. Both spectra were collected simultaneously within a single-laser-shot, and the vibrational and rotational temperatures were determined to be 3460 K and 390 K, respectively, by comparing the experimental measurements (green symbols) with theoretically calculated spectra (black curve). Because rotational temperature is determined directly from rotational transitions, the measurement of nonequilibrium is likely more sensitive using this fs/ps CARS technique. Additionally, it is often difficult to resolve the fine rotational structure from vibrational transitions while still capturing the full range of vibrational bands for an environment with high vibrational temperatures or extreme non-Boltzmann energy distributions.

To compare relative signal levels between the single-shot ns CARS measurements shown in Fig. 7.3a (blue curve) and the single-shot fs/ps CARS measurements shown in Fig. 7.3c and d (green symbols), the absolute number density of N_2 was considered. Based on experimental details, the N_2 number density was estimated to be approximately 5.9×10^{18} cm^{-3} for the scramjet combustor studied using ns CARS and 2.5×10^{18} cm^{-3} for the N_2-He plasma characterized using fs/ps CARS. Although this comparison does not account for differences in probe volume or specific energy level populations, it provides a rough comparison of how much signal could be expected from each technique when similar number densities (within a factor of two) are probed. Although the number density is likely slightly higher for the ns CARS measurements, both techniques appear to have a similar level of noise (comparing Fig. 7.3a and 7.3d) when considering the difference in y-axis scales. One limitation on ns CARS signal generation is due to Stark broadening and stimulated Raman pumping.[277] Laser pulse energies used for ns CARS must be limited to avoid such effects, limiting the intensity of signal generation; whereas the threshold for these effects occurs at a much higher pulse energy for fs/ps CARS due to the short pulse widths used, allowing for higher signal generation for the same gas environment.[278]
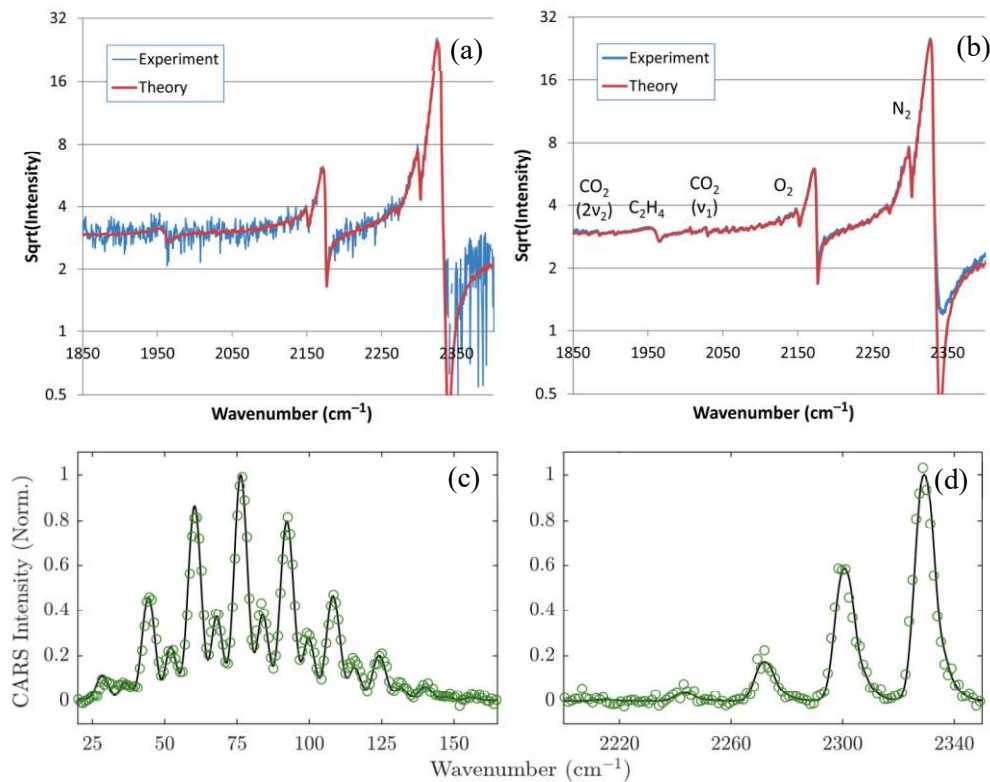
Figure 7.3. Sample ns CARS (a) single-shot and (b) shot-averaged spectra measured within a scramjet combustion cavity.[275] Sample single-shot (c) rotational and (d) vibrational hybrid fs/ps CARS spectra measured within a He-N_2 dielectric barrier discharge. Measured spectra shown as symbols and best-fit simulations as solid black lines.[276] Modified with permission of the author.

7.3. Examples of CARS Measurements

Although the application of the CARS technique comes with additional experimental complexity when compared with other diagnostics mentioned previously, it has been successfully used to measure temperature, species, and nonequilibrium of several supersonic and hypersonic flows. Two-line ns CARS was used to determine temperature and pressure simultaneously for a Mach 10 hypersonic flow.[279] Measurements were made in the R5Ch facility of ONERA using a Mach 10 nozzle in the freestream as well as near a ramp. The CARS system was tuned to two vibrational transitions in the ground vibrational band originating from different rotational levels, and their relative intensities were used to measure a rotational temperature of 55 K in the freestream. The total number density was also determined by comparing signal intensity to the intensity generated within a calibration cell. A broadband ns CARS system was implemented by Smith et al. to study static temperature within a supersonic combustion flowfield of a combustion-heated, high-enthalpy Mach 2 tunnel.[280] Recently, Cutler et al. has applied the

dual-pump ns CARS system discussed with Fig. 7.3 to measure temperature and combustion-relevant species within the freestream and combustion cavity of a Mach 2 combustion tunnel.[212,275,281]

Several studies have used CARS to characterize the degree of nonequilibrium for supersonic/hypersonic freestream flow. Vibrational/rotational nonequilibrium was measured using broadband ns CARS in a pulsed high-enthalpy shock tunnel by Fraval et al.[282] Both N_2 and air were studied for different nozzle throat diameters and lengths, with differences between vibrational and rotational temperatures on the order of 1000 K. Montello et al. used ps CARS to measure the N_2 vibrational distribution function in the plenum of a laboratory-scale Mach 5 nonequilibrium wind tunnel.[268] The tunnel used a series of pulsed and dc discharges to load energy into excited vibrational and electronic levels, and effective collisional partners were injected downstream of the plasma discharge to tailor the distribution of energy within the flow. Measurements confirmed vibrational temperatures on the order of 2000 K for a total plenum pressure of 300 Torr. Smith and coworkers used broadband CARS at Mach 10 and 14 within the AEDC Hypervelocity Wind Tunnel No. 9 facility to determine if inconsistencies between CFD and experimental tunnel measurements could be due to thermal nonequilibrium.[283] Although results were not conclusive, the implementation of CARS in such a challenging, large scale facility shows promise for future measurements.

In particular, results showing nonequilibrium energy distributions in the freestream of the electrically-heated, clean-air combustion tunnel at the University of Virginia (UVa) are shown in Fig. 7.4. This work by Cutler and coworkers[266] used the same dual-pump CARS setup discussed previously, but only collecting N_2 and O_2 CARS spectra within the freestream heated air. The goal was to study any nonequilibrium due to the sudden gas expansion experienced in the facility's nozzle, as well as the spatial distribution of the facility inflow rotational and vibrational temperatures.
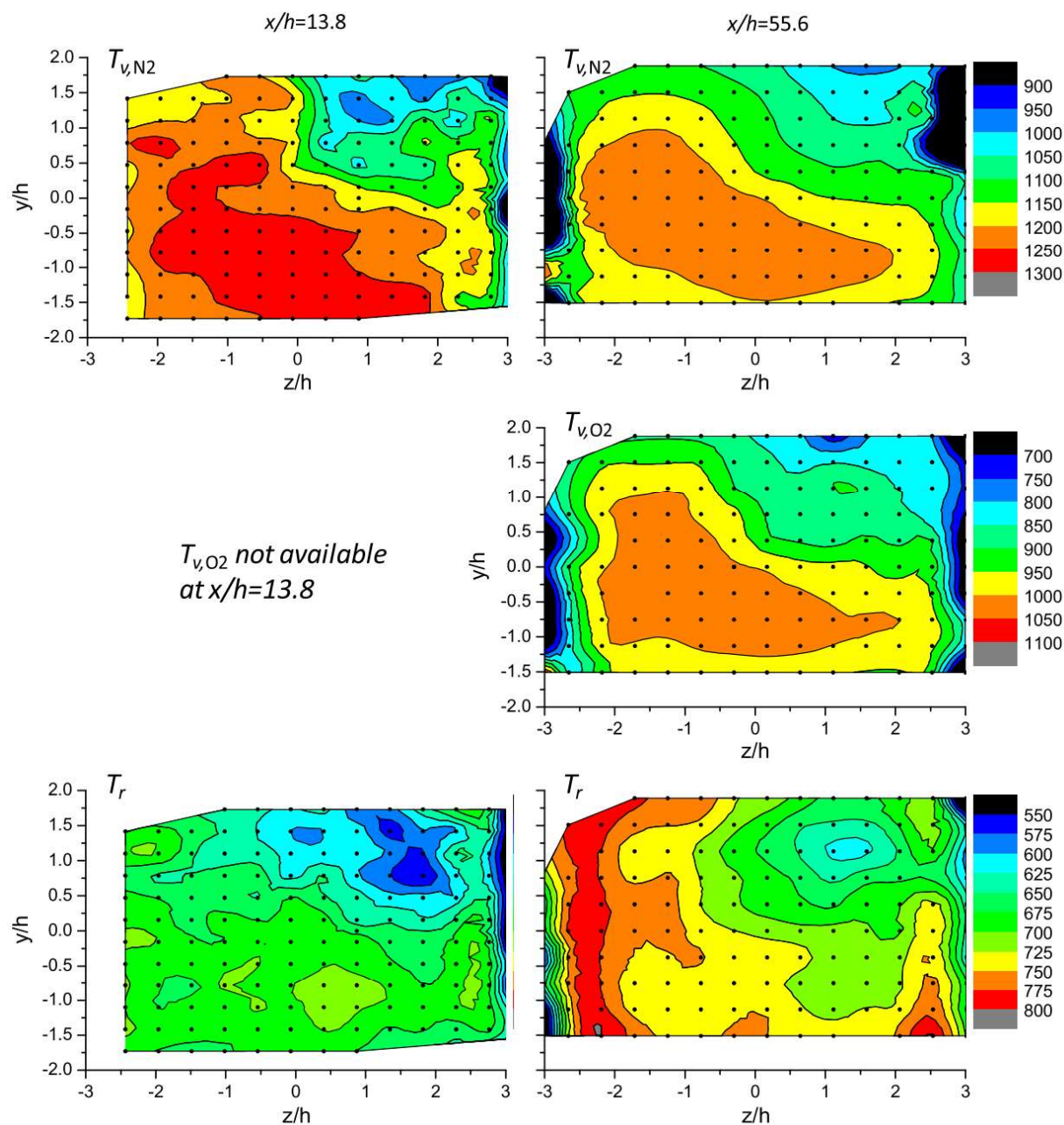
Figure 7.4. Rotational temperature and vibrational (N_2 and O_2) temperature maps reconstructed from single-point ns CARS measurements on the grid shown. Units are Kelvins. Measurements were made in free stream air at two locations downstream from the throat of a Mach 2 nozzle.[266] Reproduced with permission of the author.

As discussed in the original paper, the vibrational relaxation time for pure N_2 at these conditions is about 28 ms, but the flow velocities studied result in a residence time for the length of the scramjet of around 1 ms. Thus, vibrationally frozen flow from the exit of the tunnel nozzle would not have significant time to relax without the addition of an effective colliding species, such as water vapor, typically present

in vitiated air scramjet facilities but not normally present in the electrically-heated UVa tunnel. The results in Fig. 7.4 show the rotational and vibrational temperatures measured at the exit plane of the tunnel nozzle. Temperatures were determined separately for the measured N_2 and O_2 energy distributions. Single-point measurements were made at each grid point by translating the pitch-and-catch CARS optics. The reconstructed temperature maps show rotational temperatures around 650 K and N_2 vibrational temperatures above 1200 K, confirming the presence of frozen vibrational states near the electric heater stagnation temperature. The vibrational temperature of oxygen was also measured as approximately 100 K lower the nitrogen vibrational temperature. The addition of a small amount of water vapor (3.7%) resulted in the thermal equilibration of the N_2 and O_2 vibrational levels.

The measurements discussed thus far demonstrate the applicability and utility of CARS to supersonic and hypersonic flows. The measurements were limited to the application of ns CARS, with one demonstration of ps CARS to a laboratory-scale tunnel. Owing to the relatively recent development of fs/ps CARS, high-speed wind tunnel results are not yet available for inclusion here. However, there have been several demonstrations of the utility of fs/ps CARS within harsh measurement conditions, including metalized propellant flames[256] and high-pressure flames.[258] One study by Dedic and coworkers implemented a fs/ps CARS system to measure vibrational temperatures at the exit of a 2 mm diameter, C_2H_4-O_2-N_2 detonation tube.[257] The tube operated with gas velocities around 2200 m/s with Chapman-Jouguet (C-J) predicted detonation Mach numbers around 5.5-7. Although the measured detonation velocity determined by tracking the flame front matched C-J calculations well, the nitrogen vibrational temperatures at the exit of the tube after the passage of the wave front measured using fs/ps CARS were significantly lower than the C-J equilibrium temperature predictions.

The dual-pump vibrational/rotational fs/ps CARS technique described previously with Fig. 7.3 was used to measure nonequilibrium energy distributions of a dielectric barrier discharge,[259] and sample results are shown in Fig. 7.5.[276] The plasma was generated at atmospheric pressure within a flow of He and N_2. A sample image of the plasma emission is included in Fig. 7.5a, and fs/ps CARS measurements were made on the grid points shown. For this study, an unsteady plasma was generated by increasing the concentration of N_2 to 13%. The average vibrational and rotational temperatures determined from fitting single-shot spectra are included in Fig. 7.5b, and the standard deviations are represented as bars. The gas was flowing from above and sweeping excited species away from the center of the plasma after impinging on the bottom plate electrode, resulting in the observed decay in vibrational temperature moving away from the center of the plasma. The secondary peaks in vibrational temperature were argued to be due to secondary vibrational excitation due to the relaxation of excited electronic states. The large temperature variations observed at the center of the plasma were due to shot-to-shot variations in the plasma filament

structures. Although the measured nonequilibrium from this example was generated using a plasma instead of high-speed flow driven effects, it demonstrates the feasibility of applying fs/ps CARS to quantify nonequilibrium environments.
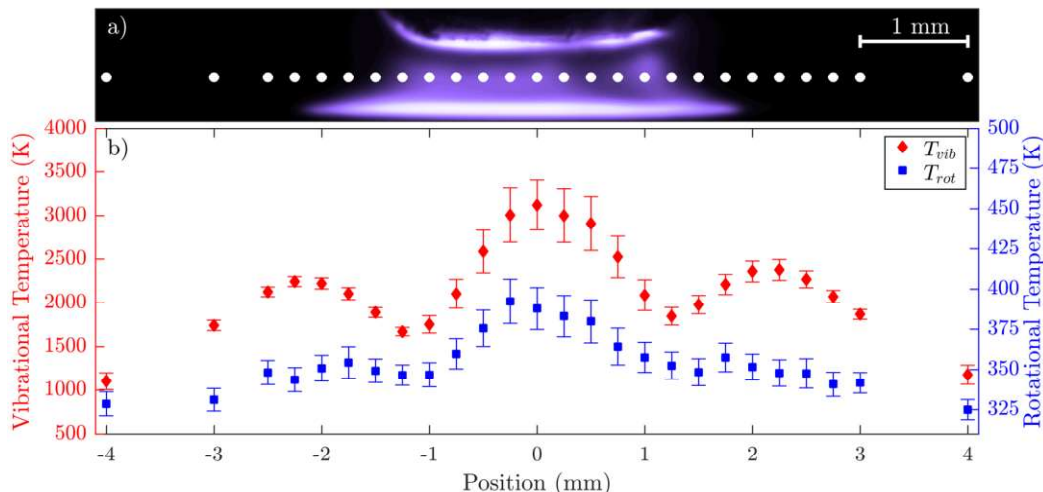

Figure 7.5. Rotational and vibrational temperature maps reconstructed from single-point ns CARS measurements on the grid shown.[276] Modified with permission of the author.

Despite additional challenges associated with moving from ns CARS to fs/ps CARS, it does offer several benefits including an increase in measurement rate from 10-30 Hz to 1-5 kHz, avoiding the use of dye lasers, suppression of nonresonant signal, and collision-free thermometry. Additionally, as discussed previously, fs/ps CARS offers the ability to measure pressure with much higher accuracy than fitting the widths of spectral lines in the frequency domain. Gas-phase pressure measurements in a static cell were reported by Kearney et al. with 2% error and 1.3% precision possible for certain measurement conditions.[255] Another notable advantage, however, is the possibility of the extending the CARS measurement from a single point to multiple dimensions. Decreasing the pulse duration from 10 ns to 100 fs allows for CARS signal generation with significantly lower total pulse energies, enabling the successful implementation of CARS imaging along a line[245,246,248,250,284] and across two-dimensional fields.[285,286] One-dimensional temperature, species, and possibly pressure imaging with fs/ps CARS is an excellent candidate for studying boundary layer development or gradients near corners and other non-smooth features of tunnels or models.

Example 1D-CARS results from within a flame by Bohlin et al. are shown in Fig. 7.6.[246] The fs/ps CARS signal was generated using a simplified two-beam configuration. The results show single-shot (black curve) and shot-averaged (red curve) temperature profiles measured at three locations within a side-wall-quenching burner. The extent of the measurement line was 5 mm, and the effective spatial

resolution along the measurement line was around 35 μm. Using careful relay imaging and spatial filtering, measurements within 30 μm of the side wall surface were possible. The precision of the single shot temperature measurement at any point along the line was reported as 2-3%. An alternative fs/ps CARS method was used that replaces the two pump pulses with supercontinuum generation to access a wide range of species.[248] In this study, supercontinuum excitation was used to measure relative mole fractions of O_2, CH_4, H_2, and CO_2, and single-shot results were possible along a ~2 mm line.
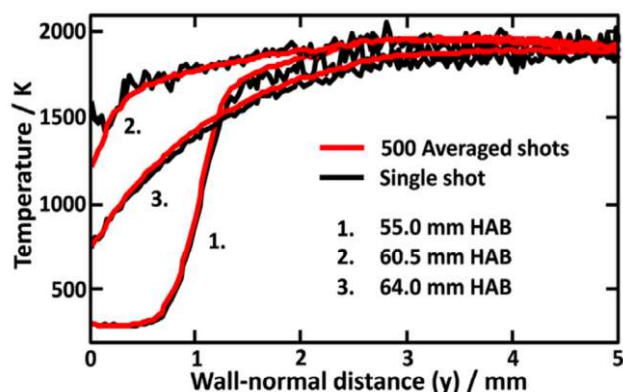
Figure 7.6. 1D-temperature profiles of a wall-quenched flame measured using fs/ps CARS.[246] Single-shot and shot-averaged temperature fits are shown as black and red lines, respectively. Reproduced with permission of the author.

Although the fs/ps CARS studies discussed and sample results shown in Figs. 7.5 and 7.6 were measured in a variety of low-speed or small-scale facilities, they demonstrate the applicability of fs/ps CARS to hypersonic wind tunnel studies for the accurate measurement of temperature, species, pressure, and vibrational/rotational nonequilibrium, and extend the previous single-point measurement limitation of ns CARS to small one- and two-dimensional fields.

7.4. Conclusions for CARS

CARS is arguably the most complicated measurement described in this manuscript but also could be considered the most capable. It offers spatial and temporal precision, accuracy and shot-to-shot measurement precision approaching 1%, and is capable of simultaneously providing temperature, pressure, and major species concentration information. CARS has been applied to a variety of reacting and nonreacting flows, including a range of spatial scales and harsh measurement conditions. Because the CARS signal is coherent, all the generated signal propagates like a laser beam in the forward direction, enabling high collection efficiencies in the convenient "pitch-and-catch" configuration. The extension of the CARS technique from traditional ns lasers to burst-mode ps laser systems and regeneratively amplified fs laser systems has allowed for an increase in measurement rate from 10 Hz to 1-100 kHz,

greatly improving measurement statistics by enabling 100-10,000x more measurements for the same amount of tunnel run time. Two variations of the CARS technique were discussed in detail: ns CARS and fs/ps CARS. Due to its relative maturity, ns CARS has already been used successfully in supersonic and hypersonic wind tunnels. Although it is a relatively new measurement, fs/ps CARS is maturing quickly and extends the single-shot CARS measurement from a single-point to one- and two-dimensional measurements. Both ns and fs/ps CARS methods can measure rotational and vibrational nonequilibrium energy distributions which are critical for hypersonic freestream flows.

8. Particle Image Velocimetry

8.1. Introduction to PIV

Particle Image Velocimetry (PIV) is a technique that measures flow velocity from light scattering from small tracer particles seeded into the flow.[287-292] The basic concept of PIV is to directly visualize and quantify the flow motions via the illumination and imaging of seeding particles that are assumed to follow the flow accurately. PIV then measures the physical displacement of particle ensembles during a small time interval from successive images of their scattered light. This differs from other particle-based techniques like laser Doppler velocimetry (LDV)[289,290] and Doppler Global Velocimetry (DGV)[291,292] in that these infer velocity from the wavelength Doppler shift that is produced by the particle motions. PIV systems have capabilities of measuring accurate instantaneous and average flow field velocities in two-dimensional (2D) planes as well as three-dimensional (3D) volumes.[287,293,304,310] PIV can also provide time-resolution using various methods as will be described in this section.[308] PIV is preferred to LDV in many applications because LDV typically measures pointwise. PIV is also preferred to DGV in many applications because although DGV is planar it is generally time averaged, it can have higher uncertainties, and is generally more difficult to set up compared to PIV. A review of DGV technique and examples were given in Section 6 of this manuscript.

LDV (also called laser Doppler anemometry, LDA)[289,290] is a pointwise particle-based technique that has high accuracy and spatial and temporal resolution. It utilizes the direct measurement of the Doppler shift between incident and scattered light from moving particles. In the basic setup, LDV utilizes two continuous wave laser beams that intersect at the region of interest to measure a velocity component. Adding extra beams can yield three components of velocity at the probed point, typically a few mm long. It does provide time series data collection that allows frequency analysis. However, being limited to a single point hinders obtaining spatial information. It also has limitations regarding implementation in harsh environments.

For the last few decades the theory and practical applications of PIV techniques have been improved to a point where high-resolution, high-accuracy data is readily attainable in a large variety of flows (laminar, turbulent, microfluidic, high-speed, etc.) and in harsh environments and facilities (wind tunnels, water tunnels, transonic compressors and turbines, jet engines, supersonic and hypersonic facilities, etc.) Nonetheless, one main challenge of the technique remains, the particle seeding, which is especially difficult in the harsh conditions and environments encountered in high-speed flows. The general requirements for a robust seeding system include delivery of a prescribed amount of particle concentration with uniformity (to yield enough data while not perturbing the flow), necessity to follow the flow velocity as accurately as possible (typically by requiring small diameter), requisite to be bright light

scatterers, and the need to be non-hazardous and non-contaminating. These requirements typically have to be addressed in the design on a case-by-case basis.

8.2. Basic theory of PIV

One of the main advantages of using large particle light scattering techniques for velocimetry is that, having sizes similar to or larger than the light wavelength (λ), they are much brighter than molecules and tiny particles of diameters < 1/10 of λ. For the larger particles, light scattering intensity is predominantly in the Mie light scattering regime[288] and is proportional to the square of the particle diameter, while scattering from molecules and tiny particles is predominantly in the Rayleigh light scattering regime and is much weaker than Mie scatter.[288] The main accomplishment of PIV is that the technique can measure instantaneous and average flow field velocities in various dimensions and environments[287,293,302,304,308,310] The main disadvantages of PIV come from the fact that it uses particles for flow seeding. This fact encompasses the difficulties aforementioned especially in high-speed phenomena that include high-speed, compressibility, sharp turns, shocks, waves, etc.[293-303] PIV can only render velocity vectors in regions containing particles and can obscure measurement of molecular thermodynamic properties.[288] A drawback compared to other techniques like DGV is that independent velocities are not measured at each pixel; instead they are averaged over an 'interrogation region' such as a 16x16 pixel region, which limits the spatial resolution.   Another drawback is that the wavelength of scattering is essentially equal to the laser's wavelength so that scattered light from surfaces interferes with the signal and, although techniques such as applying red paint have been used to optimize the measurement near surfaces, making these measurements remains challenging. This is in contrast with PLIF for which the laser and fluorescent signal are typically at different wavelengths and thus the laser scattered light can be filtered. Other significant practical disadvantages include the fact that particles can contaminate the facilities, requiring clean up after use, and that they require special/complex designs when applied in harsh pressure and temperature conditions. Nonetheless, proper seeding system designs have typically been successful in providing a full velocity field with reasonable accuracy in many applications.[293-308]

The Particle Image Velocimetry technique involves illuminating flow seeded particles with pairs of high-energy, short-duration laser pulses to 'freeze motion in time', and then capturing these instantaneous flow images with cameras that are synchronized with the light pulses (Fig. 8.1a). By acquiring two successive images within a short time interval, the velocity of the particle field can be inferred from the displacements (Fig. 8.1b).
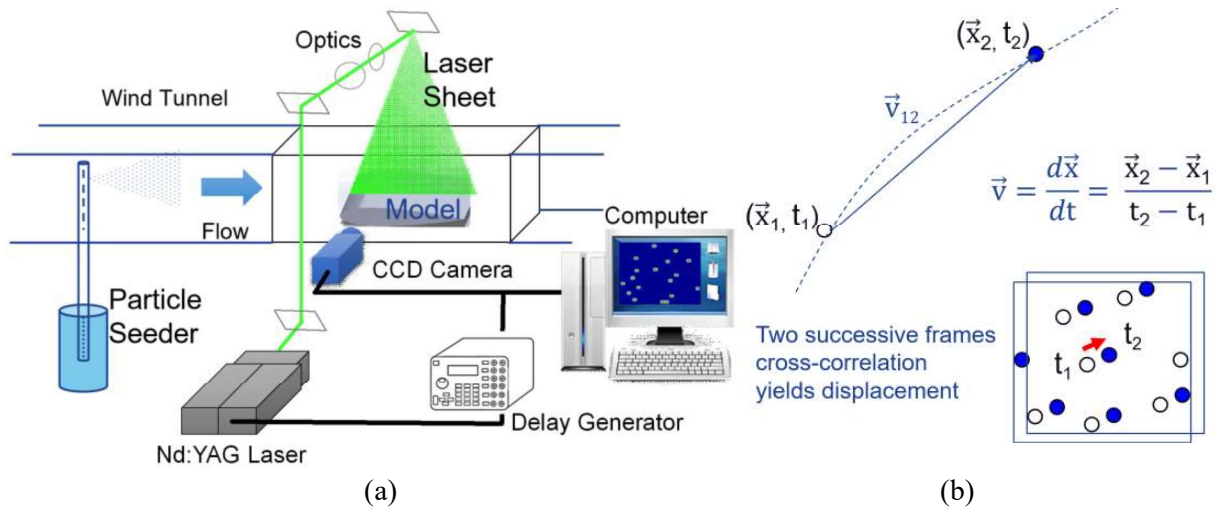
Figure 8.1 Schematic of standard PIV system components in wind tunnel test (a) and illustration of the basic principle for velocity calculations (b).

To introduce the PIV technique, a simple example is described as shown in Fig. 8.1. A standard arrangement using one camera for 2D data rendering at low repetition rates is shown. In Fig. 8.1a, a test model, such as an airfoil, wedge, ramp, sphere, etc. is installed in the test section and experiments are performed at desired flow conditions (Mach and Reynolds numbers). Illumination is provided by a double-pulsed Nd:YAG laser emitting two laser pulses with typical energies of 20-400 mJ (depending on the field of view) at a wavelength of 532 nm with a repetition rate varying from 10 Hz to tens or even hundreds of kHz.[287,311,308] The laser beam is shaped into a laser sheet (thickness <1 mm) by using mirrors and spherical and cylindrical lenses, and is directed towards the flow through optical windows. The flow is then seeded with particles such as solid Al_2O_3 or TiO_2 using solid fluidized powder bed seeders, submicron droplets produced from 'smoke' generators (e.g. using glycerin-water oil mixtures), Laskin nozzles atomizers (e.g. using DEHS oil), helium filled soap bubbles, or other "particles". Particle sizes range from 10's of nm to 100's of microns. Each type of seeding has its advantages and disadvantages as will be explained. Image acquisition is then typically performed by a high-resolution CCD camera with > 1MPix and interframe (interline transfer) capability of < 1 μs. Camera imaging is performed through optical access windows, typically with its axis perpendicular to the laser sheet to gather particle images in focus and without distortion. For high-speed applications, CMOS cameras are often used, though at reduced resolution compared to CCD cameras. The camera and the Nd:YAG lasers are connected and controlled by a workstation having internal programmable timing unit (or are synchronized with delay generators) that sets the timing of the laser/image acquisition. PIV software (designed in-house or purchased from flow diagnostic companies) includes camera target calibration, image acquisition, and

processing. During data processing the instantaneous PIV velocity vectors are obtained by interrogation of successive image frames and using cross-correlation techniques on particle image ensembles, and involve multi-pass interrogation schemes for high-accuracy and high-resolution from window size of, for example, 64×64 to 16×16 pixels. An effective overlap of 50% is typically employed to yield higher spatial resolution. A vector is obtained at each of these smallest interrogation regions that typically should contain around 10 particles for good accuracy.[287] The time delay between the two frames depends on the flow speed and magnification and typically varies from < 1µsec to 100 µs to adequately match displacements within the flow velocity dynamic range. Higher velocity flows necessitate shorter inter-frame times. The time-averaged quantities are then obtained from an ensemble of 100-1000 frames of instantaneous velocity fields for each case. With the introduction of new 'advanced' processing algorithms such as those that utilize interrogation window deformation and fractional window displacements,[293,309,315,316,332] accuracies of PIV, including that of turbulent intensities, has been reported within 1-2%.[293,294,308,332]

In order to capture the three-dimensionality of a flow, the three velocity components over a 3D volume are required. Using a two camera stereo PIV arrangement[287] allows 3-velocity component data to be obtained in a single plane (sometimes called 3C-2D). Four or more cameras can be used in a tomographic PIV arrangement[310] that allows 3-velocity component data be obtained in a 3D volume (sometimes called 3C-3D). For tomographic measurements the laser beam is simply expanded by a combination of cylindrical/spherical lenses to create a volumetric illumination in the test section. In general, more cameras allow for thicker volume interrogation, higher seeding density, higher resolution, and higher accuracy. These stereoscopic and tomographic arrangements incorporate adjustable 'Scheimpflug' adapters to ensure that the field-of-view from each angled camera is in focus. In addition, time resolution can also be obtained by using state-of-the-art high-repetition-rate systems, currently available in the ranges of 1-20 kHz for continuous operation and up to 1 MHz using the 'burst-mode' lasers which produce a short burst of pulses followed by a delay of several seconds until the next burst.[307,308,311]

It is noteworthy that recent advances in tomographic PIV algorithms such as those known as 'self-calibration', '3D reconstruction', 'MART', etc.[310] have rendered the high accuracy and high resolution 3D velocity fields that were not possible with previous techniques including previous stereoscopic methods and holographic PIV methods.[287] The 3D vector field is calculated using 3D correlation methods and a vector can be generated down to levels of individual particles. PIV algorithms currently include this particle tracking feature and the technique itself is known as particle tracking velocimetry (PTV).[287] It is noteworthy that most advanced 3D 'Lagrangian PTV' methods such as those known as 'Shake-the-box'[312] are purely particle-based, and include an iterative particle reconstruction technique in combination with

an advanced 4D-PTV algorithm (using the time-information for track reconstruction) that leads to the highest spatial resolution and positional accuracy for densely seeded flows.

8.3. Particle Seeding Considerations

Particle seeding methods and challenges are outlined in this section since this is a particular concern in high-speed flows. First, to study high-speed flows with PIV, a particle seeder has to inject a prescribed amount of particles into a plenum that is under a high pressure condition. This typically requires high pressure seeding vessel designs, some of which are commercially available. Second, the particles must be able to withstand extreme and rapid changing pressure and temperature environment as they pass through the nozzle. In most cases, solid particles such as Al_2O_3 and TiO_2 have been widely used[293,306] since they can withstand these extremes. However, since these particles tend to contaminate the wind tunnel components, other particles such as mineral oil 'smoke',[301,308] 'DEHS' oil droplet aerosols,[293,325] nanostructured tracers,[313] and CO_2 particles[314] have been used or explored for 'cleaner' seeding. Third, particles must follow the flow faithfully. This requirement is especially challenging in hypersonic flow since most particles lose their flow tracking effectiveness at high-speed and under compressible flow phenomena such as sharp turn angles, shocks, and waves. Lastly, the compressible flow changes in density can cause severe optical distortions due to the index of refraction changes and other factors.[287,288,293,315,316]

An illustrative example of such distortions is shown in Fig. 8.2 below (Courtesy of Dr. S. Beresh of Sandia National Laboratory, NM) where particles seeded in a Mach 2.5 flow undergo a shock produced by a 15° wedge. Severe optical distortion and flow tracking deficiencies produced in the shock boundary are apparent from the image close-up (b). In this case, the particle field was generated with mineral oil 'smoke generator' having diameters between 0.2 and 0.3 μm that were introduced into the main flow stream with slotted tubes inserted from a pressurized vessel into the main flow stagnation chamber.
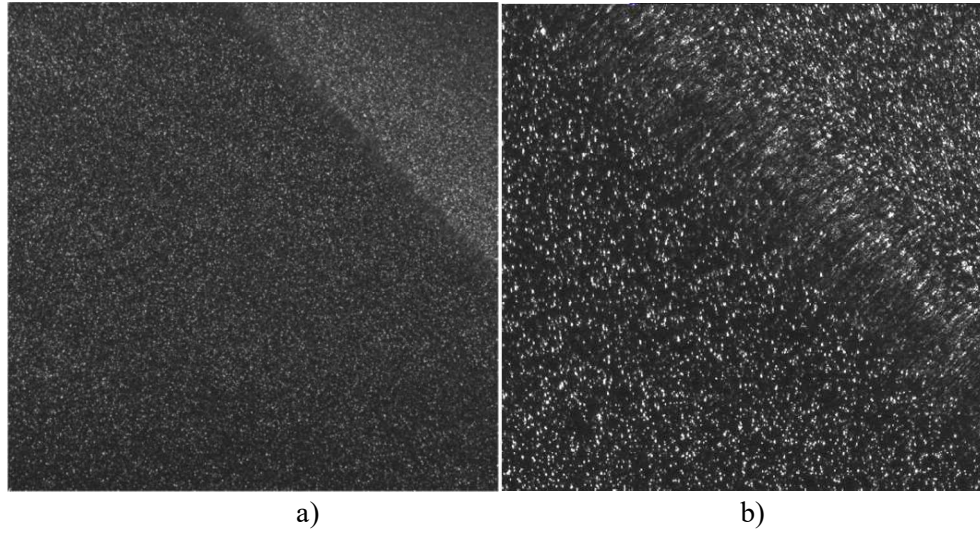
Figure 8.2 Particle field undergoing a shock in a Mach 2.5 flow (a) and close-up image of the shock region (b) (Courtesy of Dr. S. Beresh of Sandia National Laboratories, NM)

The capability of a particle to follow the flow is characterized using the 'relaxation' (also termed 'reaction', 'response', or 'decay') time (τ_p). By definition of a step response, a particle experiencing a step change in velocity (such as a strong normal shock) will take a time of τ_p to reach 63.2% of its final asymptotic value.[287] It has been studied extensively and quantified for aggressive conditions such as those of high turbulent fluctuations and high-speed flow phenomena.[293,317-332] For example, it has been found that the relaxation time of the particle mainly depends on the square of its main dimension size (e.g. diameter) and only linearly on its density, and is given by the Stokes drag[287] which for compressible flow can be modified as[293]:

$$\tau_p = d_p^2 \frac{\rho_p}{18\mu_f}(1 + 2.7Kn_d),\qquad\qquad(8.1)$$

where τ_p is the particle response time, d_p is the diameter, ρ_p is the particle density, μ_f is the fluid dynamic viscosity, and Kn_d is the Knudsen number (ratio of molecular mean free path and the d_p) that takes into account the rarefaction effects in compressible flows. Variants of this relation can be found in the literature for various high-speed conditions.[322-329,332] The Stokes number, ratio of the time response of the particle with respect to the time scale of the flow (St = τ_p / τ_f) is then used to compare the particle-to-flow tracking capability. For example, particles having St < 0.1 have been typically deemed appropriate for proper flow tracking in many examples.[287,293,332] The distances that particles travel during the response time (flow velocity * τ_p) can then be compared to the spatial resolution of the PIV system (the size of the interrogation windows) to establish whether or not the flow phenomena can be resolved.

As an illustrative example, in a study of flow phenomena at Mach 5,[332] the computed response times and traveled distances of TiO_2 particles of 0.26 μm diameter were estimated to be 4.5 μs and 3.5 mm for a 6-deg oblique shock flow condition, and 0.75 μs and 0.4 mm for a normal shock flow condition. In the study, the PIV spatial resolution was ~ 2 mm; the oblique shocks thus appeared smoothed and the resolution of the normal shock was limited by the data spatial resolution rather than by the particle response time.

8.4. Examples of PIV Measurements

A variety of PIV experiments for high-speed flow applications have been performed during last few decades,[292-300,304-308,330-332] and few illustrative examples are shown in this section. They highlight the fact that PIV remains a powerful diagnostic technique albeit with the challenges of particle seeding. PIV has been notably demonstrated in:

- Mach 2 : oblique shocks, expansion waves, and supersonic wakes,[294,295,305,306,328]
- Mach 4 : supersonic flows,[323]
- Mach 5 : compression ramps, turbulent boundary layers, and 'unstart' processes in inlet-isolator of scramjet/ramjet models at Mach 5 blowdown wind tunnels,[330,331,332]
- Mach 4.5 – 6 : freestreams, wedges, ramps, and spheres in shock tunnels and shock tubes[296,297,298,299,300,330,331] and in wedge flow in hypersonic blowdown tunnels,[296,297]
- Mach 7 flows in hypersonic facilities,[293,329]
- Mach 1.4 heated jet flow with 'tomographic PIV' arrangement displaying the 3D reconstruction of Mach disks, oblique shock, etc.[304]
- High-repetition rate 'pulse-mode' PIV applications to supersonic jets such as
  - Mach 3.73 jet in a transonic cross flow,[308]
  - Mach 1.56 jet.[307]

8.4.1. Mach 2 Examples

Illustrative examples demonstrated in turbulent boundary layer and corner flow studies under Mach 2 conditions[305,306] are shown in Fig. 8.3. The study was performed in the University of Tennessee Space Institute high-speed wind tunnel and with a goal of understanding flow in supersonic and hypersonic vehicle components having non circular internal flow paths and corners in various junctures of the vehicle. In this study, both standard PIV and Stereoscopic-PIV were performed to gather two- and three-components of velocity in a plane. The seeding particles used were TiO_2 which were entrained from a fluidized bed seeder. The estimate of time response for these particles was τ_p = 2.6 μs and a Stokes number of St = τ_p / τ_f ~ 0.09, suggesting appropriate flow tracking. The PIV settings were similar to those shown and described schematically in Fig. 8.2 with 100 mJ/pulse at 25Hz. The sample images of Fig. 8.3

show streamwise velocity contours and in-plane vectors with streamlines identifying counter-rotating corner vortices underneath the high-speed flow.
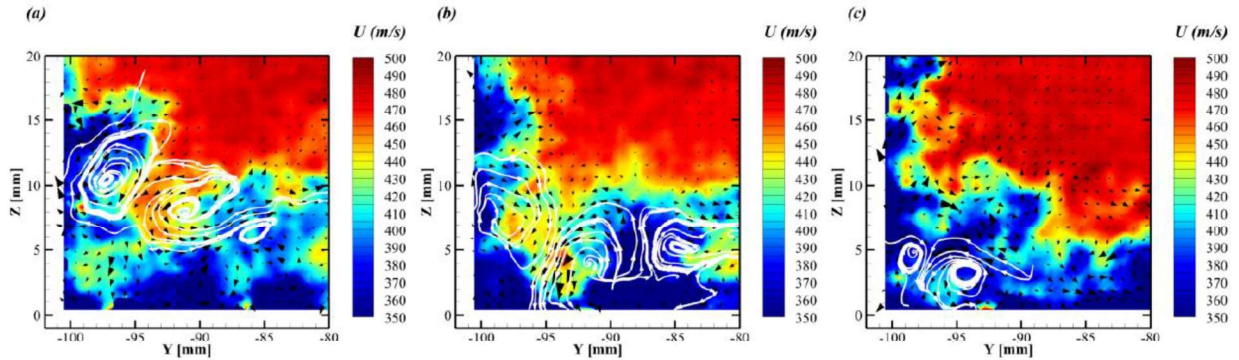
Figure 8.3 Instantaneous streamwise velocity, U, with in-plane vectors and streamlines highlighting counter-rotating corner vortices underneath the high-speed flow obtained with Stereo PIV. Reproduced with permission of the authors.[305]

8.4.2. Mach 5 Examples

Examples from experiments under Mach 5 conditions typical of hypersonic flight and scramjet/ramjet inlets conducted in blowdown wind tunnels[330-332] are shown here. The flows included compression ramps, turbulent boundary layers, and 'unstart' processes in inlet-isolator of scramjet/ramjet models.

In this study, the flow structure of the fully supersonic flow within the inlet-isolator model and the flow structure during the unstart process, as revealed with the PIV measurements, were described. The PIV system consisted of four cameras set up for panoramic plan-view measurements. The seeding system particles were TiO_2 with a manufacturer specified primary diameter of 0.02 μm that was deemed larger due to agglomeration. The particles were seeded upstream of the stagnation chamber using a fluidized-bed seeder system driven by compressed nitrogen. The wide-field PIV system utilized a typical PIV system similar to that of Fig. 8.2 with four cameras in parallel, 140 mJ/pulse lasers, and at 10Hz. The flow was imaged and illuminated through a fused-silica test section window and the acrylic isolator ceiling. The particle response was calculated to be 7 μs for freestream flow, 4.5 μs for an oblique shock generated by a Mach 5 flow over a 6-deg wedge, and 0.75 μs for a Mach 5 normal shock. Uncertainty analysis was performed accounting for hardware related uncertainties including image registration, laser pulse separation time, camera/image calibration, etc. and for data reduction/processing uncertainties such as the window interrogation algorithms, etc. The highest uncertainties were about ±17 m/s for the mean streamwise velocities near the wall and decreased to about ±6 m/s outside the boundary layer.

Samples of PIV results are shown in Figures 8.4 and 8.5 for the mean streamwise Mach number contours for the fully supersonic long isolator and for the instantaneous flow during the unstart. PIV was

succesful in resolving complex flowfields such as the boundary layer, compression ramp shock reflections, and expansion fans and reflections in various regions of interest.
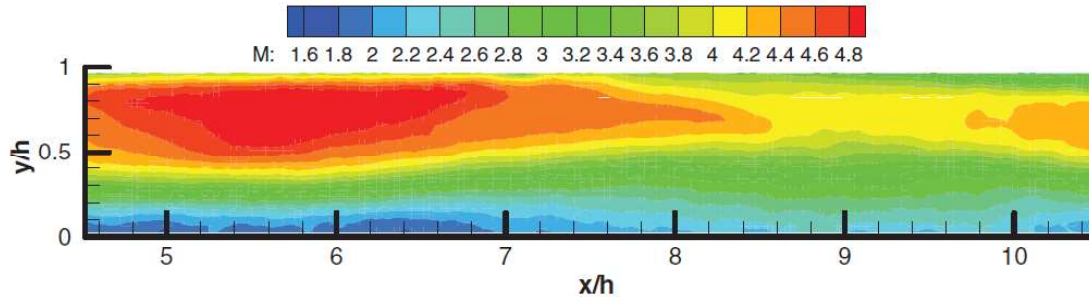
Figure 8.4 Mean Mach number contours for supersonic long isolator. Reproduced with permission of the authors.[332]

(a)

(b)
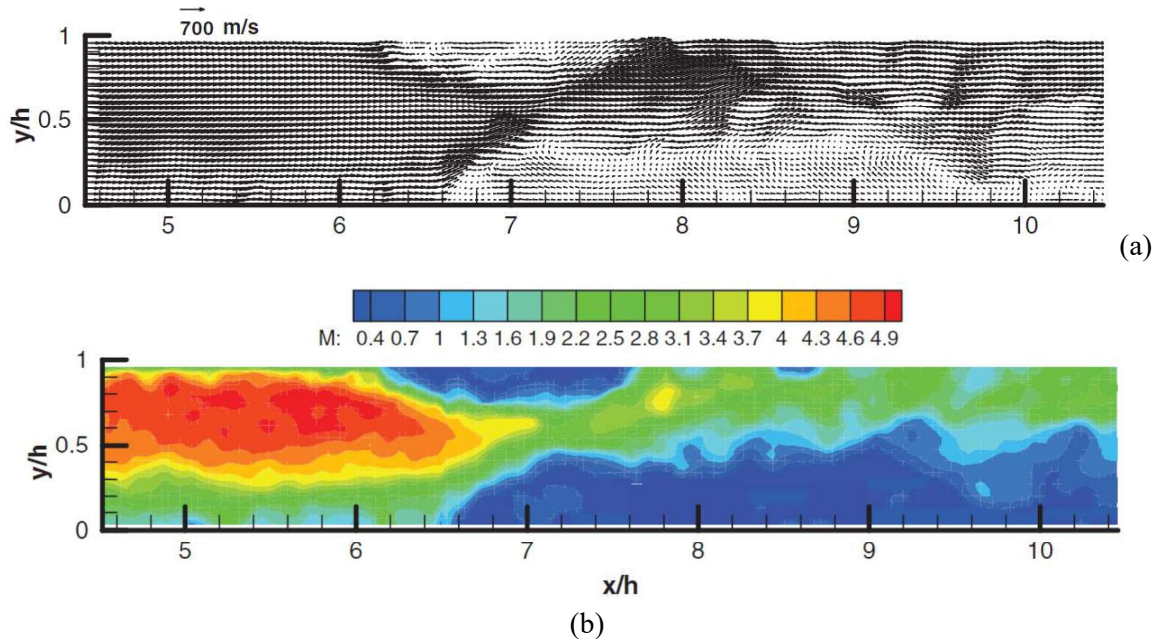
Figure 8.5 Instantaneous flow field during 'unstart' at t = 5 ms: a) velocity vectors and b) M contours.[332] Reproduced with permission of the authors.[332]

8.4.3. Mach 4.5-6 Examples

Illustrative examples of supersonic flows at Mach 4.5-6 obtained at the shock tube Laval nozzle facility in the French-German Institute of Saint-Louis (ISL) are shown in Fig. 8.6.[298-300] The shock-tunnel is a transient wind-tunnel facility with short testing times of a few milliseconds and high supersonic velocities in the km/s. In these examples, Mach flows of 4.5 and 6 are displayed for 20° wedge flows side by side. The PIV settings were similar to those shown and described schematically in Fig. 8.2 with 150

mJ/pulse lasers. The laser pulse separation between two consecutive frames was 0.5 µs, and solid particles (TiO_2 and Al_2O_3) with nominal diameters of 0.3 µm were used for seeding. For this diameter the relaxation time was calculated to be 2.1 µs. A cyclone separator was added to prevent agglomeration by filtering the larger particles, and a seeding density of ~0.15% corresponding to ~10,000 particles/mm^3 was reported corresponding to 10-20 particles within interrogation windows. However, the particle density varied considerably due to strong density gradients in the flow. Shown in Fig. 8.6 are a raw particle image sample and a PIV velocity field for the two Mach numbers. It is apparent that particle lag has an effect on the PIV results. For example, approaching at ~1500 m/s and with an expected 2.1 µs time lag the particles would travel ~3 mm before recovering the flow speed. With some optical distortions expected to contribute, it is apparent that particle lag is a main contribution to the interface's relatively rough appearance and that the shock wave is not straight and shows jittering.
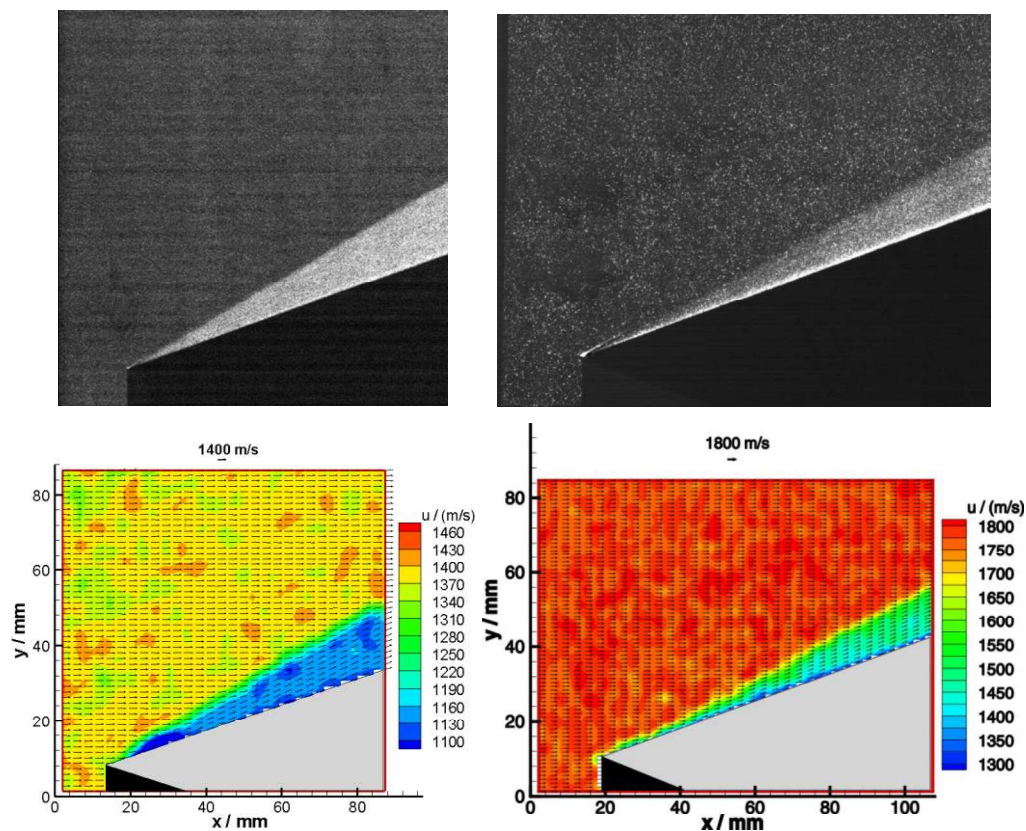
Figure 8.6 Raw images and PIV results for Mach 4.5 (left) and Mach 6 (right) flow over a 20° wedge. Reproduced with permission of the authors.[298,299,300]

8.4.4. Mach 7 Flow Examples

At the higher Mach 7, a PIV sample from a double-compression ramp is shown in Fig. 8.7. The investigation was performed at the Hypersonic Test Facility Delft.[293] A shock-shock and shock-wave-boundary-layer interaction using PIV was studied using TiO_2 particles with diameter of 400 nm and with relaxation time of 2 μs. The PIV settings were similar to those shown and described schematically in Fig. 8.2 with 400 mJ/pulse lasers. Seeding non-uniformity is noticeable and contribute to smearing. As in the previous example, the particle lag is also a big factor and a main contribution to the interface resulting unevenness.
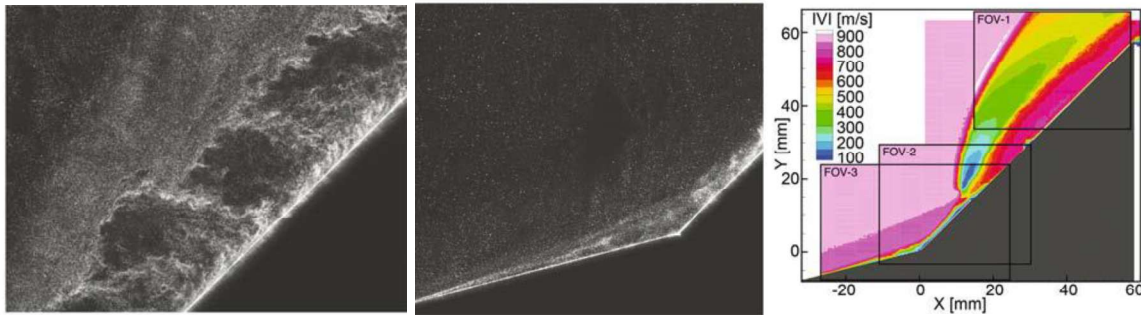
Figure 8.7 Double Ramp Flow PIV samples. Hypersonic Flow Mach 7 at Hypersonic Test Facility Delft (HTFD). Reproduced with permission of the authors.[293]

8.4.5. Tomographic PIV Example at Mach 1.4

The superior dimensional capabilities of tomographic PIV were demonstrated at NASA GRC in an underexpanded Mach 1.4 heated jet flow for acoustics research, and the 3D reconstruction of the Mach disk and oblique shock were rendered.[304] The layout of the system comprised four cameras arranged at an angle of 45° between each of them. Laser power was 400 mJ/pulse and the field of view 180 x 180 x 10 mm^3 with spatial resolution of 0.875 mm^3. It is noteworthy that tomographic data reduction and reconstruction results in significantly higher computational effort, data storage, and processing. In this experiment, flow seeding was 400 nm aluminum powder dispersed from an ethanol solution that stabilizes and prevents powder agglomeration. In the sample shown in Fig. 8.8, color contours displaying velocity magnitude in the centerline are overlaid with streamwise slices through the Tomo-PIV data sets. Tomo-PIV representation with underexpanded features and the shock cells is apparent.
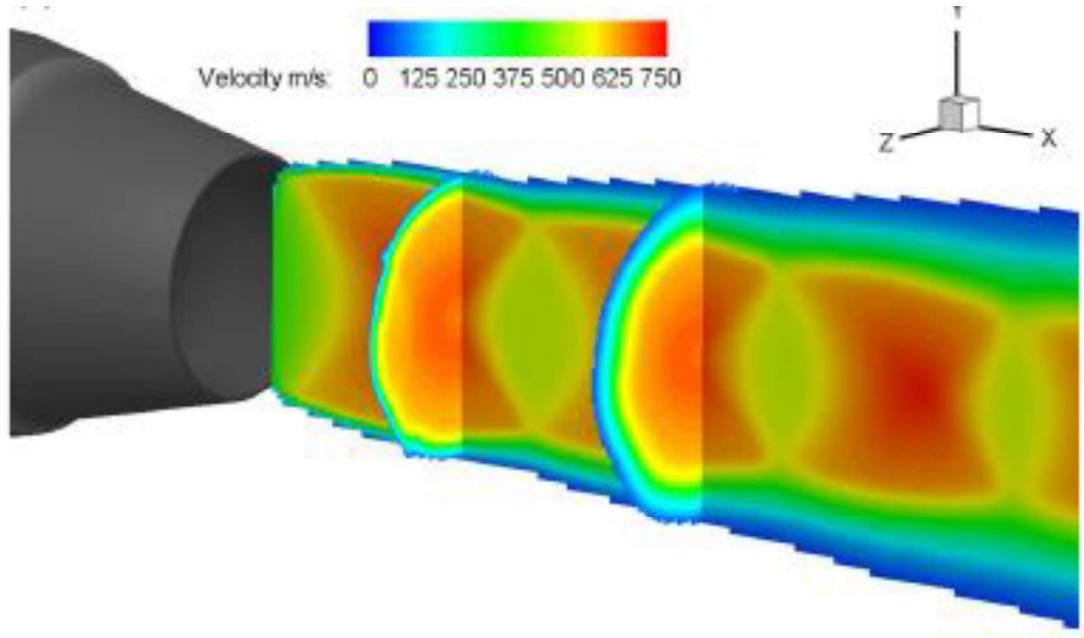
Figure 8.8 Underexpanded M 1.4 jet flow tomographic PIV measurements sample. Reproduced with permission of the author.[304]

8.4.6.   High-Repetition Rates 'Burst-mode' PIV Example

This final example demonstrates recent advances in time-resolved particle image velocimetry (TR-PIV). Here, a supersonic nitrogen jet with a design Mach number of 3.73 exhausted into a transonic crossflow (Fig. 8.9). Using a 'pulse-burst' laser, velocity field time resolved frames of compressible turbulence events were captured.[308] Requirements of the high-speed flows demand higher energy at faster pulse rates than conventional PIV. A quasi-continuous burst-mode laser (QuasiModo-1000, Spectral Energies, LLC) with both diode-pumped and flashlamp-pumped Nd:YAG amplifiers was used to produce a high-energy pulse train at 532 nm. The pulse-burst laser generates up to 10.2 ms bursts every 8 s with a maximum 532 nm pulse energy of 500 mJ at 5 kHz and 20 mJ pulse energy at its current maximum repetition rate of 500 kHz. Images were acquired using two high-speed CMOS cameras (Photron SA-X2), which have a full framing rate of 12.5 kHz and an array of 1024 × 1024 pixels at this speed. Their windowing function allows increasing framing rate by sampling a smaller region of the imaging array. In this case, each camera operated at maximum of 50 kHz with an array of 640 × 384 pixels.
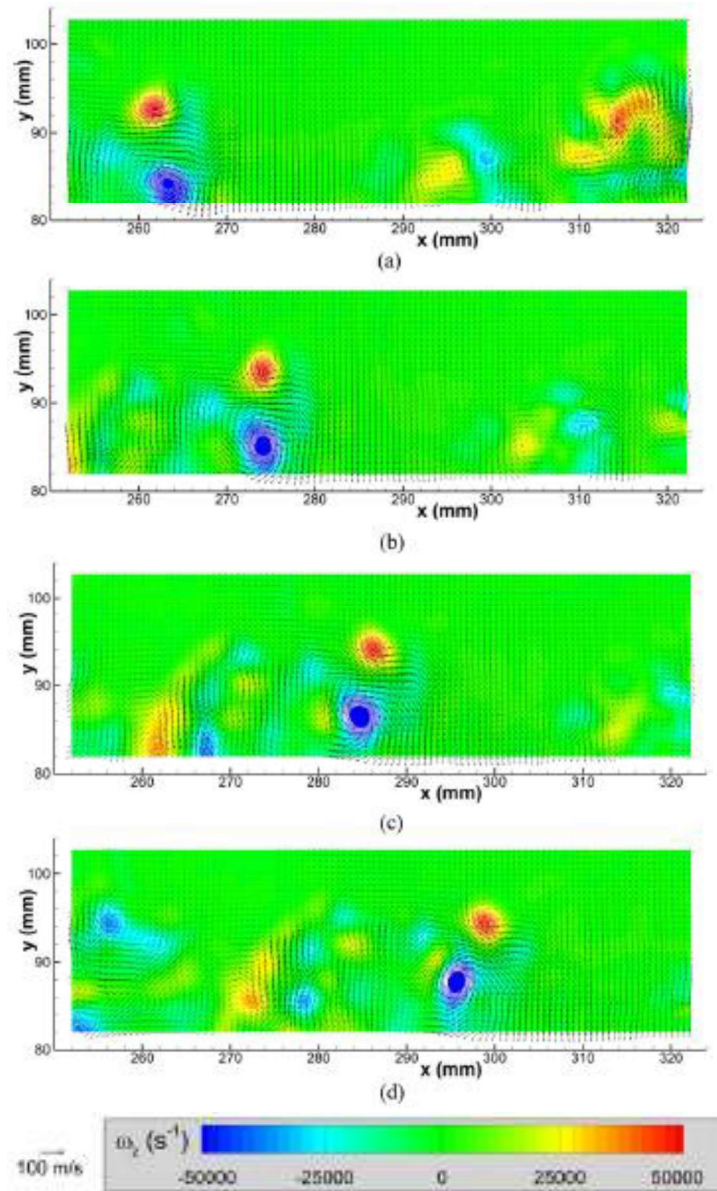
Figure 8.9 Sequence of velocity fields with vorticity extracted from a 2.5 ms burst of 58 velocity fields acquired at 25 Hz, measuring a Mach 3.7 jet issuing into a Mach 0.8 crossflow. Reproduced with permission of the authors.[308]

Two cameras were used side-by-side to extend the field of view in the streamwise direction to track the convection of turbulent eddies using two-component PIV as shown in the sample of Fig. 8.9. Seeding was provided by mineral oil smoke generator and time response was reported adequate (St <0.1). Cameras had to be canted 5° due to the camera body, but it was estimated that this did not create a perspective bias on the velocity vectors by sensitivity to the out-of-plane velocity component, and

calculations estimated that the maximum induced error in the streamwise component was no more than 2%.

A limitation of the 'pulse-burst' is that it has a duty cycle that hinders measurement of moderate frequency phenomena (say 100 Hz). One really needs to use multiple measurement systems to resolve all the time scales. Nonetheless, this example represents the use of TR-PIV in a high-speed ground-test facility and shows the power to investigate the temporal development of turbulent structures in compressible flows.

8.5. Conclusions for PIV

Particle Image Velocimetry (PIV) technique applied to high-speed velocimetry was described and illustrative examples shown. The capability of PIV systems for accurately measuring instantaneous and average flow field velocities in two-dimensional (2D) planes, three-dimensional (3D) volumes, and also provide time-resolution has been demonstrated for a variety of high-speed compressible flows. Nonetheless, particle seeding remains the primary challenge, which is especially difficult in the harsh conditions and environments encountered in high-speed flows. The general requirements for a robust seeding system include delivery of a prescribed amount of particle concentration with uniformity (to yield enough data while not perturbing the flow), necessity to follow the flow velocity as accurately as possible (typically by requiring small diameter), requisite to be bright light scatterers, and the need to be non-hazardous and non-contaminating. These requirements typically have to be addressed in the design on a case-by-case basis.

9. Emission Spectroscopy

9.1. Introduction to Emission Spectroscopy

Perhaps the simplest of optical diagnostic techniques is that of emission spectroscopy, also referred to as Optical Emission Spectroscopy (OES). All that is required to perform optical emission spectroscopy in principal is a spectrometer and a detector. The primary limitation, however, is that the system being measured must be luminous, i.e. producing some form of light that may be collected and analyzed. This requirement typically limits the application of emission spectroscopy to plasmas or combustion flows. In the context of hypersonic flows, the enthalpies must be high enough to be producing excited states of molecules, atoms, and/or ions that emit light as these states relax. The enthalpies required then will be gas dependent; typical minimum levels may be around 2 MJ/kg for CO_2, 20 MJ/kg for Air and 360 MJ/kg for H_2. These enthalpies may be obtained in high enthalpy facilities such as shock tubes or arc jets, however once the flow is expanded, the subsequent cooling and reduction in density causes the emission to drop precipitously and the nozzle flow is often no longer luminous. The application of emission spectroscopy in nozzle flows is therefore limited. The flow may become luminous again when it impinges upon the test article, and emission spectroscopy is often employed in this regime. Emission spectroscopy has been employed in various hypersonic facilities, including free flight ballistic ranges,[333,334] arc jets,[335-350] and shock tubes/tunnels.[351-368] A general review of the processes behind emission spectroscopy including both a theoretical background and specific examples of a radially symmetric flow volume is given by Danehy, et al.[13] Details of intensity calibration, optical imaging, and resolution limitations, with specific application to shock tubes, has been discussed by Cruden.[351] A detailed discussion of the atomic and molecular processes involved in emission can be found in the works of Herzberg.[369-371]

The data obtained from emission spectroscopy comes in the form of an intensity as a function of wavelength. Because different atoms and molecules emit light at different wavelengths, this spectrum may be used to identify species present. Furthermore, the emission spectrum depends on the specific states of the species involved in the emission. Therefore, the spectrum contains information about the population of electronic, vibrational, and rotational states of the species. Without performing any calibration of the spectral intensity, it is usually possible to fit the shape of a spectrum to obtain rotational and vibrational temperatures.[372] Often, the ratios of uncalibrated lines may be used to obtain relative populations of states or species. This ratiometric treatment of the emission spectrum is the underlying principle of actinometry.[373] With an intensity calibration, additional information can be obtained from emission spectroscopy. Calibration is performed by measuring a source of known radiance and ratioing the counts from the reference source and the flow under test. With the intensity converted to a value of

radiance, the intensity may be related to the absolute density of the excited states of the molecule or atom responsible for emission. This relationship is often determined through the use of a spectroscopic modeling software, such as NEQAIR[374] or SPECAIR[375], which contains the Einstein coefficients and dipole moments necessary for relating intensity to density. Relating the excited state densities to ground state densities requires some assumption regarding the temperature or Boltzmann distribution of the species. Another common application of emission spectroscopy is to evaluate the intensity of the radiation for a given shock condition.[351] This measurement is relevant for determining the heat flux impinging on a space vehicle or test article when radiation is a significant means of heating within the flow.

The enthalpies at which radiation may be detected also depend upon the wavelengths being observed. In order for a particular species to produce emission, it must undergo a transition that possesses a dipole moment. The use of OES for vibrational transitions in homo-nuclear molecules is consequently precluded, but is still possible for many electronic transitions for atoms and molecules. Heteronuclear molecules may emit from vibrationally excited states, requiring somewhat lower energy for excitation, with emission observed at higher wavelength, typically in the mid-infrared. Many hypersonic CO_2 emission studies are performed in this wavelength regime. Emission in the visible wavelength range is due to the transitions between electronic states of atoms and molecules or the recombination of electrons and ions (so-called bound-free continuum), and requires higher enthalpies to excite. At the highest enthalpies, significant emission may be observed in the vacuum ultraviolet region ($\lambda \sim 100\text{-}200$ nm or 6-12 eV), which involves transitions between widely separated electronic states.

9.2. Basic theory of Emission Spectroscopy

The basic principal of emission spectroscopy is as follows. The flow naturally emits radiation in all directions. The facility must be equipped with some form of viewport or optical fiber feedthrough through which some of this radiation passes. The light that passes through this port is collected through the optics and focused onto the slit of a spectrometer. The most common type of spectrometer is a grating spectrometer. In this type of spectrometer, the slit passes light into the spectrometer, which is then collimated through a focusing optic onto the grating. The grating has a ruled pattern such that the light diffracts, and the angle at which light reflects off the grating is a function of its wavelength (Fig. 9.1). In this way, the incoming emission is separated into its spectral content. The collimated light is then refocused by a second optic inside the spectrometer onto a detector. The focused light will be in the shape of the slit, but separated spatially by wavelength. The detector can be a point detector, such as a photomultiplier tube, in which case the spectrometer is more accurately referred to as a monochromator, since it is measuring only one wavelength (more precisely, a narrow range of wavelengths) of light. In

this case, a second slit would be on the monochromator exit plane so that wavelengths at different diffraction angles are blocked from the detector. More commonly a linear array, such as a photodiode array (PDA), is used. A linear array has multiple pixels oriented in the direction of diffraction, and hence each pixel measures different wavelengths. In the case of an imaging spectrometer, the direction along the slit may be used as a spatial dimension, and a 2D array, such as an intensified charge coupled device (ICCD) may be used with each pixel row representing one position in the flow, and the column representing the wavelength. This arrangement requires the focusing optics to perform a one-to-one mapping of position in the flow to a height on the slit, and the spectrometer's internal optics to perform a one-to-one mapping of a position of the slit to a position on the array.
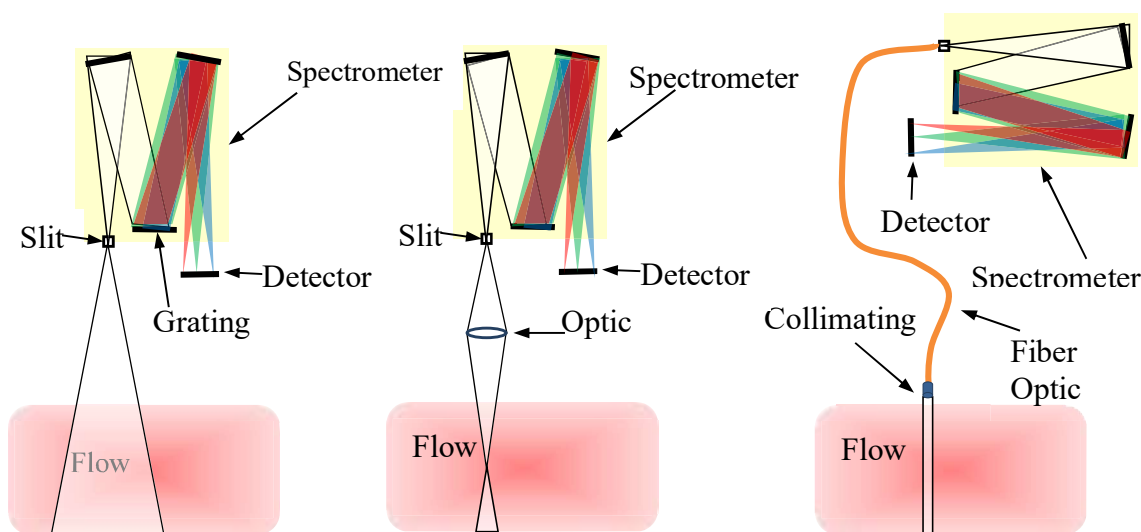
Figure 9.1. Illustration of the principal of optical emission, (left) without focusing optic, (center) with focusing optic, (right) with fiber optic and collimating attachment.

It is often preferred to use some form of optics (lenses, mirrors) to focus the light from the source onto the spectrometer. Without an optic, the spectrometer would measure a broad region of the flow (Fig. 9.1a.) The focusing optics may be used to measure a much narrower region of the flow (Fig. 9.1b), or if the optics are designed to be imaging, a linear cross-section of the flow may be measured onto a two-dimensional detector. In some cases, the light may be directed from the facility through fiber optics to the spectrometer when windows are not directly accessible to an optical bench (Fig. 9.1c). In any of these cases, the measurement is line-of-sight integrated; that is, the emission is collected along the optical path and therefore is the accumulation of signal over the entire linear distance traversed by the optical path. Moreover, the signal is collected over a conical volume (see Fig. 9.1) that is defined by both the spectrometer and external optics, so is an average of signal within this volume. Thus, every measurement

has some finite spatial resolution, extending in multiple directions, which must be considered. If it is desired to obtain spatial resolution in two or three dimensions, additional methods may be employed. A simple approach is to translate the spectrometer or optics and perform measurements at multiple positions. This strategy is only possible in steady and repeatable flows, and would not be applicable to impulse facilities. Another example is filtered imaging, where the image is focused onto a 2D array without an intervening spectrometer and band-pass filters are used to select a specific range of wavelengths.[367] In both of these cases, two-dimensional spatial resolution is obtained but the data is still line of sight integrated. In the case of radially symmetric flow, Abel inversion[341,344] or "onion peeling"[347] may be used to extract data with spatial resolution in the radial direction. A more advanced inverse analysis method involves using multiple mirrors or spectrometers to image the flow from multiple directions and use a Radon transform or other inverse methods to convert the data into three dimensions.[349] This idea is in principle very similar to computed tomography (CT) imaging. All of these inverse methods require the flow to be optically thin. "Optically thin" refers to the case where the emission is not absorbed anywhere in the flowfield, and hence the intensity is proportional to the pathlength. Furthermore, all inverse methods are ill-posed mathematical problems with multiple valid solutions, and it is typically necessary to perform some regularization, or smoothing, to prevent noise accumulation in the inversion process. Generally speaking, the more views through the flow, the higher the spatial resolution for inverse methods. Thus, spatial resolution is improved at the expense of cost, time, or complexity.

9.3. Examples of Emission Spectroscopy

One of the earliest examples of emission spectroscopy in a hypersonic flow involved the characterization of the radiative gas cap over a free flying ballistic test article.[333] In tests conducted between 1959-1965, 1-3 cm diameter blunt body models were launched using light gas guns into an enclosed ballistic range that was evacuated and filled with air at pressures between 2×10^{-4} and 2×10^{-1} atm. While the launched articles could achieve velocities of up to 8.8 km/s, in some tests a shock tube was used to launch a counter-current shock wave at velocities up to 3.6 km/s. This method produced relative velocities up to 12.4 km/s (77 MJ/kg) which exceeds escape velocities and produced a radiating gas cap that would be comparable or brighter than those encountered in the Apollo program, albeit at much smaller length scales. Results reported spanned the range of 5.4-12.4 km/s. Similar measurements were made in test gases consisting of CO_2 and N_2 at velocities between 5-8 km/s and 4×10^{-3} to 8×10^{-2} atmospheres to simulate entries to Mars and Venus.[334] In these measurements, a spectrometer was not utilized. Instead, a series of eight photomultiplier tubes, each equipped with a narrow-band optical filter was used to measure the intensity of the light in spectral ranges spanning from 200-1000 nm. In this way,

a crude spectrum of the emitted radiation could be constructed and compared against models for radiative heating. These "narrow-band radiometers" were arranged at the same axial location, and different azimuthal positions. The radiometers measured the intensity of emitted light as a function of time. A slit assembly installed on the radiometer ensured that the measurement was limited to one axial location. As the model passed over the slit assembly, a peak in the radiometer signal could be observed, corresponding to the radiating gas cap in front of the article. After the model passed from the view of the slit, a second peak could be observed, corresponding to radiation in the wake of the model. In this case, the wake radiation was only seen with a polycarbonate model, and was attributed to luminous species ablated from the test article.

Numerous applications of emission spectroscopy to arc jet flows have been reported. As an example, a schematic of the IHF arc jet at NASA Ames is given in Fig. 9.2. The high enthalpy flow is produced in an arc heated mixture of argon and air. The gas then enters a mixing (aka plenum or settling) chamber where additional air may be added to tailor the condition (i.e. enthalpy). The flow is expanded through a converging-diverging nozzle into the test chamber to produce a high enthalpy flow of sufficient diameter for testing. This flow then impinges upon a test article to simulate the environment of planetary entry. A bow shock is formed around this test article. Optical emission characterizations have been performed at all stages of the flow, including the arc column,[335] within the plenum chamber,[342,347] in the freestream,[339-341,350] and in the shock layer.[336,339-341,343]
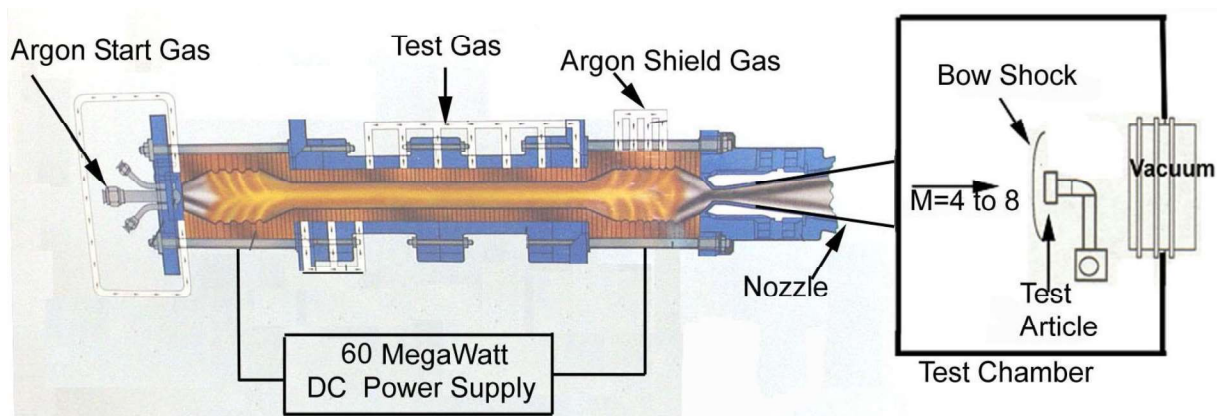
Figure 9.2. Schematic of an arc-jet facility

This review will focus specifically on emission characterizations in the NASA Ames Arc Jets. Terrazas-Salinas, et al. measured atomic lines within the arc column to estimate gas temperature.[335] Babikian, et al. used the ratio of atomic N atom radiation to that of molecular species (N_2^+, NO) to estimate enthalpy in the shock layer over a test article.[336] Park, et al. measured rotational and vibrational temperatures in both the free stream and shock layer by fitting spectra from NO, N_2^+, and atomic oxygen

lines.[339-341] Donohue, et al used emission spectroscopy to measure the electronic temperature in the plenum chamber.[342] Raiche and Driver utilized "modern" spectroscopy equipment to monitor ablating test articles.[343] Winter, et al. performed characterizations of radial uniformity in the plenum chamber,[347] as well as atomic/molecular non-equilibrium in the freestream.[350]

The work of Park, et al. sought to characterize the optical emission properties in the 20 MW Aerodynamic Heating Facility (AHF) at NASA Ames. A diagram of their spectroscopic setup is shown in Fig. 9.3. A 2.5 cm length of the flow was imaged with 4 to 1 magnification onto a mask placed in front of the spectrograph. The mask consisted of alternating opaque regions, 0.75 mm long, and open regions of 0.127 mm length. Given the system magnification, the flow was imaged at 3 mm intervals over ~0.5 mm regions as a result of the masking. Eight such regions were measured over the 2.5 cm length imaged. The light that passed through the mask was then refocused onto the spectrometer and collected on a 2D CCD array. The primary purpose of the mask was to better isolate the spatial regions of the flow to individual locations on the CCD. The effect of the mask on the optical acceptance cone is shown in Fig. 9.3c. By using the mask, cones from the adjacent regions did not intersect within the luminous region of the flow and thus each measured region is independent of its neighbors. In the absence of such a mask, the data obtained will be a convolution of the spatially resolved emission with the spatial resolution function of the optics and spectrometer.[351] The mask effectively truncates the convolving spatial resolution function. While the presence of such a convolving function does not invalidate the measurement in any way, it must be accounted for in subsequent analysis.

(a)

(b)

(c)
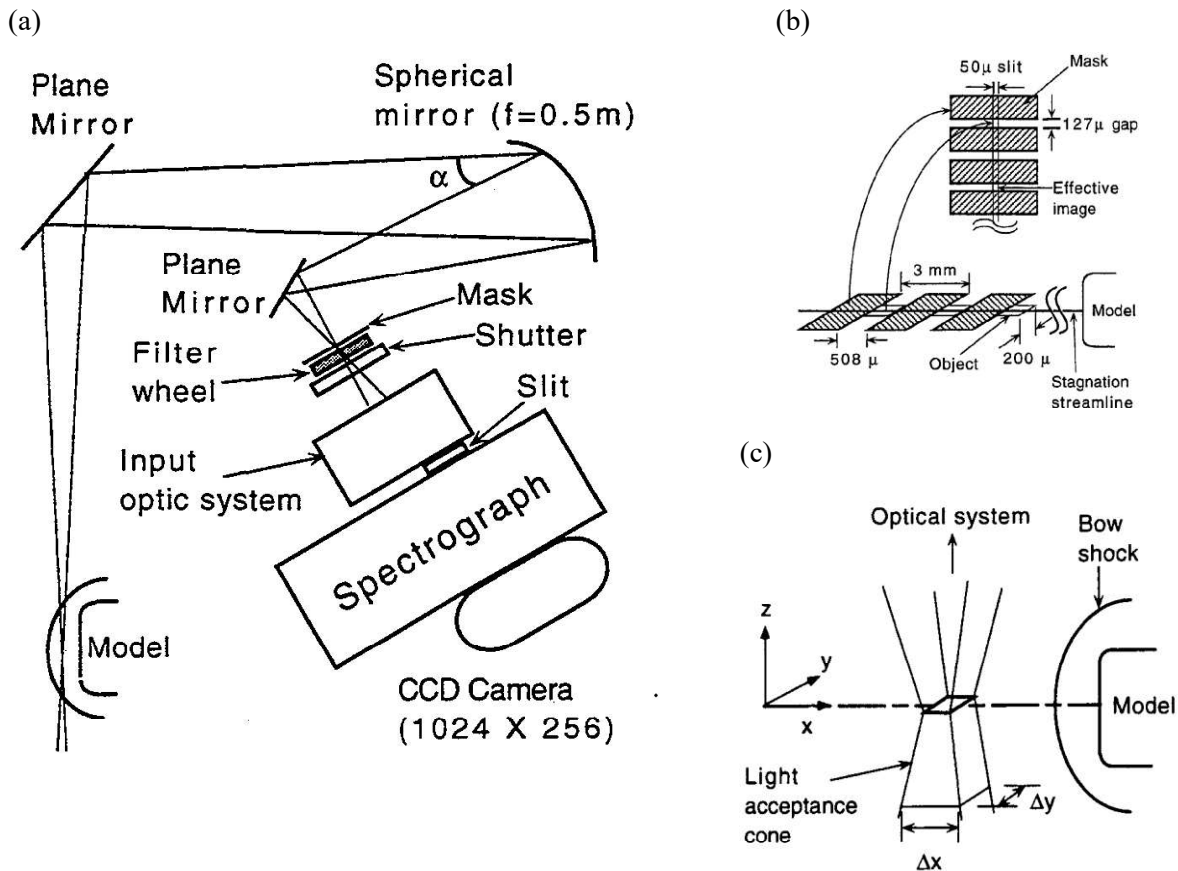
Figure 9.3. (a) Experimental set up for characterization of the high enthalpy flow in the arc jet. (b) Mask used to define imaged areas. (c) Optical acceptance cone created by the mask.[339,340] Reprinted with permission of the authors.

While the figure shows the spectroscopy being performed on the bow shock over the model surface, the model was also rotated out of the flow so that the freestream itself, without model interaction, could be measured. Due to the weakness of the freestream radiance, exposure times of 30s were required, and only spectra attributed to the NO molecule were obtained between 200-280 nm. Such a spectrum is shown in Fig. 9.4a. While two electronic states (so called γ and δ bands) of NO were observed emitting, only one vibrational quanta was identified, such that each band originated from the $v'=0$ state. The authors utilized the NEQAIR code to simulate five of the NO bands in Fig. 9.4 and obtain a correlation between the width of the band and its rotational temperature. The vibrational temperature could not be determined in the freestream since there was only one vibrational level observed, although an upper bound of 950 K could be assigned based upon the simulations and this observation. The rotational temperature did not vary with position over the 2.5 cm region resolved, and is shown in Fig. 9.4b as a

straight line. Also shown in the same plot are the temperatures (electronic, rotational, vibrational) inferred by emission spectroscopy in the presence of a model. Temperatures obtained from the 5 bands ranged from 860-990 K with uncertainties from 60-100 K at a high pressure condition, and from 570-630 K with uncertainties of 35-55 K at the low pressure condition. Simultaneous laser-induced fluorescence (LIF) measurements were obtained at 1640 ± 400 K and 820 ± 250 K for these two respective conditions. The discrepancy between LIF and emission spectroscopy temperatures was not well understood, although it is noted that LIF was performed on the centerline only, while the emission data is line-integrated. Attempts to resolve the discrepancy through Abel inversion were inconclusive.[341]
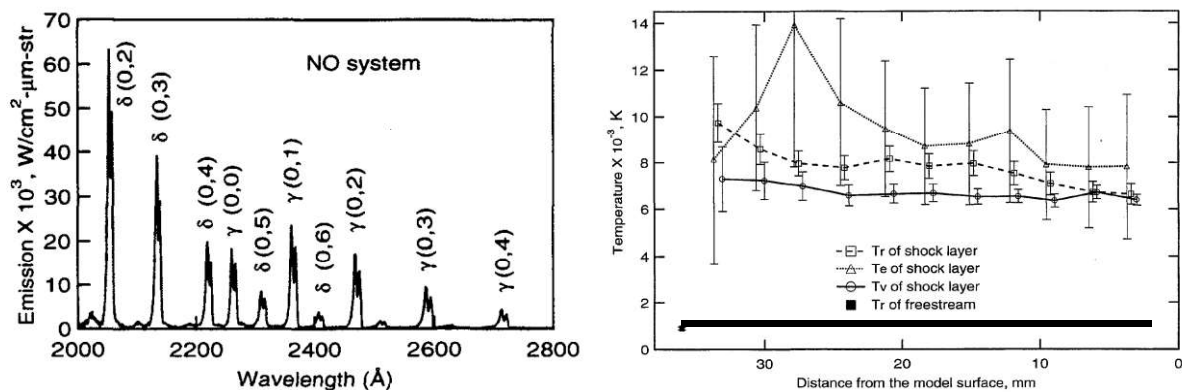
Figure 9.4. (a) Spectrally resolved data obtained in the AHF freestream. (b) Temperature estimated from emission measurements both with and without (i.e. freestream) a test article.[339,340] Reprinted with permission of the authors.

The work of Raiche and Driver in the early 2000's was the first OES application in the large 60 MW Interaction Heating Facility (IHF) arc jet. It was also the first to make use of miniaturized fiber-coupled spectrometers to obtain spectral data at high rates and with high spatial resolution. The schematic of the optical setup is given in Fig. 9.5, including a simultaneous laser scattering measurement. The fiber optic beam used a collimating optic such that it imaged a cylindrical volume, 2 mm in diameter. To verify the quality of the optic, the researchers measured a tungsten lamp source at different locations from the "field-of-view centerline", i.e. perpendicular to the optical path. The data in the figure shows that the beam image is approximately Gaussian, but the width of the beam depends upon the wavelength being measured. This distortion is known as chromatic aberration and is not uncommon for lens-focused systems. The resolution was not characterized at positions away from the facility center-line (i.e. along the optical path.)
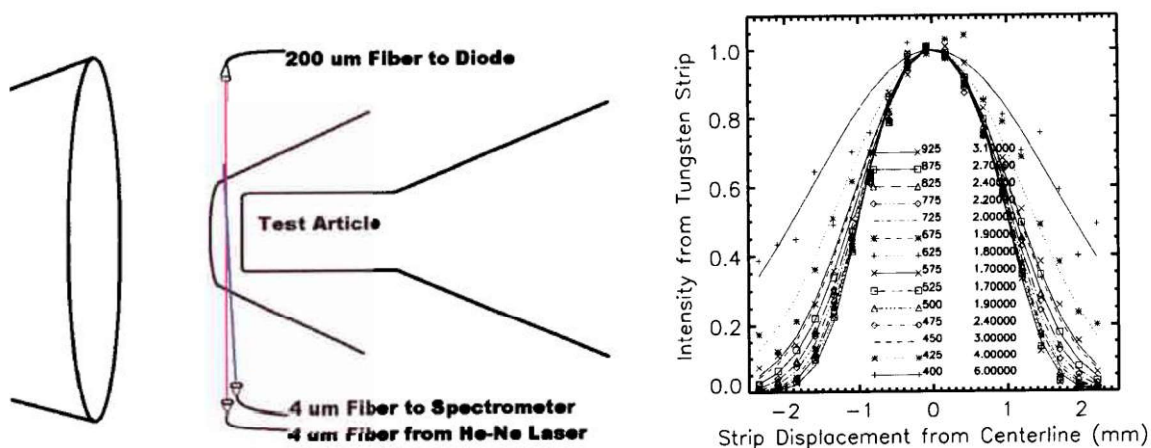
Figure 9.5. Schematic of the spectroscopic setup of Raiche and Driver (left) and measured spatial resolution profile (right).[11] Reprinted with permission of the authors.

The study utilized an Ocean Optics S2000 fiber coupled spectrometer, which still nearly reflects today's state of the art. The size of the S2000 (and similar) spectrometers is several centimeters on a side, as opposed to more traditional spectrometers that are on the order of 30-100 cm. There is some trade-off in imaging quality and spectral resolution with these spectrometers, however the performance is still quite reasonable. Raiche and Driver were able to measure 1024 wavelength points at a resolution of 4.5 nm (note that wavelength resolution is typically determined by the slit width, and not the pixel spacing – thus the resolution often spans multiple pixels). The useful wavelength measurement range of the instrument was from 300-900 nm, and spectra were collected at intervals of 10-512 ms. Figure. 9.6 shows sample data collected from the spectrometer. The images have been corrected for relative spectral sensitivity of the instrument based upon measurement of a radiometric standard. Figure 9.6a shows the spectrum obtained with a copper calibration model. The black bars and lines are useful for feature identification, representing typical relative intensities and wavelengths of different radiating species observed in the flow. Significant features are identified from N_2, N_2^+, and atomic N and O. Some impurities from Cu and CN are also identified. Figure 9.6b shows the spectral measurements as a function of time in the flow, where the spectra are plotted together to produce a greyscale image with time on one axis and wavelength on the other. Since the optical position is fixed, and the test article is recessing as the measurement is conducted, the measurement gradually moves from imaging the test article itself (black region) to the shock layer and then out into the freestream (white regions). (Note: black regions, including many of the atomic lines, are saturated.) Spectral cuts at two positions are shown in Fig. 9.6c. While the spectral features within the shock layer are similar to those observed on the copper calibration article, the region outside the shock (i.e. freestream) is characterized by a continuum radiation that may be fit with a Planck function at approximately 3840 ± 20 K, which is close to the model surface temperature. In this case,

radiation in the freestream was attributed to particles created on the model and ejected into the freestream (i.e. spallation) as no significant freestream radiation was observed in the absence of a model.

(a)   (b)   (c)
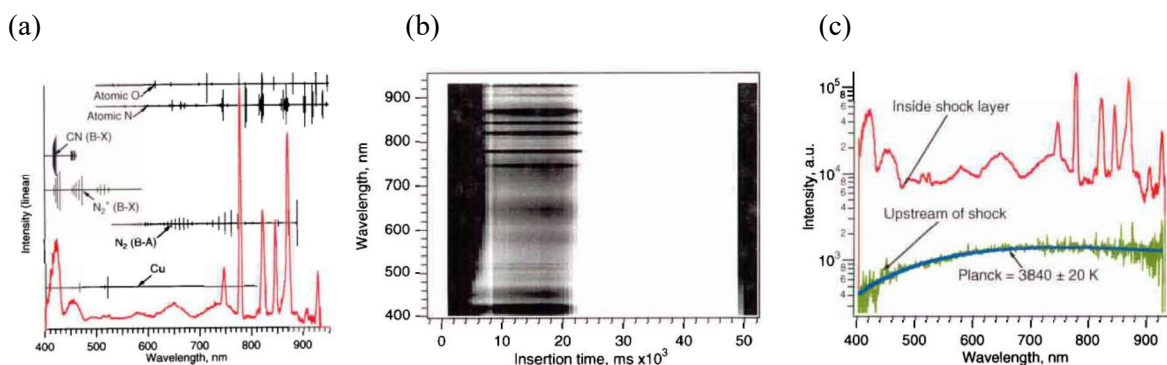
Figure 9.6. Spectroscopy traces obtained in the arc jet experiment. (a) Uncalibrated data obtained on a copper calibration model, (b) greyscale image showing multiple spectra (vertically) taken as a function of time (horizontally), (c) spectra from two positions in the grey-scale image, showing the emission measured within the bow shock and upstream of the shock (i.e. freestream), due to contamination by particles ejected from the model).[343] Reprinted with permission of the authors.

Optical emission spectroscopy measurements within shock tubes have been used to obtain fundamental data on atoms and molecules[376] and molecular reactions rates,[377,378] as well as signatures of radiative heating for planetary entry.[351,353,356] A schematic of a general shock tube or tunnel is given in Fig. 9.7 along with where optical emission measurements are typically performed. In the operation of a shock tube, the high pressure driver gas that creates the shock wave behaves much as a blunt body does when it is entering an atmosphere. That is, the driver does not mix with the *driven* gas due to the short time scales involved, rather it "pushes" and compresses the driven gas in front of it, forming a shock wave that is heated by the change in kinetic energy. This incident shock may be studied as a one-dimensional reacting flow by performing emission spectroscopy through windows in the shock tube. The shock tunnel is distinguished from a shock tube in that the gas is allowed to exit the tube section prior to analysis. In the non-reflected shock tunnel, the gas exits freely and is measured before the free expansion alters the state of the gas significantly. In an expansion tunnel, this shock would exit through a nozzle at the end of the tube. In a reflected shock tunnel, the shock is reflected off an endwall, with some flow allowed to expand through an opening in the endwall plate. In both the expansion and reflected shock tunnels, this nozzle flow enters a test section then impinges upon a test article, setting up a shock system on the model (a bow shock, for a blunt model). This bow shock has been analyzed by optical emission in several studies.[362-367] However, the condition of the nozzle flow is typically inferred from 0D or 1D models and can be a significant source of uncertainty to the measurement.[379,380] The nozzle flow is typically characterized for uniformity via Pitot rake measurements, but very few studies attempt to directly

measure the thermochemical state of the nozzle flow, or determine its implications upon the properties of the bow shock.[364,381]
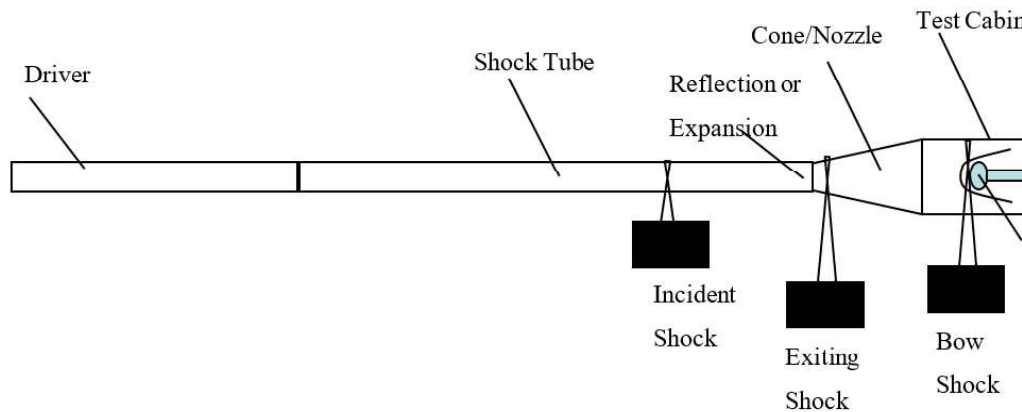
Figure 9.7. Schematic of a generic shock tube/tunnel. Emission spectroscopy is generally performed on the incident shock, the shock just as it exits the shock tube, or the bow shock formed on a test article.

The Electric Arc Shock Tube (EAST) at NASA Ames has been used extensively to study radiation and reactions in incident shocks. Independent tests at University of Queensland (X2),[358] CUBRC (LENS XX),[361] and JAXA (HVST)[357] have corroborated the data obtained in EAST. The emission spectroscopy measurements in EAST use imaging spectroscopy in order to obtain data that is resolved along the streamwise axis of the shock tube. Schematics of the optical set up in EAST are shown in Fig. 9.8, with the optical paths unfolded. Though the schematic depicts the optics as lenses, mirrors are actually used for focusing and imaging to avoid chromatic aberration (described above). Three possible optical designs are shown. Early EAST tests utilized a telescopic optical design (Fig. 9.8a), where the lines of sight enter the tube at an angle to its axis.[382] For a long optical path or small shock tube diameter, this optical design may be sufficient. However, for larger diameter tubes (as in the EAST 60 cm tube), this angle causes a loss of spatial resolution due to the line integrated nature of emission spectroscopy. This loss of resolution is apparent in the radiance profile at the shock front shown below the sketch in Fig. 9.8a. Modern EAST tests utilize a telecentric optic design (Fig. 9.8b), which ensures lines of sight all pass through the tube perpendicular to its axis.[383] The spatial resolution in this design is limited by the width of the conical volume defined by the collection optics. In optics, the F/# is the ratio of the focal distance to the diameter of the collection optic, which defines the shape of the cone. Because the diameter of the cone is inversely proportional to F/#, the amount of light collected will go approximately as $(1/F)^2$, while the spatial resolution is proportional to 1/F. Thus, it is desirable to minimize F/# while still meeting some minimum desired resolution. In the case of the 10 cm diameter EAST tube, the mirrors are oversized so that the optical diameter is determined by the spectrometer. The focal length is the spectrometer focal

length times the magnification of the optics, so that the effective F/# is the product of the spectrometer F/# and the magnification factor. For the 60 cm EAST tube, the resolution will be 6× worse for the same optical F/#, due to the increased optical pathlength. The loss of spatial resolution was sufficiently severe to warrant installation of an aperture to increase the F/# (Fig. 9.8c) at the expense of signal intensity. In order to mitigate the $(1/F)^2$ loss in intensity, a rectangular aperture was used instead of a circular aperture, with the narrow side of the aperture oriented in the axial direction of the tube. This orientation has the effect of reducing the optical collection volume in the resolved direction (parallel to the tube axis), but not altering the volume in the direction perpendicular to the tube axis, which is presumed to be uniform. The intensity thus scales as $1/F$ rather than $1/F^2$. The data in the bottom row of Fig. 9.8 show improvements in spatial resolution manifest as a more sudden risetime in the signal trace as the shock wave passes by the measurement station.
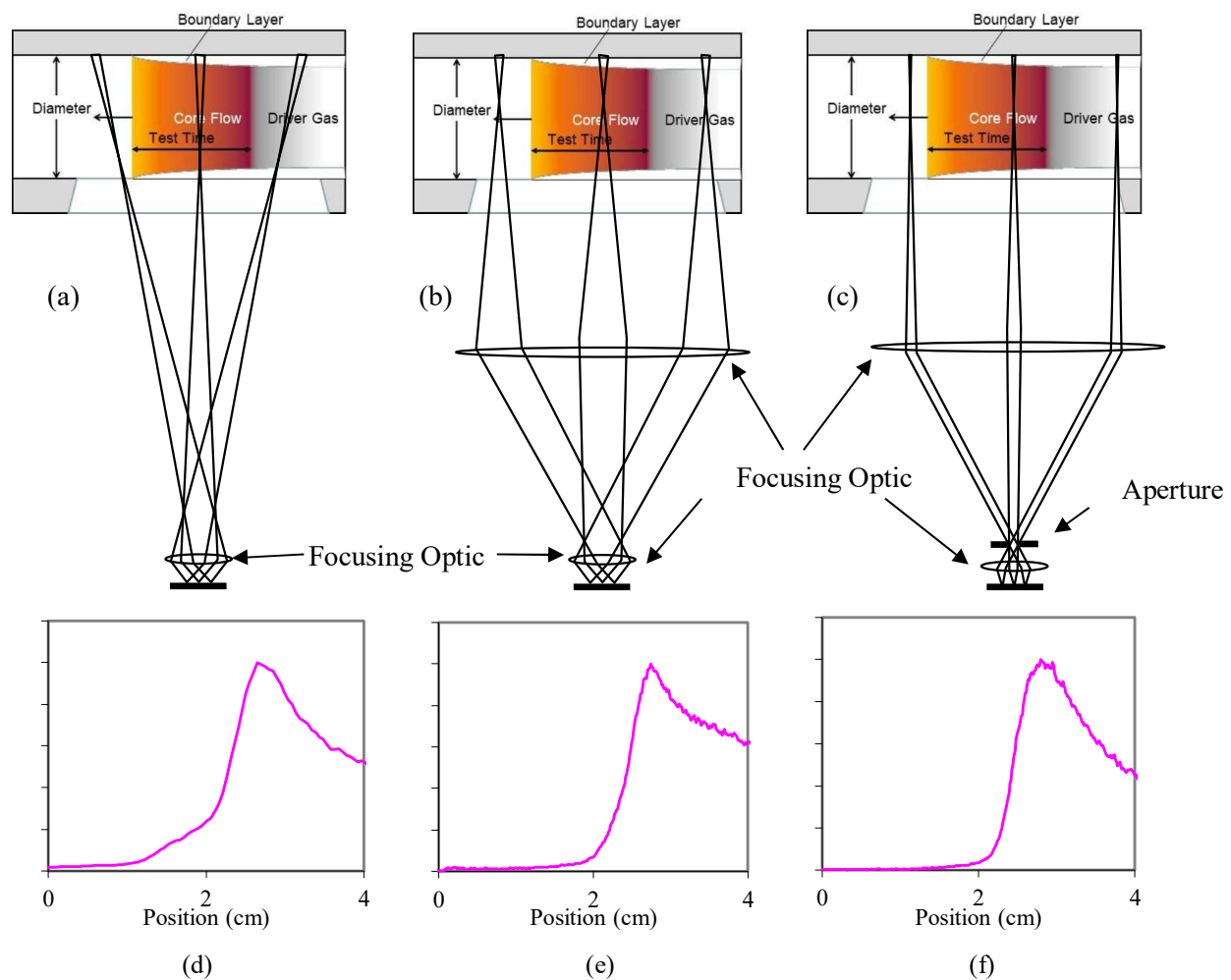
Figure 9.8. Schematic of optical arrangements in the shock tube, with spatial resolution increasing left to right. (a) Telescopic optics, (b) telecentric optics, (c) telecentric optics with aperture. Shown below each image (d)-(f) is the radiance measured at the shock front.

Data collected in the EAST creates a map of intensity versus wavelength and position in the tube. A sample raw data plot is shown in Fig. 9.9a. This raw data is normalized by a calibration response function, Fig. 9.9b, which is obtained by measuring the output of an integrating sphere that has been calibrated against a radiometric standard. The resultant data is shown in Fig. 9.9c. Cross-sections of the 3D plot taken in the vertical direction provide a measurement of radiance versus position. Cross-sections in the horizontal direction provide the spectral radiance at that position. Four such images are collected simultaneously on EAST, all looking at the same position in the tube, but differing azimuthal angles. A cross section from two similar shots, comprising eight separate spectral measurements, are co-plotted in Fig. 9.9d to show the spectral radiance at equilibrium. Much of the apparent noise below 200 nm are actually atomic lines measured at higher resolution than the rest of the plot. Tests in EAST have been performed with different gas mixtures to simulate entries into Mars,[352] Venus,[352] Earth,[384] Titan,[385] and Saturn.[386] The spatial dependence of the spectra has been used to infer and update reaction rates and radiation models for several of these atmospheres.[387-389]
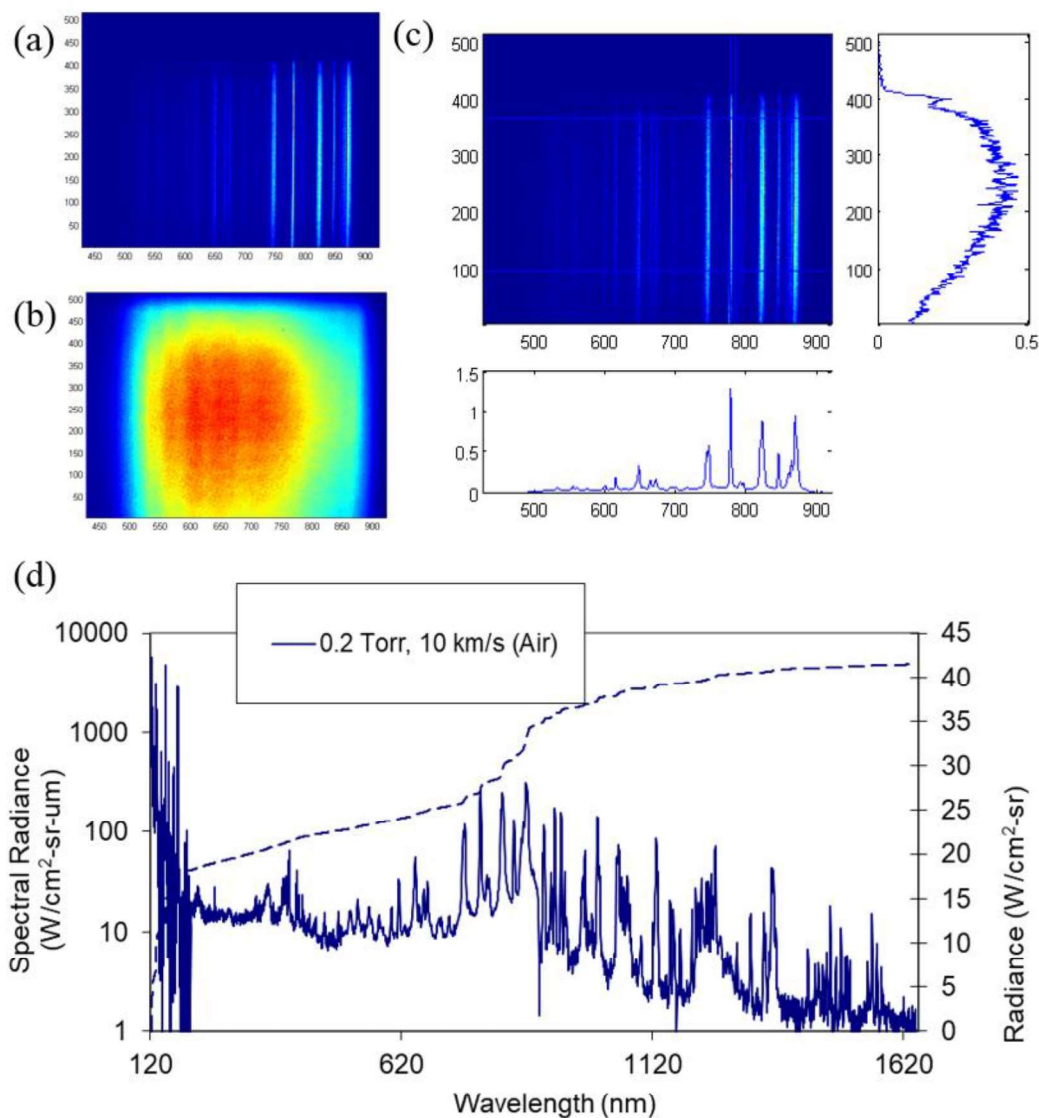
Figure 9.9. Sample of data obtained in the EAST facility. (a) Raw data from spectrometer, (b) calibration response function, (c) calibrated data with horizontal and vertical cross-sections, and (d) cross-sections in "equilibrium" region obtained from eight such spectral images.

Deeper analysis of the emission data can provide flowfield parameters such as species number densities, electron densities, and rotational, vibrational and electronic temperatures. When radiation is optically thick, the radiation is described by the Planck (blackbody, ε=1) function, which has temperature as its only dependent parameter. Three examples of optically thick radiation measured in the EAST are shown in Fig. 9.10. Figure 9.10a shows a measurement of CO radiation in the vacuum ultraviolet (VUV). The low wavelength end of the spectrum is fit with a Planck function. Fig. 9.10b shows CO_2 radiation in the mid-wave infrared (MWIR), where the upper limit of the radiation is also fit with a Planck Function.

Finally, Fig. 9.10c shows an optically thick Hydrogen line, where the flat top of the line is described by a Planck function. (Note: it is often not possible to see the Planck limit of atomic lines due to finite resolution of the spectrometer. The case shown in Fig. 9.10c is atypical. The absence of a clear Planck limit does not mean a line is optically thin!) The Planck function has a very strong temperature sensitivity, therefore temperatures determined in this way are typically very accurate, often to better than ±100 K. For all these cases, fits are performed for data that is calibrated to absolute radiation units. A relative fit could be performed for uncalibrated data, but requires the data to span a large enough wavelength range to make the temperature dependence significant, and the accuracy is reduced accordingly. For a flowfield in thermal non-equilibrium, this temperature is the effective temperature between the states involved in the transition. For the CO VUV case, it is an electronic transition, and hence can be thought of as an electronic temperature. The CO_2 MWIR transition is vibrational, and so represents the vibrational temperature. For the Hydrogen line, it is a transition between the n=2 and n=3 states of the Hydrogen atom, so the temperature is the effective temperature between these states, which would be the electronic temperature if the states are Boltzmann distributed.
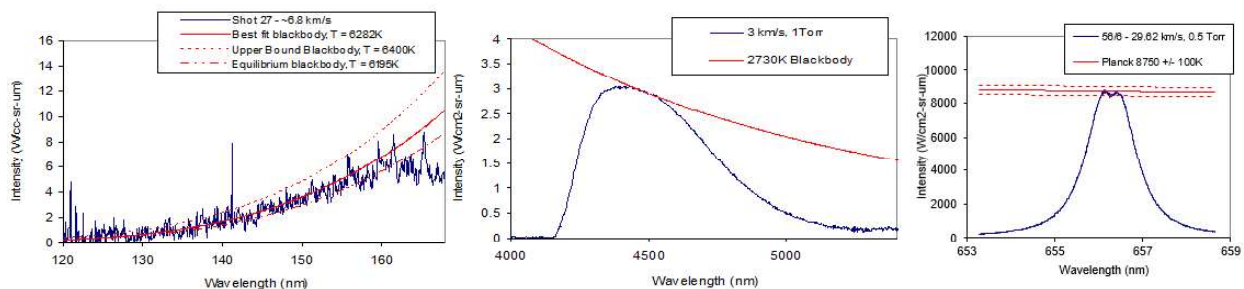
Figure 9.10. Determination of temperature from Planck Limiting (Blackbody) curves. (a) CO in vacuum ultraviolet, (b) CO_2 in mid-infrared, (c) Hydrogen in visible.

Rotational and vibrational temperatures may be obtained by fitting molecular bands. This method requires some kind of spectroscopic model. While scripts to perform such calculations may be written by the enterprising researcher, codes such as NEQAIR,[374] SPECAIR,[375] or LIFBASE[390] may also produce these spectra (the ability to fit the data, however, is not necessarily built in). Example fits of CN and C_2 spectra are shown in Fig. 9.11. The accuracy of these methods are lower than the Planck method, with typical errors on the order of 10%. For hypersonic flows approaching 10,000 K, the error could be as much as ±1000 K. This method also requires the flow be Boltzmann distributed in both rotational and vibrational modes, and that the instrument lineshape be characterized accurately. Furthermore, it technically obtains the temperature of the excited state, which is not necessarily equilibrated with the ground state. Some examples of large differences between fit emission temperatures and mean rovibrational temperatures exist in the literature.[391] However, in many cases it may work well and Fig.

9.11c has overlaid temperatures obtained with both of the methods described (rovibrational and Planck fits) with translational temperatures obtained from tunable diode laser absorption spectroscopy (TDLAS) in the same test.[392]
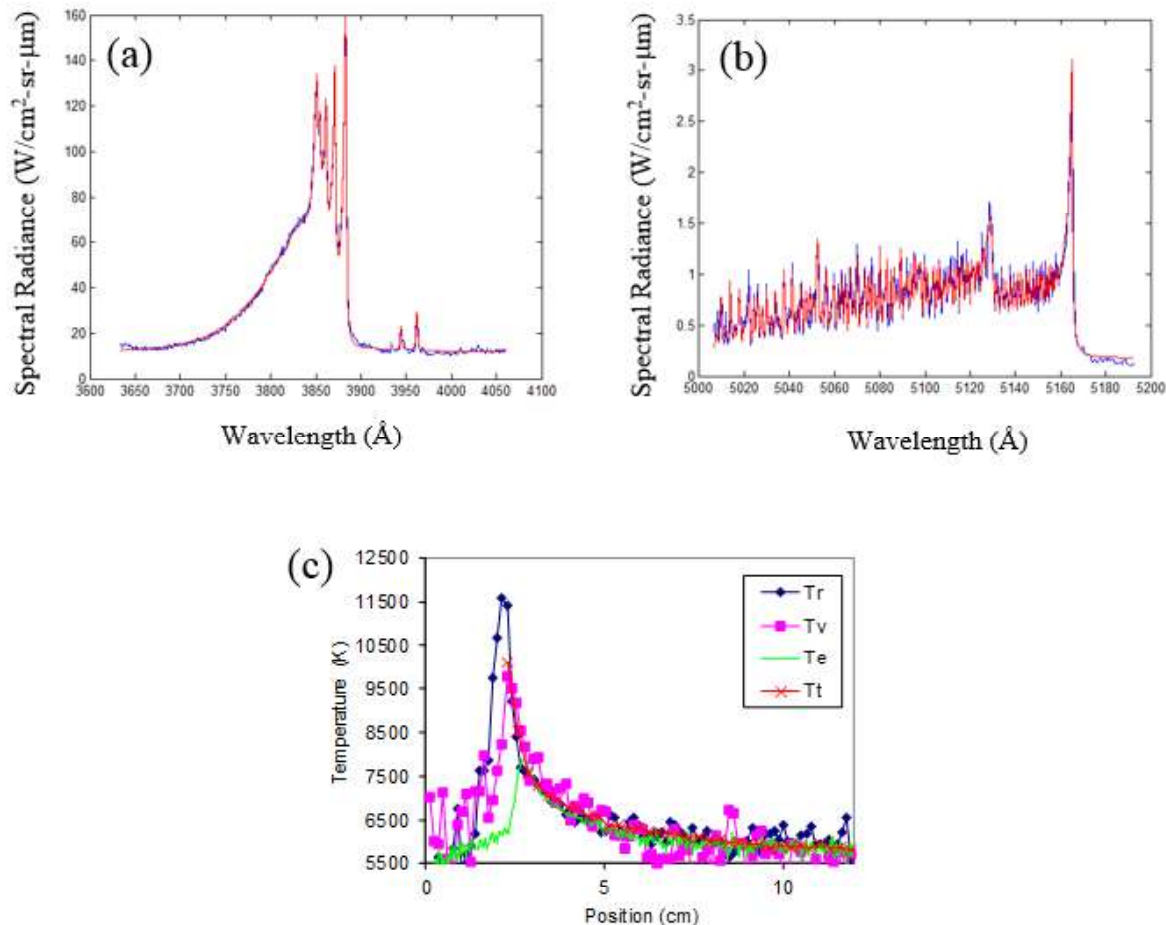
Figure 9.11. Example of spectral fits used to extract rotational and vibrational temperatures (a) CN molecule, (b) C_2 molecule. (c) Compilation of temperature extracted by Planck Method, rovibrational fitting and tunable diode laser spectroscopy in a single test as a function of distance along the viewport (streamwise).

Emission intensities are proportional to the density of excited states responsible for emission. Thus, it is sometimes possible to determine excited state density from emission data and/or produce Boltzmann plots from which the ground state density may be inferred.[348] Another density that may be inferred from emission data is electron density, for flows that are sufficiently ionized. The electron density is extracted from high resolution line-width measurements when the lineshape is dominated by the Stark effect.[368] The lineshape cannot necessarily be resolved for all lines without very powerful spectrometers. Hydrogen lines are however typically very accessible with Stark broadening and often present as an

impurity in flows. A few lines of Nitrogen and Oxygen were also identified for use in the EAST facility. Some example fits of these lines are shown in Fig. 9.12, along with a plot of electron densities obtained over a range of test conditions in EAST.[368]
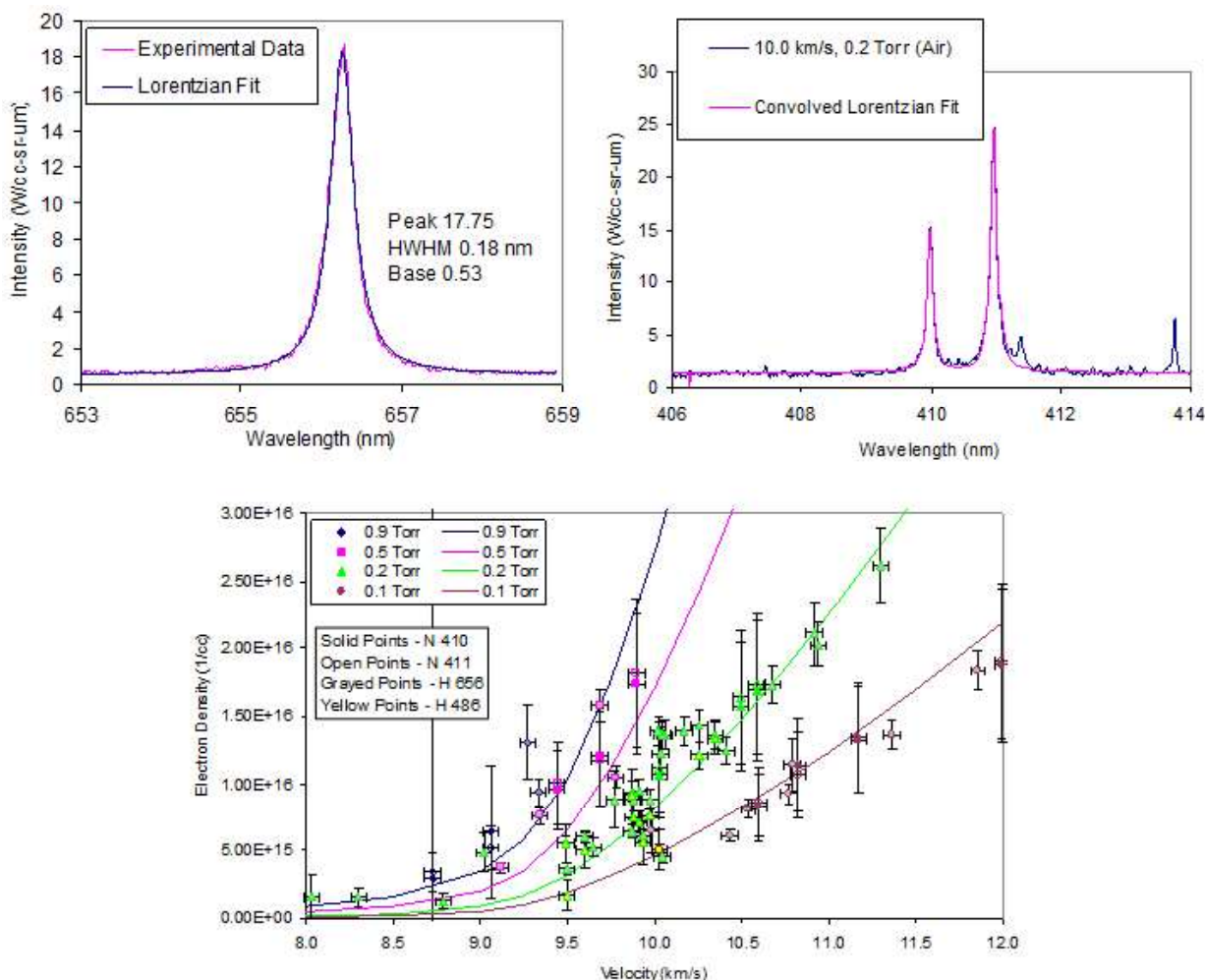
Figure 9.12. Sample lineshape fits of Hydrogen (top left) and Nitrogen (top right) to obtain electron number density. The bottom plot shows the range of electron densities obtained for different conditions in EAST, and comparison to equilibrium values.[368] Reprinted with permission of the authors.

9.4. Conclusions for Emission Spectroscopy

In summary, optical emission spectroscopy is a simple, yet powerful technique. In spite of the simplicity of the application, there are still many subtleties to the implementation to be considered, some of which were discussed here. While the implementation may be relatively straightforward, significant analysis complexity may follow to obtain meaningful interpretation of the data. In general, optical emission probes only the excited levels of molecules and atoms, such that intervening assumptions are required to translate this to ground state data. OES has been used to analyze multiple flow temperatures,

species number densities, particle-laden flows, and radiative heating magnitude. One limitation of the technique is the requirement for a luminous flow, making it inapplicable in vibrationally/electronically cold freestreams. Another limitation of the method is its path-averaged nature, though this can be overcome by measuring from multiple views and performing tomographic reconstruction.

10. Conclusions

As developers of hypersonic vehicles begin to rely increasingly on computational methods to design and optimize hypersonic vehicles, there is an increased emphasis on validating these codes. Critical to validating the codes are the inflow and boundary conditions. While some of these conditions can be measured with conventional intrusive probes, non-intrusive diagnostics show promise to measure detailed spatial and temporal information about the thermodynamic state and velocity of hypersonic facility flowfields. This manuscript reviewed the state of the art in non-intrusive flowfield measurement techniques for studying hypersonic freestream flows.

To conclude this manuscript a set of summary tables is provided in Tables 10.1-10.3. They are sorted alphabetically by measurand (the parameter being measured) rather than by technique so that different techniques measuring each property can be compared. The first table (10.1) shows a variety of different measurands while the 2nd (10.2) describes temperature measurement techniques and the final table (10.3) shows velocity measurement methods. In the tables, the following abbreviations are used:

FPST = Free Piston Shock Tunnel
ST = Shock Tube or Shock Tunnel
BD = Blowdown Wind Tunnel
AJ = Arcjet
ET = Expansion Tube
UJ = Underexpanded Jet

Below, some observations are drawn about the measurement techniques in view of the range of measurements needed (and requirements for measuring freestream perturbations) in the introductory section.

While reviewing the data in these tables and the ensuing discussion one should keep in mind that this study was not intended to be exhaustive, but indicative of some of the literature. An exhaustive review was beyond the scope of this work. Rather, the tables provides a rough idea of the state of the art and some initial references to begin a search if considering doing such measurements in the future.

A first observation is that a wide variety of measurands relevant to hypersonic freestream flows can be measured with non-intrusive measurement techniques. Comparing the mean conditions shown in Tables 10.1-3 they generally overlap well with the operating conditions shown in Table 1.1 in the introduction. That is, measurement techniques exist to measure most of the operating conditions typically occurring in different types of hypersonic wind tunnels. But many of these techniques have not yet been applied to or adopted by large-scale industrial and government wind tunnels. This would be recommended for future work.

A second observation from the tables is that there seem to be far more velocity and temperature measurement methods in the literature than other parameters. This is not surprising considering the

importance of these two parameters, temperature and velocity, which capture thermal and kinetic energy of hypersonic flows. However it is also possible that these parameters are easier to directly measure than other parameters such as gas pressure which is a less extractable quantity.

Regarding temperature measurements, several different methods have been developed to identify the different temperatures (e.g., translational, rotational, vibrational, electronic) that occur in nonequilibrium flows commonly associated with hypersonic facilities. No one measurement technique can provide all of these temperatures, so to get the complete understanding of a flow – even a freestream flow – multiple techniques are required. In terms of temperature measurement accuracy and precision, numbers in the range of 3-20% are typical with the exception of fs/ps CARS which can measure temperature with an accuracy and precision of just a few percent or less. This high precision be attributed to high signal-to-noise ratio data and very stable lasers, at least in the fs/ps regime.

Regarding velocity, there are a wide variety of techniques that have been developed. Some of these are highly facility specific such as nitric oxide PLIF which works especially well in facilities having naturally present NO (or facilities where NO can be seeded into the flow). Velocity measurements generally break down into two categories: Lagrangian tracking techniques (MTV, PIV) and Doppler-shift based methods. Based on the data in the table it is clear that the Lagrangian methods are more precise than their Doppler shift counterparts which are roughly 5x less precise on average. MTV typically measures at a point, line or a coarse grid of points or lines while Doppler shift methods can provide much higher spatial resolution with a velocity measurement at each pixel. Like with many of these techniques, different measurement needs may be addressed better by one or the other of these capabilities. While PIV is more intrusive than the other velocimetry techniques described in this manuscript (owing to the need for seeding particles) it is much further developed, allowing three- and four-dimensional reconstruction of velocity fields even with commercially off the shelf hardware and software.

In general, regarding accuracy determination, it can be challenging to compare a non-intrusive measurement to a known "truth" to establish accuracy. Typically one would compare the new measurement technique to an "accepted standard" measurement. That may work in a laboratory jet flow or flame where multiple optical and/or conventional techniques and even simple calculations can all be compared. But in an actual hypersonic facility flow there is sometimes no available comparison data. Or the existing data was obtained with a perturbative probe, which has its' own complications. In such cases it may be possible to perform the measurement in a well-understood hypersonic flow and then to compare with CFD simulations of this flow. Another approach is to plan to use multiple measurement techniques that use different physical principles to measure the same parameter in a hypersonic flow (for example using both MTV and PIV to measure velocity). The difference between these measurements (assuming

that they are both carefully implemented and validated in lower-velocity flows) could be an indication of measurement accuracy. Similarly, a caution about "precision" estimates in the literature: these can report the combined effect of both the technique measurement and the flow unsteadiness. So reported numbers could overestimate the actual instrument measurement precision.

A final observation can be made by comparing the data in Table 1.2 with the data in Tables 10.1-3. Whereas Table 1.2 shows that fluctuations less than 1% are commonly expected in hypersonic freestream flows, we see very few measurement techniques that can resolve such small fluctuations. Ideally measurement techniques would have 5x better precision than the value they are trying to measure to provide good measurement resolution. So, measurement techniques with precision on the order of 0.1% or better are needed. Only a handful of measurement techniques are close to the needed precision: PIV, FLDI, fs/ps CARS, some MTV techniques and a PLIF density measurement technique with precisions on the order of 1%. None met the required 0.1% precision required to fully resolve small freestream fluctuations in conventional tunnels and existing nonintrusive measurements are found to be especially unsuitable to resolve fluctuations in quite tunnel freestream flows. Still this is an opportunity for future work.

Measurand	Technique	Facility Type	Mach #	Seeding	Species Probed	Accuracy	Precision	Mean meas.	Spatial Resolution	Sample Time	Meas. Rate	Ref.
Concentration	Absorption	BD	N/A	None	CO, CO_2	--	5%	0.05-0.06	Path-integrated	0.17 ms	up to 6 kHz	67
Concentration	ns CARS	BD	2	None	N_2, O_2, C_2H_4, CO_2, CO, H_2	--	--	500-1300 K	0.075 mm x 1 mm	10 ns	20 Hz	281
Density	PLIF	BD	10	I_2	I_2	--	1%	3e17 mol/cm^3	0.3 mm	200 ns	30 Hz	105
Density	PLIF	BD	2.07	I_2	I_2	--	--	0.34 kg/m^3	0.1 mm	--	--	106
Density	PLIF	UJ	4.5	Kr	Kr	7%	--	0.02 kg/m^3	0.047 mm	--	--	107
Density (Δρ)	FLDI	FPST	--	None	air	--	0.5%	--	10 mm	10 ns	100 MHz	178
Electron Number Density	Emission	ST	30	0-2% H_2	H, N, O	20%	--	1e16 cm^{-3}	1 cm	1 us	single pulse	368
Flow Visualiz.	PLIF	AJ	5	None	NO, O	--	3%, 10%	--	1 mm	--	10 Hz	83
Flow Visualiz.	PLIF	FPST	7.9	None	NO	--	15.0%	--	0.25 mm	100 ns	10 Hz	92
Flow Visualiz.	PLIF	AJ	5	None	NO	--	--	--	0.1 mm	1 us	10 Hz	94
Mole Fraction	PLIF	ST	2.7	None	NO	--	10%	0.5	0.28 mm	400 ns	10 Hz	102
Mole Fraction	PLIF	ET	2.3	CH_3	CH_3	--	--	0.5	0.096 mm	400 ns	--	103
Mole Fraction	PLIF	BD	8.2	NO	NO	--	25%	0.07	0.1 mm	75 s	10 Hz	104
Number Density	Absorption	ST	30	None	CO, CO_2	30%	--	5.00E+16	5 mm	0.5 us	2 MHz	392
Number Density	LIF	AJ	2	None	None	20%	--	8.00E+15	--	180s	--	393
Number Density	Emission	AJ	4	None	N	10%	--	1e16 cm^{-3}	2 cm	--	--	350
Pressure	fs/ps CARS	gas cell	--	None	air	<7.5%	2%	0.4-3 atm	0.1 x 1 mm	<1 ns	1-10 kHz	255
Pressure	FRS	BD	2	None	air	4-5%	--	yes	0.285 mm	--	--	205
Pressure	PLIF	BD	3	NO	NO	10-30%	--	2.25 kPa	0.25 mm	217 ns	10 Hz	108
Pressure	PLIF	UJ	--	I_2	I_2	4%	5%	100 kPa	0.23 mm	60 s	3 Hz	109
Pressure	PLIF	UJ	1.5	I_2	I_2	--	8%	135 Torr	0.16 mm	250 ms	4 Hz	110
Pressure	Absorption	FPST	--	None	CO_2	--	14%	350 Pa	Integrated	20 ms	600 Hz	18

Table 10.1 Summary of some assorted measurement techniques' specifications, listed in alphabetical order by measurand.

Measurand	Technique	Facility Type	Mach #	Seeding	Species Probed	Accuracy	Precision	Mean meas.	Spatial Resolution	Sample Time	Meas. Rate	Ref.
Temperature	ns CARS	BD, Vitiated	2	None	air	2-5%	3-5%	300-2500 K	0.1 x 1 mm	10 ns	10-30 Hz	272
Temperature	ns CARS	BD	2	None	air	--	--	500-1300 K	0.1 x 1 mm	10 ns	20 Hz	266
Temperature	fs/ps CARS	flames	--	None	air	1-5%	1-1.5%	500-2500 K	0.1 x 1 mm	10-100 ps	1 kHz	243
Temperature	fs/ps CARS	Plasma, detonation	--	None	air	--	2%	300-2500 K (5000 K T_{vib})	0.1 x 1 mm	10-100 ps	1 kHz	259
Temperature	fs/ps CARS	flames	--	None	air	--	--	300-2000 K	0.035 x 1 mm	100 ps	10 Hz	246
Temperature	FRS	BD	2	None	air	2%	--	yes	0.285 mm	--	--	205
Temperature	Absorption	ST	30	None	None	10%	--	7000 K	5 mm	0.5 us	2 MHz	392
Temperature	Emission	AJ	2	None	None	10%	--	800 K	0.5 mm	30 s	--	341
Temperature	LIF	AJ	2	None	--	25%	--	1600 K	--	180s	--	393
Temperature	LIF	AJ	2	None	None	15%	--	1200 K	0.5-3 mm	100 ns	20 Hz	394
Temperature	Absorption	AJ	N/A	None	O*	--	4%	7260 K	Integrated	1 s	100 Hz	78
Temperature	Absorption	ST	N/A	None	CO	--	4%	7400 K	Integrated	20 us	50 kHz	37
Temp. (Elec.)	Emission	ST	30	None	CO	3%	--	7000 K	2 mm	.1-1 us	single pulse	352
Temp. (Rot)	PLIF	FPST	--	None	NO	--	--	700 K	--	--	--	95
Temp. (Rot)	PLIF	BD	8.2	NO	NO	3%	4%	300 K	0.1 mm	75 s	10 Hz	98
Temp. (Rot)	PLIF	BD	4.7	NO_2	NO_2	--	5%	56 K	0.028 mm	3 us	10 Hz	96
Temp. (Rot)	PLIF	UJ	12	I_2	I_2	--	--	11.5 K	0.1 mm	60 s	--	97
Temp. (Rot)	PLIF	FPST	7	None	NO	--	4%	450 K	0.11 mm	650 ns	--	99
Temp. (Rot/Vib)	Emission	ST	30	None	None	10%	--	7000 K	2 mm	0.1-1 us	--	352
Temp. (Trans)	LIF	AJ	4.8	None	O	--	~100%	1000 K	0.09 mm	--	--	101
Temp. (Vib)	PLIF	FPST	7	None	NO	--	4%	785 K	0.11 mm	650 ns	--	99

Table 10.2 Summary of some temperature measurement techniques' specifications.

120

Measurand	Technique	Facility Type	Mach #	Seeding	Species Probed	Accuracy	Precision	Mean meas.	Spatial Resolution	Sample Time	Meas. Rate	Ref.
Velocity	MTV	BD	10	NO_2	NO_2	2.80%	1%	1400 m/s	0.1 x 2 mm	2 us	10 Hz	395
Velocity	MTV	BD	5	NO_2	NO_2	--	1.6-2.5%	719 m/s	0.1 x 2 mm	2 us	500 kHz	152
Velocity	MTV (HTV)	BD, Vitiated	2	H_2O	H_2O	1.20%	1-2.2%	680 m/s	0.1 x 2 mm	10-100us	10 Hz	141
Velocity	MTV (KTV)	BD	14	Krypton	Krypton	2-3%	0.2-1.25%	1920 m/s	0.1 x 5 mm	4 us	10 Hz	168
Velocity	MTV (FLEET)	BD	14	None	air	1%	<0.5%	1920 m/s	0.1 x 10 mm	7 us	1 kHz	169
Velocity	PIV	BD	2.01	TiO_2	--	2%	--	500 m/s	3 mm	1 us	25 Hz	305, 306
Velocity	PIV	BD	5	TiO_2	--	0.50%	2%	700 m/s	1 mm	1 us	10 Hz	332
Velocity	PIV	ST	4.5 - 6	TiO_2	--	--	2%	1600 m/s	6 mm	1.5 us	10 Hz	293
Velocity	PIV	BD	7	TiO_2	--	1%	2%	1040 m/s	1 mm	1 us	10 Hz	293
Velocity	Tomo-PIV	Jet	1.4	Al_2O_3	--	--	1%-4%	750 m/s	2 mm	--	2 Hz	304
Velocity	TR-PIV	SJTCF	1.4	Oil	--	--	2%	300 m/s	0.7 mm	--	50 kHz	308
Velocity	FRS	BD	2	None	air	2-3%	--	--	0.285 mm	--	--	205
Velocity	CC-DGV	BD	1.65	alumina	--	3%	--	600 m/s	0.05 mm	2 min	--	196
Velocity	IRS	BD	--	None	air	--	3%	--	0.1 mm	30 ns	10 Hz	396
Velocity	PLIF	AJ	5	None	NO	--	13%	500 m/s	0.1 mm	72 s	10 Hz	94
Velocity	PLIF	FPST	7	None	NO	--	5%	1300 m/s	0.17 mm	50 ns	N/A	111
Velocity	PLIF	FPST	10	None	NO	--	10%	500 m/s	0.5 mm	200 ns	N/A	112
Velocity	LIF	AJ	4.8	None	O	--	11%	3600 m/s	0.09 mm	--	--	101
Velocity	LIF	AJ	N/A	None	N,O	--	10%	5000 m/s	0.5 mm	--	--	113
Velocity	LIF	UJ	5	I_2	I_2	--	2%	718 m/s	--	15 min	N/A	114
Velocity	LIF	AJ	2	None	None	5%	--	4000 m/s	0.5-3 mm	100 ns	180 sec	394
Velocity	Absorption	ST	N/A	None	K	--	4.5%	4450 m/s	Integrated	100 us	10 kHz	26

Table 10.3 Summary of some velocity measurement techniques' specifications.

References

[1] Slotnick, J., Khodadoust, A., Alonso, J., Darmofal, D., Gropp, W., Lurie, E. and Mavriplis, D., 2014. CFD Vision 2030 Study: A Path to Revolutionary Computational Aerosciences.

[2] Lu, F. K., and Marren, D. E., eds. *Advanced hypersonic test facilities*. Vol. 198. AIAA, 2002.

[3] Chazot, O. and Panerai, F., 2014. High-enthalpy facilities and plasma wind tunnels for aerothermodynamics ground testing. Hypersonic Nonequilibrium Flows: Fundamentals and Recent Advances, p.329.

[4] Davidson, D. F. and Hanson, R. K., 2004. Interpreting shock tube ignition data. *International Journal of Chemical Kinetics*, *36*(9), pp.510-523.

[5] Wagner, J. L., Beresh, S. J., Kearney, S. P., Trott, W. M., Castaneda, J. N., Pruett, B. O. and Baer, M. R., 2012. A multiphase shock tube for shock wave interactions with dense particle fields. *Experiments in fluids*, *52*(6), pp.1507-1517.

[6] Sharma, S. P. and Park, C., 1990. Operating characteristics of a 60-and 10-cm electric arc-driven shock tube. I-The driver. II-The driven section. *Journal of Thermophysics and Heat Transfer*, *4*(3), pp.259-265.

[7] Stalker, R. J., 1966. The free-piston shock tube. *The Aeronautical Quarterly*, *17*(4), pp.351-370.

[8] Vincenti, W. G. and Kruger, C. H., 1965. Introduction to physical gas dynamics (Vol. 246). New York: Wiley.

[9] Anderson Jr, J. D., 2006. Hypersonic and high-temperature gas dynamics. American Institute of Aeronautics and Astronautics.

[10] Hollis, B. R. "Real-gas flow properties for NASA Langley Research Center aerothermodynamic facilities complex wind tunnels." NASA CR-4755 (1996).

[11] Bathel, B. F., Danehy, P. M., Cutler, A. D., "Molecular-based optical measurement techniques for transition and turbulence in high-speed flow," Von Karman Institute Lecture Series Manuscript, Brussels Belgium, May 27-31, 2013.

[12] Danehy, P. M., Bathel, B. F., Johansen, C., Cutler, A. D., Hurley, S., "Spectroscopic Measurement Techniques for Aerospace Flows," Von Karman Institute Lecture Series Manuscript, Brussels Belgium, May 12-16, 2014.

[13] Danehy, P. M., Bathel, B. F., Johansen, C., Winter, M., Cutler, A. D., O'Byrne, S., "Molecular-based optical measurement techniques for Nonequilibrium Hypersonic Flows," book chapter in AIAA Progress Series Book, Vol. 247, entitled " Hypersonic Nonequilibrium Flows", edited by Eswar Josyula, published May, 2015.

[14] Zhou, X., Liu, X., Jeffries, J. B., and Hanson, R. K., "Development of a sensor for temperature and water concentration in combustion gases using a single tunable diode laser," *Measurement Science and Technology*, Vol. 14, No. 8, 2003, pp. 1459–1468.

[15] Zhou, X., Jeffries, J. B., and Hanson, R. K., "Development of a fast temperature sensor for combustion gases using a single tunable diode laser," *Applied Physics B*, Vol. 81, No. 5, 2005, pp. 711-722.

[16] Vallon, R., Soutadé, J., Vérant, J. -L., Meyers, J., Paris, S., and Mohamed, A., "A Compact Tunable Diode Laser Absorption Spectrometer to Monitor CO_2 at 2.7 µm Wavelength in Hypersonic Flows," *Sensors*, 10:6081–6091, June 2010.

[17] Meyers, J. M. and Fletcher, D., "Diode Laser Absorption Sensor Design and Qualification for CO_2 Hypersonic Flows," *Journal of Thermophysics and Heat Transfer*, Vol. 25, No. 2, 2011, pp. 193-200.

[18] Meyers, J. M., Paris, S., and Fletcher, D. G., "Characterization of CO_2 flow in a hypersonic impulse facility using DLAS," *Experiments in Fluids*, 57:25, February 2016.

[19] Wehe, S. D., Baer, D. S., and Hanson, R. K., "Tunable diode-laser absorption measurements of temperature, velocity, and H_2O in hypervelocity flows," *33rd Joint Propulsion Conference and Exhibit*. American Institute of Aeronautics and Astronautics, October 1997.

[20] Parker, R. A., Wakeman, T., MacLean, M., and Holden, M., "Nitric Oxide Concentration Measurements with a Quantum Cascade Laser in the LENS I Hypersonic Shock Tunnel Facility," *44th AIAA Aerospace Sciences Meeting and Exhibit*. American Institute of Aeronautics and Astronautics, January 2006.

[21] Parker, R. A., Wakeman, T., MacLean, M., and Holden, M., "Measuring Nitric Oxide Freestream Velocity Using Quantum Cascade Lasers at CUBRC," *45th AIAA Aerospace Sciences Meeting and Exhibit*. American Institute of Aeronautics and Astronautics, January 2007.

[22] Mohamed, A., Rosier, B., Henry, D., Louvet, Y., and Varghese, P. L., "Tunable Diode Laser Measurements on Nitric Oxide in a Hypersonic Wind Tunnel," *AIAA Journal*, Vol. 34, No. 3, 1996, pp. 494-499.

[23] Mohamed, A. K., Henry, D., Bize, D., and Beck, W. H., "Infrared diode laser absorption measurements in the HEG free stream flow," *20th AIAA Advanced Measurement and Ground Testing Technology Conference*. American Institute of Aeronautics and Astronautics, October 1998.

[24] Mohamed, A. K., Henry, D., Faléni, J. P., Sagnier, P., Soutadé, J. , Beck, W. H., and Martinez Schramm, J., "Infrared Diode Laser Absorption Spectroscopy Measurements in the S4MA, F4 and HEG Hypersonic Flows," *International Symposium on Atmospheric Reentry Vehicles and Systems*, 1999.

[25] Wehe, S. D., Baer, D. S., Hanson, R. K., and Chadwick, K. M., "Measurements of Gas Temperature and Velocity in Hypervelocity Flows using Diode-Laser Sensors," *20th AIAA Advanced Measurement and Ground Testing Technology Conference*. American Institute of Aeronautics and Astronautics, October 1998.

[26] Wehe, S. D., Baer, D. S., and Hanson, R. K., "Diode-Laser Sensor for Velocity Measurements in Hypervelocity Flows," *AIAA Journal*, Vol. 37, No. 8, 1999, pp. 1013-1015.

[27] Chang, L. S., Strand, C. L., Jeffries, J. B., Hanson, R. K., Diskin, G. S., Gaffney, R. L., and Capriotti, D. P., "Supersonic Mass-Flux Measurements via Tunable Diode Laser Absorption and Nonuniform Flow Modeling," *AIAA Journal*, Vol. 49, No. 12, 2011, pp. 2783-2791.

[28] Busa, K. M., Ellison, E. N., McGovern, B. J., McDaniel, J. C., Diskin, G. S., DePiro, M. J., Capriotti, D. P., and Gaffne,y R. L., "Measurements on NASA Langley Durable Combustor Rig by TDLAT: Preliminary Results," *51st AIAA Aerospace Sciences Meeting*. American Institute of Aeronautics and Astronautics, January 2013.

[29] Schultz, I. A., Goldenstein, C. S., Jeffries, J. B., Hanson, R. K., Rockwell, R. D., and Goyne, C. P., "Spatially Resolved Water Measurements in a Scramjet Combustor Using Diode Laser Absorption," *Journal of Propulsion and Power*, Vol. 30, No. 6, 2014, pp. 1551-1558.

[30] Busa, K. M., Rice, B. E., McDaniel, J. C., Goyne, C. P., Rockwell, R. D., Fulton, J. A., Edwards, J. R., and Diskin, G. S., "Scramjet Combustion Efficiency Measurement via Tomographic Absorption Spectroscopy and Particle Image Velocimetry," *AIAA Journal*, Vol. 54, No. 8, August 2016, pp. 2463—2471.

[31] Hanson, R. K., "Shock tube spectroscopy: advanced instrumentation with a tunable diode laser," *Applied Optics*, Vol. 16, No. 6, 1977, pp. 1479-1481.

[32] Philippe, L. C., and Hanson, R. K., "Laser-absorption mass flux sensor for high-speed airflows," *Optics Letters*, Vol. 16, No. 24, 1991, pp. 2002-2004.

[33] Philippe, L. C., and Hanson, R. K., "Laser diode wavelength-modulation spectroscopy for simultaneous measurement of temperature, pressure, and velocity in shock-heated oxygen flows," *Applied Optics*, Vol. 32, No. 30, 1993, pp. 6090-6103.

[34] Arroyo, M. P., Langlois, S., and Hanson, R. K., "Diode-laser absorption technique for simultaneous measurements of multiple gasdynamic parameters in high-speed flows containing water vapor," *Applied Optics*, Vol. 33, No. 15, 1994, pp. 3296-3307.

[35] Nagali, V., Herbon, J. T., Horning, D. C., Davidson, D. F., and Hanson, R. K., "Shock-tube study of high-pressure H_2O spectroscopy," *Applied Optics*, Vol. 38, No. 33, 1999, pp. 6942-6950.

[36] Strand, C. L. and Hanson, R. K., "Thermometry and Velocimetry in Supersonic Flows via Scanned Wavelength-Modulation Absorption Spectroscopy," *47th AIAA/ASME/SAE/ASEE Joint Propulsion Conference & Exhibit*. American Institute of Aeronautics and Astronautics, July 2011.

[37] Lin, X., Yu, X. L., Li, F., Zhang, S. H., Xin, J. G., and Chang, X. Y., "CO concentration and temperature measurements in a shock tube for Martian mixtures by coupling OES and TDLAS," *Applied Physics B*, Vol. 110, No. 3, 2013, pp. 401-409.

[38] Schultz, I. A., Goldenstein, C. S., Strand, C. L., Jeffries, J. B., Hanson, R. K., and Goyne, C.P., "Hypersonic Scramjet Testing via Diode Laser Absorption in a Reflected Shock Tunnel," *Journal of Propulsion and Power*, Vol. 30, No. 6, 2014, pp. 1586-1594.

[39] Strand, C. L. and Hanson, R. K., "Quantification of Supersonic Impulse Flow Conditions via High-Bandwidth Wavelength Modulation Absorption Spectroscopy," AIAA Journal, Vol. 53, No. 10, 2015, pp. 2978-2987.

[40] Herzberg, G., "Molecular Spectroscopy: A Personal History," *Annual Review of Physical Chemistry*, Vol. 36, No. 1, 1985, pp. 1-31.

[41] Reid, J., Shewchun, J., Garside, B. K., and Ballik, E. A., "High sensitivity pollution detection employing tunable diode lasers," *Applied Optics*, Vol. 17, No. 2, 1978, pp. 300-307.

[42] Mohamed, A. K., Vérant, J. -L., and Soutadé, J., "Infrared Diode Laser Absorption Spectroscopic Characterization of the Free-Stream in the F4 Wind Tunnel," ICIASF 2001 Record, *19th International Congress on Instrumentation in Aerospace Simulation Facilities*, 2001, pp. 302—308.

[43] Upschulte, B. L., Miller, M. F., and Allen, M. G., "Diode Laser Sensor for Gasdynamic Measurements in a Model Scramjet Combustor," *AIAA Journal*, Vol. 38, No. 7, 2000, pp. 1246-1252.

44 Lindstrom, C. D., Jackson, K. R., Williams, S., Givens, R., Bailey, W. F., Tam, C. -J., and Terry, W. F., "Shock-Train Structure Resolved with Absorption Spectroscopy Part 1: System Design and Validation," *AIAA Journal*, Vol. 47, No. 10, 2009, pp. 2368-2378.

45 Gordon, I. E., Rothman, L. S., Hill, C., Kochanov, R. V., Tan, Y., Bernath, P. F., Birk, M., Boudon, V., Campargue, A., Chance, K. V., Drouin, B. J., Flaud, J. -M., Gamache, R. R., Hodges, J. T., Jacquemart, D., Perevalov, V. I., Perrin, A., Shine, K. P., Smith, M. -A. H., Tennyson, J., Toon, G. C., Tran, H., Tyuterev, V. G., Barbe, A., Csszr, A. G., Devi, V. M., Furtenbacher, T., Harrison, J. J., Hartmann, J. -M., Jolly, A., Johnson, T. J., Karman, T., Kleiner, I., Kyuberis, A. A., Loos, J., Lyulin, O. M., Massie, S. T., Mikhailenko, S. N., Moazzen-Ahmadi, N., Mller, H. S. P., Naumenko, O. V., Nikitin, A. V., Polyansky, O. L., Rey, M., Rotger, M., Sharpe, S. W., Sung, K., Starikova, E., Tashkun, S. A., Vander Auwera, J., Wagner, G., Wilzewski, J., Wciso, P., Yu, S., and Zak, E. J., "The HITRAN2016 molecular spectroscopic database," *Journal of Quantitative Spectroscopy and Radiative Transfer*, 203, pp. 3-69, 2017. HITRAN2016 Special Issue.

46 Rothman, L. S., Gordon, I. E., Barber, R. J., Dothe, H., Gamache, R. R., Goldman, A., Perevalov ,V. I., Tashkun, S. A., and Tennyson, J., "HITEMP, the high-temperature molecular spectroscopic database," *Journal of Quantitative Spectroscopy & Radiative Transfer*, 111, pp. 2139-2150, October 2010.

47 Mihalcea, R. M., Webber, M. E., Baer, D. S., Hanson, R. K., Feller, G. S., and Chapman, W. B., "Diode-laser absorption measurements of CO_2 , H_2O, N_2O, and NH_3 near 2.0 μm," *Applied Physics B*, 67(3):283–288, Sep 1998.

48 Farooq, A., Jeffries, J. B., and Hanson, R. K., "CO_2 concentration and temperature sensor for combustion gases using diode-laser absorption near 2.7 μm," *Applied Physics B*, Vol. 90, No. 3, 2008, pp. 619-628.

49 Werle, P., "A review of recent advances in semiconductor laser based gas monitors," S*pectrochimica Acta Part A: Molecular and Biomolecular Spectroscopy*, Vol. 54, No. 2, 1998, pp. 197-236.

50 Meyers, J., "Tunable Diode Laser Absorption Spectroscopy Characterization of Impulse Hypervelocity CO_2 Flows," PhD Thesis, Universit Libre de Bruxelles, 2009.

51 Sanders, S. T., Mattison, D. W., Jeffries, J. B., and Hanson, R. K., "Rapid temperature tuning of a 1.4- μm diode laser with application to high-pressure H_2O absorption spectroscopy," *Optics Letters*, Vol. 26, No. 20, 2001, pp. 1568-1570.

52 Krishna, Y., O'Byrne, S., and Kurtz, J. J., "Baseline correction for stray light in log-ratio diode laser absorption measurements," *Applied Optics*, Vol. 53, No. 19, 2014, pp. 4128-4135.

53 Li, H., Rieker, G. B., Liu, X., Jeffries, J. B., and Hanson, R. K., "Extension of wavelength-modulation spectroscopy to large modulation depth for diode laser absorption measurements in high-pressure gases," *Applied Optics*, Vol. 45, No. 5, February 2006.

54 Rieker, G. B., Jeffries, J. B., and Hanson, R. K., "Calibration-free wavelength-modulation spectroscopy for measurements of gas temperature and concentration in harsh environments," *Applied Optics*, 48:5546–60, Oct 2009.

55 Sun, K., Chao, X., Sur, R., Goldenstein, C. S., Jeffries, J. B., and Hanson, R. K., "Analysis of calibration-free wavelength-scanned wavelength modulation spectroscopy for practical gas sensing using tunable diode lasers," *Measurement Science and Technology*, Vol. 24, No. 12, 2013, 125203.

56 Louviot, M., Suas-David, N., Boudon, V., Georges, R., Rey, M., and Kassi, S., "Strong thermal nonequilibrium in hypersonic CO and CH_4 probed by CRDS," *The Journal of Chemical Physics*, Vol. 142, No. 21, 2015,214305.

57 Nations, M., Wang, S, Goldenstein, C. S., Sun, K., Davidson, D. F., Jeffries, J. B., and Hanson, R. K., "Shock-tube measurements of excited oxygen atoms using cavity-enhanced absorption spectroscopy," *Applied Optics*, Vol. 54, No. 29, 2015, pp. 8766-8775.

58 Li, F., Yu, X., Gu, H., Li, Z., Zhao, Y., Ma, L., Chen, L., and Chang, X., "Simultaneous measurements of multiple flow parameters for scramjet characterization using tunable diode-laser sensors," *Applied Optics*, Vol. 50, No. 36, 2011, pp. 6697-6707.

59 Weisberger, J. M., DesJardin, P. E., MacLean, M., Parker, R., and Carr, Z., "Near-Surface Carbon-Dioxide Tunable Diode Laser Absorption Spectroscopy Concentration Measurements in Hypervelocity Flow," *Journal of Spacecraft and Rockets*, Vol. 52, No. 6, 2015, pp. 1551-1562.

60 Krishna, Y., O'Byrne, S., Wittig, S., and Kurtz, J. J., "Numerically Determining Mach Number and Orientation in Hypersonic Inlets Using Absorption Spectroscopy," *Journal of Propulsion and Power*, Vol. 31, No. 1, 2015, pp. 123-132.

[61] Ma, L., Li, X., Sanders, S. T., Caswell, A. W., Roy, S., Plemmons, D. H., and Gord, J. R., "50-kHz-rate 2D imaging of temperature and H_2O concentration at the exhaust plane of a J85 engine using hyperspectral tomography," *Optics Express*, Vol. 21, No. 1, 2013, pp. 1152-1162.

[62] Meyers, J. M. and Fletcher, D. G., "Development of Diode Laser Absorption Instrument for Free Stream Measurements in Hypervelocity CO_2 Flows," *45th AIAA Aerospace Sciences Meeting and Exhibit*. American Institute of Aeronautics and Astronautics, January 2007.

[63] Meyers, J. M., Paris, S., and Fletcher, D. G., "Development of Diode Laser Absorption Instrument for Free Stream Measurements in Hypervelocity CO_2 Flows," *26th AIAA Aerodynamic Measurement Technology and Ground Testing Conference*. American Institute of Aeronautics and Astronautics, 2008.

[64] Meyers, J. M., Paris, S., and Fletcher, D. G., "Diode Laser Absorption Measurements of Free Stream Hypervelocity CO_2 Flow at 1.6 μm," *41st AIAA Thermophysics Conference*. American Institute of Aeronautics and Astronautics, October 2009.

[65] Mohamed, A. K. and Lefebvre, M., "Laser Absorption Spectroscopy to Probe Chemically Reacting Flows," *AerospaceLab*, 2009, pp. 1–12.

[66] Cai, T., Gao, G., Chen, W., Liu, G., and Gao, X. "Simultaneous Measurements of CO 2 and CO Using a Single Distributed-Feedback (DFB) Diode Laser Near 1.57 μm at Elevated Temperatures," *Applied Spectroscopy*, Vol. 65, No. 1, 2011, pp. 108-112.

[67] Spearrin, R. M., Goldenstein, C. S., Schultz, I. A., Jeffries, J. B., and Hanson, R. K., "Simultaneous sensing of temperature, CO, and CO_2 in a scramjet combustor using quantum cascade laser absorption spectroscopy," *Applied Physics B*, Vol. 117, No. 2, 2014, pp 689-698.

[68] MacDonald, M. E., Brandis, A. M., and Cruden, B. A., "Temperature and CO Number Density Measurements in Shocked CO and CO_2 via Tunable Diode Laser Absorption Spectroscopy," *2018 Joint Thermophysics and Heat Transfer Conference*. American Institute of Aeronautics and Astronautics, October 2018.

[69] Chen, J., Hangauer, A., Strzoda, R., and Amann, M.-C., "VCSEL-based calibration-free carbon monoxide sensor at 2.3 μ m with in-line reference cell," *Applied Physics B*, Vol. 102, No. 2, 2011, pp. 381-389.

[70] Sagnier, P. and Verant, J.-L., "Flow Characterization in the ONERA F4 High-Enthalpy Wind Tunnel," *AIAA Journal*, Vol. 36, No. 4, 1998, pp. 522-531.

[71] Chao, X., Jeffries, J. B., and Hanson, R. K., "Wavelength-modulation-spectroscopy for real-time, in situ NO detection in combustion gases with a 5.2 μm quantum-cascade laser," *Applied Physics B*, Vol. 106, No. 4, 2012, pp. 987-997.

[72] Lindstrom, C., Tam, C.-J., Davis, D., Eklund, D., and Williams, S., "Diode Laser Absorption Tomography of Two Dimensional Supersonic Flow," *43rd AIAA/ASME/SAE/ASEE Joint Propulsion Conference and Exhibit*. American Institute of Aeronautics and Astronautics, 2007.

[73] Lyle, K. H., Jeffries, J. B., and Hanson, R. K., "Diode-Laser Sensor for Air-Mass Flux 1: Design and Wind Tunnel Validation," *AIAA Journal*, Vol. 45, No. 9, 2007, pp. 2204-2212.

[74] Busa, K. M., Bryner, E., McDaniel, J. C., Goyne, C. P., Smith, C. T., and Diskin, G. S., "Demonstration of Capability of Water Flux Measurement in a Scramjet Combustor using Tunable Diode Laser Absorption Tomography and Stereoscopic PIV," *49th AIAA Aerospace Sciences Meeting*. American Institute of Aeronautics and Astronautics, January 2011.

[75] Krishna, Y., Sheehe, S. L., and O'Byrne, S., "Detection of Spatial Variation in Hypersonic Nozzle Flow Using Diode Laser Spectroscopy," *AIAA Journal*, Vol. 56, No. 7, 2018, pp. 2930-2935.

[76] Zhang, F. -Y., Komurasaki, K., Iida, T., and Fujiwara, T., "Diagnostics of an argon arcjet plume with a diode laser," *Applied Optics*, Vol. 38, No. 9, 1999, pp. 1814-1822.

[77] Mattison, D. W., Oehlschlaeger, M. A., Jeffries, J. B., and Hanson, R. K., "Pulse Detonation Tube Characterization using Laser Absorption Spectroscopy," *41st Aerospace Sciences Meeting and Exhibit*. American Institute of Aeronautics and Astronautics, 2003.

[78] Nations, M., Chang, L. S., Jeffries, J. B., Hanson, R. K., MacDonald, M. E., Nawaz, A., Taunk, J. S. T., Gökçen, T., and Raiche, G., "Characterization of a Large-Scale Arcjet Facility Using Tunable Diode Laser Absorption Spectroscopy," *AIAA Journal*, Vol. 55, No. 11, 2017, pp. 3757-3766.

[79] Beck, W. H., "Spectroscopic Techniques for Measurement of Velocity and Temperature in the DLR High Enthalpy Shock Tunnel HEG," *Technical Report ADP010746*, Institute of Fluid Mechanics, German Aerospace Center (DLR), 2000.

80 Meyers, J., "Tunable Diode Laser Absorption Spectroscopy Characterization of Impulse Hypervelocity CO_2 Flows," PhD Thesis, Université libre de Bruxelles, 2009.

81 Johansen, C., Danehy, P., Ashcraft, S., Bathel, B., Inman, J., and Jones, S., "Planar laser-induced fluorescence of Mars Science Laboratory Reaction Control System jets," *Journal of Spacecraft and Rockets*, Vol. 50, 2013, pp. 781-792, doi:10.2514/1.A32214.

82 Arisman, C., Johansen, C. T., Bathel, B., and Danehy, P., "Investigation of gas seeding for planar laser-induced fluorescence in hypersonic boundary layers," *AIAA Journal*, Vol. 53, No. 12, 2015, pp. 3637-3651, DOI 10.2514/1.J053892.

83 Johansen, C. T., Lincoln. D, Bathel, B., Inman, J., and Danehy, P., "Simultaneous nitric oxide / atomic oxygen laser-induced fluorescence in an arc jet facility," *Thermophysics and Heat Transfer*, Vol. 30, No. 4, 2016, pp. 912-918 DOI 10.2514/1.T4691.

84 Takayanagi, H., Mizuno, M., Fujii, K., Suzuki, T., Fujita, K., "Arc heated wind tunnel flow diagnostics using laser-induced fluorescence of atomic species" AIAA 2009-1449, *47th AIAA Aerospace Sciences Meeting*, Orlando FL, 2009.

85 Balla, J., "Iodine tagging velocimetry and mechanism in the hypersonic near wake of a multipurpose crew vehicle," NASA/TM-2013-218027, 2013.

86 Grinstead, J. H., Driver, D., and Raiche, G., "Radial profiles of arcjet flow properties measured with laser-induced fluorescence of atomic nitrogen," AIAA 2003-400, *41st Aerospace Sciences Meeting*, Reno, NV, 2003.

87 Gamba, M., Miller, V. A., Mungal, M. G., and Hanson, R. K., "Temperature and number density measurements in non-uniform supersonic flowfields undergoing mixing using toluene PLIF thermometry," *Applied Physics B,* Vol. 120, 2015, pp. 285-304.

88 Eckbreth, A. C., "Laser diagnostics for combustion temperature and species," *Combustion Science & Technology Book Series*, Vol 3, CRC Press, 1996.

89 Palma, P. C., "Laser induced fluorescence imaging in free piston shock tunnels," Ph.D. thesis, Australian National University, 1999.

90 Lam, K-Y., Pickles, J. D., Narayanaswamy, V., Carter, C. D., and Kimmel, R. L., "High-Speed Schlieren and 10-Hz Kr PLIF for the new AFRL Mach-6 Ludwieg Tube Hypersonic Wind Tunnel," AIAA 2017-0550, *55th AIAA Aerospace Sciences Meeting*, Grapevine, TX, 2017.

91 Jiang, N., Bruzzese, J., Patton, R., Sutton, F., Yentsch, R., Gaitonde, D. V., Lempert, W. R., Miller, J. D., Meyer, T. R., Parker, R., Wadham, T., Holden, M., and Danehy, P. M., "NO PLIF imaging in the CUBRC 48-inch shock tunnel," *Experiments in Fluids*, Vol. 53, 2012, pp. 1637-1646.

92 O'Byrne, S., Danehy, P. M., and Houwing, A. F. P., "Investigation of hypersonic nozzle flow uniformity using NO fluorescence," *Shock Waves,* Vol. 15, No. 2, 2006, pp. 81–87, doi:10.1007/s00193-006-0013-6.

93 McRae, C. D., Johansen, C. T., Danehy, P. M., Gallo, E. C. A., Cantu, L. M. L., Cutler, A. D., Rockwell, R. D., Goyne, C. P., and McDaniel, J. C., "Image Analysis of Hydroxyl-Radical Planar Laser-Induced Fluorescence in Turbulent Supersonic Combustion", *Journal of Propulsion and Power*, Vol. 32, No. 3, 2016, pp. 542-559.

94 Inman, J., Bathel, B., Johansen, C., Danehy, P., Jones, S., Gragg, J., and Splinter, S., "Nitric oxide planar laser-induced fluorescence measurements in the Hypersonic Materials Environment Test System," *AIAA Journal*, Vol. 51, No. 10, 2013, pp. 2365-2379, doi:10.2514/1.J052246

95 Beck, W. H., Trinks, O., Wollenhaupt, M., Mohamed, A., Niederbäumer, C., Andresen, P., Kishimoto, T., and Bito, H., "Probing of the reservoir, free stream and shock layers in HEG using spectroscopic techniques," *21st International Symposium on Shock Waves*, Great Keppel Island, Australia, July 20-25, 1997.

96 Sanchez-Gonzalez, R., Bowersox, R. D. W., and North, S. W., "Simultaneous velocity and temperature measurements in gaseous flowfields using vibrationally excited nitric oxide monitoring technique: a comprehensive study," *Applied Optics*, Vol. 51, No. 9, 2012, pp. 1216-1228.

97 Cecil, E., and McDaniel, J. C., "Planar velocity and temperature measurements in rarefied hypersonic flow using iodine LIF," AIAA Paper 2005-4695, *38th AIAA Thermophysics Conference*, Toronto, Canada, June 6-9, 2005

98 McDougall, C., Hinman, W. S., Johansen, C. T., Bathel, B., Inman, J., and Danehy, P., "Nitric oxide planar laser-induced fluorescence thermometry in a hypersonic boundary layer," AIAA 2018-3629, *AIAA Aviation*, Atlanta, GA., 2018 doi:10.2514/6.2018-3629.

99 Palma, P., Danehy, P., Houwing, A. F. P., "Fluorescence imaging of rotational and vibrational temperature in shock-tunnel nozzle flow," *AIAA Journal,* Vol. 41, No. 9, 2003, pp. 1722-1732.

[100] Gnoffo, P. A., Gupta, R. N., and Shinn, J. L., "Conservations equations and physical models for hypersonic air flows in thermal and chemical nonequilibrium," *NASA Technical Paper 2867*, 1989, pp. 1-58.

[101] Takayanagi, H., Kato, S., Sakai, T., Mizuno, M., Fujii, K., Fujita, K., Matsui, M., and Yamagiwa, Y., "Translational temperature distribution measurements in high enthalpy flows by laser-induced fluorescence," AIAA 2013-0741, *51st AIAA Aerospace Sciences Meeting*, Grapevine, TX, 2013.

[102] Rossmann, T., Mungal, M. G., and Hanson, R., "Nitric-oxide planar laser-induced fluorescence applied to low-pressure hypersonic flow fields for the imaging of mixture fraction," *Applied Optics,* Vol. 42, No. 33, 2003, pp. 6682-6695.

[103] Gamba, M., Miller, V. A., Mungal, M. G., and Hanson, R. K., "Temperature and number density measurement in non-uniform supersonic flowfields undergoing mixture using toluene PLIF thermometry," *Applied Physics B*, Vol. 120, 2015, pp. 285-304.

[104] McDougall, C. C., Hinman, W. S., Johansen, C. T., Bathel, B. F., Inman, J. A., and Danehy, P. M., "Quantitative analysis of planar laser-induced fluorescence measurements in a hypersonic boundary layer," *19th International Symposium on the Application of Laser and Imaging Techniques to Fluid Mechanics*, Lisbon, Portugal, 2018.

[105] Balla, J., and Everhart, J. L., "Air density measurements in a Mach 10 wake using iodine Cordes bands," *AIAA Journal*, Vol. 50, No. 6, 2012, pp. 1388-1397.

[106] Fletcher, D. G., and McDaniel, J. C., "Laser-induced iodine fluorescence technique for quantitative measurement in a nonreacting supersonic combustor," *AIAA Journal,* Vol. 27, No. 5, 1989, pp. 575-580.

[107] Narayanaswamy, V., Burns, R., and Clemens, N. T., "Kr-PLIF for scaling imaging in supersonic flows," *Optic Letters,* Vol. 36, No. 21, 2011, pp. 4185-4187.

[108] Lachney, E. R., and Clemens, N. T., "PLIF imaging of mean temperature and pressure in a supersonic bluff wake," *Experiments in Fluids,* Vol. 24, 1998, pp. 354-363.

[109] Lemoine, F., and Leporcq, B., "An efficient optical pressure measurement in compressible flows: laser-induced iodine fluorescence," *Experiments in Fluids,* Vol. 19, 1995, pp. 150-158.

[110] Hiller, B., and Hanson, R. K., "Simultaneous planar measurements of velocity and pressure fields in gas flows using laser-induced fluorescence," *Applied Optics,* Vol. 27, No. 1, 1988, pp. 33-48.

[111] Danehy, P. M., Mere, P., Gaston, M. J., O'Byrne, S., Palma P. C., and Houwing, A. F. P., "Fluorescence velocimetry of the hypersonic, separated flow over a cone," *AIAA Journal,* Vol. 39, No. 7, 2001, pp. 1320-1328.

[112] Hruschka, R., O'Byrne, S., and Kleine, H., "Two-component Doppler-shift fluorescence velocimetry applied to a generic planetary entry probe model," *Experiments in Fluids,* Vol. 48, 2010, pp. 1109-1120.

[113] Suess, L. E., Milhoan, J. D., Oelke, L., Godfrey, D., Larin, M. Y., Scott, C. D., Grinstead, J. H., and Del Papa, S., "Enthalpy distributions of arc jet flow based on measured laser induced fluorescence, heat flux and stagnation pressure distributions," AIAA Paper 2011-3778, *42nd AIAA Thermophysics Conference*, Honolulu Hawaii, June 27-30, 2011.

[114] McDaniel, J. C., Hiller, B., and Hanson, R. K., "Simultaneous multiple-point velocity measurements using laser-induced iodine fluorescence," *Optics Letters*, Vol. 8, No. 1, 1983, pp. 51-53.

[115] Koochesfahani, M. M. and Nocera, D. G., "Molecular Tagging Velocimetry," *Handbook of Experimental Fluid Dynamics*, Chapter 5.4, editors: J. Foss, C. Tropea and A. Yarin, Springer-Verlag, 2007.

[116] Koochesfahani, M. M., "Special Feature: Molecular Tagging Velocimetry," *Meas. Sci. Technol.*, Vol. 11, No. 9, 2000, pp. 1235-1300.

[117] R.E. Falco, D. G. Nocera: Quantitative multipoint measurements and visualization of dense solid-liquid flows using laser induced photochemical anemometry (LIPA). In: *Particulate Two-Phase Flow*, ed. by M.C. Rocco (Butterworth-Heinemann, London 1993), pp. 59–126.

[118] Koochesfahani, M. M., Cohn, R. K., Gendrich, C. P., Nocera, D. G., "Molecular tagging diagnostics for the study of kinematics and mixing in liquid phase flows," *Proc. Eighth Int. Symp. Appl. Laser Tech. Fluids Mech.* Lisbon, Vol. I (1996) 1–12.

[119] Koochesfahani, M. M., "Molecular tagging velocimetry (MTV): Progress and applications," AIAA Paper, Vol. 1999-3786 (1999).

[120] Lempert, W. R., Harris, S. R., "Molecular tagging velocimetry," In: *Flow Visualization – Techniques and Examples*, ed. by A.J. Smits, T.T. Lim (Imperial College Press, London 2000) pp. 73–92.

[121] Danehy, P. M., Bathel, B. F., Calvert, N. D., Dogariu, A., and Miles, R. B., "Three component velocity and acceleration measurement using FLEET," AIAA-2014-2228, *30th AIAA Aviation Conference*, Atlanta, GA, June 16–20 (2014).

[122] Matos P. S., Barreta L. G., Martins C. A., "Velocity and NO-Lifetime Measurements in an Unseeded Hypersonic Air Flow," *ASME. J. Fluids Eng.*, Vol. 140, No. 12, 2018, 121105-1-121105-8. doi:10.1115/1.4039863.

[123] Gendrich, C. P., Bohl, D. G., Koochesfahani, M. M., "Whole-field measurements of unsteady separation in a vortex ring/wall interaction," AIAA Paper, Vol. 97-1780 (1997).

[124] Miller S., "Photochemical reaction for the study of velocity patterns and profiles. B.A.Sc. Thesis (University of Toronto, Ontario 1962).

[125] Popovich, A. T., Hummel, R. L., "A new method for nondisturbing turbulent flow measurement very close to a wall," *Chem. Eng. Soc.*, Vol. 22, 1967, pp. 21-25.

[126] Frantisak, F., Palade de Iribarne, A., Smith, J. W., Hummel, R. L., "Nondisturbing tracer technique for quantitative measurements in turbulent flows," *Ind. Eng. Chem. Fund.*, Vol. 8, 1969, pp. 160-167.

[127] Hummel, R. L., "Nondisturbing flow measurement using a photochromic tracer technique. High speed photography," *Proc. SPIE,* Vol. 97, 1976, pp. 302-307.

[128] Ojha, M., Cobbold, R. S. C., Johnston, K. W., Hummel, R., "Pulsatile flow through constricted tubes: an experimental investigation using photochromic tracer methods," *J. Fluid Mech.*, Vol. 203, 1989, pp. 173-197.

[129] Littleton, B. N., Bishop, A. I., McIntyre, T. J., Barker, P. F., and Rubinsztein-Dunlop, H., "Flow tagging velocimetry in a superorbital expansion tube," *Shock Waves*, Vol. 10, No. 3, pp. 225-228.

[130] Falco, R. E., Chu, C. C., "Measurement of two-dimensional fluid dynamic quantities using a photochromic grid tracing technique," *Proc. SPIE,* Vol. 814, 1987, pp. 706-710.

[131] Miles, R., Cohen, C., Conners, J., Howard, P., Huang, S., Markovitz, E., Russell, G., "Velocity measurements by vibrational tagging and fluorescent probing of oxygen," *Opt. Lett.,* Vol. 12, No. 11, 1987, pp. 861-863.

[132] Miles, R. B., Connors, J. J., Markovitz, E. C., Howard, P. J., Roth, G. J., "Instantaneous profiles and turbulence statistics of supersonic free shear layers by Raman Excitation plus Laser-Induced Electronic Fluorescence (RELIEF) velocity tagging of oxygen," *Exp. Fluids,* Vol. 8, 1989, pp. 17-24.

[133] Miles, R. B., Connors, J., Markovitz, E., Howard, P., Roth, G., "Instantaneous supersonic velocity profiles in an underexpanded sonic air jet by oxygen flow tagging," *Phys. Fluids,* Vol. 1, No. 2, 1989, pp. 389-393.

[134] Miles, R. B., Zhou, D., Zhang, B., Lempert, W. R., She, Z. S., "Fundamental turbulence measurements by RELIEF flow tagging," *AIAA Journal*, Vol. 31, No. 3, 1993, pp. 447-452.

[135] Miles, R. B., Lempert, W. R., "Quantitative flow visualization in unseeded flows," *Ann. Rev. Fluid Mech.*, Vol. 29, 1997, pp. 285-326.

[136] Miles, R. B., Grinstead, J., Kohl, R. H., and Diskin, G., *"The RELIEF flow tagging technique and its application in engine testing facilities and for helium-air mixing studies*," *Measurement Science and Technology*, Vol. 11, No. 9, 2000, pp. 1272-1281.

[137] Webster, M. C., and Lempert, W. R., "2009 Simplification of RELIEF velocimetry using pico-second tagging and broad band interrogation MS Thesis," The Ohio State University.

[138] Wehrmeyer, J. A., Ribarov, L. A., Oguss, D. A., Batliwala, F., Pitz, R.W., DeBarber, P.A., "Flow tagging velocimetry for low and high temperature flowfields," AIAA Paper 99-0646 (1999).

[139] Wehrmeyer, J. A., Ribarov, L. A., Oguss, D. A., Pitz, R. W., "Flame flow tagging velocimetry with 193 nm H_2O photodissociation," *Applied Optics*, Vol. 38, 1999, pp. 6912-6917.

[140] Pitz, R. W., Wehrmeyer, J. A., Ribarov, L. A., Oguss, D. A., Batliwala, F., DeBarber, P. A., Deusch, S., Dimo takis, P. E., "Unseeded molecular flow tagging in cold and hot flows using ozone and hydroxyl tagging velocimetry," *Meas. Sci. Technol.* Vol. 11, No. 9, 2000, pp. 1259-1271.

[141] Pitz, R. W., Lahr, M. D., Douglas, Z. W., Wehrmeyer, J. A., Hu, S., Carter, C. D., Hsu, K. -Y., Lum, C., Koochesfahani, M. M., "Hydroxyl tagging velocimetry in a supersonic flow over a cavity," *Applied Optics*, Vol. 44, No. 31, 2005, pp. 6692-6700.

[142] Ribarov, L. A., Wehrmeyer, J. A., Pitz, R. W., Yetter, R. A., "Hydroxyl tagging velocimetry (HTV) in experimental airflows," *Appl. Phys. B,* Vol. 74, 2002, pp. 175-183.

[143] Ribarov, L. A., Wehrmeyer, J. A., Hu, S., Pitz, R. W., "Multiline hydroxyl tagging velocimetry measurements in reacting and nonreacting experimental flows," *Exp. Fluids,* Vol. 37, 2004, pp. 65-74.

[144] Pitz, R. W., Brown, T. M., Nandula, S. P., Skaggs, P. A., DeBarber, P. A., Brown, M. S., Segall, J., "Unseeded velocity measurement by ozone tagging velocimetry," *Opt. Lett.,* Vol. 21, No. 10, 1996, pp. 755-757.

[145] Ribarov, L. A., Wehrmeyer, J. A., Batliwala, F., Pitz, R. W., DeBarber, P. A., "Ozone tagging velocimetry using narrowband excimer lasers," *AIAA Journal*, Vol. 37, No. 6, 1999, pp. 708-714.

[146] Orlemann, C., Schulz, C., Wolfrum, J., "NO-flow tagging by photodissociation of NO_2. A new approach for measuring small-scale flow structures," *Chem. Phys. Lett.,* Vol. 307, No. 1-2, 1999, pp. 15-20.

[147] Krüger, S., Grünefeld, G., "Stereoscopic flow-tagging velocimetry," *Appl. Phys. B,* Vol. 69, 1999, pp. 509-512.

[148] Krüger, S., Grünefeld, G., "Gas-phase velocity field measurements in dense sprays by laser-based flow tagging," *Appl. Phys. B*, Vol. 70, 2000, pp. 463-466.

[149] ElBaz, A. M. and Pitz, R. W., "N_2O molecular tagging velocimetry," *Appl. Phys. B* 106, 961–969 (2012).

[150] Laan, van der, W. P. N., Tolboom, R. A. L., Dam, N. J., and Meulen, ter, J. J., "Molecular tagging velocimetry in the wake of an object in supersonic flow," *Exp. Fluid*, Vol. 34, 2003, pp. 531–533.

[151] Dam, N., Klein-Douwel, R. J. H., Sijtsema, N. M., and Meulen, ter, J. J., "Nitric oxide flow tagging in unseeded air," *Opt. Lett.*, Vol. 26, 2001, pp. 36–38.

[152] Jiang, N., Nishihara, M., and Lempert, W. R., "Quantitative NO_2 molecular tagging velocimetry at 500 kHz frame rate," *Appl. Phys. Lett.*, Vol. 97, 2010, 221103.

[153] Lempert, W. R., Jiang, N., Samimy, M., "Development of molecular tagging velocimetry for high speed flows in micro systems," AIAA2002-0296, *40th AIAA Aerospace Sciences Meeting, Reno*, Nev., 14–17 January, 2002a.

[154] Lempert, W. R., Jiang, N., Sethuram, S., Samimy, M., "Molecular tagging velocimetry measurements in supersonic micro jets," *AIAA Journal*, Vol. 40, 2002b, pp. 1065–1070.

[155] Balla, R. J., "Iodine tagging velocimetry in a Mach 10 wake," *AIAA Journal*, *51*(7), pp.1783-1786, 2013.

[156] Hiller, B., Booman, R. A., Hassa, C., and Hanson, R. K., "Velocity Visualization in Gas Flows Using Laser-Induced Phosphorescence of Biacetyle," *Review of Scientific Instruments*, Vol. 55, No. 12, 1984, pp. 1964-1967.

[157] Michael, J. B., Edwards, M. R., Dogariu, A., and Miles, R. B., "Femtosecond laser electronic excitation tagging for quantitative velocity imaging in air," *Applied Optics*, Vol. 50, No. 26, 2011, pp. 5158-5162.

[158] Jiang, N., Halls, B. R., Stauffer, H. U., Danehy, P. M., Gord, J. R., and Roy, S., "Selective two-photon absorptive resonance femtosecond laser electronic excitation tagging velocimetry," *Optics Letters*, Vol. 41, No. 10, 2016, pp. 2225-2228.

[159] Jiang, N., Mance, J.G., Slipchenko, M.N., Felver, J.J., Stauffer, H.U., Yi, T., Danehy, P.M., and Roy, S., "Seedless velocimetry at 100 kHz with picosecond-laser electronic-excitation tagging," *Optics Letters*, Vol. 42, No. 2, 2017, pp. 239-242.

[160] Mills, J. L., Sukenik, C. I., and Balla, R. J., "Hypersonic Wake Diagnostics Using Laser Induced Fluorescence Techniques," *42nd AIAA Plasmadynamics and Lasers Conference*, AIAA 2011-3459, Honolulu, Hawaii, 2011. doi: 10.2514/6.2011-3459.

[161] Balla, R. J. and Everhart, J. L., "Rayleigh Scattering Density Measurements, Cluster Theory, and Nucleation Calculations at Mach 10," *AIAA Journal*, Vol. 50, No. 3, 2012, pp. 698-707. doi: 10.2514/1.J051334.

[162] Parziale, N. J., Smith, M. S., and Marineau, E. C., "Krypton tagging velocimetry of an underexpanded jet," *Applied Optics*, Vol. 54, No. 16, 2015, pp. 5094–5101. doi: 10.1364/AO.54.005094.

[163] Mustafa, M. A. and Parziale, N. J., "Simplified read schemes for krypton tagging velocimetry in N_2 and air," *Optics Letters*, Vol. 43, No. 12, 2018, pp. 2909–2912. doi: 10.1364/OL.43.002909.

[164] Zahradka, D., Parziale, N. J., Smith, M. S., and Marineau, E. C., "Krypton tagging velocimetry in a turbulent Mach 2.7 boundary layer," *Experiments in Fluids*, Vol. 57, No. 62, 2016. doi: 10.1007/s00348-016-2148-2.

[165] Mustafa, M. A., , Parziale, N. J., Smith, M. S., and Marineau, E. C., "Amplification and Structure of Streamwise-Velocity Fluctuations in Four Shock-Wave/Turbulent Boundary-Layer Interactions," *Proceedings of AIAA Aviation 2018*, AIAA-2018-3704, Atlanta, Georgia, 25-29 June 2018. doi: 10.2514/6.2018-3704.

[166] Hsu, A. G., Narayanaswamy, V., Clemens, N. T., and Frank, J. H., "Mixture fraction imaging in turbulent non-premixed flames with two-photon LIF of krypton," *Proceedings of the Combustion Institute*, Vol. 33, No. 1, 2011, pp. 759–766. doi: 10.1016/j.proci.2010.06.051.

[167] Zelenak, D. and Narayanaswamy, V., "Composition-independent mean temperature measurements in laminar diffusion flames using spectral lineshape information," *Experiments in Fluids*, Vol. 58, No. 147. Doi: 10.1007/s00348-017-2430-y.

[168] Mustafa, M. A., Parziale, N. J., Smith, M. S., and Marineau, E. C., "Nonintrusive Freestream Velocity Measurement in a Large-Scale Hypersonic Wind Tunnel," *AIAA Journal*, Vol. 55, No. 10, 2017, pp. 3611–3616. doi: 10.2514/1.J056177.

[169] Dogariu, L. E., Dogariu, A., Miles, R. B., Smith, M. S., and Marineau, E. C., "Non-intrusive Hypersonic Freestream and Turbulent Boundary-Layer Velocity Measurements in AEDC Tunnel 9 using FLEET," In *2018 AIAA Aerospace Sciences Meeting*, Kissimmee, Florida, USA, 2018. AIAA 2018-1769.

[170] Danehy, P. M., O'Byrne, S., Houwing, A. F. P., Fox, J. S., and Smith, D. R., "Flow-tagging velocimetry for hypersonic flows using fluorescence of nitric oxide," *AIAA Journal* 41, 263–271 (2003).

[171] Pitz, R. W., Lahr, M. D., Douglas, Z. W., Wehrmeyer, J. A., Hu, S., Carter, C. D., Hsu, K. Y., Lum, C., and Koochesfahani, M. M., "Hydroxyl Tagging Velocimetry in a Supersonic Flow Over a Cavity," *Applied Optics*, Vol. 44, No. 31, 2005, pp. 6692–6700. doi:10.1364/AO.44.006692.

[172] Smeets, G., "Laser Interferometer for High Sensitivity Measurements on Transient Phase Objects," *IEEE Transactions on Aerospace and Electronic Systems*, Vol. AES-8, No. 2, 1972, pp. 186–190. doi:10.1109/TAES.1972.309488.

[173] Smeets, G. and George, A., "Anwendungen des Laser Differentialinterferometers in der Gasdynamik," French–German Research Institute Rept. 28/73, Saint-Louis, France, 1973; also "Laser Differential Interferometer Applications in Gas Dynamics," Translated by Goetz, A., ADA307459, 1996.

[174] Smeets, G., "Flow Diagnostics by Laser Interferometry," *IEEE Transactions on Aerospace and Electronic Systems*, Vol. AES-13, No. 2, 1977, pp. 82–90. doi:10.1109/TAES.1977.308441.

[175] Parziale, N. J., "Slender-Body Hypervelocity Boundary-Layer Instability," PhD thesis, California Institute of Technology, 2013.

[176] Parziale, N. J., Shepherd, J. E., and Hornung, H. G., "Free-stream density perturbations in a reflected-shock tunnel," *Experiments in Fluids*, Vol. 55, No. 2, 2014, pp. 1–10. doi: 10.1007/s00348-014-1665-0.

[177] Jewell, J. S., "Boundary-layer transition on a slender cone in hypervelocity flow with real gas effects," Ph.D. thesis, California Institute of Technology, 2014.

[178] Parziale, N. J., Shepherd, J. E., and Hornung, H. G., "Differential Interferometric Measurement of Instability in a Hypervelocity Boundary Layer," *AIAA Journal*, Vol. 51, No. 3, 2013, pp. 750–754. doi: 10.2514/1.J052013.

[179] Parziale, N. J., Shepherd, J. E., and Hornung, H. G., "Observations of hypervelocity boundary-layer instability," *Journal of Fluid Mechanics*, Vol. 781, 2015, pp. 87–112. doi: 10.1017/jfm.2015.489.

[180] Chou, A., Leidy, A., King, R. A., Bathel, B. F., and Herring, G., "Measurements of Freestream Fluctuations in the NASA Langley 20-Inch Mach 6 Tunnel," *AIAA Aviation Forum*, AIAA 2018-3073, Atlanta, Georgia. doi: 10.2514/6.2018-3073.

[181] Fulghum, M. R., "Turbulence measurements in high-speed wind tunnels using focusing laser differential interferometry," Ph.D. thesis, The Pennsylvania State University, 2014.

[182] Settles, G. S. and Fulghum, M. R., "The Focusing Laser Differential Interferometer, an Instrument for Localized Turbulence Measurements in Refractive Flows," *Journal of Fluids Engineering*, Vol. 138, No. 10., 2016 doi: 10.1115/1.4033960.

[183] Schmidt, B. E. and Shepherd, J. E., "Analysis of focused laser differential interferometry," *Applied Optics*, Vol. 54, No. 28, 2015, pp. 8459-8472, doi: 10.1364/AO.54.008459.

[184] Jewell, J. S., Parziale, N. J., Lam, K. -Y., Hagen B. J. and Kimmel, R. L., "Disturbance and Phase Speed Measurements for Shock Tubes and Hypersonic Boundary-Layer Instability," *AIAA Aviation 2016*, AIAA 2016-3112, Washington, DC. doi: 10.2514/6.2016-3112.

[185] Hedlund, B., Houpt, A., Gordeyev, S., and Leonov, S., "Measurement of Flow Perturbation Spectra in Mach 4.5 Corner Separation Zone," *AIAA Journal*, Vol. 56, No. 7, 2018, pp. 2699-2711. doi: 10.2514/1.J056576.

[186] Harris, A. J., Kreth, P. A., Combs, C. S., Schmisseur, J. D., "Laser Differential Interferometry and Schlieren as an Approach to Characterizing Freestream Disturbance Levels," *AIAA SciTech Forum*, AIAA 2018-1100, Kissimmee, Florida, doi: 10.2514/6.2018-1100.

[187] Sayler, T. R., Collicott, S. H., and Schneider, S. P., "Feedback Stabilized Laser Differential Interferometry for Supersonic Blunt Body Receptivity Experiments," *38th Aerospace Sciences Meeting*, AIAA 2000-0416, Reno, Nevada, doi: 10.2514/6.2000-416.

[188] Ceruzzi, A., and Cadou, C. P., "Turbulent Air Jet Investigation using Focused Laser Differential Interferometry," *53rd AIAA/SAE/ASEE Joint Propulsion Conference*, AIAA 2017-4834, Atlanta, Georgia. doi: 10.2514/6.2017-4834.

[189] Komine, H., "System for measuring velocity field of fluid flow utilizing a laser-doppler spectral image converter," 4919536, 1990.

[190] Charrett, T., Nobes, D., and Tatam, R, "Investigation into the selection of viewing configurations for three-component planar Doppler velocimetry measurements," *Applied Optics*, Vol. 4116, 2007, pp. 4102-4116.

[191] Miles, R. B., Lempert, W. R., and Forkey, J. N., "Laser Rayleigh scattering," *Measurement Science and Technology*, Vol. 12, 2001.

192 Meyers, J. F., Lee, J. W., and Schwartz, R. J., "Characterization of measurement error sources in Doppler global velocimetry," *Measurement Science and Technology,* Vol. 12, 2001.

193 Landolt, A., and Roesgen, T., "Global Doppler frequency shift detection with near-resonant interferometry," *Experiments in Fluids,* Vol. 47, 2009, pp. 733-743.

194 Lu, Z. H., Charrett, T. O. H., and Tatam, R. P., "Three-component planar velocity measurements using Mach-Zehnder interferometric filter-based planar Doppler velocimetry (MZI-PDV)," *Measurement Science and Technology,* Vol. 20, 2009.

195 Thurow, B. S., Jiang, N., Lempert, W. R., and Samimy, M., "Development of Megarhertz-Rate Planar Doppler Velocimetry for High-Speed Flows," *AIAA Journal*, Vol. 43, 2005.

196 Cadel, D. R., and Lower, K. T., "Cross-correlation Doppler global velocimetry (CC-DGV)," *Optics and Lasers in Engineering*, Vol. 71, 2015, pp. 51-61.

197 Thorpe, S. J., Ainsworth, R, W., and Manners, R. J., "The development of a Doppler global velocimeter and its application to a free jet flow," *ASME/EALA 6th Int. Conference on Laser Anemometry Advances and Applications,* Hilton Head, SC, USA: 1995.

198 Charrett, T. O. H., Ford, H. D., Nobes, D. S., and Tatam, R. P., "Two-frequency planar Doppler velocimetry (2v-PDV)," *Review of Scientific Instruments,* Vol. 75, 2004, pp. 4487-4496.

199 Fischer, A., Büttner, L., Czarske, J., Eggert, M., Grosche, G., and Müller, H., "Investigation of time-resolved single detector Doppler global velocimetry using sinusoidal laser frequency modulation," *Measurement Science and Technology*, Vol. 18, 2007, pp. 2529-2545.

200 Müller, H., Eggert, M., Czarske, J., Büttner, L., and Fischer, A., "Single-camera Doppler global velocimetry based on frequency modulation techniques," *Experiments in Fluids*, Vol. 43, 2007, pp. 223-232.

201 Roehle, I., and Schodl, R., "Evaluation of the accuracy of the Doppler global technique." *Proc. Optical Methods and Data Processing in Heat and Fluid Flow,* London: 1994, pp. 156-161.

202 Mckenzie, R. L., "Measurement capabilities of planar Doppler velocimetry using pulsed lasers," *Applied Optics*, Vol. 35, 1996, pp. 948-964.

203 Roehle, I., and Willert, C. E., "Extension of Doppler global velocimetry to periodic flows," *Measurement Science and Technology,* Vol. 12, 2001, pp. 420-431.

204 Tenti, G., Boley, C. D., and Desai, R. C., "On the Kinetic Model Description of Rayleigh-Brillouin Scattering from Molecular Gases," *Canadian Journal of Physics,* Vol. 52, 1974, pp. 285-290.

205 Forkey, J. N., Lempert, W. R., and Miles, R. B., "Accuracy limits for planar measurements of flow field velocity, temperature and pressure using Filtered Rayleigh Scattering," *Experiments in Fluids,* Vol. 24, 1998, pp 151-162.

206 Seasholtz, R. G., Buggele, A. E., and Reeder, M. F., "Flow measurements based on Rayleigh scattering and Fabry-Perot interferometer," *Optics and Lasers in Engineering*, Vol. 27, 1997, pp. 543-570.

207 Bivolaru, D., Danehy, P, M., and Lee, J. W., "Intercavity Rayleigh-Mie scattering for multipoint, two-component velocity measurement," *Optics Letters,* Vol. 31, 2006, pp. 1645-1647.

208 Kojima, J. J., and Fischer, D. G., "Multiscalar Analyses of High-Pressure Swirl-Stabilized Combustion via Single-Shot Dual-SBG Raman Spectroscopy," *Combustion Science and Technology*, Vol. 185, 2013, pp. 1735-1761.

209 Sharma, S. P., and Ruffint, S. M., "Vibrational Relaxation Measurement in an Expanding Flow Using Spontaneous Raman Scattering," Vol. 7, 1993.

210 Eckbreth, A. C., "Laser Diagnostics for Combustion Temperature and Species, Volume 3," of *Combustion Science and Technology Book Series*, Gordon and Breach Publishers, 2nd ed., 1996.

211 Roy, S., Gord, J. R., and Patnaik, A. K., "Recent advances in coherent anti-Stokes Raman scattering spectroscopy: Fundamental developments and applications in reacting flows," *Progress in Energy and Combustion Science*, Vol. 36, No. 2, 2010, pp. 280–306.

212 Cutler, A. D., Magnotti, G., Cantu, L., Gallo, E., Rockwell, R., and Goyne, C., "Dual-Pump Coherent Anti-Stokes Raman Spectroscopy Measurements in a Dual-Mode Scram-jet," *Journal of Propulsion and Power*, Vol. 30, No. 3, 2014, pp. 539–549.

213 Maker, P., and Terhune, R., "Study of Optical Effects Due to an Induced Polarization Third Order in the Electric Field Strength," *Physical Review*, Vol. 137, No. 3A, 1965, pp. 801–818.

214 Begley, R. F., Harvey, A. B., and Byer, R. L., "Coherent anti-Stokes Raman spectroscopy," *Applied Physics Letters*, Vol. 25, No. 7, 1974, pp. 387–390.

[215] Regnier, P. R., Moya, F., and Taran, J. P. E., "Gas Concentration Measurement by Coherent Raman Anti-Stokes Scattering," *AIAA Journal*, Vol. 12, No. 6, 1974, pp. 826– 831.

[216] Moya, F., Druet, S. A. J., and Taran, J. P. E., "Gas spectroscopy and temperature measurement by coherent Raman anti-Stokes scattering," *Optics Communications*, Vol. 13, No. 2, 1975, pp. 169–174.

[217] Eckbreth, A. C., "Recent Advances in Laser Diagnostics for Temperature and Species Concentration in Combustion," *Symposium (International) on Combustion*, Vol. 18, No. 1, 1981, pp. 1471–1488.

[218] Clark, G., Palmer, R. E., and Farrow, R. L., "The CARSFT Code: User and Programmer Information," 1990.

[219] Eckbreth, A. C., "Cars Thermometry in Practical Combustors." *Combustion and Flame*, Vol. 39, No. 2, 1980, pp. 133–147.

[220] Alessandretti, G. C., and Violino, P., "Thermometry by CARS in an automobile engine," *Journal of Physics D (Applied Physics)*, Vol. 16, No. 9, 1983, pp. 1583–1594.

[221] Weikl, M. C., Beyrau, F., Leipertz, A., "Simultaneous temperature and exhaust-gas recirculation-measurements in a homogeneous charge-compression ignition engine by use of pure rotational coherent anti-Stokes Raman spectroscopy," *Applied Optics*, Vol. 45, 2006, pp. 3646-3651.

[222] Brackmann, C., Bood, J., Bengtsson, P. -E. , Seeger, T., Schenk, M., Leipertz, A., "Simultaneous vibrational and pure rotational coherent anti-stokes Raman spectroscopy for temperature and multispecies concentration measurements demonstrated in sooting flames," *Applied Optics,* Vol. 41, No. 3, 2002, pp. 564–572.

[223] Geigle, K. P., Kohler, M., O'Loughlin, W., Meier, W., "Investigation of soot formation in pressurized swirl flames by laser measurements of temperature, flame structures and soot concentrations," *Proceedings of the Combustion Institute*, Vol. 35, No. 3, 2015, pp. 3373–3380.

[224] Stricker, W., Woyde, M., Lückerath, R., and Bergmann, V., "Temperature Measurements in High Pressure Combustion," *Berichte der Bunsengesellschaft fur physikalische Chemie*, Vol. 97, No. 12, 1993, pp. 1608–1618.

[225] Kearney, S. P., Lucht, R. P., and Jacobi, A. M., "Temperature measurements in convective heat transfer flows using dual-broadband, pure-rotational coherent anti-Stokes Raman spectroscopy (CARS)," *Experimental Thermal and Fluid Science*, Vol. 19, No. 1, 1999, pp. 13–26.

[226] Kearney, S. P., Grasser, T. W., "Laser-diagnostic mapping of temperature and soot statistics in a 2-m diameter turbulent pool fire," *Combustion and Flame,* Vol. 186, 2017, pp. 32–44.

[227] Eckbreth, A. C., and Anderson, T. J., "Dual broadband CARS for simultaneous, multiple species measurements," *Applied Optics*, Vol. 24, No. 16, 1985, pp. 2731.

[228] Seeger, T., Beyrau, F., Bräuer, A., and Leipertz, A., "High-pressure pure rotational CARS: comparison of temperature measurements with O_2, N_2 and synthetic air," *Journal of Raman Spectroscopy*, Vol. 34, No. 12, 2003, pp. 932–939.

[229] Roy, S., Meyer, T. R., and Gord, J. R., "Broadband coherent anti-Stokes Raman scattering spectroscopy of nitrogen using a picosecond modeless dye laser." *Optics Letters*, Vol. 30, No. 23, 2005, pp. 3222–4.

[230] Meyer, T. R., Roy, S., and Gord, J. R., "Improving Signal-to-Interference Ratio in Rich Hydrocarbon–Air Flames Using Picosecond Coherent Anti-Stokes Raman Scattering," *Applied Spectroscopy*, Vol. 61, No. 11, 2007, pp. 1135–1140.

[231] Seeger, T., Kiefer, J., Leipertz, A., Patterson, B. D., Kliewer, C. J., and Settersten, T. B., "Picosecond time-resolved pure-rotational coherent anti-Stokes Raman spectroscopy for N_2 thermometry," *Optics Letters*, Vol. 34, No. 23, 2009, pp. 3755–7.

[232] Kliewer, C. J., Gao, Y., Seeger, T., Kiefer, J., Patterson, B. D., and Settersten, T. B., "Picosecond time-resolved pure-rotational coherent anti-Stokes Raman spectroscopy in sooting flames," *Proceedings of the Combustion Institute*, Vol. 33, No. 1, 2011, pp. 831– 838.

[233] Beaud, P., Frey, H. M., Lang, T., and Motzkus, M., "Flame thermometry by femtosecond CARS," *Chemical Physics Letters*, Vol. 344, No. 3-4, 2001, pp. 407–412.

[234] Wrzesinski, P. J., Stauffer, H. U., Kulatilaka, W. D., Gord, J. R., and Roy, S., "Time-resolved femtosecond CARS from 10 to 50 Bar: Collisional sensitivity," *Journal of Raman Spectroscopy*, Vol. 44, No. 10, 2013, pp. 1344–1348.

[235] Richardson, D. R., Lucht, R. P., Kulatilaka, W. D., Roy, S., and Gord, J. R., "Chirped-probe-pulse femtosecond coherent anti-Stokes Raman scattering concentration measurements," *Journal of the Optical Society of America B (JOSA B)*, Vol. 30, No. 1, 2013, pp. 188–196.

236 Hsu, P. S., Kulatilaka, W. D., Gord, J. R., and Roy, S., "Single-shot thermometry using fiber-based picosecond coherent anti-stokes Raman scattering (CARS) spectroscopy," *Journal of Raman Spectroscopy*, Vol. 44, No. 10, 2013, pp. 1330–1335.

237 Prince, B. D., Chakraborty, A., Prince, B. M., and Stauffer, H. U., "Development of simultaneous frequency- and time-resolved coherent anti-Stokes Raman scattering for ultrafast detection of molecular Raman spectra," *The Journal of Chemical Physics*, Vol. 125, 2006, pp. 44502.

238 Pestov, D., Murawski, R. K., Ariunbold, G. O., Wang, X., Zhi, M., Sokolov, A. V., Sautenkov, V. A., Rostovtsev, Y. V., Dogariu, A., Huang, Y., Scully, M. O., "Optimizing the laser-pulse configuration for coherent Raman spectroscopy," *Science* 316, 2007, pp. 265–268.

239 Miller, J. D., Slipchenko, M. N., Meyer, T. R., Stauffer, H. U., and Gord, J. R., "Hybrid femtosecond/picosecond coherent anti-Stokes Raman scattering for high-speed gas-phase thermometry," *Optics Letters*, Vol. 35, No. 14, 2010, pp. 2430–2.

240 Miller, J. D., Dedic, C. E., and Meyer, T. R., "Vibrational femtosecond/picosecond coherent anti-Stokes Raman scattering with enhanced temperature sensitivity for flame thermometry from 300 to 2400 K," *Journal of Raman Spectroscopy*, Vol. 46, No. 8, 2015, pp. 702–707.

241 Miller, J. D., Roy, S., Slipchenko, M. N., Gord, J. R., and Meyer, T. R., "Single-shot gas-phase thermometry using pure-rotational hybrid femtosecond/picosecond coherent anti-Stokes Raman scattering," *Optics Express*, Vol. 19, No. 16, 2011, pp. 15627–15640.

242 Kearney, S. P., and Scoglietti, D. J., "Hybrid femtosecond/picosecond rotational coherent anti-Stokes Raman scattering at flame temperatures using a second-harmonic bandwidth-compressed probe," *Optics Letters*, Vol. 38, No. 6, 2013, pp. 833–835.

243 Kearney, S. P., "Hybrid fs/ps rotational CARS temperature and oxygen measurements in the product gases of canonical flat flames," *Combustion and Flame*, Vol. 162, No. 5, 2015, pp. 1748-1758.

244 Courtney, T. L., Bohlin, A., Patterson, B. D., and Kliewer, C. J., "Pure-rotational H_2 thermometry by ultrabroadband coherent anti-stokes Raman spectroscopy," *The Journal of Chemical Physics*, Vol. 146, No. 22, 2017, pp. 224202.

245 Bohlin, A., Patterson, B. D., Kliewer, C. J., "Communication: Simplified two-beam rotational CARS signal generation demonstrated in 1D," *Journal of Chemical Physics*, Vol. 138, No. 8, 2013, pp. 081102.

246 Bohlin, A., Jainski, C., Patterson, B. D., Dreizler, A., Kliewer, C. J., "Multiparameter spatio-thermochemical probing of flame-wall interactions advanced with coherent Raman imaging," *Proceedings of the Combustion Institute*, Vol. 36, No., 3, 2017, pp. 4557-4564.

247 Brady, J., Farrell, M. E., and Pellegrino, P. M., "Discrimination of chemical warfare simulants via multiplex coherent anti-Stokes Raman scattering and multivariate statistical analysis," *CBRNE Sensing XI*, Vol. 53, No. 2, 2014, pp. 021105.

248 Bohlin, A., and Kliewer, C. J., "Two-beam ultrabroadband coherent anti-Stokes Raman spectroscopy for high resolution gas-phase multiplex imaging," *Applied Physics Letters*, Vol. 104, No. 3, 2014, pp. 031107.

249 Dedic, C. E., Miller, J. D., and Meyer, T. R., "Dual-pump vibrational/rotational femtosecond/picosecond coherent anti-Stokes Raman scattering temperature and species measurements," *Optics Letters*, Vol. 39, No. 23, 2014, pp. 6608–6611.

250 Retter, J. E., Elliott, G. S., Kearney, S. P., "Dielectric-barrier-discharge plasma-assisted hydrogen diffusion flame. Part 1: Temperature, oxygen, and fuel measurements by one-dimensional fs/ps rotational CARS imaging," *Combustion and Flame*, Vol. 191, 2018, pp. 527-540.

251 Kulatilaka, W. D., Hsu, P. S., Stauffer, H. U., Gord, J. R., and Roy, S., "Direct measurement of rotationally resolved H_2 Q-branch Raman coherence lifetimes using time-resolved picosecond coherent anti-Stokes Raman scattering," *Applied Physics Letters*, Vol. 97, No. 8, 2010, pp. 081112.

252 Miller, J. D., Roy, S., Gord, J. R., and Meyer, T. R., "Communication: Time-domain measurement of high-pressure N_2 and O_2 self-broadened linewidths using hybrid femtosecond/picosecond coherent anti-Stokes Raman scattering," *The Journal of Chemical Physics*, Vol. 135, No. 20, 2011, pp. 201104.

253 Kliewer, C. J., Bohlin, A., Nordstrom, E., Patterson, B. D., Bengtsson, P. -E., and Settersten, T. B., "Time-domain measurements of S-branch N_2–N_2 Raman linewidths using picosecond pure rotational coherent anti-Stokes Raman spectroscopy," *Applied Physics B*, Vol. 108, No. 2, 2012, pp. 419–426.

[254] Miller, J. D., Dedic, C. E., Roy, S., Gord, J. R., and Meyer, T. R., "Interference-free gas- phase thermometry at elevated pressure using hybrid femtosecond/picosecond rotational coherent anti-Stokes Raman scattering," *Optics Express*, Vol. 20, No. 5, 2012, pp. 5003– 5010.

[255] Kearney, S. P., and Danehy, P. M., "Pressure measurements using hybrid femtosecond/picosecond rotational coherent anti-Stokes Raman scattering," *Optics Letters*, Vol. 40, No. 17, 2015, pp. 4082.

[256] Kearney, S. P., and Guildenbecher, D. R., "Temperature measurements in metalized propellant combustion using hybrid fs/ps coherent anti-Stokes Raman scattering," *Applied Optics*, Vol. 55, No. 18, 2016, pp. 4958–4966.

[257] Dedic, C. E., Michael, J. B., and Meyer, T. R., "Investigation of energy distributions behind a microscale gas-phase detonation tube using hybrid fs/ps coherent anti-Stokes Raman scattering," *55th AIAA Aerospace Sciences Meeting*, AIAA SciTech Forum, 2017, pp. AIAA 2017–0030.

[258] Stauffer, H. U., Rahman, K. A., Slipchenko, M. N., Roy, S., Gord, J. R., and Meyer T. R., "Interference-free hybrid fs/ps vibrational CARS thermometry in high-pressure flames," *Optics Letters,* Vol. 43 No. 20, 2018, pp. 4911-4914.

[259] Dedic, C. E., Meyer, T. R., and Michael, J. B., "Single-shot ultrafast coherent anti-Stokes Raman scattering of vibrational/rotational nonequilibrium," *Optica*, Vol. 4, No. 5, 2017, pp. 563–570.

[260] Dedic, C. E., and Michael, J. B., "Evaluation of vibrational excitation in a microwave plasma enhanced flame using hybrid fs/ps CARS," *2018 AIAA Aerospace Sciences Meeting*, AIAA SciTech Forum, 2018, pp. AIAA 2018-1025.

[261] Lucht, R. P., "Three-laser coherent anti-Stokes Raman scattering measurements of two species," *Optics Letters*, Vol. 12, 1987, pp. 78–80.

[262] Magnotti, G., Cutler, A. D., Danehy, P. M., "Development of a dual-pump coherent anti-Stokes Raman spectroscopy system for measurements in supersonic combustion," *Applied Optics*, Vol. 52, 2013, pp. 4779–4791.

[263] Miller, J. D., Slipchenko, M. N., and Meyer, T. R., "Probe-pulse optimization for non-resonant suppression in hybrid fs/ps coherent anti-Stokes Raman scattering at high temperature," *Optics Express*, Vol. 19, No. 14, 2011, pp. 13326–33.

[264] Dedic, C. E., Michael, J. B., Meyer, T. R., "Hybrid fs/ps coherent anti-Stokes Raman scattering in a non-equilibrium environment initiated by a ns laser spark," in *46th AIAA Plasmadynamics and Lasers Conference, AIAA AVIATION Forum*, (Dallas, TX, 2015), AIAA 2015–2962.

[265] Stauffer, H. U., Miller, J. D., Slipchenko, M. N., Meyer, T. R., Prince, B. D., Roy, S., and Gord, J. R., "Time- and frequency-dependent model of time-resolved coherent anti- Stokes Raman scattering (CARS) with a picosecond-duration probe pulse," *The Journal of Chemical Physics*, Vol. 140, No. 2, 2014, pp. 024316.

[266] Cutler, A. D., Cantu, L. M. L., Gallo, E. C. A., Baurle, R., Danehy, P. M., Rockwell, R., Goyne, C., and McDaniel, J., "Nonequilibrium Supersonic Freestream Studied Using Coherent Anti-Stokes Raman Spectroscopy," *AIAA Journal*, Vol. 53, No. 9, 2015, pp. 2762–2770.

[267] Lempert, W. R., and Adamovich, I. V., "Coherent anti-Stokes Raman scattering and spontaneous Raman scattering diagnostics of nonequilibrium plasmas and flows," *Journal of Physics D: Applied Physics*, Vol. 47, 2014, pp. 433001.

[268] Montello, A., Nishihara, M., Rich, J. W., Adamovich, I. V., and Lempert, W. R., "Nitrogen Vibrational Population Measurements in the Plenum of a Hypersonic Wind Tunnel," *AIAA Journal*, Vol. 50, No. 6, 2012, pp. 1367–1376.

[269] Montello, A., Yin, Z., Burnette, D., Adamovich, I. V., and Lempert, W. R., "Picosecond CARS measurements of nitrogen vibrational loading and rotational/translational temperature in non-equilibrium discharges," *Journal of Physics D: Applied Physics*, Vol. 46, No. 46, 2013, pp. 464002.

[270] Roy, S., Hsu, P. S., Jiang, N., Slipchenko, M. N., and Gord, J. R., "100-kHz-rate gas-phase thermometry using 100-ps pulses from a burst-mode laser," *Optics Letters*, Vol. 40, 2015, pp. 5125.

[271] Eckbreth, A. C., "BOXCARS: Crossed-beam phase-matched CARS generation in gases," *Applied Physics Letters*, Vol. 32, No. 7, 1978, pp. 421–423.

[272] Seeger, T., and Leipertz, A., "Experimental comparison of single-shot broadband vibrational and dual-broadband pure rotational coherent anti-Stokes Raman scattering in hot air," *Applied Optics*, Vol. 35, 1996, pp. 2665-2671.

[273] Beyrau, F., Datta, A., Seeger, T., and Leipertz, A., "Dual-pump CARS for the simultaneous detection of N_2, O_2 and CO in CH_4 flames," *J. Raman Spectrosc.*, Vol. 33, 2002, pp. 919–924.

274 Tedder, S. A., Wheeler, J. L., Cutler, A. D., and Danehy, P. M., "Width-increased dual-pump enhanced coherent anti-Stokes Raman spectroscopy," *Applied Optics*, Vol. 49, No. 8, 2010, pp. 1305–13.

275 Cutler, A. D., Gallo, E. C. A., Cantu, L. M. L., "Coherent anti-Stokes Raman spectroscopy measurement of ethylene in combustion," *Applied Optics,* Vol. 56, No. 11, 2017, pp. 30–36.

276 Dedic, C. E., "Hybrid fs/ps coherent anti-Stokes Raman scattering for multiparameter measurements of combustion and nonequilibrium," PhD, Iowa State University, 2017.

277 Magnotti, G., Cutler, A. D., Herring, G. C., Tedder, S. A., and Danehy, P. M., "Saturation and Stark broadening effects in dual-pump CARS of N2, O2, and H2," *Journal of Raman Spectroscopy*, Vol. 43, 2012, 611–620.

278 Patnaik, A., Roy, S., Gord, J., "Saturation of vibrational coherent anti-Stokes Raman scattering mediated by saturation of the rotational Raman transition," *Physical Review A*, Vol. 87, No. 4, 2013, pp. 043801.

279 Grisch, F., Bouchardy, P., Pealat, M., Chanetz, B., Pot, T., and Coet, M. C., "Rotational temperature and density measurements in a hypersonic flow by dual-line CARS," *Applied Physics B Photophysics and Laser Chemistry*, 1993.

280 Smith, M. W., Jarrett, O., Antcliff, R. R., Northam, G. B. , Cutler, A. D., and Taylor, D. J., "Coherent anti-Stokes Raman spectroscopy temperature measurements in a hydrogen-fueled supersonic combustor," *Journal of Propulsion and Power*, Vol. 9, No. 2, 1993, pp. 163-168.

281 Cutler, A. D., Gallo, E. C. A., Cantu, L. M. L., Rockwell, R. D., Goyne, C. P., "Coherent anti-Stokes Raman spectroscopy of a premixed ethylene–air flame in a dual-mode scramjet," *Combustion and Flame*, Vol. 189, 2018, pp.92-105.

282 Fraval, E., Danehy, P. M., Houwing, A. F. P., "Single-Shot Broadband Coherent Anti-Stokes Raman Scattering Measurements in a Free Piston Shock Tunnel Nozzle Expansion," in *Proceedings of 23rd International Symposium on Shock Waves*, Fort Worth, Texas, Published by The University of Texas at Arlington, Arlington, Texas, USA. (CD ROM), pap. num. 1717, July 22-27, 2001, pp. 396-402.

283 Smith, M., and Coblish, J., "Measurements to Assess the Degree of Thermal Nonequilibrium at AEDC Hypervelocity Wind Tunnel No. 9," *24th AIAA Aerodynamic Measurement Technology and Ground Testing Conference*, June 28-July 1, 2004, pp. AIAA 2004-2399.

284 Richardson, D. R., Roy, S., Gord, J. R., and Kearney, S. P., "Two-Beam Femtosecond Rotational CARS for One-Dimensional Thermometry in a Turbulent, Sooting Jet Flame," *55th AIAA Aerospace Sciences Meeting, AIAA SciTech Forum*, Grapevine, Texas, 2017, pp. AIAA 2017-0031.

285 Bohlin, A., and Kliewer, C. J., "Communication: Two-dimensional gas-phase coherent anti-Stokes Raman spectroscopy (2D-CARS): Simultaneous planar imaging and multiplex spectroscopy in a single laser shot," *The Journal of Chemical Physics,* Vol. 138, No. 22, 2013, pp. 221101.

286 Miller, J. D., Slipchenko, M. N., Mance, J. G., Roy, S., Gord, J. R., "1-kHz two-dimensional coherent anti-Stokes Raman scattering (2D-CARS) for gas-phase thermometry," *Optics Express*, Vol. 24, No. 22, 2016, pp. 24971.

287 Raffel, M., Willert, C. E., Wereley, S. T., and Kompenhans, J., "Particle Image Velocimetry: A practical guide," 2nd Ed., Springer, Berlin, 2007.

288 Miles, R. B., Lempert, W. R., and Forkey, J. N., "Laser Rayleigh Scattering," *Meas. Sci. Technol.,* Vol. 12, R33-R51, 2001.

289 Tropea, C., "Laser Doppler anemometry: recent developments and future challenges," *Meas. Sci. Technol.*, Vol. 6, 1995.

290 Hunter Jr., W. W., Gartrell, L. R., Humphreys, W. M., Witte, D. W., Nichols Jr., and C. E., "Development and Assessment of an LDV System for Mach 6 Flow Field Measurements," In: Boutier A. (eds) New Trends in Instrumentation for Hypersonic Research. NATO ASI Series (Series E: Applied Sciences), Vol. 224. Springer, Dordrecht, 1993, doi.org/10.1007/978-94-011-1828-6_31.

291 Meyers, J. F., Lee, J. W., and Schwartz, R. J., "Characterization of measurement error sources in Doppler global velocimetry," *Meas. Sci. Technol.,* Vol. 12, 357–68, 2001.

292 Samimy, M., and Wernet, M. P., "A review of planar multiple-component velocimetry in high speed flows," *AIAA Journal*, Vol. 38, 553–74, 2000.

293 Scarano, F., "Overview of PIV in Supersonic Flows," In: Particle Image Velocimetry. *Topics in Applied Physics*, Springer, Berlin, Heidelberg , January 2008.

294 Scarano, F., and van Oudheusden, B. W., "PIV investigation of a planar supersonic wake flow," Paper 34_1, *11th International Symposium on Applications of Laser Techniques to Fluid Mechanics*, Lisbon, Portugal, July 8 - 11, 2002.

295 Souverein, L. J., van Oudheusden, B. W., and Scarano, F., "Particle Image Velocimetry Based Loads Determination in Supersonic Flows," AIAA 2007-50, *45th AIAA Aerospace Sciences Meeting and Exhibit*, 8-11 January Reno, NV, 2007 .

296 Humphreys, W. M., Rallo, R. A., Hunter, W. W., Bartram, S. M., Blackshire, J. L., "Application of particle image velocimetry to Mach 6 flows," *Proceedings Fifth International Conference on Laser Anemometry: Advances and Applications*, Vol. 2052, (1993), doi.org/10.1117/12.150545.

297 Humphreys, W., Bartram, S. M., Blackshire, J. L., "A survey of particle image velocimetry applications in Langley aerospace facilities," *31st Aerospace Sciences Meeting, Reno*, NV, 1993, doi.org/10.2514/6.1993-411.

298 Haertig, J., Havermann, M., Rey, C., and George, A., "Particle Image Velocimetry in Mach 3.5 and 4.5 Shock-Tunnel Flows," *AIAA Journal*, Vol. 40, No. 6, June 2002.

299 Havermann, M., Haertig J., Rey C., George A., "PIV Measurements in Shock Tunnels and Shock Tubes," In: Particle Image Velocimetry. *Topics in Applied Physics,* Vol. 112. Springer, Berlin, Heidelberg, 2007.

300 Havermann, M., Haertig J., Rey C., George A., "Application of Particle Image Velocimetry to High-Speed Supersonic Flows in a Shock Tunnel," *11th International Symposium on Applications of Laser Techniques to Fluid Mechanics*, Lisbon, Portugal, July 8 - 11, 2002.

301 Bell, G., Soria, J., Honnery, D., Edgington-Mitchell, D. "An experimental investigation of coupled underexpanded supersonic twin-jets," *Experiments in Fluids*, Vol. 59, 139, 2018.

302 Estevadeordal, J., Gogineni, S., Goss, L., Copenhaver, W., Gorrell, S., "Study of Wake-Blade Interactions in a Transonic Compressor Using Flow Visualization and DPIV," *J. Fluids Eng.*, Vol. 124, No. 1, 2001, pp. 166-175, doi:10.1115/1.1429638.

303 Langford, M. D., Breeze-Stringfellow, A., Guillot, S. A., Solomon, W., Ng, W. F., and Estevadeordal, J., "Experimental Investigation of the Effects of a Moving Shock Wave on Compressor Stator Flow," ASME Paper No. GT2005-68722, Vol. 6, 2005, pp. 1383-1395, doi:10.1115/GT2005-68722.

304 Wernet, M. P., "Application of Tomo-PIV in a large-scale supersonic jet flow facility," *Exp. Fluids*, Vol. 57, 2016, 144, doi: 10.1007/s00348-016-2228-3.

305 Rice, B. E., Bisek, N. J., Peltier, S. J., and Hofferth, J. W., "Investigation of Secondary Motion in High-Speed Flow," AIAA Paper 2017-0526, *55th AIAA Aerospace Sciences Meeting, AIAA Science and Technology Forum* and *Exposition,* Grapevine, TX, 9-13 January 2017.

306 Peltier, S. J., Rice, B. E., Bisek, N. J., McKenna, C. K., and Hofferth, J. W., "Structure of Secondary Motion in a Mach 2 Boundary Layer," *56th AIAA Aerospace Sciences Meeting, AIAA Science and Technology Forum and Exposition,* Kissimmee, FL, 8-12 January 2018.

307 Bryan B. B., Harris H. R., Thurow, B. S., Lyons, G., and Murray, N. E., "An examination of MHz rate PIV in a heated supersonic jet," *AIAA2014-1102, AIAA 52nd Aerospace Sciences Meeting*, National Harbor, Maryland, January 13-17, 2014.

308 Beresh, S., Kearney, S., Wagner, J., Guildenbecher, D., Henfling, J., Spillers, R., Pruett, B., Jiang, N., Slipchenko, M., Mance, J., and Roy, S., "Pulse-burst PIV in a high-speed wind tunnel," *Meas. Sci. Technol.,* Vol. 26, 2015, doi: 10.1088/0957-0233/26/9/095305.

309 Scarano, F., and Riethmuller, M. L., "Advances in Iterative Multigrid PIV Image Processing," *Experiments in Fluids*, Vol. 29, No. 7, 2000, pp. S51–60. doi:10.1007/s003480070007.

310 Scarano, F., "Tomographic PIV: principles and practice," *Meas. Sci. technol.*, Vol. 24, No. 1, 2012.

311 Wernet, M. P., "Temporally-resolved PIV for space-time correlations in both cold and hot jet flows," Meas. Sci. Technol., Vol. 18, 2007, pp. 1387-1403.

312 Schanz, D., Gesemann, S., and Schröder, A., "Shake-The-Box: Lagrangian particle tracking at high particle image densities," *Exp. in Fluids*, Vol. 57, No. 5, 2016, pp. 1-27. doi: 10.1007/s00348-016-2157-1 ISSN 0723-4864.

313 Ghaemi, S., Schmidt-Ott, A., and Scarano, F., "Nanostructured tracers for laser-based diagnostics in high-speed flows," *Meas. Sci. Technol.,* Vol. 21, 2010, 105403, doi: 10.1088/0957-0233/21/10/105403.

314 Reeder, M. F., Crafton, J. W., Estevadeordal, J., Delapp, J., McNiel, C., Peltier, D., Reynolds, T., "Clean seeding for flow visualization and velocimetry measurements," *Exp. in Fluids*, Vol. 48, Issue 5, 2010, pp. 889-900, 10.1007/s00348-009-0784-5.

315 Elsinga, G. E., van Oudheusden, B. W., and Scarano, F., "Evaluation of aero-optical distortion effects in PIV," *Exp. Fluids*, Vol. 39, 2005, pp. 246-256.

316 Elsinga, G. E., and Orlicz, G. C., "Particle Imaging through planar shock waves and associated velocimetry errors," *Exp. Fluids*, Vol. 56, No. 6, 2015, pp. 1-12.

317 Tedeschi, G., Gouin, H., Elena, M., "Motion Particles in supersonic flows," *Exp. in Fluids*, Vol. 26, 1999, pp. 288-296.

318 Mei, R., "Velocity fidelity of flow tracer particles," Exp. Fluids, Vol. 22, 1996, pp. 1-13.

319 Melling, A., "Tracer particles and seeding for Particle Image Velocimetry," *Meas. Sci. Technol.*, Vol. 8, No. 8, 1997, pp 1406-1416.

320 Vergine, F., and Maddalena, L., "Stereoscopic particle image velocimetry measurements of supersonic, turbulent, and interacting streamwise vortices: challenges and application," *Progress in Aerospace Sciences,* Vol. 66, 2014, pp. 1-16.

321 Lang, N., "Investigation of the flow tracking capabilities of tracer particles for the application of PIV to supersonic flow fields," In: Krner H, Hilbig R, editors, New results in numerical and experimental fluid mechanics, Notes on numerical fluid mechanics, Vol. 72, 1999, pp. 266–73.

322 Williams, O. J. H., Nguyen, T., Schreyer, A-M., and Smits, A., "Particle response analysis for particle image velocimetry in supersonic flows," *Physics of Fluids*, Vol. 27, 2015, 076101, doi: 10.1063/1.4922865

323 Fang, C., Hong, L., Zifeng, Y., and Hui, H., "Tracking characteristics of tracers particles for PIV measurements in supersonic flows," *Chinese J. of Aeronautics*, Vol. 30, No. 2, 2017, pp. 577-585.

324 Koroteeva, E., Mursenkova, I., Liao, Y., and Znamenskaya, I., "Simulating particle inertia for velocimetry measurements of a flow behind an expanding wave," *Physics of Fluids*, Vol. 30, 2018, 011702, doi: 10.1063/1.5012122.

325 Ragni, D., Schrijer, F., van Oudheusden, B. W., and Scarano, F., "Particle tracer response across shocks measured by PIV," *Exp. Fluids*, Vol. 50, 2011, pp. 53-64, doi: 10.1007/s00348-010-0892-2.

326 Humble, R. A., Peltier, S. J., and Bowersox, R. D. W., "Visualization of the structural response of a hypersonic turbulent boundary layer to convex curvature," *Physics of Fluids*, Vol. 24, 2012, 106103, doi: 10.1063/1.4761833.

327 Herring, G. C., Meyers, J. F., and Hart, R. C., "Shock-strength determination with seeded and seedless laser methods," *Meas. Sci. Technol.,* Vol. 20, 2009, 045304, doi: 10.1088/0957-0233/20/4/045304.

328 Lowe, K. T., Byun, G., and Simpson, R. L., "The Effect of Particle Lag on Supersonic Turbulent boundary Layer Statistics," *52nd Aerospace Sciences Meeting*, 13-17 January, 2014.

329 Sahoo, D., Schultze, M., and Smits, A. J., "Effects of Roughness on a Turbulent Boundary Layer in Hypersonic Flow," AIAA 2009-3678, *39th AIAA Fluid Dynamics Conference*, 22-25 June, San Antonio, TX, 2009.

330 Beresh, S. J., Comninos, M., Clemens, N. T., and Dolling, D. S., "The Effects of the Incoming Turbulent Boundary Layer Structure on a Shock-Induced Separated Flow," *36th AIAA Aerospace Sciences Meeting and Exhibit*, Aerospace Sciences Meetings, Reno, NV, 1997, doi.org/10.2514/6.1998-620 .

331 Combs, C. S., Clemens, N. T., "Simultaneous Measurements of Scalar and Velocity in a Mach 5 Turbulent Boundary Layer using Naphthalene PLIF and PIV," *54th AIAA Aerospace Science Meeting*, San Diego, CA, 4-8 January, 2016.

332 Wagner, J. L., Yuceil, K. B., Clemens, N. T., "Velocimetry Measurements of Unstart in an Inlet-Isolator Model in Mach 5 Flow," *AIAA Journal,* Vol. 48, No. 9, September 2010.

333 Page, W. A., and Arnold, J. O., "Shock Layer Radiation of Blunt Bodies at Reentry Velocities," NASA TR R-193.

334 James, C. S., "Experimental study of radiative transport from hot gases simulating in composition the atmospheres of mars and venus," *AIAA Journal*, Vol. 2, No. 3, 1964, pp. 470-475.

335 Terrazas-Salinas, I., Park, C., Strawa, A. W., Gopaul, N. K. J. M., and Taunk, J. S., "Spectral measurements in the arc column of an arc-jet wind tunnel," AIAA Paper 1994-2595.

336 Babikian, D., Park, C., and Raiche, G., "Spectroscopic determination of enthalpy in an arc-jet wind tunnel," AIAA Paper 95-0712.

337 Rob, M., Mack, H. J. L., Arepalli, S., and Scott, C., "Spectral measurements in the plenum of an arcjet wind tunnel," AIAA Paper 95-2126.

338 Mack, L., Rob, M., Arepalli, S., Scott, C., Milhoan, J., and Laux, C., "Radial spectral measurements in the plenum region of an arc jet wind tunnel," AIAA Paper 96-1897.

339 Park, C. S., Gokcen, T., Newfield, M. E., Fletcher, D. G., and Sharma, S. P., "Spectroscopic emission measurements within the blunt-body shock layer in an arc-jet flow," AIAA Paper 1997-0990.

340 Park, C. S., Newfield, M. E., Fletcher, D. G., and Gokcen, T., "Spectroscopic Measurement of the Flows in an Arc-Jet Facility," AIAA Paper 1998-0893.

341 Park, C. S., Fletcher, D. G., and Donohue, J. M., "Spatially Resolved Shock Layer Emission Measurements in an Arc-Jet Facility and Analysis," AIAA Paper 1999-1036.

342 Donohue, J., Fletcher, D., and Park, C., "Emission spectral measurements in the plenum of an arc-jet wind tunnel," AIAA Paper 98-2946.

343 Raiche, G., and Driver, D., "Shock Layer Optical Attenuation and Emission Spectroscopy Measurements During Arc Jet Testing with Ablating Models," AIAA Paper 2004-825.

344 Lequang, D., Babou, Y., Chazot, O., and André, P., "Investigation of Super-Sonic Air Plasma Jet Produced in the VKI Plasmatron Facility," *5th International Workshop Radiation of High Temperature Gases in Atmospheric Entry*. ESA, Barcelona, Spain, 2012.

345 Cipullo, A., Savino, L., Marenna, E., and De Filippis, F., "Thermodynamic state investigation of the hypersonic air plasma flow produced by the arc-jet facility SCIROCCO," *Aerospace Science and Technology*, Vol. 23, No. 1, 2012, pp. 358-362.

346 Helber, B., Chazot, O., Magin, T., and Hubin, A., "Space and Time-Resolved Emission Spectroscopy of Carbon Phenolic Ablation in Air and Nitrogen Plasmas," AIAA Paper 2013-2770.

347 Winter, M., and Prabhu, D. K., "Radiation Transport Analysis of Emission Spectroscopic Measurements in the Plenum Region of the NASA IHF Arc Jet Facility," AIAA Paper 2014-2489.

348 Hermann, T., Löhle, S., Zander, F., Fulge, H., and Fasoulas, S., "Characterization of a Reentry Plasma Wind-Tunnel Flow with Vacuum-Ultraviolet to Near-Infrared Spectroscopy," J*ournal of Thermophysics and Heat Transfer*, Vol. 30, No. 3, 2016, pp. 673-688.

349 Hermann, T. A., and Loehle, S., "Tomographic Optical Emission Spectroscopy for Plasma Wind Tunnel Testing," AIAA Paper 2016-3203.

350 Winter, M. W., Srinivasan, C., Charnigo, R., and Prabhu, D. K., "Spectroscopic Analysis of Nonequilibrium Excited State Chemistry in a NASA Arc Jet," *Journal of Thermophysics and Heat Transfer*, 2018, pp. 1-11.

351 Cruden , B. A., "Absolute Radiation Measurements in Earth and Mars Entry Conditions," RTO-EN-AVT-218, NATO, 2014.

352 Cruden, B. A., Prabhu, D., and Martinez, R., "Absolute Radiation Measurement in Venus and Mars Entry Conditions," *Journal of Spacecraft and Rockets*, Vol. 49, No. 6, 2012, pp. 1069-1079.

353 Brandis, A. M., Morgan, R. G., McIntyre, T. J., and Jacobs, P. A., "Nonequilibrium Radiation Intensity Measurements in Simulated Titan Atmospheres," *Journal of Thermophysics and Heat Transfer*, Vol. 24, No. 2, 2010, pp. 291-300.

354 Parker, R., MacLean, M., Holden, M., and Wakeman, T., "Shock Front Radiation Studies at CUBRC," *48th AIAA Aerospace Sciences Meeting*. AIAA, Orlando, Florida, 2010.

355 Takayanagi, H., and Fujita, K., "Absolute Radiation Measurements Behind Strong Shock Wave In Carbon Dioxide Flow for Mars Aerocapture Missions," AIAA Paper 2012-2744.

356 Takayanagi, H., and Fujita, K., "Infrared Radiation Measurement behind Shock Wave in Mars Simulant Gas for Aerocapture Missions," AIAA Paper 2013-2504.

357 Takayanagi, H., Fujita, K., Ishida, H., Yamada, K., and Abe, T., "Radiation intensity measurement in VUV wavelength region behind strong shock wave for future sample return missions," AIAA Paper 2014-2965.

358 Brandis, A. M., Cruden, B. A., Prabhu, D., Bose, D., McGilvray, M., and Morgan, R. G., "Analysis of Air Radiation Measurements Obtained in the EAST and X2 Shocktube Facilities," AIAA Paper 2010-4510.

359 Kozlov, P. V., "Experimental investigation of nitric oxide radiation in the shock-heated air," *J. Phys.*: Conf. Ser., Vol. 815, 2017, pp. 012033.

360 Zalogin, G. N., Kozlov, P. V., Kuznetsova, L. A., Losev, S. A., Makarov, V. N., Romanenko, Y. V., and Surzhikov, S. T., "Radiation excited by shock waves in a CO_2-N_2-Ar mixture: Experiment and theory," *Technical Physics*, Vol. 46, No. 6, 2001, pp. 654-661.

361 Parker, R., Dufrene, A., Holden, M., and Wakeman, T., "Shock-Front Emission Measurements at 10 km/s," AIAA Paper 2011-715.

362 Parker, R., MacLean, M., Dufrene, A., Holden, M., Desjardin, P., Weisberger, J., and Levin, D., "Emission Measurements from High Enthalpy Flow on a Cylinder in the LENS-XX Hypervelocity Expansion Tunnel," AIAA Paper 2013-1058.

[363] Takayanagi, H., Nomura, S., and Fujita, K., "Emission Intensity Measurements around Mars Entry Capsule with a Free-Piston-Driven Expansion Tube," AIAA Paper 2014-0516.

[364] Gu, S., Morgan, R. G., and McIntyre, T. J., "Study of the Afterbody Radiation during Mars Entry in an Expansion Tube," AIAA Paper 2017-0212.

[365] Nomura, S., Takayanagi, H., Fujita, K., Tanno, H., Komuro, T., and Itoh, K., "Spectroscopic Investigation on Anomalous Heating in Free Piston Shock Tunnel HIEST," AIAA Paper 2014-2545.

[366] Cruden, B. A., Brandis, A. M., Grinstead, J. H., Olejniczak, J., Kirk, L., Lillard, R. P., Tanno, H., and Komuro, T., "Measurement of Ultraviolet Radiative Heating Augmentation in HIEST Reflected Shock Tunnel," AIAA Paper 2015-2512.

[367] Sheikh, U. A., Wei, H., Lewis, S. W., James, C. M., Leyland, P., Morgan, R. G., and McIntyre, T. J., "Spectrally Filtered Imaging and Vacuum Ultraviolet Spectroscopy of Preheated Models in X2," *AIAA Journal*, Vol. 55, No. 12, 2017, pp. 4167-4180.

[368] Cruden, B. A., "Electron Density Measurement in Reentry Shocks for Lunar Return," *Journal of Thermophysics and Heat Transfer*, Vol. 26, No. 2, 2012, pp. 222-230.

[369] Herzberg, G., "Molecular Spectra and Molecular Structure I. Spectra of Diatomic Molecules," Malabar, FL: Krieger Publishing Co., 1950.

[370] Herzberg, G., "Molecular Spectra and Molecular Structure. II. Infrared and Raman Spectra of Polyatomic Molecules," Malabar, FL: Krieger Publishing Co., 1988.

[371] Herzberg, G., and Spinks, J. W. T., "Atomic spectra and atomic structure," Courier Corporation, 1944.

[372] Cruden, B. A., Rao, M. V. V. S., Sharma, S. P., and Meyyappan, M., "Neutral gas temperature estimates in an inductively coupled CF_4 plasma by fitting diatomic emission spectra," *J Appl Phys*, Vol. 91, 2002, pp. 8955-8964.

[373] Coburn, J. W., and Chen, M., "Optical emission spectroscopy of reactive plasmas: A method for correlating emission intensities to reactive particle density," *J Appl Phys*, Vol. 51, No. 6, 1980, p. 3134.

[374] Whiting, E., Park, C., Liu, Y., Arnold, J., and Paterson, J., "NEQAIR96, Nonequilibrium and Equilibrium Radiative Transport and Spectra Program: User's Manual," NASA RP-1389, 1996.

[375] Laux, C. O., "Radiation and Nonequilibrium Collisional-Radiative Models," von Karman Institute Lecture Series 2002-07, Physico-Chemical Modeling of High Enthalpy and Plasma Flows, 2002.

[376] Ciffone, D. L., and Borucki, J. G., "Spectral measurements of nitrogen continuum radiation behind incident shocks at speeds up to 13 km/sec," *Journal of Quantitative Spectroscopy and Radiative Transfer*, Vol. 11, No. 9, 1971, pp. 1291-1310.

[377] Hanson, R. K., "Shock-tube study of carbon monoxide dissociation kinetics," *The Journal of Chemical Physics*, Vol. 60, No. 12, 1974, pp. 4970.

[378] Kruse, T., and Roth, P., "Kinetics of C_2 Reactions during High-Temperature Pyrolysis of Acetylene," *J. Phys. Chem. A*, Vol. 101, 1997, pp. 2138-2146.

[379] Dufrene, A., MacLean, M., and Holden, M., "High Enthalpy Studies of Capsule Heating in an Expansion Tunnel Facility," AIAA Paper 2012-2998.

[380] Hollis, B. R., and Prabhu, D. K., "Assessment of Laminar, Convective Aeroheating Prediction Uncertainties for Mars-Entry Vehicles," *Journal of Spacecraft and Rockets*, Vol. 50, No. 1, 2013, pp. 56-68.

[381] MacLean, M. G., Dufrene, A. T., Carr, Z. R., Parker, R. A., and Holden, M. S., "Measurements and Analysis of Mars Entry, Decent, and Landing Aerothermodynamics at Flight-Duplicated Enthalpies in LENS-XX Expansion Tunnel," AIAA Paper 2015-1897.

[382] Grinstead, J. H., Wilder, M. C., Olejniczak, J., Bogdanoff, D. W., Allen, G. A., Dang, K., and Forrest, M. J., "Shock-heated Air Radiation Measurements at Lunar Return Conditions," AIAA Paper 2008-1244.

[383] Greenberg, R. B., Cruden, B. A., Grinstead, J. H., and Yeung, D., "Collection optics for imaging spectroscopy of an electric arc shock tube," *Proccedings of the SPIE*, Novel Optical Systems Design and Optimization XII. Vol. 7429, 2009, p. 74290H.

[384] Brandis, A. M., Johnston, C. O., Cruden, B. A., and Prabhu, D. K., "Equilibrium Radiative Heating from 9.5 to 15.5 km/s for Earth Atmospheric Entry," *Journal of Thermophysics and Heat Transfer*, 2016, pp. 1-15.

[385] Brandis, A. M., and Cruden , B. A., "Titan Atmospheric Entry Radiative Heating," AIAA Paper 2017-4534.

[386] Cruden, B. A., and Bogdanoff, D. W., "Shock Radiation Tests for Saturn and Uranus Entry Probes," *Journal of Spacecraft and Rockets*, Vol. 54, No. 6, 2017, pp. 1246-1257.

[387] Cruden, B. A., and Brandis, A. M., "Measurement and Prediction of Radiative Non-equilibrium for Air Shocks Between 7-9 km/s," AIAA Paper 2017-4535.

[388] Johnston, C. O., and Brandis, A. M., "Modeling of nonequilibrium CO Fourth-Positive and CN Violet emission in CO2–N2 gases," *Journal of Quantitative Spectroscopy and Radiative Transfer*, Vol. 149, 2014, pp. 303-317.

[389] Cruden, B. A., Brandis, A. M., and MacDonald, M. E., "Characterization of CO Thermochemistry in Incident Shockwaves," AIAA Paper 2018-3768.

[390] Luque, J. "LIFBASE, Database and spectral simulation for diatomic molecules." *SRI International Report* 99 (1999).

[391] Tibère-Inglesse, A. C., McGuire, S., and Laux, C. O., "Nonequilibrium radiation from a recombining nitrogen plasma," AIAA Paper 2018-0241.

[392] MacDonald, M. E., Brandis, A. M., and Cruden, B. A., "Temperature and CO Number Density Measurements in Shocked CO and CO_2 via Tunable Diode Laser Absorption Spectroscopy," AIAA Paper 2018-4067.

[393] Fletcher, D.G., "Arcjet Flow Properties Determined from Laser-Induced Fluorescence of Atomic Nitrogen," AIAA Paper 98-0205, Jan. 1998.

[394] Grinstead, J. H., Wilder, M. C., Porter, B., Brown, J., Yeung, D., Battazzo, S., and Brubaker, T., "Consolidated Laser-Induced Fluorescence Diagnostic Systems for the NASA Ames Arc Jet Facilities," *32nd AIAA Aerodynamic Measurement Technology and Ground Testing Conference*, AIAA AVIATION Forum, (AIAA 2016-4159). https://doi.org/10.2514/6.2016-4159.

[395] Bathel, B. F., Johansen, C. T., Danehy, P. M., Inman, J. A., Jones, S. B., and Goyne, C. P., "Hypersonic Boundary Layer Transition Measurements Using $NO_2 \rightarrow NO$ Photo-dissociation Tagging Velocimetry," *41st AIAA Fluid Dynamics Conference and Exhibit*, 2011.

[396] Bivolaru, D., Danehy, P. M., Gaffney, R. L. Jr., and Cutler, A. D., "Direct-View Multi-Point Two-Component Interferometric Rayleigh Scattering Velocimeter," *46th AIAA Aerospace Sciences Meeting and Exhibit*, 7-10 January 2008, Reno, Nevada, AIAA Paper 2008-236.